Distribution Agreement

In presenting this thesis or dissertation as a partial fulfillment of the requirements for an advanced degree from Emory University, I hereby grant to Emory University and its agents the non-exclusive license to archive, make accessible, and display my thesis or dissertation in whole or in part in all forms of media, now or hereafter known, including display on the world wide web. I understand that I may select some access restrictions as part of the online submission of this thesis or dissertation. I retain all ownership rights to the copyright of the thesis or dissertation. I also retain the right to use in future works (such as articles or books) all or part of this thesis or dissertation.

Signature:

_____ _____

Neil R. Anthony Date

Advanced Time-Resolved Fluorescence Microscopy Techniques for the Investigation of Peptide Self-Assembly

By

Neil R. Anthony
Doctor of Philosophy

Physics

_____
Dr. Keith M. Berland
Advisor

_____
Dr. Stefan Boettcher
Committee Member

_____
Dr. David Lynn
Committee Member

_____
Dr. Connie Roth
Committee Member

_____
Dr. Eric Weeks
Committee Member

Accepted:

_____
Lisa A. Tedesco, Ph.D.
Dean of the James T. Laney School of Graduate Studies

_____ Date

Advanced Time-Resolved Fluorescence Microscopy Techniques for the Investigation of Peptide Self-Assembly

By

Neil R. Anthony
MPhys., University of Bath, UK, 2007

Advisor: Keith M. Berland, PhD.

An abstract of
A dissertation submitted to the Faculty of the
James T. Laney School of Graduate Studies of Emory University
in partial fulfillment of the requirements for the degree of
Doctor of Philosophy
in Physics
2013

Abstract

Advanced Time-Resolved Fluorescence Microscopy Techniques for the Investigation of Peptide Self-Assembly

By Neil R. Anthony

The ubiquitous cross β sheet peptide motif is implicated in numerous neurodegenerative diseases while at the same time offers remarkable potential for constructing isomorphic high-performance bionanomaterials. Despite an emerging understanding of the complex folding landscape of cross β structures in determining disease etiology and final structure, we lack knowledge of the critical initial stages of nucleation and growth. In this dissertation, I advance our understanding of these key stages in the cross-β nucleation and growth pathways using cutting-edge microscopy techniques. In addition, I present a new combined time-resolved fluorescence analysis technique with the potential to advance our current understanding of subtle molecular level interactions that play a pivotal role in peptide self-assembly.

Using the central nucleating core of Alzheimer's Amyloid-β protein, Aß(16 22), as a model system, utilizing electron, time-resolved, and non-linear microscopy, I capture the initial and transient nucleation stages of peptide assembly into the cross β motif. In addition, I have characterized the nucleation pathway, from monomer to paracrystalline nanotubes in terms of morphology and fluorescence lifetime, corroborating the predicted desolvation process that occurs prior to cross-β nucleation. Concurrently, I have identified unique heterogeneous cross β domains contained within individual nanotube structures, which have potential bionanomaterials applications. Finally, I describe a combined fluorescence theory and analysis technique that dramatically increases the sensitivity of current time-resolved techniques. Together these studies demonstrate the potential for advanced microscopy techniques in the identification and characterization of the cross-β folding pathway, which will further our understanding of both amyloidogenesis and bionanomaterials.

Advanced Time-Resolved Fluorescence Microscopy Techniques for the Investigation of Peptide Self-Assembly

By

Neil R. Anthony
MPhys., University of Bath, UK, 2007

Advisor: Keith M. Berland, PhD.

A dissertation submitted to the Faculty of the
James T. Laney School of Graduate Studies of Emory University
in partial fulfillment of the requirements for the degree of
Doctor of Philosophy
in Physics
2013

Acknowledgements

I would like to thank my advisor Keith for teaching me the many skills needed to be a successful microscopist. I have learned a great deal from Keith's unfaltering and vast technical knowledge. I truly appreciate his influence as a scientist and his attitude towards the scientific endeavor, principles which I will continue to apply in my coming career. Keith sets the bar high, and has given me space to rise to the challenge. Also, I'd like to thank my committee for their time and feedback throughout the stages of my research.

In addition, I would like to thank all the great people I've worked and socialized with from David Lynn's laboratory, who adopted me as a pseudo lab member through our collaboration. It has been a real pleasure interacting and collaborating with everybody. Thank you to Savannah for her friendship and great sense of humour, to Dibyendu for his warm and positive attitude, and Tony, Tolu, Lisa, JunJun, and Chen for their interesting collaborations. Also, thank you to Seth for his time and enthusiasm in our collaborations, and notably for his discovery of the fundamental Seth particle and all its flavours. I want to make a special thanks to Jay and Anil, with whom I would have never been able to get to grips with the chemistry aspect of my dissertation research. Their friendship, good coffee and conversation over the years have been a salvation from the frustrations of experimental work, and provided the opportunity for invaluable discourse. I am extremely grateful for Anil's help during the stressful dissertation writing stages. And of course, I would like to thank Dave for his unwaning positive attitude and drive to bring out the best in people. Dave has played a significant role in

numerous avenues of my personal development, through collaborations, my ORDER teacher/scholarship, and outreach work with the Emory Arts.

I'd like to thank all the great people of the physics department, past and present, that have been a pleasure to work with over the years, including Suzette, Bill, Jessica, Kazem, Trent, Adonis, Hanlin, Justin, Kurt, Laura, and Vincent. Thank you to all the Young Emory Physics members and association for the great times during planning and events, and to the biophysics group for the journal clubs and fun picnics. I would like to specifically thank Art and Jason for their IT feedback and conversation, Cody for his help making things for work and for bike projects, and to Jon for his electronics know-how, bike talk and laughter. Also, thanks to Connie, Paulette, and Calvin for their administration help. And last but definitely not least, I'd like to thank Wesley for his friendship, advice, and laughter, from my internship to degree completion and hopefully long into the future.

In terms of coding and data analysis I'd like to thank all of Wavemetrics staff for their excellent customer support, specifically John 'the fit' Weeks for his help understanding the subtleties of Igor's fitting routines. Also, I thank everybody of the Igor mailing list group that have been an invaluable resource.

Across the pond, I thank all of my Family in the UK for their support in my previous careers (or lack there of) and into my return to education, both in Bath and here in Atlanta. Without their help I would not have been able to change directions, for which I am extremely grateful. Here in the US, I thank all my in-laws for their warm welcoming nature and support. I hope to attend the next family event without a laptop and work to be done.

Last, and the inverse of least, I would like to thank my lovely wife Shana for her love and support for every step of the journey. She has been a great source of academic advice, helping to keep me on the right track, a teacher, helping my writing take form, and my best friend who has always been there for me. I thank Shana for all these things in addition to putting up with the grumpy old man that I am at times, exacerbated by the trials and tribulations of a PhD.

Table of Contents

Figure List

Figure 8–6 –Sections of χ_R^2 surfaces obtained from fitting single species models to calculated data of a binary mixture over a range of parameter values.

Table List

Chapter 1

Introduction and Scope

1.1 Microscopy in Scientific Research

The turn of the 17th century saw the first investigations of biological specimens using light microscopy [1]. These early glimpses into the microscopic world marked the beginning of a longstanding and continuing synergy between the life sciences and microscopy. The microscope has played a seminal role in the discoveries of cellular biology; from the first intravital studies of Antoni van Leeuwenhoek using a single lens microscope [2] and Robert Hooke's observations of cells with a compound microscope [3], to Robert Brown's naming of the cell nucleus [4]. These microscopic discoveries gave rise to numerous fields of research, including cell biology, virology, genetics, pathology, and neuroscience [5]. This symbiosis continues to strengthen into the 21st century with the development of clinical applications of advanced microscopy and optical techniques [6-10]; whereby 400 years of discovery directly impact the longevity and quality of our lives. Here I continue the longstanding tradition of microscopy in the life sciences through the application of time-resolved fluorescence techniques (Chapter 2) toward the investigation of amyloidogenic peptide nanotubes.

Light microscopy offers a unique set of capabilities amenable to cellular and sub-cellular investigations. The weak interaction of light with matter permits visualization of cellular structure without excessive perturbation of the system. The use of visible light in microscopy is capable of providing resolution high enough to discern, for example, red blood cells, colloids, bacteria, and sub-cellular compartments. Many of the early advances in light microscopy stemmed from the seminal optical theory developed by Ernst Abbe in 1873 [11], and his exquisite production of reduced aberration optical components [12]. His theory is often referred to as 'diffraction limited' resolution, and until recently [13-17] has set the limit of resolution attainable in optical microscopy. An

ever closer view into cellular structure was provided *via* the significantly shorter wavelength of electrons, harnessed by Knoll and Ruska in 1931 [18]. Electron microscopy (EM), however, requires harsh sample preparation incongruous to imaging live samples, and as such light microscopy has been continually developed towards *in vivo* application.

Biological samples are for the most part transparent to visible light, thus additional methods to provide contrast are required. A number of optical contrast methods including dark field [19], phase-contrast [20], and interference microscopy [21] have been developed, yet for the most part exogenous dyes and stains have been used to provide additional contrast, paving the way towards biospecificity in microscopy. During the mid 19th Century, David Brewster, John Herschel, and Edmond Becquerel all made observations of a "dispersive" light, emitted from solutions irradiated by white light. These observations were accredited as the first documented cases of the fluorescence phenomenon [22]. Shortly after, Sir George Stokes coined the term 'fluorescence', and described that fluorescence emission occurs at longer wavelengths than the exciting light. This offset is referred to as the Stokes Shift [23], and fortuitously permits the effective optical separation of the excitation and emission wavelengths in a fluorescence microscope (Chapter 2). Subsequent development of fluorescence compounds developed quickly, starting with the early work by Henry Perkin during the same decade [24], Adolph Von Baeyer in 1871 [25], the pivotal biospecific immunofluorescence probes of Albert Coons in 1941 [26], and the famous discovery of fluorescent proteins by Shimomura, Johnson and Saiga in 1962 [27]. There are now a vast array of fluorescent dyes and proteins commonly used in life sciences research [28-31] and in combination with biospecific conjugates and probes [23, 32-34] provide both exquisite sensitivity and biospecificity in biological fluorescence imaging.

The early microscopic investigations were for the most part qualitative, from the human eye as the primary detector to the first recorded images using photography. An example that transitioned into quantitative microscopy was developed by Nipkow in the late 19th Century in the form of a "flying spot" raster scanning microscope that translated images into Morse code [29, 35], although it wasn't until the 1950s that the "Nipkow Disk" was used to produce cellular images [36]. Later that decade, in 1957, Marvin Minsky designed the confocal microscope [37], revolutionizing quantitative microscopy. The confocal design utilizes a pinhole to reduce the field of view, blocking out of focus light and thus providing optical sectioning, improved resolution and signal to noise, and serves as a platform for numerous subsequent quantitative applications [29]. Essentially the same design is used today, almost 6 decades on, and has become one of the most commonly used microscopic imaging methods in the life sciences [29]. An additional technical advance of particular relevance is that of non-linear microscopy. Maria Göppert-Mayer's two-photon quantum transition theory of 1931 [38] was first experimentally realized using a ruby laser in 1961 [39]. Two-photon excitation was subsequently applied to laser scanning microscopy in the 1970s [40, 41] and to biological samples in 1990 [42] providing intrinsic (pin-hole free) optical sectioning deep within biological samples.

The optically and theoretically well defined sub-micrometer resolution observed at the objective focus, was paralleled by an evolution in fluorescence detection (from photocells, to photomultipliers and semiconductor photodiodes), which completed the transition from qualitative cellular level imaging to the current era of quantitative single molecule sensitivity microscopy. The combination of confocal and non-linear microscopy with time-resolved spectroscopies, such as fluorescence correlation

spectroscopy (FCS) [43-45], and fluorescence lifetime measurements [46, 47], provided spatially resolved spectroscopy, radically enhancing our view of molecular level behaviour. The use of quantitative fluorescence is an increasingly important part of biomolecular research, and forms a running thread throughout the chapters of this dissertation. Chapter 2 serves as an introduction to quantitative fluorescence microscopy, highlighting fluorescence measurements applied throughout the remaining chapters.

1.2 Alzheimer's Disease and Amyloid-β

The 'father of modern pathology', Ruldolf Virchow, demonstrated early biospecificity in 1854 using iodine stain to classify the pathological aggregate amyloid [48, 49] (Chapter 3). Later, Congo Red dye binding in combination with the characteristic apple green birefringence under polarized microscopy became the first adopted diagnostic criterion of amyloid formation [48]. It was not until 1959 that the second characteristic of amyloid emanated with EM, revealing the ubiquitous, micrometer long, twisted fibrils ~100Å wide [50].

Shortly after the turn of the 20th century, Alois Alzheimer reported medical cases associating dementia with neurofibrillary tangles [51-53]. Although Alzheimer himself did not claim to have discovered a new disease, Emil Kraepelin assigned the disease in his name resulting in what is currently and incorrectly referred to as Alzheimer's disease [54]. The neurofibrillary tangles and extracellular plaque pathologies of Alzheimer's disease are associated with the microtubule stabilizing Tau protein and the Amyloid-β peptide respectively [55]. Currently 25 different proteins are associated with the mounting list amyloidogenic diseases [56], the majority of which are thought to stem

from protein misfolding events and aggregation, yet the exact pathogenesis still remains elusive [57].

The insoluble plaques common to Alzheimer's disease have been long suspected as the toxic species [58, 59], yet recent work suggests the role of soluble oligomers in toxicity [59, 60], although a general consensus is that the entire process leading to insoluble fibrous plaques is of vital interest. As such, research from numerous scientific disciplines have culminated in investigating the stages of the nucleation and growth pathways. In this dissertation, florescence techniques are applied to understand the assembly of the central nucleating core of the Amyloid-β peptide: Aß(16-22). This seven residue sequence is one of the shortest sequences to form amyloid, verified by its cross-β [61, 62] structure (Chapter 3), apple green birefringence, and micrometer long fibers observed by EM [62-65]. Aß(16-22) is highly responsive to solvent pH, forming characteristic amyloid fibers at pH 7 and bilayer ~53 nm diameter nanotubes at pH 2 [61, 66]. Aß(16-22) is the second of the two paralleling threads of this dissertation, and as such, Chapter 3 provides an introduction to the characterization and imaging of Aß(16-22) amyloidogenic structures, including both previous work of our collaborating groups and others, together with some introductory highlights of Chapters 4 to 6.

Hydrophobic peptide collapse into unstructured aggregates[*], provides an environment where the initial stages of nucleation can occur [67-70]. Within this solvent-excluding environment, intermolecular interactions and conformational sampling become more energetically favorable, allowing the initial three-dimensional organization of the amyloid nucleus. The different manifestations of peptide structure and morphology are

[*] Unstructured peptide aggregates are also referred to as "molten globules", with reference to protein folding.

termed 'peptide phases'. These phases are not connected in a simple linear fashion, but instead the accessible phases form a network, where for example, monomers can exchange with both unstructured aggregates and mature elongated cross-β structures [71]. Chapter 4 describes the observed transitions between unstructured aggregates and the initial formation of crystalline cross-β phases, providing insights into the multidimensional folding/misfolding pathways between accessible phases.

In vitro studies of amyloid nucleation have consistently revealed a 'lag-phase'[†] [72, 73], whereby solutions containing amyloidogenic peptide appear inactive for an initial period of time before the appearance of insoluble aggregates. The inactivity depends on a multitude of experimental parameters, including peptide sequence, concentration, solvent, etc. The lag phase is also determined by the resolution of the experimental technique used to assess the degree of aggregation. At the molecular level, inactive solutions are assumed to be in the early stages of nucleation and aggregation, as peptides sample the initial stages of interaction and collapse. A number of more recent studies have highlighted the role of interfaces in the nucleation process. Air-water-interfaces (AWIs), hydrophobic-hydrophilic-interfaces (HHIs), and lipid bilayers and micelles have been shown to dramatically decrease the nucleation lag phase [60, 74-80]. The propensity for peptide alignment at interfaces, together with the increase in concentration transitioning from three- to two-dimensions, creates a local environment amenable for phase transitions. Interfaces are also thought to allow access to subtly different nucleation pathways leading to variations in final amyloid form [60, 74, 81], with a role implicated in toxicity, which is yet to be determined. Chapter 5 utilizes AWIs and HHIs for the nucleation of Aß(16-22) cross-β peptide nanotubes, and using a small

[†] A lag-phase refers to a temporal delay in peptide assembly that precedes nucleation and should not be confused with peptide phase, used as a synonym for a state of matter.

fraction of incorporated fluorescent peptide (Rh17-22) I begin to map the stages of nanotube nucleation and structure pathways using fluorescence lifetime measurements.

1.3 Fluorescence Lifetime and Rh17-22

In addition to his early observation of fluorescence, Becquerel also was the first to investigate temporal nature of phosphorescence [22], a closely related process. Both fluorescence and phosphorescence require an excitation source, and result in emission at a longer wavelength (lower energy) (Chapter 2.2 What is fluorescence?). This excitation/emission process is not instantaneous, by which molecules remain in an excited state for a finite length of time. Given that fluorescence has an excited state lifetime of nanoseconds, compared to the phosphorescence lifetime of seconds, it is of no surprise that phosphorescence was studied long before fluorescence. The excited state fluorescence lifetime depends not only on the molecule's structure, but the influence of its immediate surroundings, which can perturb the excited state, altering the time to emission or removing the excited state energy by means other than fluorescence.

The modern day equivalent of Becquerel's phosphorscope can be found in time-correlated single photon counting (TCSPC) hardware [82]. Using accurate pulsed-excitation sources together with extremely sensitive single photon counting detectors, TCSPC setups can determine the time difference between excitation and emission to an accuracy of picoseconds. This allows for changes in the fluorescence lifetime of single molecules to be detected and the effects of their immediate environment to be tested (~nm). A hybrid peptide designed for following the dynamics Aß(16-22) nucleation and growth [83], Rh17-22, has been developed by replacing residue 16, K (Lys), with a similarly charged rhodamine-110 dye. Chapter 5 combines the fluorescence lifetime

reported by the Rh17-22 probe across the different available peptide phases and phase transitions discussed in Chapter 4 in order to build a prospective mapping between fluorescence lifetime value and phase structure.

1.4 Bionanomaterials and Exogenous Factors

Exogenous factors in nucleation such as protein chaperones [84, 85], nucleic-acid bases [86], and metal ions [87-89] can significantly influence the nucleation pathways of amyloid formation. Metal ions are thought to play a specific role in cellular toxicity [89-91]. Interestingly, different metal ions can switch between accelerating and inhibiting fiber formation [87, 88, 91, 92]. For functionalized bionanomaterials, metal binding sites on amyloid nanotubes are being examined for potential nanotemplating and self-assembling nanocircuity [93-95]. Our groups have previously demonstrated the potential of functionalized peptide nanotubes using exogenous Rh16-22 fluorescence labels for light harvesting when co-assembled with Aß(16-22) [96]. The influence of exogenous factors in the perturbed nucleation of hybrid amyloid structures is investigated in Chapter 6, following the influence of rhodamine in the initial collapse and evolution of low concentration solutions of Rh17-22.

First noted in yeast prion proteins [97], the polymorphic nature of amyloid formation has been strongly implicated in pathogenesis [98-100]. Even in our simple Aß(16-22) model system, stark polymorphism (from fibers to nanotubes) can be induced by a single proton [61], exemplifying the sensitively of self-assembled systems. Commonly used techniques for determining amyloid structure can determine polymorphisms in terms of sub-populations of bulk measurements [101], yet are not able to discern the difference between two distinct populations that contribute to the entire single *vs.* different sub-

regions of a single population of elongated structures. Thioflavin-T (ThT) fluorescence and atomic force microscopy (AFM) analyses, however, can determine heterogeneous amyloid growth *via* morphology and persistence length [102, 103]. AFM requires dried samples, while ThT binds to amyloid structures only once they have matured[‡]. Using our incorporated Rh17-22 fluorescent reporter, in Chapter 8 I detail the characterization of heterogeneous nanotube structures using fluorescence lifetime imaging microscopy (FLIM). In combination with the observed heterogeneities in amyloid structure, secondary nucleation and pathways are beginning to be discussed [102, 103, 106-109]. The propagation of long range order from heterogeneous seeding points in secondary nucleation, and the propagation of structural changes within a single structure discussed Chapter 8, have potential applications for modulated chemical potential gradients in bionanomaterials.

1.5 Time-Resolved Fluorescence Microscopy

Fluorescence lifetime bolsters the information available from incorporated Rh17-22 labels, providing feedback on local environment in addition to the locality and morphology provided by fluorescence imaging. While the application of fluorescence techniques is extremely valuable for investigations of peptide aggregation, improvements in resolution would provide the much needed extra pieces of the puzzle. The observation of Aß(16-22) nanotube nucleation and growth was investigated in the studies that first employed the Rh17-22 fluorescent probe [83]. Using fluorescence recovery after photobleaching (FRAP), nanotube growth was seen to stem from unstructured aggregates and continue from the nascent ends of the growing nanotube structures. In addition, the composition of the soluble species near growing nanotubes was assessed

[‡] also reported to bind non-amyloid structures [104, 105].

using fluorescence correlation spectroscopy (FCS), and found to be monomer within the resolution of FCS. Time resolved analysis of fluorescence fluctuations allows FCS to determine molecular diffusion coefficients, concentrations and molecular brightnesses of fluorescent species in solution. The resolution of FCS requires that a monomer must aggregate to a minimum of a five molecules (5-mer) before it can be distinguished by its change in diffusion coefficient. Given the implicated toxicity of transient oligomeric species the investigations presented in Chapters 4-7 could benefit from a more sensitive technique capable of distinguishing monomers from dimers. In Chapter 8 I describe a newly developed combined analysis technique, τFCS, which is able to resolve diffusing species with identical diffusion coefficients and brightnesses, using fluorescence lifetime as a distinguishing metric. The application of this technique will provide a much needed increase in resolvability of dynamic species, and hopefully become the successor to FCS measurements.

In this dissertation I have detailed a journey through applying advanced time-resolved fluorescence techniques for investigating amyloid nanotube nucleation and heterogeneity. This research elucidates key but subtle points in the murky results of protein mis-folding and self-assembly. Upon retrospection we truly are "standing on the shoulders of giants", from the earliest musings of Euclid, on the concept of light itself, to the scientific revolution harnessing light in the 'new' field of optics, to the current boom of photonics, biophotonics, and bionanoengineering. Never in history has there been a time where more overlapping culminations of scientific research can be found connected by focus of a single objective lens.

1.6 Literature Cited

1. Bradbury, S., *Landmarks in Biological Light Microscopy*. Journal of Microscopy, 1989. **155**(3): p. 281-305.
2. van Leeuwenhoek, A., *Arcana Naturae Detecta*. 1696, Netherlands: Leiden.
3. Hooke, R., *Micrographia*. 1665: London.
4. R., A.B., *Robert Brown and the Cell Theory*. Nature, 1932. **130**: p. 66-66.
5. Masters, B.R., *History of the Optical Microscope in Cell Biology and Medicine*, in *Els*. 2001, John Wiley & Sons, Ltd.
6. Yang, Y., et al., *Integrated Optical Coherence Tomography, Ultrasound and Photoacoustic Imaging for Ovarian Tissue Characterization*. Biomedical optics express, 2011. **2**(9): p. 2551-2561.
7. Hamdan, R., et al., *Optical Coherence Tomography: From Physical Principles to Clinical Applications*. Archives of Cardiovascular Diseases, 2012. **105**(10): p. 529-534.
8. Sevick-Muraca, E.M., *Translation of near-Infrared Fluorescence Imaging Technologies: Emerging Clinical Applications*, in *Annual Review of Medicine, Vol 63*, C.T. Caskey, C.P. Austin, and J.A. Hoxie, Editors. 2012, Annual Reviews: Palo Alto. p. 217-231.
9. Weinigel, M., et al., *Clinical Multiphoton Endoscopy with Flim Capability*. 2013: p. 85882E-85882E.
10. Orosco, R., R. Tsien, and Q. Nguyen, *Fluorescence Imaging in Surgery*. Biomedical Engineering, IEEE Reviews in, 2013. **PP**(99): p. 1-1.
11. Abbe, E., *Beiträge Zur Theorie Des Mikroskops Und Der Mikroskopischen Wahrnehmung*. Archiv für mikroskopische Anatomie, 1873. **9**(1): p. 413-418.
12. Volkmann, H., *Ernst Abbe and His Work*. Applied Optics, 1966. **5**(11): p. 1720-&.
13. Hell, S.W. and J. Wichmann, *Breaking the Diffraction Resolution Limit by Stimulated-Emission - Stimulated-Emission-Depletion Fluorescence Microscopy*. Optics Letters, 1994. **19**(11): p. 780-782.

14. Huang, B., et al., *Three-Dimensional Super-Resolution Imaging by Stochastic Optical Reconstruction Microscopy*. Science, 2008. **319**(5864): p. 810-813.

15. Gustafsson, M.G.L., *Extended Resolution Fluorescence Microscopy*. Current Opinion in Structural Biology, 1999. **9**(5): p. 627-628.

16. Gustafsson, M.G.L., *Nonlinear Structured-Illumination Microscopy: Wide-Field Fluorescence Imaging with Theoretically Unlimited Resolution*. Proceedings of the National Academy of Sciences of the United States of America, 2005. **102**(37): p. 13081-13086.

17. Hess, S.T., T.P.K. Girirajan, and M.D. Mason, *Ultra-High Resolution Imaging by Fluorescence Photoactivation Localization Microscopy*. Biophysical Journal, 2006. **91**(11): p. 4258-4272.

18. Knoll, M. and E. Ruska, *The Electron Microscope*. Zeitschrift Fur Physik, 1932. **78**(5-6): p. 318-339.

19. Koehler, A., *New Method of Illumination for Phomicrographical Purposes*. JR Microsc. Soc, 1894. **14**: p. 261-262.

20. Zernike, F., *The Concept of Degree of Coherence and Its Application to Optical Problems*. Physica, 1938. **5**(8): p. 785-795.

21. Francon, M. and G. Nomarski, *Lame De Phase a Contraste Variable Par Reflexion*. Comptes Rendus Hebdomadaires Des Seances De L Academie Des Sciences, 1950. **230**(15): p. 1392-1394.

22. Valeur, B. and M.r.N. Berberan-Santos, *A Brief History of Fluorescence and Phosphorescence before the Emergence of Quantum Theory*. Journal of Chemical Education, 2011. **88**(6): p. 731-738.

23. Lakowicz, J., *Principles of Fluorescence Spectroscopy*. 3rd ed. 2006: Springer.

24. Meth-Cohn, O. and M. Smith, *What Did W. H. Perkin Actually Make When He Oxidised Aniline to Obtain Mauveine?* Journal of the Chemical Society, Perkin Transactions 1, 1994. **0**(1): p. 5-7.

25. Baeyer, A., *Ueber Eine Neue Klasse Von Farbstoffen*. Berichte der deutschen chemischen Gesellschaft, 1871. **4**(2): p. 555-558.

26. Coons, A.H., H.J. Creech, and R.N. Jones, *Immunological Properties of an Antibody Containing a Fluorescent Group*. Proceedings of the Society for Experimental Biology and Medicine, 1941. **47**(2): p. 200-202.

27. Shimomura, O., F.H. Johnson, and Y. Saiga, *Extraction, Purification and Properties of Aequorin, a Bioluminescent Protein from Luminous Hydromedusan, Aequorea*. Journal of Cellular and Comparative Physiology, 1962. **59**(3): p. 223-&.

28. Johnson, I., *Practical Considerations in the Selection and Application of Fluorescent Probes*, in *Handbook of Biological Confocal Microscopy*, J.B. Pawley, Editor. 2006, Springer US. p. 353-367.

29. Pawley, J., *Handbook of Biological Confocal Microscopy*. 3rd ed. 2006: Springer.

30. Johnson, I., *Review: Fluorescent Probes for Living Cells*. The Histochemical Journal, 1998. **30**(3): p. 123-140.

31. Giepmans, B.N.G., et al., *The Fluorescent Toolbox for Assessing Protein Location and Function*. Science, 2006. **312**(5771): p. 217-224.

32. Lee, K., L.K. Povlich, and J. Kim, *Recent Advances in Fluorescent and Colorimetric Conjugated Polymer-Based Biosensors*. Analyst, 2010. **135**(9): p. 2179-2189.

33. Feng, X.L., et al., *Water-Soluble Fluorescent Conjugated Polymers and Their Interactions with Biomacromolecules for Sensitive Biosensors*. Chemical Society Reviews, 2010. **39**(7): p. 2411-2419.

34. Thomas, S.W., G.D. Joly, and T.M. Swager, *Chemical Sensors Based on Amplifying Fluorescent Conjugated Polymers*. Chemical Reviews, 2007. **107**(4): p. 1339-1386.

35. Nipkow, P., *Optical Disk*. German patent, 1884. **30**(105): p. 15.

36. Mellors, R.C. and R. Silver, *A Microfluorometric Scanner for the Differential Detection of Cells - Application to Exfoliative Cytology*. Science, 1951. **114**(2962): p. 356-360.

37. Minsky, M., *Memoir on Inventing the Confocal Scanning Microscope*. Scanning, 1988. **10**(4): p. 128-138.

38. Göppert-Mayer, M., *Über Elementarakte Mit Zwei Quantensprüngen*. Annalen der Physik, 1931. **401**(3): p. 273-294.

39. Kaiser, W. and C.G.B. Garrett, *2-Photon Excitation in Caf2 - Eu2+*. Physical Review Letters, 1961. **7**(6): p. 229-&.

40. Sheppard, C.J.R. and R. Kompfner, *Resonant Scanning Optical Microscope*. Applied Optics, 1978. **17**(18): p. 2879-2882.

41. Hellwart.R and Christen.P, *Nonlinear Optical Microscopic Examination of Structure in Polycrystalline Znse*. Optics Communications, 1974. **12**(3): p. 318-322.

42. Denk, W., J.H. Strickler, and W.W. Webb, *2-Photon Excitation in Laser Scanning Microscopy*. Science, 1990. **248**(4951): p. 73-76.

43. Magde, D., *Chemical-Kinetics and Fluorescence Correlation Spectroscopy*. Quarterly Reviews of Biophysics, 1976. **9**(1): p. 35-47.

44. Krichevsky, O. and G. Bonnet, *Fluorescence Correlation Spectroscopy: The Technique and Its Applications*. Reports on Progress in Physics, 2002. **65**(2): p. 251-297.

45. Mutze, J., T. Ohrt, and P. Schwille, *Fluorescence Correlation Spectroscopy in Vivo*. Laser & Photonics Reviews, 2011. **5**(1): p. 52-67.

46. Rodgers, M.A.J. and P.A. Firey, *Instrumentation for Fluorescence Microscopy with Picosecond Time Resolution*. Photochemistry and Photobiology, 1985. **42**(5): p. 613-616.

47. Minami, T., et al., *Fluorescence Lifetime Measurements under a Microscope by the Time-Correlated Single-Photon Counting Technique*. Journal of Luminescence, 1986. **35**(5): p. 247-253.

48. Sipe, J.D. and A.S. Cohen, *Review: History of the Amyloid Fibril*. J. Struct. Biol., 2000. **130**(2-3): p. 88-98.

49. Virchow, R., *Zur Cellulose-Fruge*. Virchows Arch., 1855. **8**: p. 140-144.

50. Shiraham.T and A.S. Cohen, *High-Resolution Electron Microscopic Analysis of Amyloid Fibril*. Journal of Cell Biology, 1967. **33**(3): p. 679-&.

51. Alzheimer, A., *Über Eine Eigenartige Erkrankung Der Hirnrinde*. Allgemeine Zeits. Psychiat. Psychisch-Gerichtlich Med., 1907. **64**: p. 146-148.

52. Alzheimer, A., *Über Den Abbau Des Nervengewebes*. Centralblatt für Nervenheilkunde und Psychiatrie, 1906. **29**: p. 526-528.

53. Alzheimer, A., *Über Eigenartige Krankheitsfälle Des Späteren Alters*. Zeitschrift für die gesamte Neurologie und Psychiatrie, 1911. **4**(1): p. 356-385.

54. Berrios, G.E., *Alzheimer's Disease: A Conceptual History*. International Journal of Geriatric Psychiatry, 1990. **5**(6): p. 355-365.

55. Murphy, M.P. and I.I.I.H. LeVine, *Alzheimer's Disease and the Amyloid-B Peptide*. Journal of Alzheimer's Disease, 2010. **19**(1): p. 311-323.

56. Eisenberg, D. and M. Jucker, *The Amyloid State of Proteins in Human Diseases*. Cell, 2012. **148**(6): p. 1188-203.

57. Selkoe, D.J., *Preventing Alzheimer's Disease*. Science, 2012. **337**(6101): p. 1488-92.

58. Murphy, R.M., *Peptide Aggregation in Neurodegenerative Disease*. Annual Review of Biomedical Engineering, 2002. **4**: p. 155-174.

59. Chiti, F. and C.M. Dobson, *Protein Misfolding, Functional Amyloid, and Human Disease*, in *Annual Review of Biochemistry*. 2006. p. 333-366.

60. Nichols, M.R., et al., *Amyloid-B Aggregates Formed at Polar-Nonpolar Interfaces Differ from Amyloid-B Protofibrils Produced in Aqueous Buffers*. Microscopy Research and Technique, 2005. **67**(3-4): p. 164-174.

61. Mehta, A.K., et al., *Facial Symmetry in Protein Self-Assembly*. J. Am. Chem. Soc., 2008. **130**(30): p. 9829-9835.

62. Balbach, J.J., et al., *Amyloid Fibril Formation by Aβ16-22, a Seven-Residue Fragment of the Alzheimer's B-Amyloid Peptide, and Structural Characterization by Solid State Nmr*. Biochemistry, 2000. **39**(45): p. 13748-13759.

63. Tjernberg, L.O., et al., *Arrest of β-Amyloid Fibril Formation by a Pentapeptide Ligand*. J. Biol. Chem., 1996. **271**(15): p. 8545-8548.

64. Hilbich, C., et al., *Aggregation and Secondary Structure of Synthetic Amyloid Beta-A4 Peptides of Alzheimers-Disease*. Journal of Molecular Biology, 1991. **218**(1): p. 149-163.

65. Fraser, P.E., et al., *Conformation and Fibrillogenesis of Alzheimer a-Beta Peptides with Selected Substitution of Charged Residues*. Journal of Molecular Biology, 1994. **244**(1): p. 64-73.

66. Lu, K., et al., *Exploiting Amyloid Fibril Lamination for Nanotube Self-Assembly*. J. Am. Chem. Soc., 2003. **125**(21): p. 6391-6393.

67. Li, I.T.S. and G.C. Walker, *Signature of Hydrophobic Hydration in a Single Polymer*. Proceedings of the National Academy of Sciences, 2011. **108**(40): p. 16527-16532.

68. Tanizaki, S., et al., *Conformational Sampling of Peptides in Cellular Environments*. Biophysical Journal, 2008. **94**(3): p. 747-759.

69. Berne, B.J., J.D. Weeks, and R. Zhou, *Dewetting and Hydrophobic Interaction in Physical and Biological Systems*. Annu Rev Phys Chem, 2009. **60**: p. 85-103.

70. Fernández, A., *Intramolecular Modulation of Electric Fields in Folding Proteins*. Physics Letters A, 2002. **299**(2–3): p. 217-220.

71. Childers, W.S., et al., *Phase Networks of Cross-Beta Peptide Assemblies*. Langmuir, 2012. **28**(15): p. 6386-6395.

72. Cohen, S.I.A., et al., *From Macroscopic Measurements to Microscopic Mechanisms of Protein Aggregation*. Journal of Molecular Biology, 2012. **421**(2-3): p. 160-171.

73. Morris, A.M., M.A. Watzky, and R.G. Finke, *Protein Aggregation Kinetics, Mechanism, and Curve-Fitting: A Review of the Literature*. Biochim. Biophys. Acta, 2009. **1794**(3): p. 375-97.

74. Chi, E.Y., et al., *Amyloid-ß Fibrillogenesis Seeded by Interface-Induced Peptide Misfolding and Self-Assembly*. Biophysical Journal, 2010. **98**(10): p. 2299-2308.

75. Jiang, D., et al., *A Kinetic Model for Beta-Amyloid Adsorption at the Air/Solution Interface and Its Implication to the Beta-Amyloid Aggregation Process*. Journal of Physical Chemistry B, 2009. **113**(10): p. 3160-3168.

76. Hoernke, M., et al., *Triggers for Beta-Sheet Formation at the Hydrophobic-Hydrophilic Interface: High Concentration, in-Plane Orientational Order, and Metal Ion Complexation*. Langmuir, 2011. **27**(23): p. 14218-14231.

77. Lee, C.F., et al., *Combined Effects of Agitation, Macromolecular Crowding, and Interfaces on Amyloidogenesis*. Journal of Biological Chemistry, 2012. **287**(45).

78. Lopes, D.H.J., et al., *Mechanism of Islet Amyloid Polypeptide Fibrillation at Lipid Interfaces Studied by Infrared Reflection Absorption Spectroscopy*. Biophysical Journal, 2007. **93**(9): p. 3132-3141.

79. Schladitz, C., et al., *Amyloid-Beta-Sheet Formation at the Air-Water Interface*. Biophysical Journal, 1999. **77**(6): p. 3305-3310.

80. Sharp, J.S., J.A. Forrest, and R.A.L. Jones, *Surface Denaturation and Amyloid Fibril Formation of Insulin at Model Lipid–Water Interfaces*. Biochemistry, 2002. **41**(52): p. 15810-15819.

81. Nichols, M., et al., *Rapid Assembly of Amyloid-B Peptide at a Liquid/Liquid Interface Produces Unstable B-Sheet Fibers†*. Biochemistry, 2005. **44**(1): p. 165-173.

82. Phillips, D., et al., *Time Correlated Single-Photon Counting (Tcspc) Using Laser Excitation*. Analytical Instrumentation, 1985. **14**(3-4): p. 267-292.

83. Liang, Y., D.G. Lynn, and K.M. Berland, *Direct Observation of Nucleation and Growth in Amyloid Self-Assembly*. J. Am. Chem. Soc., 2010. **132**(18): p. 6306-6308.

84. Wyatt, A.R., et al., *Roles of Extracellular Chaperones in Amyloidosis*. Journal of Molecular Biology, 2012. **421**(4–5): p. 499-516.

85. Narayan, P., et al., *Amyloid-B Oligomers Are Sequestered by Both Intracellular and Extracellular Chaperones*. Biochemistry, 2012. **51**(46): p. 9270-9276.

86. Liu, P., et al., *Nucleobase-Directed Amyloid Nanotube Assembly*. Journal of the American Chemical Society, 2008. **130**(50): p. 16867-16869.

87. Dong, J., et al., *Modulating Amyloid Self-Assembly and Fibril Morphology with Zn(Ii)*. Journal of the American Chemical Society, 2006. **128**(11): p. 3540-3542.

88. Morgan, D.M., et al., *Metal Switch for Amyloid Formation: Insight into the Structure of the Nucleus*. Journal of the American Chemical Society, 2002. **124**(43): p. 12644-12645.

89. Liu, B., et al., *Iron Promotes the Toxicity of Amyloid Beta Peptide by Impeding Its Ordered Aggregation*. J Biol Chem, 2011. **286**(6): p. 4248-56.

90. Garai, K., et al., *Selective Destabilization of Soluble Amyloid Beta Oligomers by Divalent Metal Ions*. Biochemical and biophysical research communications, 2006. **345**(1): p. 210-215.

91. Dong, J., et al., *Engineering Metal Ion Coordination to Regulate Amyloid Fibril Assembly and Toxicity*. Proceedings of the National Academy of Sciences of the United States of America, 2007. **104**(33): p. 13313-8.

92. Zhou, X., et al., *The Opposite Effects of Cu(Ii) and Fe(Iii) on the Assembly of Glucagon Amyloid Fibrils*. RSC Advances, 2012.

93. Reches, M. and E. Gazit, *Casting Metal Nanowires within Discrete Self-Assembled Peptide Nanotubes*. Science, 2003. **300**(5619): p. 625-7.

94. Mitraki, A., et al., *Design of Metal-Binding Sites onto Self-Assembled Peptide Fibrils*. Biopolymers, 2009. **92**(3): p. 164-172.

95. Scheibel, T., et al., *Conducting Nanowires Built by Controlled Self-Assembly of Amyloid Fibers and Selective Metal Deposition*. Proceedings of the National Academy of Sciences of the United States of America, 2003. **100**(8): p. 4527-4532.

96. Liang, Y., et al., *Light Harvesting Antenna on an Amyloid Scaffold*. Chem. Commun., 2008(48): p. 6522-6524.

97. Chien, P., J.S. Weissman, and A.H. DePace, *Emerging Principles of Conformation Based Prion Inheritance*. Annual Review of Biochemistry, 2004. **73**: p. 617-656.

98. Petkova, A.T., et al., *Self-Propagating, Molecular-Level Polymorphism in Alzheimer's β-Amyloid Fibrils*. Science, 2005. **307**(5707): p. 262-5.

99. Paravastu, A.K., et al., *Seeded Growth of Beta-Amyloid Fibrils from Alzheimer's Brain-Derived Fibrils Produces a Distinct Fibril Structure*. Proceedings of the National Academy of Sciences of the United States of America, 2009. **106**(18): p. 7443-7448.

100. Wetzel, R., S. Shivaprasad, and A.D. Williams, *Plasticity of Amyloid Fibrils*. Biochemistry, 2007. **46**(1): p. 1-10.

101. Tycko, R., *Molecular Structure of Amyloid Fibrils: Insights from Solid-State Nmr*. Quarterly Reviews of Biophysics, 2006. **39**(01): p. 1.

102. Alexandrescu, A.T., et al., *Heterogeneous Amylin Fibril Growth Mechanisms Imaged by Total Internal Reflection Fluorescence Microscopy*. Biochemistry, 2011. **50**(14): p. 2808-2819.

103. Ramachandran, G. and J.B. Udgaonkar, *Evidence for the Existence of a Secondary Pathway for Fibril Growth During the Aggregation of Tau*. Journal of Molecular Biology, 2012. **421**(2-3): p. 296-314.

104. Groenning, M., et al., *Study on the Binding of Thioflavin T to Beta-Sheet-Rich and Non-Beta-Sheet Cavities*. J Struct Biol, 2007. **158**(3): p. 358-69.

105. Biancalana, M., et al., *Molecular Mechanism of Thioflavin-T Binding to the Surface of Beta-Rich Peptide Self-Assemblies*. Journal of Molecular Biology, 2009. **385**(4): p. 1052-1063.

106. Cohen, S.I., et al., *From Macroscopic Measurements to Microscopic Mechanisms of Protein Aggregation*. J. Mol. Biol., 2012. **421**(2-3): p. 160-71.

107. Cohen, S.I.A., et al., *Nucleated Polymerization with Secondary Pathways. Iii. Equilibrium Behavior and Oligomer Populations*. Journal of Chemical Physics, 2011. **135**(6).

108. Cohen, S.I.A., et al., *Nucleated Polymerization with Secondary Pathways. Ii. Determination of Self-Consistent Solutions to Growth Processes Described by Non-Linear Master Equations*. Journal of Chemical Physics, 2011. **135**(6).

109. Cohen, S.I.A., et al., *Nucleated Polymerization with Secondary Pathways. I. Time Evolution of the Principal Moments*. Journal of Chemical Physics, 2011. **135**(6).

Chapter 2

Principles of Fluorescence for Quantitative Fluorescence Microscopy

Neil R. Anthony, Peng Guo, and Keith M. Berland

Department of Physics, Emory University, Atlanta, GA 30322

This chapter was published in:

FLIM Microscopy in Biology and Medicine

Chapter 2 - Principles of Fluorescence for Quantitative Fluorescence Microscopy

2.1 Introduction

Continuing developments in fluorescence microscopy are providing increasingly sophisticated research tools that support detailed non-invasive investigations of molecular level functions in biological systems, including the capability to investigate molecular dynamics, interactions, and structure with exquisite sensitivity and specificity. Many of the important fluorescence microscopy based research methods employ sophisticated data collection and analysis procedures, and a clear understanding of the fundamental principles of molecular fluorescence is a prerequisite for their successful implementation. This chapter therefore aims to introduce the basic photophysical properties of fluorescent molecules and to discuss some of the ways in which these properties influence experimental design and analysis in quantitative fluorescence microscopy. The emphasis is on fundamental principles rather than specific methods or applications.

2.2 What is Fluorescence?

Fluorescence is a molecular luminescence processes in which molecules spontaneously emit a photon as they relax from an excited electronic state to their ground state following absorption of energy, typically within a few nanoseconds or less following excitation. The characteristic electronic states and relaxation processes involved in fluorescence emission are illustrated in Figure 2-1, commonly referred to as a Jablonski diagram [1-3]. The nature and significance of the molecular transitions shown as arrows in the diagram are discussed in detail throughout this chapter. The states S_0 and S_1 are the ground state and lowest energy excited singlet electronic states, and T_1 is the lowest energy triplet state for the molecule. Singlet and triplet states are distinguished by the

orientation of their electron spins[§]. The closely spaced levels within each electronic state represent the vibrational energy levels of the molecule, which are typically similar for the different electronic states. The different vibrational states are responsible for the characteristic shape of the absorption and emission spectral properties of a fluorescent molecule. The absorbance and emission of light is a quantum process, and the energy is absorbed and emitted in discrete units called photons. A single photon has energy $h\nu$ where h is Planck's constant (6.63×10^{-34} Joule sec) and ν refers to the frequency of the radiation. The frequency and the wavelength, λ, of light are related parameters as their product is always the speed of light, i.e. $\lambda\nu = c$, where $c = 3 \times 10^8$ m s^{-1}). Thus, the photon energy can also be calculated as $E = hc/\lambda$. A convenient mnemonic for calculating the photon energy (in electron Volts, 1 eV = 1.6×10^{-19} Joule) is $E = 1243/\lambda$, where λ is the wavelength in nanometers. The wavelengths of the visible spectrum run from approximately 400 nm (blue) to 700 nm (red), corresponding to frequencies of 7.5×10^{14} and 4.3×10^{14} Hertz (Hz) respectively.

[§] Singlet states have *antiparallel* electron spins, while triplet states have *parallel* electron spins.

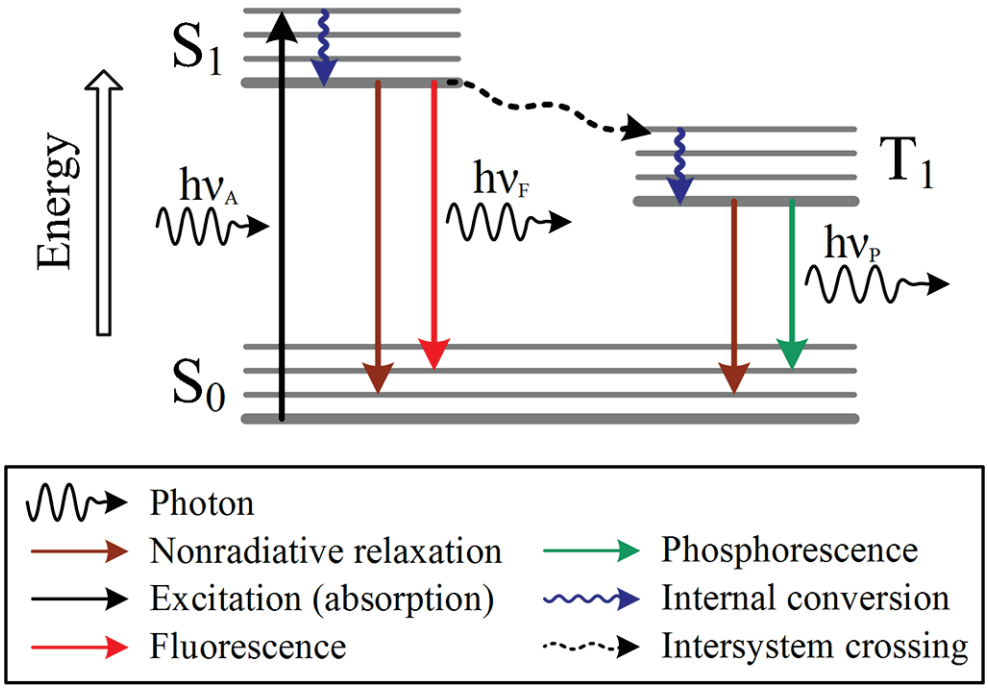

Figure 2-1 – A Jablonski diagram representing the energy levels of a fluorescent molecule and several important transitions. The states S_0 and S_1 are the ground state and lowest energy excited singlet electronic states, and T_1 is the lowest energy triplet state for the molecule. Singlet and triplet states are distinguished by the orientation of their electron spins. The closely spaced levels within each electronic state (fine lines) represent the vibrational energy levels of the molecule, which are typically similar for the different electronic states. Each arrow represents a transition from one state to another, including absorption of light, internal conversion, non-radiative relaxation, fluorescence emission, intersystem crossing to the triplet state, and phosphorescence. Planck's constant ($h = 6.63 \times 10^{-34}$ Joule sec) relates a photon's energy, E, to its frequency, ν, as $E = h\nu$.

2.2.1 Absorption

Fluorescence is produced when molecules relax from an excited electronic state to the ground state, yet at room temperature virtually the entire population of any fluorescent molecules used in microscopy will occupy the ground state S_0. Thus, fluorescence emission requires an energy source to pump the molecules into an excited state from which they can then emit fluorescence [3, 4]. The energy source is typically an external light source such as a laser, lamp, or diode, which provides the excitation energy in form of photons [5]. The energy of the absorbed photons must correspond to the energy difference between the ground state and one of the excited states. The Jablonski diagram in Figure 2-1 shows only a single absorption transition, which would produce a narrow spectrum (Figure 2-2A). For molecules in solution there will generally be a wide range of allowed transitions of differing energy/frequency [3, 4, 6], corresponding to the different vibrational energy levels of the molecule, as shown in Figure 2-2B. Some of the transitions are more favorable than others, and the relative strength of each transition can be found by measuring the absorption spectrum of a particular molecule. Photons with energies corresponding to the peaks of the absorption spectrum are more likely to interact with a fluorescent molecule than photons whose energies are not at the peak, although photons of many different wavelengths are capable of exciting the molecule. The absorption spectra of some common fluorescent proteins are also shown in Figure 2-2C. The spectra are normalized, so the figure only provides information about the spectral shape and not the relative strength of the different absorbers. Such normalized spectra can be misleading: one is naturally tempted to assume the curve with a higher value at a particular wavelength is the stronger absorber at that wavelength, although this may not be accurate. For example, the extinction coefficient (§ 2.2.3) for the yellow fluorescent protein (YFP) is ~2-3 times larger than that for the Cyan fluorescent protein

(CFP) [7]. There are thus wavelengths in the ~460-475 nm range for which YFP is the stronger absorber even though the CFP spectrum appears to have the larger value in the figure.

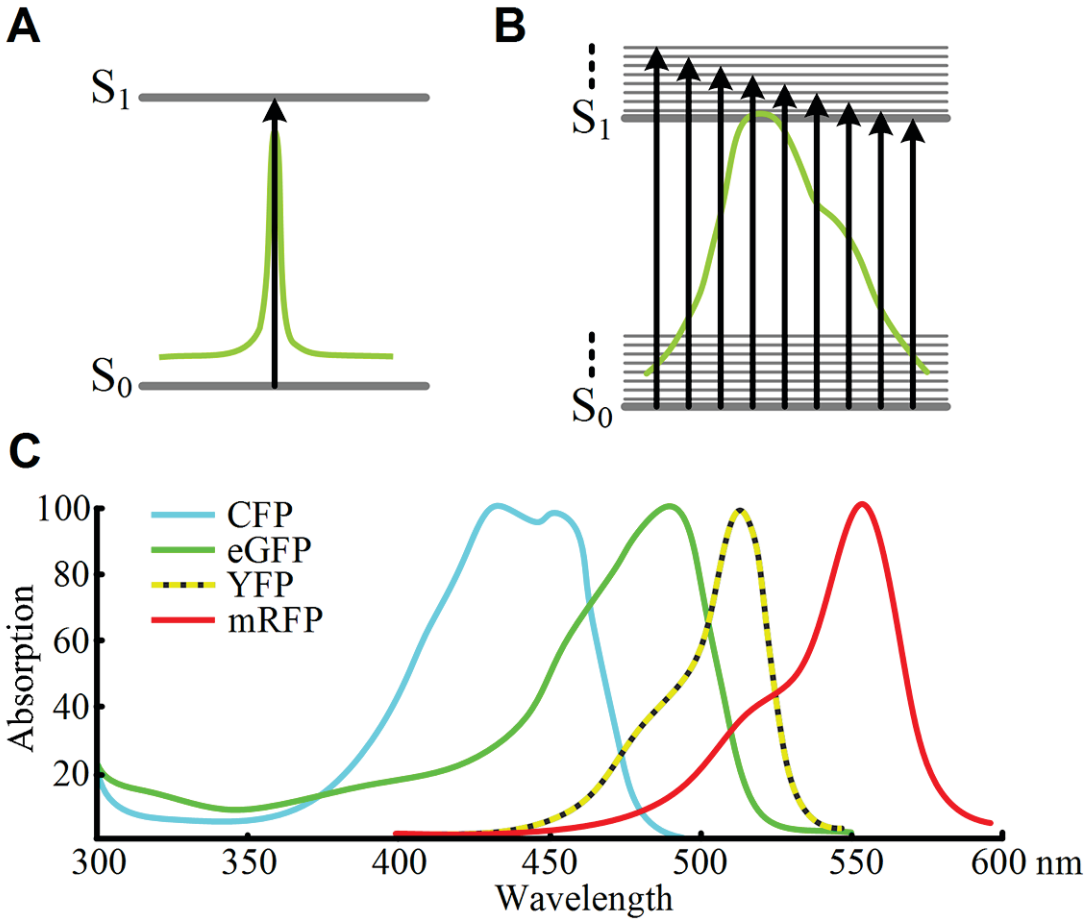

Figure 2-2 – Absorption of light involves pumping the molecule from the ground electronic and vibrational states to an excited state. A single transition from one energy state to another would produce a sharp absorption peak as shown in (**A**). Molecules in solution have numerous closely spaced vibrational energy levels, and fluorescent molecules can be excited to many of these vibronic states resulting in broad absorption spectra (**B**). The relative strength of each allowed energy level transition determines the shape of the absorption spectrum, with the most favorable transitions corresponding to

the peak of the absorption spectrum. Typical absorption spectra for several fluorescent proteins commonly used in microscopy are shown in **C**.

In microscopy, it is very common for samples to contain multiple fluorescent species such as experiments designed using multiple fluorescent probes to measure fluorescent signals from several different molecules of interest simultaneously. Even experiments designed with only a single fluorescent probe may still contain multiple emitting species since living systems can produce significant quantities of autofluorescing molecules [8-10]. Since each type of fluorescent molecule has a unique absorption spectrum, varying the excitation wavelengths offers an opportunity to enhance or diminish the excitation of a particular fluorophore relative to the other fluorescent molecules present in the sample. One can therefore use excitation wavelength as a tool to optimize imaging conditions. Often the optimal excitation corresponds to the absorption peak, but it is not uncommon that one can optimize the signal to background and/or signal to noise ratios in a particular sample using off peak excitation wavelengths.

The most commonly used excitation conditions for microscopy are designed to maximize excitation of a particular probe and minimize the excitation of other fluorophores present in the sample. In modern automated digital imaging systems an alternate approach is to image samples using multiple excitation wavelengths. When coupled with image processing algorithms this approach can be used to separate the signals from multiple fluorescent emitters provided the fluorescent probes have different excitation spectra, as they generally will. This approach is sometimes referred to as excitation fingerprinting [3, 11], and can even allow separation of fluorescence from multiple probes with similar or even un-resolvable emission spectra. Selecting excitation wavelengths that efficiently excite multiple species and separating their signals with

image processing can also improve the overall signal to noise ratios in imaging data [12, 13].

2.2.2 Molecular Excitation Rates

A detailed description of the interaction between light and matter is beyond the scope of this chapter, although a basic physical description of molecular absorption is helpful for selecting appropriate excitation wavelengths and powers, and also for understanding signal levels and artifacts in fluorescence microscopy. The total fluorescence signal generated from a given region of a microscopy sample will depend on how many fluorescent molecules are located at that position, their photophysical properties, and the rate at which those molecules are excited over time by the light source. The latter quantity is the focus of this section, in which we discuss absorption for both one-photon and two-photon excitation. For each case the rate at which individual fluorescent molecules in the sample are pumped from the ground state into an excited state will be specified by the quantity $w_i(\mathbf{r},t)$ which has units of inverse seconds and may be a function of time, *t*, and position, **r**, within the sample. The index *i* specifies one- ($i=1$) or two- ($i=2$) photon excitation. The molecular excitation rate depends on both the absorption properties of the fluorescent molecule itself and the flux of exciting photons seen by each molecule. In most microscopy applications the excitation source is not uniform throughout the sample, and therefore the fluorescence signals generated at any given time are also not spatially uniform. For example, confocal and two-photon laser scanning microscopy [5, 14-22] both employ focused laser excitation which excites molecules in the center of the focused beam more efficiently than those on the periphery of the focal spot. Moreover, the focused laser only illuminates a small fraction of the sample at any given time. The focused beam is then raster scanned across the sample and the fluorescence signal from each successive position is measured sequentially and

stored. The data is subsequently reconstructed into an image for visualization on a computer. The detailed functions describing the spatial profile of the focused laser beam for different microscope designs will not be discussed here [16, 23, 24]. We will instead use generic notation with the dimensionless function $S(\mathbf{r})$ representing any normalized distribution function, with unit peak value, that models the three-dimensional spatial profile of the illumination source.

2.2.3 One-Photon Excitation

The most familiar parameter that specifies how strongly a molecule interacts with light is the molar extinction coefficient, $\varepsilon(\lambda)$. The extinction coefficient is often reported in terms of its peak value, although we here write it as a function of wavelength to emphasize that wavelength selection can be used advantageously in microscopy. The Beer-Lambert law states that for a beam of monochromatic light with initial intensity I_o, traversing a pathlength l of an absorbing solution with molar concentration c, the extinction coefficient can be used to compute the transmitted intensity, I, using:

$$I = I_0 10^{-\varepsilon(\lambda)cl} \tag{2.1}$$

A graphical representation of the Beer-Lambert law can be seen in Figure 2-3. A more fundamental measure of absorption on the molecular scale is a related parameter called the absorption cross section, $\sigma_1(\lambda)$. In the context of microscopy $\sigma_1(\lambda)$ is the more natural quantity to work with as microscopy samples may not be spatially homogeneous and transmission pathlengths are in some cases not easily defined. Both $\sigma_1(\lambda)$ and $\varepsilon(\lambda)$ measures how strongly a particular molecule interacts with light of a given wavelength, and the two quantities are related by:

$$\sigma_1(\lambda) = 3.8 \times 10^{-21} \varepsilon(\lambda) \tag{2.2}$$

In Eq. (2.2), the cross section $\sigma_1(\lambda)$ has units of cm², and $\varepsilon(\lambda)$, units of Molar^{-1} cm^{-1}. Good absorbers including many commonly used fluorescence probes have cross sections on the order of 10^{-16} cm². For example, the widely used green fluorescent protein (GFP) has a peak extinction coefficient of 57,000 M^{-1} cm^{-1} which corresponds to a cross section of 2.2×10^{-16} cm² [25] . Some other common fluorescent proteins have cross sections of similar magnitude such as the cyan (ECFP, 32,500 M^{-1} cm^{-1}, 1.2×10^{-16} cm²) and yellow (EYFP, 84,000 M^{-1} cm^{-1}, 3.2×10^{-16} cm²) fluorescent proteins [7, 25].

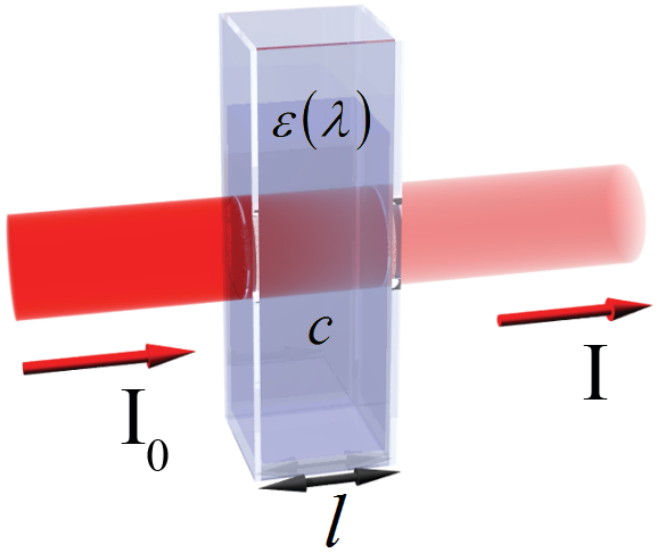

Figure 2-3 – The Beer-Lambert law uses the extinction coefficient, ε(λ), the molecular concentration, *C*, and the transmission pathlength, *l*, to compute the fraction of incident photons transmitted through a homogenous solution (Eq. (2.1)). In microscopy, the absorption cross section, $\sigma_1(\lambda)$, is a more natural measure of absorption as described in the text.

Computing the approximate number of molecular excitation events per unit time allows one to estimate how many fluorescence photons can be measured for a particular experimental system. For one-photon excitation, the rate that molecules are pumped from the ground to the excited state at position **r** is linearly proportional to the excitation flux and is computed as:

$$w_1(\mathbf{r}) = \sigma_1 I_0(t) S(\mathbf{r}) \tag{2.3}$$

The quantity $I_0(t)$ represents the peak photon flux of the laser excitation as a function of time with units of photons cm^{-2} s^{-1}. Equation (2.3) has a useful geometric interpretation: the flux multiplied by the cross section yields a product of, i) the number of photons per second passing through an illuminated area *A* within the sample and, ii) the ratio of the absorption cross section to area *A*. In other words, the ratio of the cross section to the illuminated area specifies the fraction of the excitation photons passing through that area that will be absorbed. To better visualize this ratio, Figure 2-4 shows fluorescent molecules with absorption cross section σ_1 in the focal plane of an objective lens. Note that the only spatial dependence in Eq. (2.3) comes from $S(\mathbf{r})$ itself, so in the absence of saturation (§ 2.6.4) the spatial pattern of the excited molecules will match the profile of the excitation source.

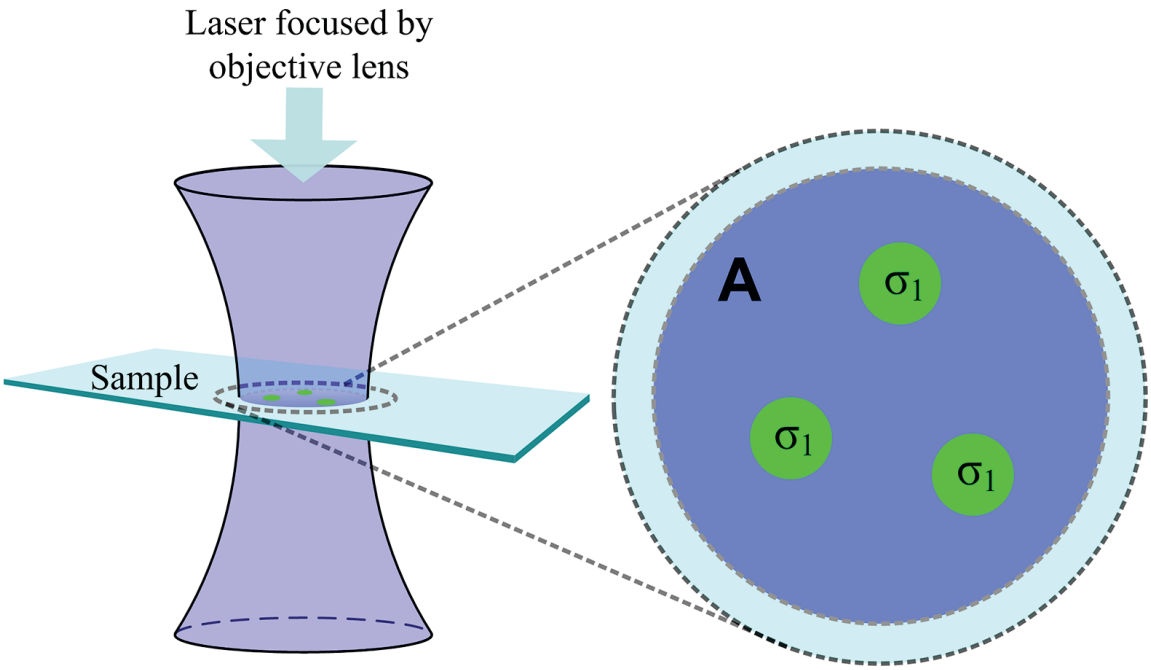

Figure 2-4 – A geometrical interpretation of the absorption cross section. When a sample is illuminated with photon flux of I_o photons cm^{-2} s^{-1}, this can be interpreted as a certain number of photons per second passing by area A defined by the physical size of the light source. The cross section represents the effective area of the molecule (white circles) such that the quantity σ_1/A determines the fraction of photons passing through area A captured by each molecule. The cross section is an effective area since it depends on the electronic properties of the molecule and not directly on its physical size.

Photon flux is difficult to measure directly, and in the laboratory one generally measures average power instead. The relationship between the photon flux at the sample and the average power of the source depends on the spatial pattern of the excitation source at the sample and how tightly it is focused in the sample. A precise description of the illumination pattern can be rather complex, although for reasonably accurate estimates of the molecular excitation rate it is often sufficient to assume the illumination profile is that of a focused Gaussian beam [5, 24, 26]. In this case, assuming constant power

excitation is used (i.e. continuous wave (cw) non-pulsed sources), the peak intensity can be computed from the average power in Watts using the expression $I_{0,CW} = 2\langle P \rangle / h\nu \, \pi\omega_0^2$, where ω_0 is the beam waist of the focused laser and $h\nu$ is the photon energy. The beam waist can be estimated by the expression $\omega_0 = \lambda / \pi NA$ where NA is the effective numerical aperture of the lens focusing the illumination source.

2.2.4 Two-Photon Excitation

Two-photon excitation has been demonstrated to offer several important advantages for many applications of fluorescence microscopy such as enhanced depth penetration, reduced photobleaching, and reduced photodamage in living specimen [18, 20, 22, 27-29]. Two-photon excitation refers to the simultaneous absorption of two photons by a single fluorescent molecule, with the sum of the photon energies matching the molecular transition energy from ground to excited state, as shown in Figure 2-5A. Achieving significant fluorescence excitation by two-photon absorption requires high photon densities [18, 22]. Appreciable two-photon excitation in fluorescence microscopy thus generally requires ultrafast pulsed lasers focused using high numerical aperture lenses to concentrate photons in both space and time [24, 27]. Unlike one-photon excitation, for which the molecular excitation rate is linearly proportional to the illumination intensity, two photon absorptions rates are proportional to the square of the excitation intensity. This "power squared" dependence of two photon absorption is what gives rise to the three-dimensional resolution of two-photon microscopes without the use of confocal pinholes (which are required for one-photon confocal microscopy to eliminate out of focus emission) [18, 22]. The rate that molecules are pumped from the ground to the excited state by two photon absorption is given by:

$$w_2(\mathbf{r},t) = \frac{\sigma_2 I_0^2(t) S^2(\mathbf{r})}{2} \tag{2.4}$$

where σ_2 is the two-photon absorption cross section [30, 31]. The preferred unit for two-photon cross sections is the Göppert-Mayer (GM), where 1GM = 10^{-56} m^4 sec. The unit is named after Nobel laureate Maria Göppert-Mayer who first developed the theory of two-photon excitation [32]. Good two-photon absorbers typically have cross sections with order of magnitudes of ~100 GM [22, 24, 31].

Typical laser systems for two photon excitation have temporal pulse widths of ~100 femtoseconds and pulse repetition frequencies on the order of $f_p = 80MHz$. The pulsewidth and repetition rate are generally significantly faster than the timescale of interest in a particular experiment and one is instead primarily interested in the average molecular excitation rate, which can be computed by integrating the total probability of molecular excitation per laser pulse and multiplying by the laser pulse repetition frequency. Thus, the average excitation rate is given by $\langle w_2(\mathbf{r}) \rangle = f_p \int w_2(\mathbf{r},t)\, dt$, where the integral is computed over a single pulse and the angular brackets represent time averaging [26, 33].

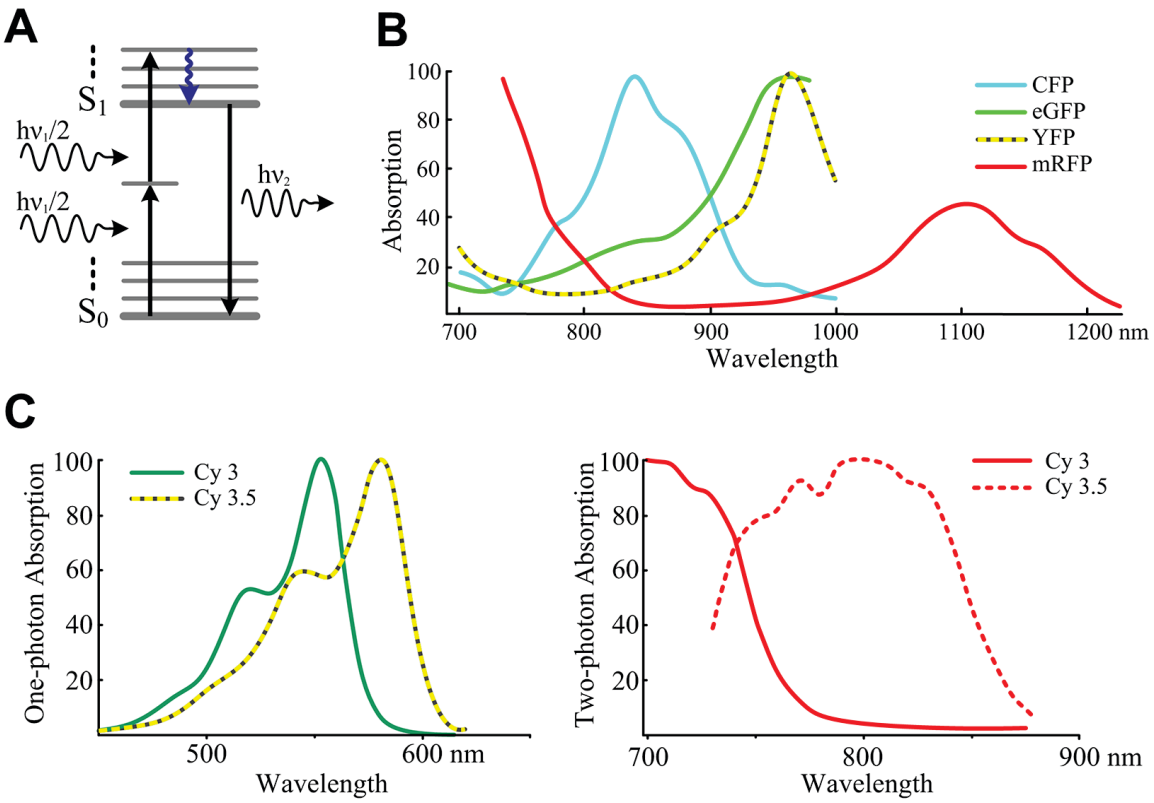

Figure 2-5 – Two-photon excitation. **A**) A Jablonski diagram showing the molecular excitation transition in which two photons of equal energy provide the energy required to excite the molecule. **B**) Two-photon excitation spectra of some commonly used fluorescent proteins including the enhanced green fluorescent protein (EGFP), cyan fluorescent protein (CFP), yellow fluorescent protein (YFP), and monomeric red fluorescent protein (mRFP). **C**) The one-photon (left)- and two-photon (right) absorption spectra for the dyes Cy 3 and Cy 3.5. Two-photon absorption spectra sometimes have the same spectral shapes as their one-photon spectra while in other cases they may be quite different, highlighting the importance of acquiring information about two-photon absorption spectra for probes used in two-photon microscopy.

Box 2-1 – Computation of the average molecular excitation rate for GFP.

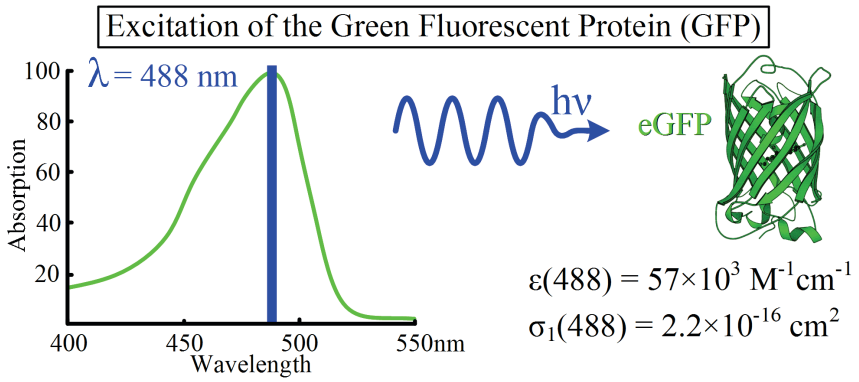

The 488 nm excitation source is selected to match the peak of the EGFP absorption, with an absorption cross section of 2.2×10^{-16} cm² (extinction coefficient of 57,000 M^{-1} cm^{-1}).

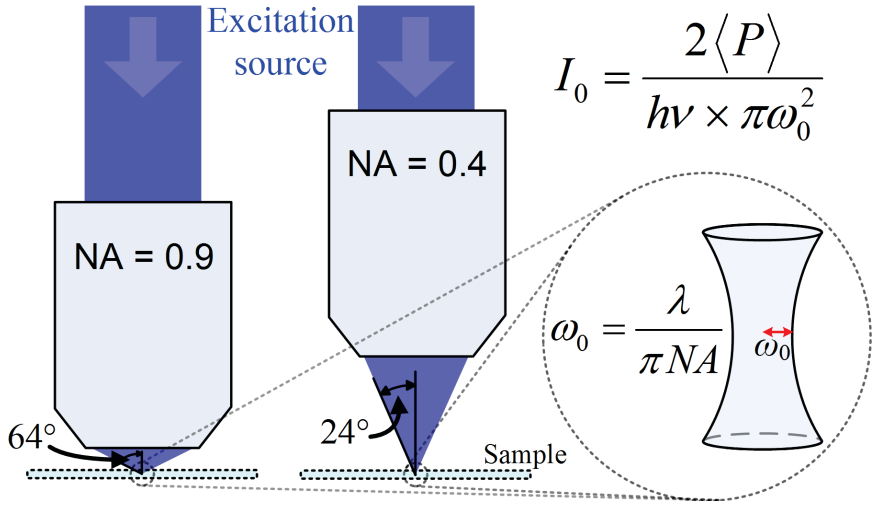

The laser excitation is focused by the objective lens, with higher NA lenses resulting in tighter focusing of the excitation source. The peak incidence angle is also a function of the numerical aperture, with $NA=n\sin\theta$ where θ is the half angle shown and n is the refractive index of the medium traversed by the focused light. The relationship between the incident power and intensity is defined in the text. Since the molecular excitation rate depends on intensity and not average power, the higher NA lens produces a higher molecular absorption rate, $\langle w_1 \rangle$, for the same power, as shown in the table below.

	NA = 0.9		NA = 0.4	
$\langle P \rangle (\mu W)$	I_0 (photons cm^{-2} s^{-1})	$\langle w_1 \rangle$ (events s^{-1})	I_0 (photons cm^{-2} s^{-1})	$\langle w_1 \rangle$ (events s^{-1})
10	5.4×10^{22}	1.2×10^{7}	1.0×10^{22}	2.2×10^{6}
100	4.3×10^{23}	9.5×10^{7}	1.0×10^{23}	2.2×10^{7}

As in the one photon case, computing photon fluxes in terms of the easily measured average power requires knowledge about the temporal profile of the laser pulses as well as the spatial profile of the focused excitation source. If for simplicity one assumes a Gaussian profile in both space and time [33, 34], then the photon flux can be computed in terms of the average power as:

$$I_0(t) = \frac{\langle P \rangle}{h\nu} \frac{2}{\pi\omega_0^2} \frac{2\sqrt{\ln 2}}{\sqrt{\pi}} \frac{1}{f_p \alpha} e^{-\ln(2)\left(\frac{2(t-t_0)}{\alpha}\right)^2} = I_{0,peak} e^{-\ln(2)\left(\frac{2(t-t_0)}{\alpha}\right)^2} \quad (2.5)$$

where $\langle P \rangle$ is the time averaged laser power (in Watts), ω_0 is the focused beam waist, and α is the temporal width (full width at half maximum) of the Gaussian pulse. One can then also compute the average molecular excitation rate as:

$$\langle w_2(\mathbf{r}) \rangle = \sigma_2 I_{0,peak}^2 S^2(\mathbf{r}) \alpha f_p \frac{\sqrt{\pi}}{4\sqrt{\ln 4}} \quad (2.6)$$

Measurements of two-photon absorption spectra and cross sections are significantly more complicated than one-photon spectra and generally require specialized knowledge and equipment. Fortunately, two-photon absorption spectra of the most common fluorescent probes for microscopy are now available in the literature or from online sources [35-38]. The two-photon excitation spectra for four commonly used fluorescent proteins are shown in Figure 2-5B. Many molecules have two-photon absorption spectra that essentially match their one photon spectra in shape (with the wavelength axis of an absorption plot multiplied by two), while other molecules have two-photon absorption spectra that are completely different than their one-photon spectra (the emission spectra are almost always the same for one- and two-photon excitation) [39, 40]. An example of this is shown in Figure 2-5C, which shows one- and two-photon absorption spectra for the dyes Cy3 and Cy3.5. Their one photon absorption spectra are quite similar (left), yet the two photon spectra are drastically different (right). Therefore, it is important to

measure or look up the two-photon absorption spectrum whenever working with a new fluorophore.

2.3 Fluorescence and Molecular Relaxation Pathways

2.3.1 Internal Conversion

Once a molecule is pumped into an excited state it will relax to the ground vibrational level of electronic excited state S_1 on a picoseconds (10^{-12} sec) timescale by a process termed internal conversion [39]. As a consequence of this rapid loss of vibrational energy, all subsequent molecular relaxation pathways proceed from the lowest vibrational level of the electronic excited state. Fluorescence emission spectra are thus typically independent of the excitation pathway (e.g. one- or two-photon excitation) and excitation wavelength. The timescale of internal conversion is usually significantly faster than subsequent relaxation processes. Due to the separation of timescales between internal conversion and other pathways it is reasonable to ignore the internal conversion process when interpreting fluorescence signals from the microscope. Following internal conversion, molecules will subsequently relax back to the ground state either *via* fluorescence emission or by other competing relaxation pathways that are non-radiative. These possibilities are summarized in Figure 2-6, where the constants k_1 and Γ represent the relaxation rates associated with internal conversion within the excited state manifold and fluorescence emission respectively. The rate constants k_{FRET} and k_{OTHER} represent the relaxation rate associated with Forster resonance energy transfer (FRET, § 2.4.1) and the sum of all other non-radiative relaxation rates respectively. From a physical perspective, k_{FRET} is simply one of the "other" non-radiative relaxation

processes, but it has been noted separately here due to the high importance of FRET measurements for studying molecular interactions in microscopy [41-44].

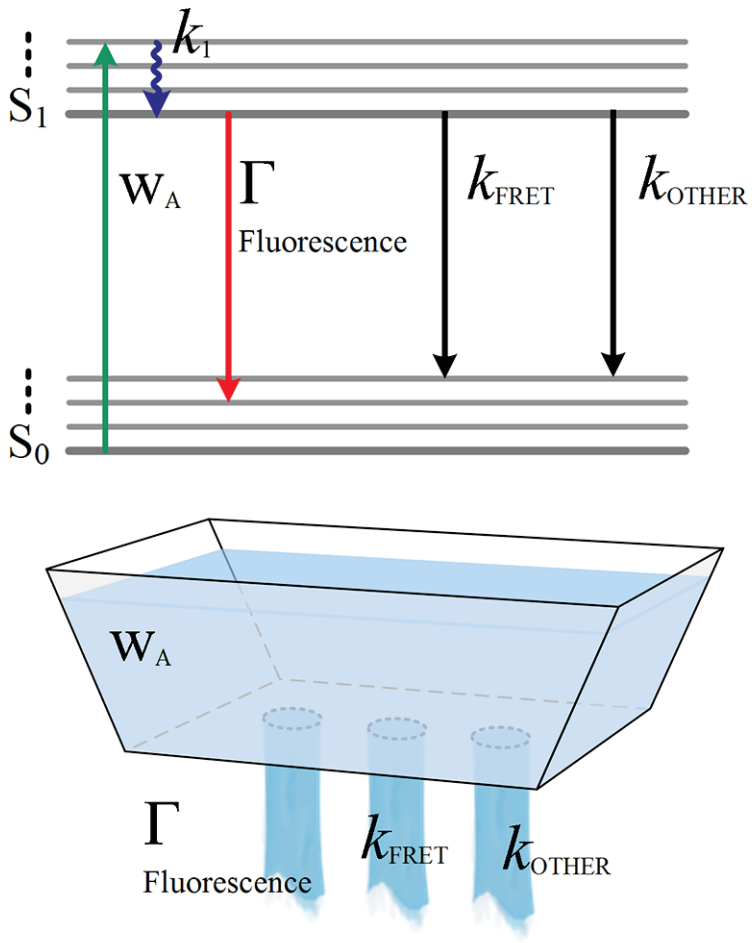

Figure 2-6 – Molecular transitions are represented by arrows, and each arrow has an associated rate constant (units of s^{-1}). The rapid loss of vibrational energy (k_1) causes all further relaxation to begin in the ground vibrational state of S_1. The net rate at which the molecule relaxes back to the ground state is determined by the sum rates for all the available relaxation processes, which here include fluorescence, FRET, and other non-radiative energy loss mechanisms. A physical analogy that represents a similar process is emptying a trough of water through holes in the bottom. Molecular excitation (W_A) is like filling the trough. The various relaxation pathways each correspond to a hole in the

trough and the rate for each process is represented by the size of the hole. The time that the water remains in the trough is analogous to the lifetime of the excited state, and the fraction that drains through the fluorescence hole is analogous to the quantum yield.

2.3.2 Fluorescence Emission

For fluorescence microscopy, the fluorescence molecular relaxation process produces the photons that are detected – without fluorescence emission there is no signal (excluding other types of non-fluorescent signals such as second harmonic generation, [45, 46]. Due to competing mechanisms for an excited state molecule to release its excess energy (see Figure 2-6), only a fraction of excited fluorescent molecules will relax via fluorescence emission. The availability of different relaxation pathways depends not only on the specific fluorescent molecule, but also its environment, which can reflect molecular interactions or solvent conditions [39]. Therefore, imaging methods that quantitatively measure the dynamics of the molecular relaxation process have the potential to provide more information than is available from measurements of the fluorescence intensity alone [39, 44, 47-50]. Two important parameters that are related to the prevalence or absence of competing relaxation mechanisms are the quantum yield and the excited state lifetime.

2.3.3 Quantum Yield

The quantum yield of a fluorescent molecule is a measure of its fluorescence efficiency, defined as the probability that an excited molecule will emit a fluorescence photon. For populations of molecules the quantum yield also specifies the fraction of excited molecules that relax by fluorescence emission. A water basin draining through multiple

holes, as shown in Figure 2-6, provides a useful macroscopic analogy for the quantum yield. Each hole in the basin represents a specific relaxation mechanism and the size of each hole represents the relaxation rate for that pathway, with larger holes corresponding to faster relaxation rates. While it is not possible to predict which hole any given water molecule will drain through, it is straight forward to determine the fraction of water molecules that will drain through each hole. By analogy, the quantum yield represents the fraction of excited state molecules that "drain" through the "fluorescence" hole in the basin. Quantitatively, the quantum yield is defined in terms of the rate constants as:

$$Q = \frac{\Gamma}{\Gamma + k_{FRET} + k_{OTHER}} \tag{2.7}$$

It is apparent from this definition that the quantum yield has a maximum value of unity only when fluorescence is the single allowed relaxation process. Fluorescent molecules commonly used as probes in microscopy have quantum yields ranging from very low values (<0.05) to near unity. Table 2-1 shows the quantum yield and spectral properties of some fluorescent proteins and other common fluorescent dyes. High quantum yield probes are generally desirable in most imaging applications as they are brighter than lower yield fluorescent molecules. However, as noted above, the availability of non-fluorescent relaxation pathways is sensitive to the environment of a fluorophore, and this sensitivity can be exploited to probe the nanoscale surroundings of a specific type of probe molecule. For example, FRET microscopy is widely used to investigate molecular interactions, and this capability arises from the different photophysical dynamics of the donor fluorophore in the presence or absence of a FRET acceptor [44, 51]. The quantum yield is difficult to directly measure experimentally, but the quantum yield related information about the environment of a particular fluorophore is also available through measurements of the fluorescence lifetime.

Table 2-1 – Quantum yield and spectral properties of some common fluorescent proteins and fluorescent dyes.

Probe	Quantum Yield (QY)	Excitation wavelength	Emission wavelength
ECFP	0.37	440	485
EYFP	0.61	520	542
EGFP	0.6	488	535
Cerulean	0.62	440	485
Venus	0.6	520	542
DsRed	0.79	558	583
mRFP1	0.25	584	607
mHoneydew	0.12	487/504[a]	537/562[a]
mBanana	0.70	540	553
mOrange	0.69	548	562
tdTomato	0.69	554	581
mTangerine	0.30	568	585
mStraberry	0.29	574	596
mCherry	0.22	587	610
mKO (Kusabira)	0.6	548	559
mKate (Katuska)	0.33	588	635
Alexa488	0.81	488	535
Alexa555 (Cy3)	0.13	555	575
Alexa647 (Cy5)	0.11	647	665

[a] Denotes wavelengths of multiple peaks.

2.3.4 Fluorescence Lifetimes

Fluorescence emission is a random process, and any particular fluorescent molecule will spend a random but finite amount of time in the excited state prior to releasing its energy to the environment as it relaxes to the ground state. However, each type of fluorescent molecule in a particular environment has a well defined average time that a

molecule will spend in the excited state following excitation. This average time is referred to as the fluorescence lifetime, τ. Using the water basin example from above, the lifetime is analogous to the average time each water molecule poured into the basin (the pouring is analogous to molecular excitation) will remain prior to draining out (molecules relaxing back to the ground state). Clearly the average time must be determined by the inverse of the sum of all the drainage rates, which in the case of fluorescence the lifetime is given by:

$$\tau = \frac{1}{\Gamma + k_{NF}} \tag{2.8}$$

where k_{NF} includes all non-fluorescent relaxation pathways. The sum of the relaxation rate constants ($\Gamma + k_{NF} = 1/\tau$) specifies the rate at which excited state molecules relax back to the ground state. This rate is constant over time, and the temporal relaxation for a population of excited molecules will therefore follow an exponential decay with time constant τ (i.e. $\exp(-t/\tau)$). The fluorescence signal is proportional to the excited state population and thus the fluorescence signal will decay with exponential kinetics (or possibly multi-exponential kinetics if there are multiple lifetimes) following pulsed excitation. The lifetime of many common probes is on the order of a few nanoseconds but will in general vary over a wide range depending on the specific fluorescent molecule, the solvent/environment, and other factors [39]. The lifetimes of several common fluorescent proteins are listed in Table 2-2. Occasionally it is useful to consider a quantity referred to as the natural lifetime, which refers to the lifetime a molecule would have in the absence of any non-fluorescent relaxation pathways (i.e. k_{nf} =0). Thus, the natural lifetime is given by $\tau_n = 1/\Gamma$.

Box 2-2 – Forster resonance energy transfer (FRET) example.

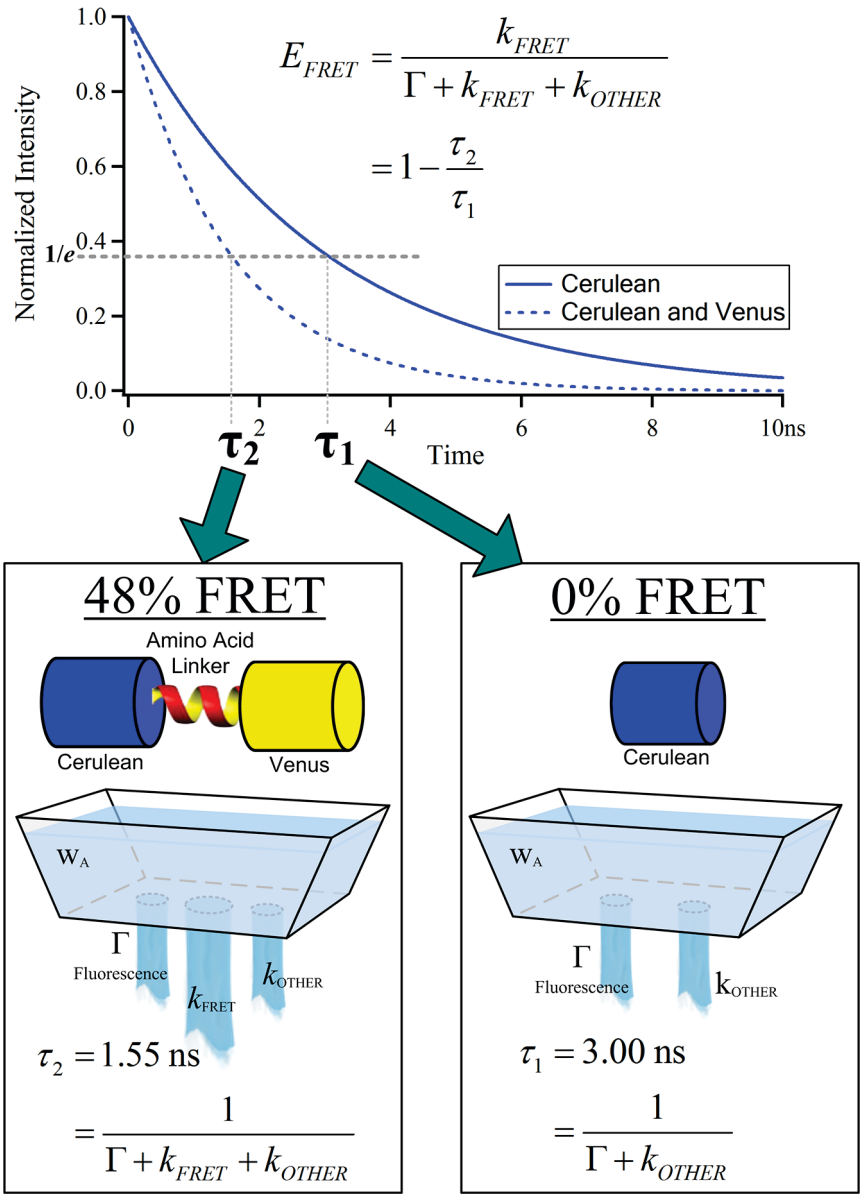

Fluorescence lifetimes can be used to measure quantum yields or FRET efficiencies (E_{FRET}). When a donor molecule (cerulean) has no FRET acceptor available, it has a lifetime of $\tau_1 = 3.00$ nanoseconds, represented by the exponential decay (solid line, top). When a FRET acceptor (Venus) is held nearby, in this case by a 5 amino acid linker, an additional relaxation pathway is opened up while the other relaxation rates remain unchanged. This new relaxation path has two effects: 1) a reduction in the fraction of excited state molecules that relax *via* fluorescence emission, and 2) a reduction in the average amount of time a molecule will spend in the excited state. This is seen in the reduced lifetime, with $\tau_2 = 1.55$ nanoseconds (dashed line, top). This corresponds to a 48% FRET efficiency, calculated by $E_{FRET} = 1 - \tau_2/\tau_1$.

Table 2-2

Fluorescent protein	Lifetime (ns)	Source
EGFP	2.45	[52]
ECFP	3.6 and 1.2[a]	[53]
EYFP	2.9	[54]
Cerulean	3.0	[55]

[a] Double component exponential decay

The versatile utility of fluorescence lifetime in microscopy arises because the lifetime is an accurate reporter of the relaxation pathways available to each molecule and thus of their local environment. The lifetime is an intrinsic property of a particular type of fluorescent molecule in a specific environmental condition. A very significant advantage of this fact for microscopy is that fluorescence lifetime measurements, unlike intensity measurements, are therefore not explicitly dependent upon molecular concentrations. This can be an important advantage in cells and tissue where one is interested in probing molecular interactions or environmental surroundings but for which the concentrations of fluorescent reporter molecules may be far from uniform.

2.3.5 Fluorescence Emission Spectra

Due to internal conversion in the excited state following excitation, the energy of the excited state is lowered and the fluorescence emission is red shifted (i.e. lower energy and thus longer wavelength photons) relative to the excitation wavelength. In addition, the excited molecule usually relaxes from the lowest vibrational level of the excited state to a higher vibrational level of the ground electronic state, further lowering its energy compared with the excitation photon energy. This change in energy of the emission

compared to the absorbed energy is called the Stokes shift. This shift in wavelength of the emission compared to the excitation is usually considerable (tens to hundreds of nanometers), and is very important for high sensitivity fluorescence measurements as it allows for the use of optical filters which block the excitation source from reaching the detector. Fluorescence detection can therefore be measured against very low background signal, which allows even single fluorescent molecules to be detected under optimized conditions [56]. As for absorption, Figure 2-1 shows just one of the characteristic transitions involved in fluorescence emission. However, the complete emission spectrum is made up of multiple transitions from the lowest vibrational state of S_1 back to the various available vibrational levels of the ground state. Some transitions will be more favorable than others and together they determine the overall shape of the emission spectrum. In general, fluorescent probes in solution will have broad emission spectra. For example, Figure 2-7 shows the emission spectra of some common fluorescent protein variants. Broad emission spectra present a challenge for fluorescence microscopy as they can make it difficult to separate the signals from multiple probes that are imaged simultaneously. Both high quality optical filters and image processing techniques are helpful for resolving multiple fluorophores with overlapping emission spectra. The recent introduction of spectrally resolved detection in microscopes has also greatly enhanced the capability to resolve fluorescence signals from multiple probes by using linear unmixing algorithms [57-60]. Fluorescence lifetime microscopy (FLIM) can offer another important tool to distinguish multiple probes, through measurements of their different fluorescence lifetimes [47, 61-64].

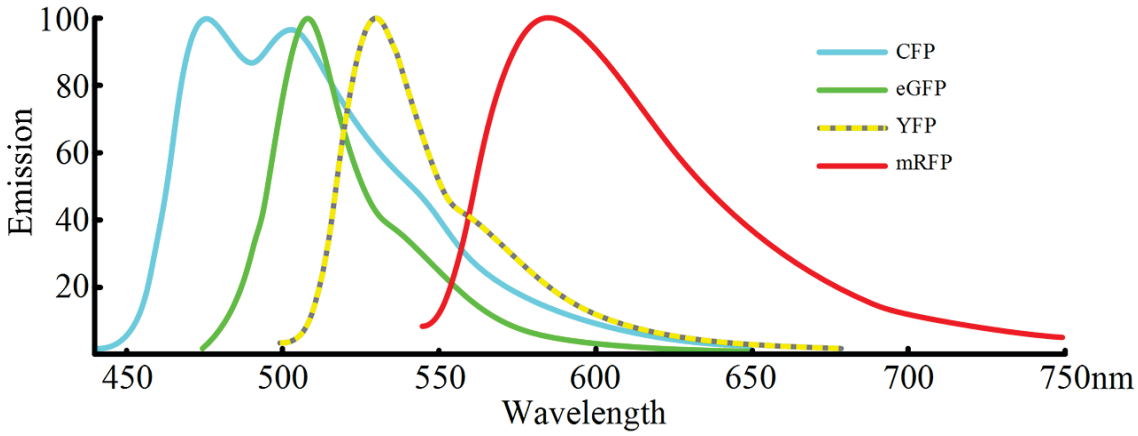

Figure 2-7 – The emission spectra of some commonly used fluorescent proteins, including the cyan fluorescent protein (CFP), enhanced green fluorescent protein (EGFP), yellow fluorescent protein (YFP), and monomeric red fluorescent protein (mRFP).

2.4 Non-Radiative Relaxation Pathways

The availability of non-radiative relaxation pathways reduces the fluorescence signal compared to what it would be in the absence of non-fluorescent energy loss. For intensity based fluorescence imaging, a reduction in quantum yield is undesirable; higher intensities allow high quality images to be acquired in less time. The most commonly used fluorescent dyes and fluorescent proteins have therefore been selected for their bright fluorescence signals, a property that arises from both strong absorption coefficients and high quantum yields. However, as noted above, there are some applications of fluorescence microscopy in which experimental conditions are intentionally designed to produce reductions in quantum yield for certain sub-populations of fluorescent molecules. The most widely used example of this is Forster resonance energy transfer (FRET) microscopy [44, 51, 65], which is widely used to

measure molecular interactions by measuring the efficiency of non-radiative energy transfer between donor and acceptor fluorophores.

2.4.1 Basics of FRET

FRET is a process in which an excited state molecule (the "donor") transfers its energy to a nearby molecule (the "acceptor") through near-field electromagnetic interactions. It falls in the category of non-radiative relaxation pathways as there is no fluorescence emission associated with the energy loss for the donor molecule. The rate of FRET energy transfer is related to the overlap between the donor emission and acceptor absorption spectra (Figure 2-8), the distance between donor and acceptor molecules, and the relative positioning and orientation of the donor and acceptor transition dipoles [39, 66, 67]. These factors go into computation of what is referred to as the Förster radius, R_0, which corresponds to the donor/acceptor separation at which there is a 50% FRET efficiency [51]. The energy transfer efficiency has very strong dependence on the physical separation, *r*, between donor and acceptor molecules, with the transfer rate varying with the inverse sixth power of the separation:

$$k_{FRET} = \frac{1}{\tau_D^0}\left(\frac{R_0}{r}\right)^6 \tag{2.9}$$

Here $\tau^o{}_D$ is the lifetime of the donor in the absence of the acceptor molecule. The distances over which efficient FRET is achieved are typically below 100 Å. This short length scale and the sixth power dependence of k_{FRET} on separation distance are the factors that lead to the usefulness of FRET for measuring molecular interactions and distances between donor and acceptor molecules using FRET [44, 51, 62, 68]. The distance dependence and orientational sensitivity of FRET can also be exploited to probe conformational changes in biomolecules [56, 69-71].

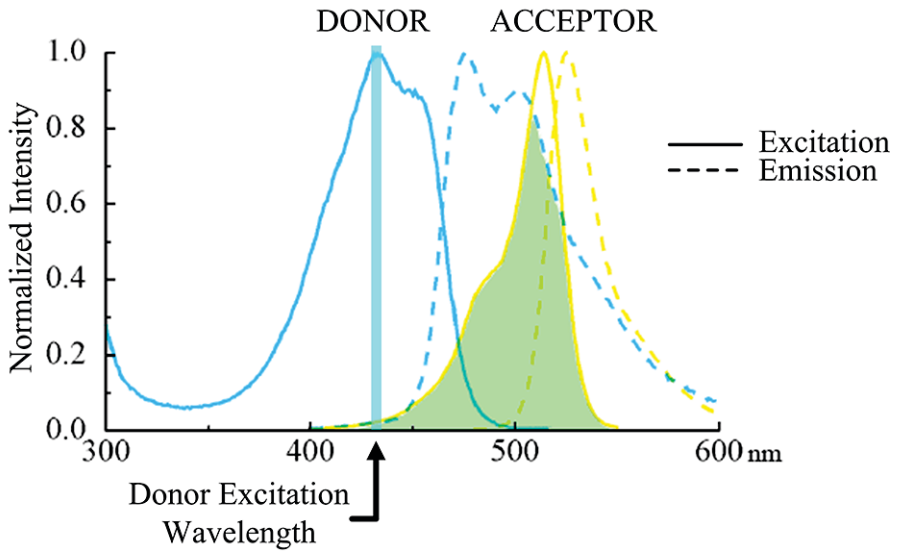

Figure 2-8 - Efficient Forster resonance energy transfer (FRET) requires significant overlap between the donor emission and acceptor excitation spectra. This figure shows the absorption and emission spectra for both donor and acceptor molecules of an efficient FRET pair. The arrow indicates the donor excitation wavelength, and the shaded region exemplifies the spectral overlap required for FRET.

Spectral overlap is a requirement for FRET, and thus FRET measurements in the microscope must find ways to quantitatively separate fluorescence signals from donor and acceptor molecules even though they have substantial spectral overlap. Moreover, accurate FRET measurements also require corrections for differences in the efficiency of the optics and detectors for the donor and acceptor fluorescence. A variety of data processing algorithms are used to correct for spectral cross-talk in FRET measurements [72, 73]. Alternatively, FRET efficiencies can also be accurately measured using fluorescence lifetime microscopy (FLIM), since donor molecules that have FRET relaxation pathways available will have shorter lifetimes compared with donor molecules

that do not relax *via* FRET [44, 61, 62, 74, 75]. FRET standards based on cyan and yellow fluorescent proteins have recently been introduced, and can be useful for calibrating FRET measurements in microscopy [61].

2.4.2 Intersystem Crossing and Phosphorescence

Intersystem crossing occurs when an excited state molecule relaxes to the triplet excited state, T_1. Molecules which reach the triplet state can relax either *via* photon emission or non-radiative relaxation. The radiative transition from the triplet state is called phosphorescence. The characteristic timescale for phosphorescence relaxation is much longer than fluorescence emission. For most applications of fluorescence microscopy, phosphorescence is not highly important. A possible exception is triplet saturation, in which a population of molecules builds up in the triplet state. This can reduce fluorescence signals since molecules in the excited triplet state may remain there for relatively long time periods (with typical average lifetimes of microseconds and longer) and are not able to produce fluorescence photons while they occupy the triplet state [76].

2.5 Photo-Selection and Anisotropy

The transition dipole moments for molecular absorption and fluorescence are vectors and have a spatial orientation that moves with the molecule. When a sample is illuminated with polarized light, molecules oriented such that their absorption dipole vectors are aligned with the electric field of the excitation light are preferentially excited. Polarized excitation thus photo-selects a sub-population from a randomly oriented sample, resulting in a partially oriented or anisotropic excited state population. As a result, fluorescence emission is also partially polarized, i.e. anisotropic. This effect is

often ignored in microscopy without significant consequences. However, it can be important for several reasons. First, by measuring the extent of anisotropy one can investigate molecular rotations [77]. This is possible since molecular rotation during the time a molecule occupies the excited state causes a re-orientation of the emission dipoles, thus reducing the anisotropy. Second, it is important to account for the effects of anisotropy changes (due to rotations) in order to accurately measure fluorescence lifetimes [39, 47, 78].

Two related parameters, anisotropy (r) and polarization (P), are commonly used to measure the degree of polarization. They are defined in terms of the fluorescence intensity polarized parallel (||) and perpendicular (⊥) to the excitation polarization:

$$r = \frac{I_{\parallel} - I_{\perp}}{I_{\parallel} + 2I_{\perp}} \qquad P = \frac{I_{\parallel} - I_{\perp}}{I_{\parallel} + I_{\perp}} \tag{2.10}$$

These two quantities are easily interconverted [**].

2.6 Measuring Fluorescence in the Microscope

When measuring fluorescence in the microscope, one is often dealing with weak signals from relatively small molecular populations, which necessitates careful optimization of signal acquisition. In addition, fluorescent molecules may be spatially confined, immobile, or slowly moving, and photobleaching can become an important concern [79-81]. Finally, because the spatial distribution of fluorescence signals is a primary concern in microscopy, it is useful to understand in detail how the fluorescence signal levels

[**] $r = \frac{2P}{3-P}$. $P = \frac{3r}{2+r}$.

correspond to molecular populations and their spatial distribution. In this final section we consider each of these topics.

2.6.1 Sensitivity of Fluorescence Measurements

A variety of factors influence how effectively fluorescence signals are measured in the microscope. Most important among these are the collection efficiency of the objective lens, the throughput of the optics and filters, and the efficiency of the optical detectors. Since fluorescence emission for freely rotating molecules is isotropic (emitted in all directions) it is not possible for an objective lens to collect the entire emitted fluorescence signal. The collection efficiency (C.E.) for an objective lens is primarily a function of its numerical aperture (*NA*); higher numerical aperture lenses collect more light [82, 83]. Provided one assumes fluorescence emission is spatially isotropic the collection efficiency of an objective lens (for an emitter at the focal point) is given by:

$$C.E. = \frac{1-\cos(\theta)}{2} \tag{2.11}$$

The angle θ is determined from the numerical aperture of the lens by: $n\sin(\theta) = NA$ where n is the index of refraction (n = 1 for air lenses, n = 1.3 for water immersion lenses, and $n \sim 1.5$ for common immersion oil lenses). Thus for example, an air lens with *NA* =*0 .9* will collect about 28% of the fluorescence emission. This means that most of the fluorescence will never make it through the lens to the detector. On the other hand, high *NA* lenses collect substantially more light than low *NA* lenses and thus optimize signal levels. High NA lenses also maximize spatial resolution. One trade-off is that high NA lenses can cause problems in quantifying polarization as the steep focusing angles distort the polarization of the laser excitation [84, 85]. Another drawback of higher NA lenses is

that they tend to have smaller working distances, defined as the space between the physical lens and the focal plane.

A second factor influencing the overall efficiency of fluorescence measurements in the microscope is the throughput (transmission) of the optics including objective and other lenses, filters, windows, and mirrors. Throughput can vary substantially for different designs and materials such that careful selection of optics can dramatically enhance measurement sensitivity. For example, while many band pass filters used to measure fluorescence have transmission efficiencies in the range of 60-80%, specialized filters with efficiencies exceeding 90% are readily available from commercial sources. Similarly, objective lenses of different design, materials, and lens coatings can have widely different throughputs, ranging from very poor to over 90% transmission. Objective transmission can also vary substantially for different wavelengths. Given each of these factors, it is clear that measurements will benefit from selecting optimized optics and lenses with high efficiencies.

Finally, optical detectors only record a fraction of the photons incident upon them. This fraction is referred to as the quantum efficiency of the detector – not to be confused with the quantum yield of the fluorescent molecules relaxing from the excited state. Surprisingly, detector efficiencies can be as small as a few percent or less for many commonly used detectors. On the other hand, highly sensitive photon counting detectors and cameras with much higher quantum efficiencies (up to ~90%) are now commercially available – providing an excellent resource to optimize fluorescence signal detection efficiency. Detector quantum efficiencies typically vary substantially for different wavelengths of light which must be considered in selecting appropriate detectors. [86]

Taking each of these factors together, one can estimate the total efficiency with which emitted photons can be detected by the microscope. If one assumes 30% collection by the objective, and 90% transmission efficiency for each of the other elements including the dichroic mirror, emission filter, objective lens, other microscope optics (e.g. mirrors and windows), then the overall efficiency of directing fluorescence emission to the detector would come out at near 20%, as shown in Table 2-3. With a 50% efficient detector, this would correspond to detecting ~10% of the fluorescence signal. This may seem small, but in fact represents a significant improvement over what was achievable not long ago.

Table 2-3

Microscope Elements	Optimized Collection Efficiency
Objective Lens: Numerical Aperture	0.3
Objective Lens: Transmission	0.9
Dichroic Mirror	0.9
Microscope Throughput[a]	0.9
Filters	0.9
Total Collection Efficiency	~20%
Total Detection Efficiency (Detector with 50% Efficiency)	10%

[a] The light transfer efficiency from the objective to the detector, excluding other listed elements. This accounts for losses due to windows, mirrors and prisms, and apertures.

2.6.2 Fluorescence Signals

The fluorescence signal detected from any position within the sample will be proportional to the concentration of fluorescent molecules at that location, the rate that the molecules are pumped into the excited state, and the detection efficiency. The fluorescence signal measured from a particular sample region can thus be written as $\kappa C(\mathbf{r},t)w(\mathbf{r})\Omega(\mathbf{r})$ where κ is a constant that accounts for both the quantum yield of the fluorophore and the fluorescence collection and detection efficiency of the microscope. The distribution function $\Omega(\mathbf{r})$ is included to describe any spatial filtering in the optical system, such as in confocal microscopy where pinholes are employed so that only fluorescence from certain sample regions reaches the detector. The function $\Omega(\mathbf{r})$ has unit value if there are no important apertures or pinholes, as is often but not always the case in two-photon microscopes. The total measured fluorescence signal can then be computed by integrating the contribution from different sample regions, with:

$$\langle F \rangle = \kappa \int C(\mathbf{r}) \langle w(\mathbf{r}) \rangle \Omega(\mathbf{r}) d\mathbf{r} \tag{2.12}$$

For two-photon excitation this integral has a finite value even without confocal pinholes, while for one-photon excitation a confocal pinhole is required for the integral to have a finite value. Equation (2.12) computes the average fluorescence signal from a particular spatial location within the sample, i.e. from the focused laser spot in a confocal or two-photon microscope. The laser is then scanned over various positions within the sample with other factors otherwise held constant so that the fluorescence intensity from any given location is primarily determined by the local fluorophore concentration.

2.6.3 Observation Volumes and Molecular Brightness

In recent years a variety of fluorescence fluctuation spectroscopy techniques have emerged that provide powerful capabilities for measuring molecular dynamics and interactions on the microscope and thus complement other fluorescence imaging methods [87-97]. While detailed descriptions of fluctuation measurements are beyond the scope of this chapter, there are two important concepts that have emerged from the development of fluctuation methods that are of significant value for understanding fluorescence signals in microscope. First, the concept of an observation volume has been introduced and provides a method to estimate the size and shape of the spatial region from which fluorescence signals are measured in two-photon and confocal microscopes. While there is no rigorous definition for a physical volume (i.e. a container of some exact size), one can compute the approximate measurement observation volume by dividing the total measured fluorescence signal (from a single position of a focused laser beam), by the amount of fluorescence per unit volume emitted when molecules are located in the center of the focal plane [26, 98]. Formally, the volume is thus defined:

$$V = \int \frac{w(\mathbf{r})\Omega(\mathbf{r})}{w(0)\Omega(0)} d\mathbf{r} \tag{2.13}$$

The volume, V, estimates the approximate size of the physical region which contributes substantially to the measured fluorescence signal when a focused laser beam illuminates a single position within the sample for confocal or two-photon microscopy. Images are created by moving the volume (i.e. the laser spot) across the sample in a raster pattern. The spatial dimensions of the observation volume can be useful to consider when selecting image pixel sizes. Pixels much larger than the volume will not optimize the available spatial resolution of the microscope optics.

Once the observation volume has been defined and assuming molecules are dispersed uniformly throughout the volume, Eq. (2.12) can be rewritten as $\langle F \rangle = \varepsilon \langle C \rangle V$, where the parameter ε is referred to as the molecular brightness, and is defined by:

$$\varepsilon = \kappa \langle w(0) \rangle \Omega(0) = \kappa \langle w(0) \rangle \tag{2.14}$$

The molecular brightness specifies the average number of photons measured per unit time from a single molecule located at the center of the focused laser excitation. The molecular brightness is dependent upon the photophysical properties of the fluorescent molecule and the excitation conditions as well as the microscope filters, optics, and detectors. It is therefore not a fundamental quantity, but it is measurable for any given experimental apparatus.

Both the volume and molecular brightness are valuable quantities in that they allow a fluorescence signal to be calibrated (by determining the volume and molecular brightness of any given fluorescent molecule on a particular instrument) so that the number of molecules responsible for a measured fluorescence signal can be determined.

This has proved useful not only for measuring molecular concentrations, but also for investigating molecular interactions in the microscope (e.g. dimers, trimers, etc, as well as binding between two different molecular species such as between a labeled protein and a labeled ligand) [91-94, 99, 100].

2.6.4 Saturation

On average, a fluorescent molecule can emit no more than $1/\tau$ photons per second. With tightly focused laser excitation sources used in microscopy, it is not unusual to illuminate fluorescent molecules with photon fluxes for which the nominal excitation rates for one and two-photon excitation, defined above, approach or exceed this maximum average fluorescence emission rate. When this occurs, the excitation is saturated and the fluorescence excitation will deviate from the linear (one-photon) or quadratic (two-photon) dependence on input power [26, 101, 102]. When the excitation is saturated, further increases in laser power do not proportionally increase the signal from the molecules within the observation volume. Instead, saturation tends to increase the size of the effective observation volume [101]. In the microscope, increasing illumination levels to increase signal levels can thus have the unintended effect decreasing image resolution. Saturation can also introduce artifacts into quantitative analysis of fluorescence signal, both because the signals are not proportional to illumination levels and because one may be comparing signals measured from differently sized sample regions. For strongly absorbing molecules, saturation can be an important effect even at average laser power levels that many researchers may consider “low power” excitation. Details of these effects are described in the literature [26, 101-103].

2.6.5 Photobleaching

Unfortunately fluorescent molecules are often not terribly robust, and bleaching is often an important concern in fluorescence imaging. Upon repeated excitation fluorescent molecules will undergo irreversible chemical reactions after which they no longer fluoresce. This is a statistical process and each fluorophore in a certain environment will photobleach, on average, after a certain number of excitations (i.e. there is a certain rate of photolysis once the molecule is in the excited state, and the photolysis pathway competes with the other pathways of de-excitation). Photobleaching rates are highly dependent upon the illumination level, although the chemical mechanisms responsible for the bleaching process are often not fully understood. One of the known bleaching mechanisms is due to interaction with molecular oxygen [104, 105]. The ground state of oxygen is a triplet, and after intersystem crossing of the excited fluorophore to the triplet state the triplet fluorophore can interact with the triplet oxygen creating the singlet ground state of the fluorophore and the singlet state of oxygen. Singlet oxygen is highly reactive and can chemically destroy the fluorophore as well as react with other surrounding molecules, creating reactive oxygen species which can also react with the fluorophore. Multi-photon absorption, and excited state absorption can also play a role in the bleaching of some molecular systems [106-108]. The average number of emission cycles which occur before photobleaching depends on both the molecule in question and the environment [106, 109]. Some molecules may bleach after emitting only a few photons, while other more robust probes can emit millions of fluorescence photons (on average) before bleaching. Photobleaching can cause artifacts in fluorescence microscopy and for quantitative fluorescence measurements it is always important to determine whether or not one observes significant photobleaching under illumination conditions. This is also true for FLIM microscopy since photobleaching can distort lifetime measurements when multiple lifetime components are involved.

It is sometimes possible to chemically reduce the photobleaching rate. For example, since bleaching is often highly dependent on oxygen concentration, various methods to remove oxygen from the sample can be very effective in stabilizing fluorescence emission [105]. This of course assumes that the reduced oxygen concentration and the method used to remove the oxygen are not otherwise detrimental to the system under investigation. It is worth noting that while bleaching can impede imaging applications, it can also be used to great advantage. For example, acceptor photobleaching is a useful tool for confirming molecular interactions as measured by FRET [110, 111]. Fluorescence photobleaching methods are also widely used to measure molecular dynamics [80].

2.7 Summary

The aim of this chapter has been to introduce the fundamental concepts and parameters which characterize molecular fluorescence, and some concepts relevant to measurement of fluorescence signals in microscopy. It is hoped that an understanding of this information will aid researchers in correctly applying fluorescence imaging technology, and in interpreting experimental results. The concepts introduced can also serve as the foundation for understanding the sophisticated applications of fluorescence in microscopy.

2.8 References

1. Kasha, M., *50 Years of the Jablonski Diagram*. Acta Physica Polonica A, 1987. **71**(5): p. 661-670.
2. Frackowiak, D., *The Jablonski Diagram*. Journal of Photochemistry and Photobiology B-Biology, 1988. **2**(3): p. 399-408.
3. Lakowicz, J., *Principles of Fluorescence Spectroscopy*. 3rd ed. 2006: Springer.
4. Valeur, B., *Molecular Fluorescence: Principles and Applications*. 1st ed. 2001: Wiley-VCH.
5. Pawley, J., *Handbook of Biological Confocal Microscopy*. 3rd ed. 2006: Springer.
6. Berlman, I.B., *Handbook of Fluorescence Spectra of Aromatic Molecules*. 2nd ed. 1971: Academic Press.
7. Rizzo, M.A., et al., *An Improved Cyan Fluorescent Protein Variant Useful for Fret*. Nat Biotechnol, 2004. **22**(4): p. 445-9.
8. Aubin, J.E., *Autofluorescence of Viable Cultured Mammalian Cells*. Journal of Histochemistry & Cytochemistry, 1979. **27**(1): p. 36-43.
9. Andersson, H., et al., *Autofluorescence of Living Cells*. Journal of Microscopy, 1998. **191**(1): p. 1-7.
10. Benson, R.C., et al., *Cellular Autofluorescence--Is It Due to Flavins?* Journal of Histochemistry & Cytochemistry, 1979. **27**(1): p. 44-8.
11. Dickinson, M.E., et al., *Multiphoton Excitation Spectra in Biological Samples*. J Biomed Opt, 2003. **8**(3): p. 329-38.
12. Thaler, C., et al., *Quantitative Multiphoton Spectral Imaging and Its Use for Measuring Resonance Energy Transfer*. Biophysical Journal, 2005. **89**(4): p. 2736-2749.
13. Koushik, S.V., et al., *Cerulean, Venus, and Venus(Y67c) Fret Reference Standards*. Biophysical Journal, 2006. **91**(12): p. L99-L101.

14. Guild, J.B., C. Xu, and W.W. Webb, *Pulse Dispersion by High Numerical Aperture Objectives for Nonlinear Microscopy Using Two-Photon Fluorescence Excitation*. Biophysical Journal, 1996. **70**(2): p. WP284-WP284.

15. Conchello, J.-A. and J.W. Lichtman, *Optical Sectioning Microscopy*. Nat Meth, 2005. **2**(12): p. 920-931.

16. Wilson, T., *Confocal Microscopy*. 1990: Academic Press.

17. Masters, B.R., *Confocal Microscopy and Multiphoton Excitation Microscopy: The Genesis of Live Cell Imaging*. 2006: SPIE Publications.

18. Denk, W., J.H. Strickler, and W.W. Webb, *2-Photon Excitation in Laser Scanning Microscopy*. Science, 1990. **248**(4951): p. 73-76.

19. Williams, R.M., D.W. Piston, and W.W. Webb, *Two-Photon Molecular Excitation Provides Intrinsic 3-Dimensional Resolution for Laser-Based Microscopy and Microphotochemistry*. Faseb Journal, 1994. **8**(11): p. 804-13.

20. Masters, B.R. and P. So, *Handbook of Biomedical Nonlinear Optical Microscopy*. 1st ed. 2008: Oxford University Press.

21. Diaspro, A., *Confocal and Two-Photon Microscopy: Foundations, Applications and Advances*. 1st ed. 2001: Wiley-Liss.

22. So, P.T., et al., *Two-Photon Excitation Fluorescence Microscopy*. Annu Rev Biomed Eng, 2000. **2**: p. 399-429.

23. Born, M. and E. Wolf, *Principles of Optics: Electromagnetic Theory of Propagation, Interference and Diffraction of Light*. 7th ed. 1999: Cambridge University Press.

24. Xu, C. and W. Webb, *Multiphoton Excitation of Molecular Fluorophores and Nonlinear Laser Microscopy*, in *Topics in Fluorescence Spectroscopy*, J. Lakowicz, Editor. 2002, Springer US. p. 471-540.

25. Tsien, R.Y., *The Green Fluorescent Protein*. Annual Review of Biochemistry, 1998. **67**: p. 509-544.

26. Nagy, A., J. Wu, and K.M. Berland, *Observation Volumes and Gamma-Factors in Two-Photon Fluorescence Fluctuation Spectroscopy*. Biophys. J., 2005. **89**(3): p. 2077-2090.

27. Zipfel, W.R., R.M. Williams, and W.W. Webb, *Nonlinear Magic: Multiphoton Microscopy in the Biosciences*. Nat Biotech, 2003. **21**(11): p. 1369-1377.

28. Squirrell, J.M., et al., *Long-Term Two-Photon Fluorescence Imaging of Mammalian Embryos without Compromising Viability*. Nat Biotech, 1999. **17**(8): p. 763-767.

29. Helmchen, F. and W. Denk, *Deep Tissue Two-Photon Microscopy*. Nat Meth, 2005. **2**(12): p. 932-940.

30. Xu, C. and W.W. Webb, *Measurement of Two-Photon Excitation Cross Sections of Molecular Fluorophores with Data from 690 to 1050 Nm*. Journal of the Optical Society of America B-Optical Physics, 1996. **13**(3): p. 481-491.

31. Xu, C., et al., *Multiphoton Fluorescence Excitation: New Spectral Windows for Biological Nonlinear Microscopy*. Proceedings of the National Academy of Sciences of the United States of America, 1996. **93**(20): p. 10763-10768.

32. Göppert-Mayer, M., *Über Elementarakte Mit Zwei Quantensprüngen*. Annalen der Physik, 1931. **401**(3): p. 273-294.

33. Xu, C. and W.W. Webb, *Multiphoton Excitation of Molecular Fluorophores and Nonlinear Laser Microscopy*, in *Topics in Fluorescence Spectroscopy: Nonlinear and Two-Photon Induced Fluoresence*, C.D.G. Joseph R. Lakowicz, Editor. 1991, Springer.

34. Masters, B.R. and P.T.C. So, *Handbook of Biomedical Nonlinear Optical Microscopy*. 2008: Oxford University Press.

35. Najechalski, P., et al., *Two-Photon Absorption Spectrum of Poly(Fluorene)*. Chemical Physics Letters, 2001. **343**(1-2): p. 44-48.

36. Yamaguchi, S. and T. Tahara, *Two-Photon Absorption Spectrum of All-Trans Retinal*. Chemical Physics Letters, 2003. **376**(1-2): p. 237-243.

37. Heikal, A.A., S.T. Hess, and W.W. Webb, *Multiphoton Molecular Spectroscopy and Excited-State Dynamics of Enhanced Green Fluorescent Protein (Egfp): Acid-Base Specificity*. Chemical Physics, 2001. **274**(1): p. 37-55.

38. Webb, W.W. *Multiphoton (Mpe) Index*. 2003; Available from: www.drbio.cornell.edu/MPE/mpe.html.

39. Lakowicz, J.R., *Principles of Fluorescence Spectroscopy, 3rd Ed*. 2007, New York: Plenum Press.

40. Spiess, E., Bestvater, F. A., Heckel-Pompey K. Toth M. Hacker G. Stobrawa T. Feurer C. Wotzlaw U. Berchner-Pfannschmidt T. Porwol H. Acker, *Two-Photon Excitation and Emission Spectra of the Green Fluorescent Protein Variants Ecfp, Egfp and Eyfp*. Journal of Microscopy, 2005. **217**(3): p. 200-204.

41. Jares-Erijman, E.A. and T.M. Jovin, *Fret Imaging*. Nat Biotech, 2003. **21**(11): p. 1387-1395.

42. Periasamy, A., *Methods in Cellular Imaging* ed. A. Periasamy. 2001: Oxford University Press.

43. Clegg, R.M., *Fluorescence Resonance Energy Transfer*. Current Opinion in Biotechnology, 1995. **6**: p. 103-110.

44. Periasamy, A. and N.R. Day, *Molecular Imaging* ed. A. Periasamy and N.R. Day. 2005: Oxford University Press.

45. Campagnola, P.J. and L.M. Loew, *Second-Harmonic Imaging Microscopy for Visualizing Biomolecular Arrays in Cells, Tissues and Organisms*. Nat Biotech, 2003. **21**(11): p. 1356-1360.

46. Campagnola, P.J., et al., *Three-Dimensional High-Resolution Second-Harmonic Generation Imaging of Endogenous Structural Proteins in Biological Tissues*. Biophys. J., 2002. **82**(1): p. 493-508.

47. Becker, W., *The Becker Hickl Tcspc Handbook* 2007: Becker & Hickl Gmbh.

48. Davidson, M.W., et al. *Molecular Expressions Optical Microscopy Primer*. 2005; Available from: http://micro.magnet.fsu.edu/primer/index.html.

49. So, P.T.C., et al., *Time-Resolved Fluorescence Microscopy Using Two-Photon Excitation*. Bioimaging, 1995. **3**: p. 49-63.

50. Clegg, R.M., O. Holub, and C. Gohlke, *Fluorescence Lifetime-Resolved Imaging: Measuring Lifetimes in an Image*. Methods in enzymology, 2003. **360**: p. 509-542.

51. Clegg, R.M., *Fluorescence Resonance Energy Transfer*, in *Fluorescence Imaging Spectroscopy and Microscopy* X.F. Wang and B. Herman, Editors. 1996, Wiley-Interscience.

52. Hillesheim, L.N., Y. Chen, and J.D. Muller, *Dual-Color Photon Counting Histogram Analysis of Mrfp1 and Egfp in Living Cells*. Biophysical Journal, 2006. **91**(11): p. 4273-4284.

53. Rizzo, M.A., et al., *An Improved Cyan Fluorescent Protein Variant Useful for Fret*. Nature Biotechnology, 2004. **22**(4): p. 445-449.

54. Ganesan, S., et al., *A Dark Yellow Fluorescent Protein (Yfp)-Based Resonance Energy-Accepting Chromoprotein (Reach) for Forster Resonance Energy Transfer with Gfp*. Proceedings of the National Academy of Sciences of the United States of America, 2006. **103**(11): p. 4089-4094.

55. Koushik, S.V., et al., *Cerulean, Venus, and Venusy67c Fret Reference Standards*. Biophysical Journal, 2006. **91**(12): p. L99-101.

56. Selvin, P.R. and T. Ha, eds. *Single Molecule Techniques: A Laboratory Manual*. 2008, Cold Spring Harbor Laboratory Press.

57. Zimmermann, T., J. Rietdorf, and R. Pepperkok, *Spectral Imaging and Its Applications in Live Cell Microscopy*. FEBS Letters, 2003. **546**(1): p. 87-92.

58. Thaler, C. and S.S. Vogel, *Quantitative Linear Unmixing of Cfp and Yfp from Spectral Images Acquired with Two-Photon Excitation*. Cytometry Part A, 2006. **69A**(8): p. 904-911.

59. Neher, R.A. and E. Neher, *Applying Spectral Fingerprinting to the Analysis of Fret Images*. Microscopy Research and Technique, 2004. **64**(2): p. 185-195.

60. Kawata, S. and K. Sasaki, *Multispectral Image Processing for Component Analysis*, in *Fluorescence Imaging Spectroscopy and Microscopy*, X.F. Wang and B. Herman, Editors. 1996, John Wiley and Sons: New York.

61. Koushik, S.V., et al., *Cerulean, Venus, and Venusy67c Fret Reference Standards*. Biophys. J., 2006. **91**(12): p. L99-101.

62. Wallrabe, H. and A. Periasamy, *Imaging Protein Molecules Using Fret and Flim Microscopy*. Current Opinion in Biotechnology, 2005. **16**(1): p. 19-27.

63. Kapusta, P., et al., *Fluorescence Lifetime Correlation Spectroscopy*. Journal of Fluorescence, 2007. **17**(1): p. 43-48.

64. Kühnemuth, R. and A.M.C. Seidel, *Principles of Single Molecule Multiparameter Fluorescence Spectroscopy*. Single Molecules, 2001. **2**(4): p. 251-254.

65. Wu, P.G. and L. Brand, *Resonance Energy Transfer: Methods and Applications*. Analytical Biochemistry, 1994. **218**(1): p. 1-13.

66. Forster, T., *Delocalized Excitation and Excitation Transfer*. Modern Quantum Chemistry, ed. Sinanoglu. Vol. 3. 1965, New York: Academic Press.

67. Stryer, L., *Fluorescence Energy Transfer as a Spectroscopic Ruler*. Annual Review of Biochemistry, 1978. **47**: p. 819-46.

68. Sekar, R.B. and A. Periasamy, *Fluorescence Resonance Energy Transfer (Fret) Microscopy Imaging of Live Cell Protein Localizations*. J. Cell Biol., 2003. **160**(5): p. 629-633.

69. Truong, K. and M. Ikura, *The Use of Fret Imaging Microscopy to Detect Protein-Protein Interactions and Protein Conformational Changes in Vivo*. Current Opinion in Structural Biology, 2001. **11**(5): p. 573-578.

70. Heyduk, T., *Measuring Protein Conformational Changes by Fret/Lret*. Current Opinion in Biotechnology, 2002. **13**(4): p. 292-296.

71. Rasnik, I., S.A. McKinney, and T. Ha, *Surfaces and Orientations: Much to Fret About?* Acc. Chem. Res., 2005. **38**(7): p. 542-548.

72. Tron, L., et al., *Flow Cytometric Measurement of Fluorescence Resoncance Energy Transfer on Cell Surfaces*. Biophys. J., 1984. **45**.

73. Gordon, G.W., et al., *Quantitative Fluorescence Resoncance Energy Transfer Measurements Using Fluorescence Microscopy*. Biophys. J., 1998. **74**: p. 2702-2713.

74. Wang, Y., J.Y.J. Shyy, and S. Chien, *Fluorescence Proteins, Live-Cell Imaging, and Mechanobiology: Seeing Is Believing*. Annual Review of Biomedical Engineering, 2008. **10**(1): p. 1-38.

75. Chen, Y., James D. Mills and Ammasi Periasamy, *Protein Localization in Living Cells and Tissues Using Fret and Flim*. Differentiation, 2003. **71**(9-10): p. 528-541.

76. Tsien, R.Y. and A. Waggoner, *Fluorophores for Confocal Microscopy*, in *Handbook of Biological Confocal Microscopy 2nd Edition*, J.B. Pawley, Editor. 1995, Plenum: New York. p. 267-279.

77. Steiner, R.F., *Fuorescence Anisotropy: Theory and Applications*, in *Topics in Fluorescence Spectroscopy: Techniques*, J.R. Lakowicz, Editor. 1991, Springer.

78. Fixler, D., et al., *Influence of Fluorescence Anisotropy on Fluorescence Intensity and Lifetime Measurement: Theory, Simulations and Experiments*. Biomedical Engineering, IEEE Transactions on, 2006. **53**(6): p. 1141-1152.

79. Eggeling, C., et al., *Photobleaching of Fluorescent Dyes under Conditions Used for Single-Molecule Detection: Evidence of Two-Step Photolysis*. Anal. Chem., 1998. **70**(13): p. 2651-2659.

80. Axelrod, D., et al., *Mobility Measurement by Analysis of Fluorescence Photobleaching Recovery Kinetics*. Biophys. J., 1976. **16**(9): p. 1055-69.

81. Kenworthy, A.K., *Photobleaching Fret Microscopy*, in *Molecular Imaging* A. Periasamy and N.R. Day, Editors. 2005, Oxford University Press.

82. Kazuko, K., et al., *High Collection Efficiency in Fluorescence Microscopy with a Solid Immersion Lens*. Applied Physics Letters, 1999. **75**(12): p. 1667-1669.

83. Lindek, S., J. Swoger, and E.H.K. Stelzer, *Single-Lens Theta Microscopy: Resolution, Efficiency and Working Distance*. Journal of Modern Optics, 1999. **46**(5): p. 843-858.

84. Axelrod, D., *Carbocyanine Dye Orientation in Red Cell Membrane Studied by Microscopic Fluorescence Polarization*. Biophys J, 1979. **26**(3): p. 557-573.

85. Piston, D.W., M.A. Rizzo, and F.S. Kevin, *Fret by Fluorescence Polarization Microscopy*, in *Methods in Cell Biology*. 2008, Academic Press. p. 415-430.

86. Hamamatsu. *Quantum Efficiency*. Concepts in Digital Imaging Technology 2008; Available from: http://digitalimagingu.com/articles/quantumefficiency.html.

87. Rigler, R. and E. Elson, eds. *Fluorescence Correlation Spectroscopy Theory and Applications*. Chemical Physics. 2000, Springer: New York

88. Schwille, P., *Fluorescence Correlation Spectroscopy and Its Potential for Intracellular Applications*. Cell Biochemistry and Biophysics, 2001. **34**(3): p. 383-408.

89. Hess, S.T., et al., *Biological and Chemical Applications of Fluorescence Correlation Spectroscopy: A Review*. Biochemistry, 2002. **41**(3): p. 697-705.

90. Webb, W.W., *Fluorescence Correlation Spectroscopy: Inception, Biophysical Experimentations, and Prospectus*. Applied Optics, 2001. **40**(24): p. 3969-3983.

91. Berland, K.M., *Quantifying Molecular Interactions with Fluorescence Correlation Spectroscopy*, in *Molecular Imaging: Fret Microscopy and Spectroscopy*, A. Periasamy and R.N. Day, Editors. 2005, Oxford University Press: New York.

92. Hillesheim, L.N., Y. Chen, and J.D. Muller, *Dual-Color Photon Counting Histogram Analysis of Mrfp1 and Egfp in Living Cells*. Biophys. J., 2006. **91**(11): p. 4273-4284.

93. Wu, B. and J.D. Muller, *Time-Integrated Fluorescence Cumulant Analysis in Fluorescence Fluctuation Spectroscopy*. Biophys. J., 2005. **89**(4): p. 2721-2735.

94. Muller, J.D., *Cumulant Analysis in Fluorescence Fluctuation Spectroscopy*. Biophysical Journal, 2004. **86**(6): p. 3981-3992.

95. Muller, J.D., Y. Chen, and E. Gratton, *Fluorescence Correlation Spectroscopy*, in *Methods in Enzymology*. 2003. p. 69-92.

96. Chen, Y., et al., *Two-Photon Fluorescence Fluctuation Spectroscopy*, in *New Trends in Fluorescence Spectroscopy: Applications to Chemical and Life Sciences*, B. Valeur and J.C. Brochon, Editors. 2001, Springer-verlag: Berlin.

97. Chen, Y., et al., *Fluorescence Fluctuation Spectroscopy*. Methods, 1999. **19**(2): p. 234-252.

98. Hess, S.T. and W.W. Webb, *Focal Volume Optics and Experimental Artifacts in Confocal Fluorescence Correlation Spectroscopy*. Biophys. J., 2002. **83**(4): p. 2300-2317.

99. Schwille, P., F.J. Meyer-Almes, and R. Rigler, *Dual-Color Fluorescence Cross-Correlation Spectroscopy for Multicomponent Diffusional Analysis in Solution*. Biophysical Journal, 1997. **72**(4): p. 1878-1886.

100. Eigen, M. and R. Rigler, *Sorting Single Molecules - Application to Diagnostics and Evolutionary Biotechnology*. Proceedings of the National Academy of Sciences of the United States of America, 1994. **91**(13): p. 5740-5747.

101. Cianci, C.G., Jianrong Wu, Keith M. Berland, *Saturation Modified Point Spread Functions in Two-Photon Microscopy*. Microscopy Research and Technique, 2004. **64**(2): p. 135-141.

102. Wu, J. and K. Berland, *Fluorescence Intensity Is a Poor Predictor of Saturation Effects in Two-Photon Microscopy: Artifacts in Fluorescence Correlation Spectroscopy*. Microscopy Research and Technique, 2007. **70**(8): p. 682-686.

103. Nagy, A., J. Wu, and K.M. Berland, *Characterizing Observation Volumes and the Role of Photophysical Dynamics in One-Photon Fluorescence Fluctuation Spectroscopy*. J Biomedical Optics, 2005. **10**(4): p. 1-9.

104. Corbett, J.D., M.R. Cho, and D.E. Golan, *Deoxygenation Affects Fluorescence Photobleaching Recovery Measurements of Red Cell Membrane Protein Lateral Mobility*. Biophys. J., 1994. **66**(1): p. 25-30.

105. Rasnik, I., S.A. McKinney, and T. Ha, *Nonblinking and Long-Lasting Single-Molecule Fluorescence Imaging*. Nat Meth, 2006. **3**(11): p. 891-893.

106. Patterson, G.H., Piston, David W., *Photobleaching in Two-Photon Excitation Microscopy*. Biophys. J., 2000. **78**(4): p. 2159-2162.

107. Rubart, M., *Two-Photon Microscopy of Cells and Tissue*. Circ Res, 2004. **95**(12): p. 1154-1166.

108. Svoboda, K. and R. Yasuda, *Principles of Two-Photon Excitation Microscopy and Its Applications to Neuroscience*. Neuron, 2006. **50**(6): p. 823-839.

109. Hirschfeld, T., *Quantum Efficiency Independence of the Time Integrated Emission from a Fluorescent Molecule*. Applied Optics, 1976. **15**: p. 3135-3139.

110. Kenworthy, A.K., *Imaging Protein-Protein Interactions Using Fluorescence Resonance Energy Transfer Microscopy*. Methods, 2001. **24**(3): p. 289-296.

111. Zal, T. and N.R.J. Gascoigne, *Photobleaching-Corrected Fret Efficiency Imaging of Live Cells*. Biophys. J., 2004. **86**(6): p. 3923-3939.

Chapter 3

Imaging Nucleation, Growth and Heterogeneity in Self-Assembled Amyloid Phases

Neil R. Anthony*, Anil K. Mehta†, W. Seth Childers†‡, Keith M. Berland*, and David G. Lynn†

*Department of Physics, Emory University, Atlanta, GA 30322

†Center for Fundamental and Applied Molecular Evolution, NSF/NASA Center for Chemical Evolution, Departments of Chemistry and Biology, Emory University, Atlanta, GA 30322

‡Current address: Department of Developmental Biology, Stanford University School of Medicine, Stanford, California, 94305

This chapter is currently in press:

Neil R. Anthony, Anil K. Mehta, W. Seth Childers, Keith M. Berland, David G. Lynn, Bionanoimaging, Part 1. Nanoimaging and nanotechnology of aggregating proteins: A. In vitro approaches – Imaging Nucleation, Growth and Heterogeneity in Self-Assembled Amyloid Phases

3.1 Abstract

Advances in electron and fluorescence microscopy imaging are now providing molecular level resolution of macromolecular and supramolecular dynamic self-organization. Nowhere has this information been more impactful than in understanding the increasing diversity of biomolecular misfolding diseases. The amyloid-β protein associated with Alzheimer's disease and its congeners have now offered insight into both neurodegenerative disease as well as functional scaffolds for constructing bio-inspired nanomaterials. Here we discuss the exploitation of these methods within these dynamic networks of paracrystalline supramolecular phases, and define minimal nucleation events, resolve the templated propagation events, and reveal the complex dynamic molecular networks of these polymorphic assemblies.

Keywords

Peptide Aggregation, Alzheimer's Disease, Amyloid-β(16-22), Peptide Nanotubes, Electron Microscopy, Fluorescence Lifetime Imaging Microscopy, FLIM, Molten Particles, Fluorescence Correlation Spectroscopy, FCS, Förster Energy Resonance Transfer, FRET.

3.2 Introduction

Amyloid may have been first detected as abnormal extracellular deposits in the liver that turned violet upon addition of sulfuric acid to iodine treated samples [1]. These amyloid plaques were later shown to be fibrous β-sheet rich proteins [2-4], and the positive iodine stain was derived from proteoglycans bound to amyloid [5]. Divry and Florkin stained the plaques with Congo red (CR) [6] and found that linearly polarized light illumination gave a characteristic pink hue. The now more characteristic apple-green birefringence was observed with crossed polarizers and has been shown to result from CR molecules organized along the amyloid assembly (see [7] and references therein [chapter ref]). Other dyes, most characteristically thioflavin T (ThT) that shows enhanced fluorescence (λ_{ex} = 450 nm, λ_{em} = 482 nm) upon binding to amyloid, have been developed as fluorescence markers for high throughput screens of amyloid aggregation *in vitro* [8] and in primary diagnostic assays of amyloid assemblies [9]. Given that these protein phases have now been implicated in as many as 50 diseases [10], and serve as natural elements for epigenetic inheritance, adhesive materials, and robust molecular scaffolds [10-17], major efforts have focused on delineating the apparent structural differences between toxic, benign, and functional forms of the amyloid assemblies.

X-ray and electron diffraction analyses of oriented ~100 Å diameter fibers reveal orthogonal arcs with d-spacings at 4.7 Å and ~10 Å [4, 18, 19]. These reflections arise from the periodic spacing of H-bonded peptides within a β-sheet (4.7 Å) with the H-bonds aligned parallel to the fiber axis, and the roughly 10 Å stacking (lamination) of β-sheets mediated by side-chain associations. These orthogonal diffractions have been described as the cross-β architecture, a tertiary arrangement common to all amyloid assemblies. While such oriented diffraction information reveals the long-range

paracrystalline organization of the peptides with respect to the fiber axis, solid-state NMR methods have provided valuable complementary information regarding the relative peptide strand positions. Isotopic enrichment in the peptide backbone carbonyls through synthesis has enabled very precise measurements of ^{13}C-^{13}C dipolar coupling [20-22], defining distances up to ~6 Å. Initial measurements of the Alzheimer's associated protein Amyloid-β (Aβ) directly constrained the peptides to be in register parallel β-sheet arrangements [20, 21, 23], and since then solid-state NMR methods have provided a critical constraints for many diverse cross-β assemblies.

The combination of diffraction [4, 24-26], solid-state NMR [20, 21, 23, 27], and X-ray crystallography [28, 29] developments have enabled structural definition of the common cross-β core of these amyloid assemblies, setting the stage for addressing their many biological functions. For a field that began with optical imaging, the potential to observe the assembly process in the context of structural constraints, to image variations in morphology and assembly dynamics in the context of atomic level structure, and to reveal structural reorganizations in response to environmental perturbations both *in vitro* and *in vivo* in real time could now dramatically impact the development of diagnostics and therapeutics for this rapidly growing class of protein misfolding diseases.

3.3 Diversity in Cross-β Assemblies

The energy landscape for peptide assembly into amyloid is quite diverse, and the many distinct morphologies that appear may impact the observed phenotypes [30-33]. For example, the assembly of even the simple nucleating core [34-38] of the Aβ peptide associated with Alzheimer's disease, Aβ(16-22) constructed as Ac-KLVFFAE-NH_2, shows a phase behavior that is highly responsive to small changes in environmental conditions

[39, 40]. At neutral pH, Aβ(16-22) peptides assemble into typical amyloid fibers [40, 41] as visualized by transmission electron microscopy (TEM; Figure 3–1a). Uranyl acetate produces negative stain contrast in TEM micrographs due to its exclusion from the dense ordered peptide structures, providing dark highlights along the fiber edges. These fibers have minimal widths of 5 nm but can access either straight or twisted dimer topologies under these conditions (Figure 3–1a with inset).

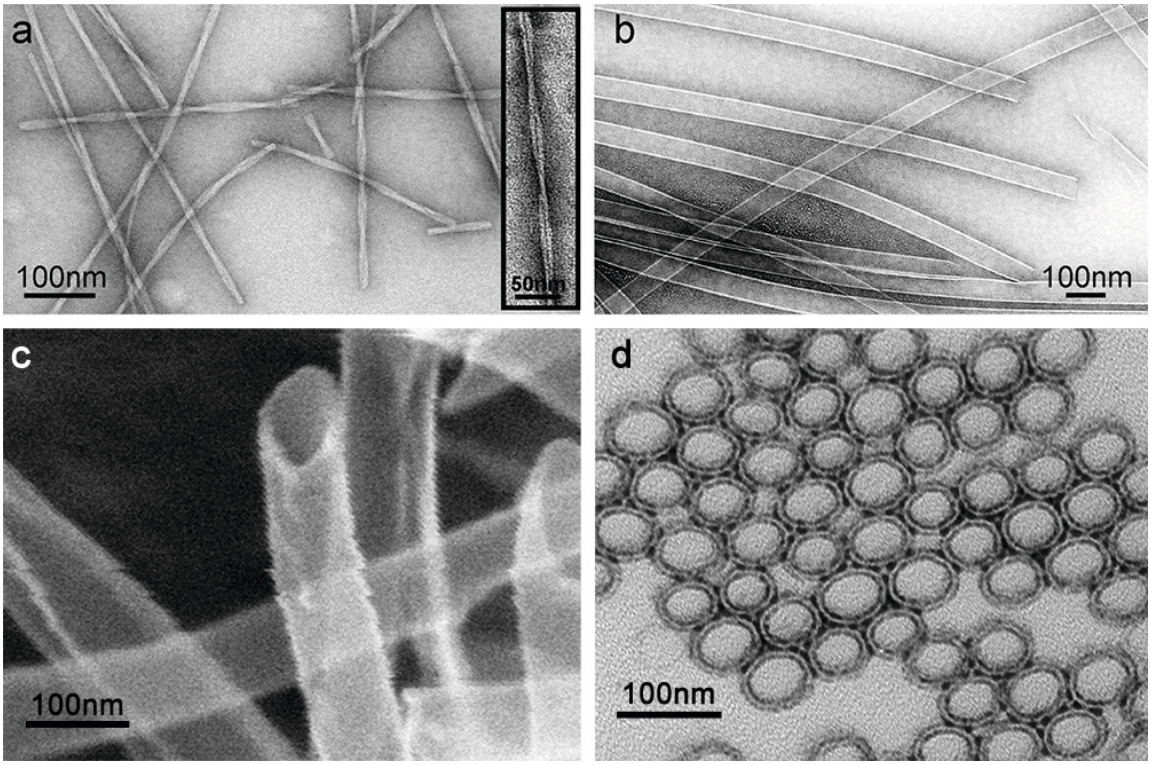

Figure 3–1 – Aß(16-22) pH dependent morphology. Negative stain TEM images of Aß(16-22) peptides assembled in 40% acetonitrile at (a) neutral pH and (b) acidic pH. (c) Cryo-etch HR-SEM images of Aß(16-22) peptides nanotube assemblies at acidic pH and (d) cross-sectioned epoxy resin embedded nanotube assemblies oriented perpendicular to the tube's long-axis. Adapted from [40] copyright 2008 American Chemical Society and from [42] copyright 2010 WILEY-VCH Verlag GmbH & Co.

At acidic pH (Figure 3–1b-d), Aβ(16-22) peptides assemble into nanotubes with widths an order-of-magnitude larger than the fibers [43] but maintain the hallmark diffraction and Congo red birefringence signatures of amyloid [40, 44]. In addition to markedly different TEM-determined widths, the acidic pH structures trap uranyl acetate stain within their interior and display distinct white borders where stain is excluded (Figure 3–1b). Cryo-etch high-resolution scanning electron microscopy (HR-SEM; Figure 3–1c) [40], scattering [43] and cross-sectioning of epoxy resin embedded assemblies [42] (Figure 3–1d) indicate that these assemblies are hollow 54 nm diameter nanotubes with a peptide wall that is 4.4 nm thick. The radical morphological change for Aβ(16-22) peptides from fibers to hollow nanotubes results from the formation of anti-parallel out-of-register β-sheets that lead to extended β-sheet lamination [40, 43, 45]. While amyloid fibers are composed of 5 laminated β-sheets (Figure 3–2a), nanotubes have 150 laminated β-sheets that helically coil into a tube (Figure 3–2b) [40, 44].

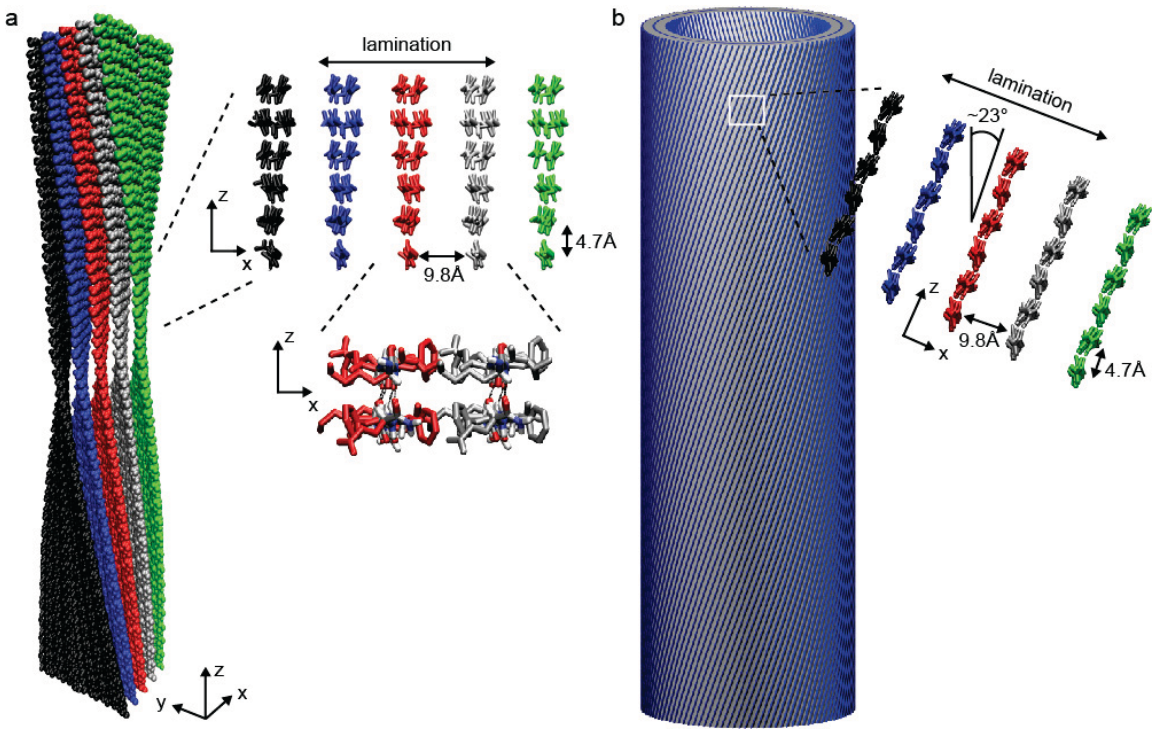

Figure 3–2 – Structure models for the cross-β assemblies of Aβ(16-22) fibers and nanotubes with direction of β-sheet H-bonds defined as the z-axis and lamination along the x-axis. The amyloid fiber (a) has five β-sheets arranged with the peptide backbone perpendicular to the fiber z-axis. Expansions show individual peptides and side-chains that direct lamination. The peptide nanotube (b) is comprised of 150 laminated β-sheets that helically coil to form nanotubes with the β-sheet H-bonds oriented 23° from the tube long axis (expansion). Adapted from [40], copyright 2008 American Chemical Society.

To visually assess these distinct phases, labeled peptide probes [46, 47] were created by replacing the lysine of Aβ(16-22) with a positively charged rhodamine-110 fluorophore (denoted as Rh17-22; Figure 3–3a). When a small fraction of Rh17-22 (<1%) is co-assembled with Aβ(16-22), highly fluorescent nanotubes are seen, which are morphologically identical with the TEM images (Figure 3–3c). The uniform fluorescence

(homogeneous to ~500 nm optical resolution) along the length of the tube suggests that Rh17-22 is dispersed randomly throughout the tube structure, and localized to the inner and outer surface of the nanotube walls (Figure 3–3b).

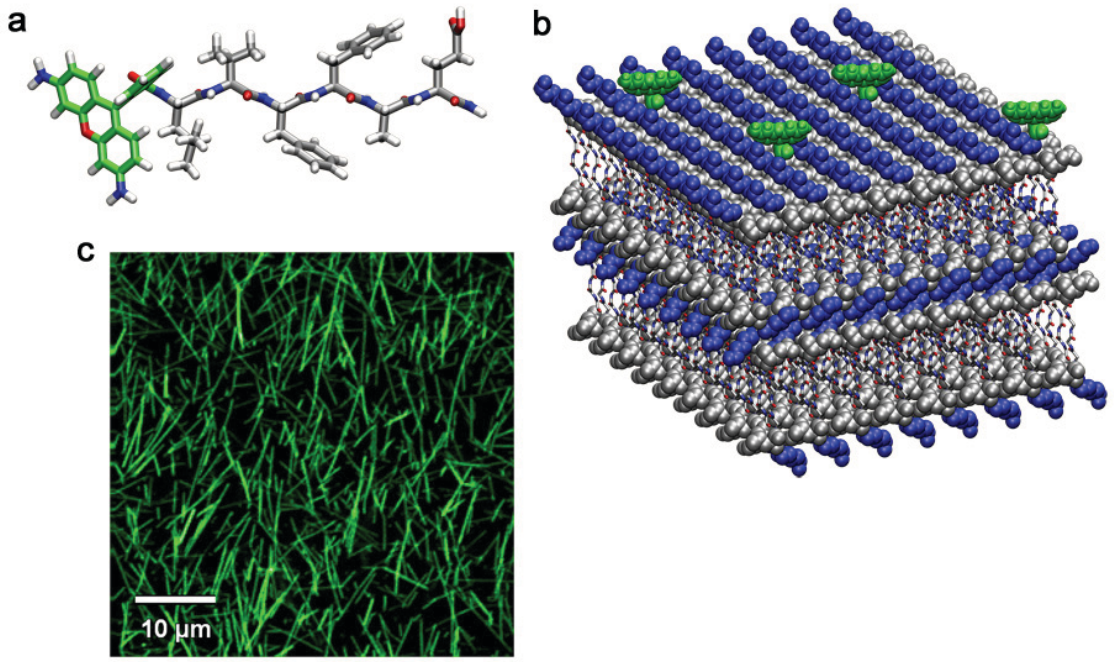

Figure 3–3 – Rh17-22 peptide (a) formed by replacing the Lys residue in KLVFFAE with the rhodamine-110 fluorophore. Model of Rh17-22 incorporated into the Aβ(16-22) nanotube bilayer surface (b) where lysine side-chains are presented as blue spheres and leucines and protonated glutamate side-chains as gray spheres. The remaining side-chains are hidden for clarity. Homogeneous Rh17-22 incorporation observed using two-photon fluorescence imaging (c). Adapted from [48], copyright 2009, Elsevier.

3.4 Particle Phases

The initial transition to polypeptide particles appears to be necessary for the formation of the paracrystalline phase of amyloid [9, 39, 47, 49, 50]. These particles probably emerge through intermolecular hydrophobic collapse into a less-hydrated molten-state that provides a dense peptide liquid phase promoting β-sheet secondary structure assembly. Such molten phases have been predicted in numerous simulations of Aβ(16-22) assembly (see references in [39]), but nucleation within these particles is stochastic and remains challenging to observe. Perturbing this nucleation pathway with different solvent and temperature regimes can slow crystallization [39, 47]. For example, Aβ(16-22) peptides assembled between 4°C and 30°C in acidic 40% aqueous acetonitrile yields micrometer long, 50nm diameter nanotubes at equilibrium (Figure 3–1b-e & 4a), while above 40°C no particles and no assemblies form. In a small temperature window centered around 37°C, both small (~88 nm) and large (~197 nm) particles can be detected by electron microscopy (Figure 3–4b&c). After lowering the temperature, the particles completely transition back to nanotubes structures [39].

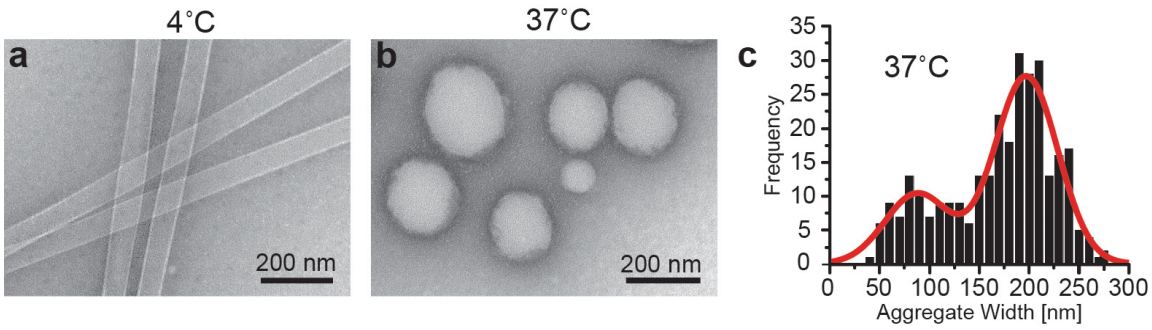

Figure 3–4 – Arresting nucleation using temperature. Aβ(16-22) assembled at low temperatures forms nanotubes (a) while assembly at 37°C yields spherical particles when visualized by TEM with uranyl acetate negative staining (b). Analysis of particle widths

yields a bimodal distribution centered at 88 and 197 nm (c). Reprinted from [39] with copyright 2012 American Chemical Society.

The β-strand structure of these assemblies can be ascertained *via* the characteristic circular dichroism (CD) spectral transition at 215 nm that arises from exciton coupling of the amide electronic transitions [51, 52]. CD spectra of the 4°C and 30°C nanotubes reveal that peptides adopt a β-sheet structure, but at higher temperatures a weaker β-sheet signature is detected [39]. Indeed, the CD signals from the 37°C particles suggests the particles are a mixture of peptides with β-sheet and random coil conformations. For particles assembled at 37°C in the presence of uranyl acetate (Figure 3–5a), two distinct regions that exclude stain are observed by electron microscopy. The uranyl acetate contrast resolves rod-like regions within the particles that are consistent with ordered peptide phases. The decreased uranyl acetate penetration into these rod-like regions is diagnostic of the more ordered structures resulting from crystallization [39].

To further evaluate these phases during nucleation, the Rh17-22:Aβ(16-22) peptide mixtures were observed in real time. Fluorescence lifetime imaging microscopy (FLIM) of peptide aggregates adhered to microscope slide surfaces exhibit considerably shorter lifetimes than monomer Rh17-22 (3.4 ± 0.1ns). More significantly, densely packed regions are located at the center of nanotube growth (Figure 3–5b; blue regions), consistent with these regions harboring nucleation. We surmise that these short lifetime growth centers contain numerous liquid-liquid phases similar to those arrested at 37°C.

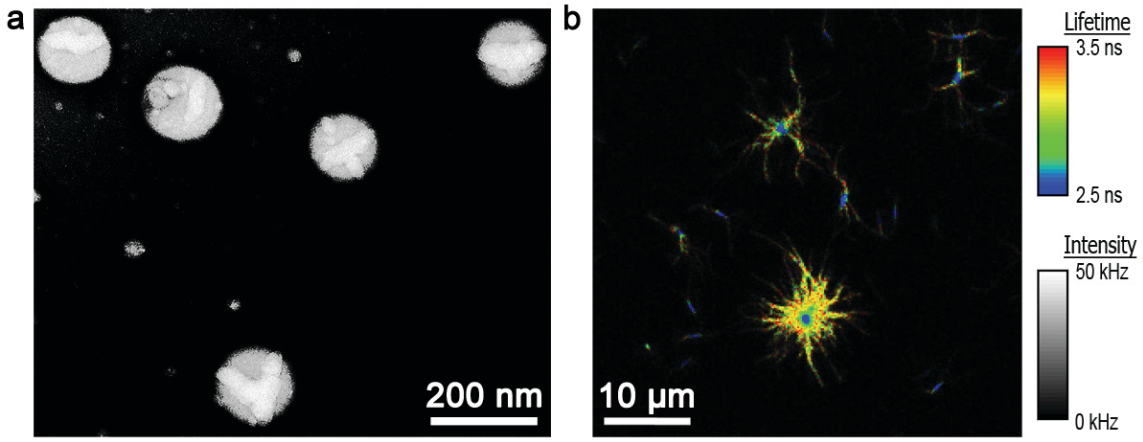

Figure 3–5 – Uranyl acetate contrast enhanced TEM of Aβ(16–22) particles (a) assembled from peptide solutions incubated with 1 wt % uranyl acetate under acidic conditions at 37°C. FLIM images of Rh17-22:Aβ(16-22) aggregates (b) adhered to the microscope slide display macroscale phases; considerably shorter fluorescent lifetimes appear at the epicenter than the growing nanotube structures. Reprinted from [39] with copyright 2012 American Chemical Society.

3.5 Paracrystallization

The bimodal distribution of small and larger particles observed by TEM (Figure 3–4b&c) suggests they are structurally distinct and dynamic. Following adjustment of pH from 2 to 7 (Figure 3–6b-d) or temperature from 37°C to 4°C (Figure 3–6e-g) filaments begin emerging from the larger particles. After 2 weeks nanotubes have formed at pH 2 and 4°C and fibers at pH 7 and 37°C, and all particles have been consumed [39]. These phases are interconnected with complex phase boundaries, and the nature of and site of the transition to the more crystalline phases remain poorly defined.

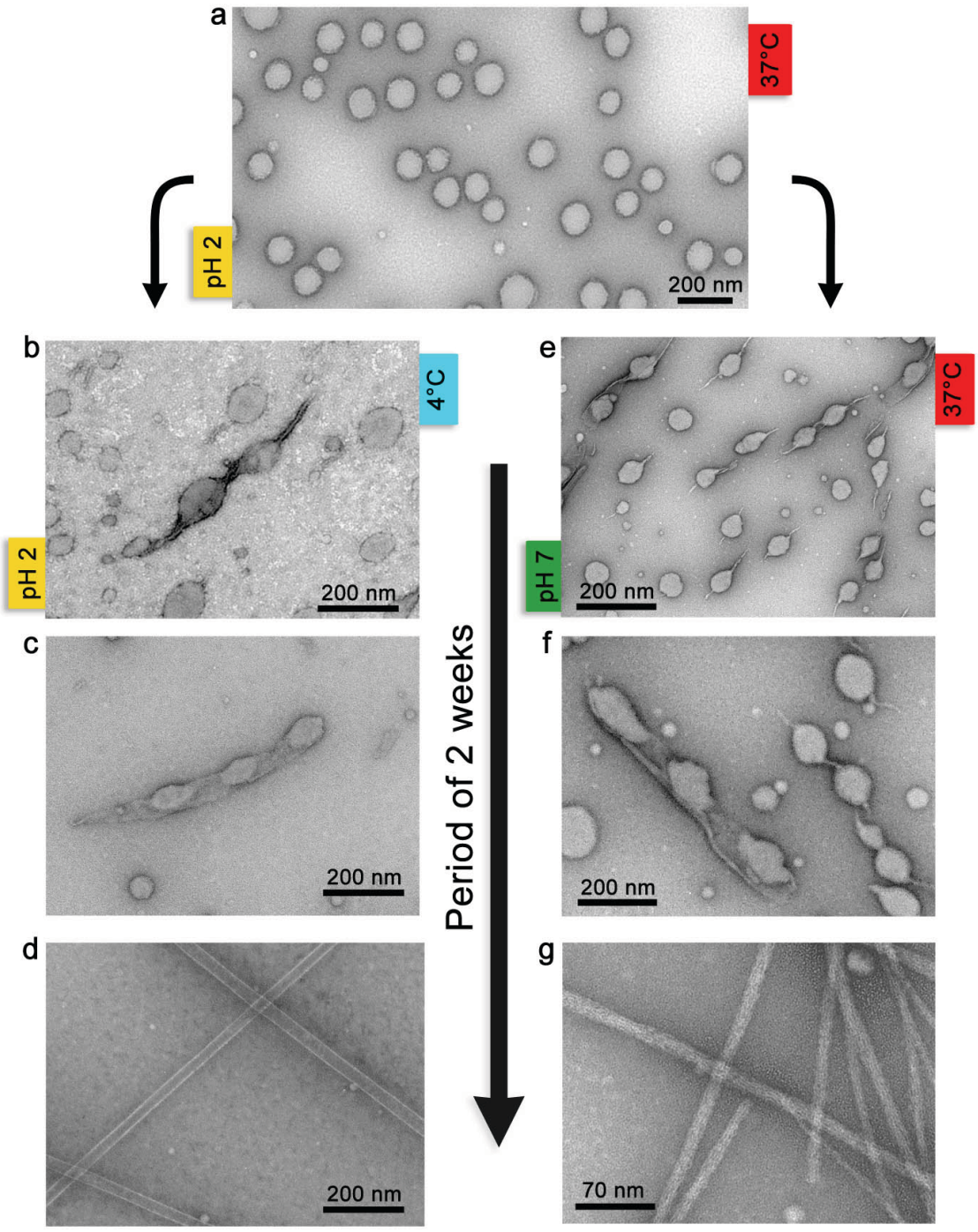

Figure 3–6 – TEM images of growth from arrested particles induced by environment change. Mature Aβ(16–22) particle assemblies formed at 37 °C in acidic media (a). Adjusting either temperature (b-d) or pH (e-g) and following over a 2 week period sees a

return to environmental dependent morphology. Reprinted from [39] with copyright 2012 American Chemical Society.

A number of kinetic models describing the growth of cross-β structures have been developed [49, 50] whereby propagation generally involves monomer addition onto preformed templates. The co-assembly of Aβ(16-22) with Rh17-22 provided an opportunity to directly investigate this growth in real time. When Aβ(16-22) is incubated above its critical concentration of ~0.5 mM, large fluorescent aggregates, ranging from 2 to 8 μm in diameter (Figure 3–7a), form spontaneously [47]. Vertical sectioning of these large aggregates with two-photon laser scanning microscopy reveals the interiors to be structurally homogeneous (Figure 3–7a; upper panels). Fluorescence recovery after photobleaching (FRAP) analysis demonstrated that fluorescence recovered within minutes (Figure 3–7b; squares) supporting the computational models of dynamic exchange with free peptides in solution. Under these conditions, ~50% of the total peptide resides in the particles. The more ordered paracrystalline phases of the tubes (Figure 3–7a; lower panels & 3–7b; circles) do not recover from photobleaching over this time period. This dynamic exchange of peptides inside the aggregate with peptides in solution implies a liquid-liquid phase separation analogous to the prerequisite hydrophobic collapse documented for protein crystallization [53-56].

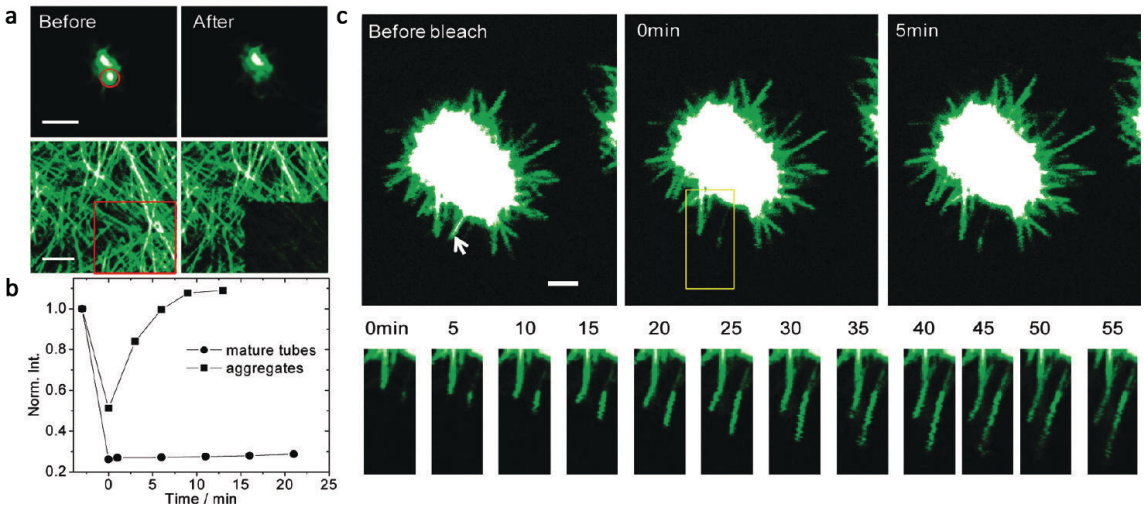

Figure 3–7 – Nucleation and growth of Aß(16-22):Rh17-22 mixtures. (a) Particles (upper) and mature nanotubes (lower). (b) Recovery after photobleaching particles (squares) and mature nanotubes (spheres). (c) Photobleaching of nanotube growth emanating from aggregates. Reprinted from [47] with copyright 2010 American Chemical Society.

At later times, nanotubes are observed growing from the aggregates (Figure 3–7c), consistent with nucleation initiated within these dynamic assemblies. Time-lapse images reveal fast nanotube growth emerging from the aggregate, maintaining an average growth rate of 3-4 nm/s (see supplementary movies [47]). Also, the incorporation of Rh17-22 peptide appears homogeneous along each structure. Photobleaching of these emerging nanotubes and time-lapse analyses (Figure 3–7c; lower panels) indicate that while these structures nucleate within the aggregates, they grow from the tip of the emerging structure and are not pushed out into solution from within the peptide-dense particle (Figure 3–7c; center & right).

The possibility that the more hydrophobic Rh17-22 was aggregating with Aβ(16-22) in solution prior to tube growth was tested using fluorescence correlation spectroscopy (FCS), which measures the diffusion coefficient and molecular brightness of the fluorescent species [57, 58]. The diffusion coefficient can determine if Rh17-22 associates with Aß(16-22) (assuming aggregates greater than 5 molecules), while the molecular brightness quantifies the light collected from each diffusing species [59, 60], and as such can identify Rh17-22 dimerization. The molecular brightness and diffusion coefficient of Rh17-22 in Aß(16-22):Rh17-22 mixtures, above and below the critical concentration (i.e. solutions with and without nucleation and growth), were consistent with monomer values determined using extremely dilute Rh17-22 solutions [47]. Therefore, β-sheet growth occurs predominantly *via* monomer addition tube ends. Given the detailed knowledge of nanotube structure (accounting for a 52 nm tube diameter composed of peptide bilayers with 4.7 Å H-bonding spacing, 9.8 Å lamination, and a pitch of 23° [40]), the monomer addition occurs at an average rate of ~2000 peptides per second.

3.6 Paracrystalline Polymorphism

The environmental conditions for assembly clearly impact paracrystalline polymorphism of the cross-β assemblies, and now the mixed Rh17-22 and Aβ(16-22) assemblies allow subtle differences to be probed on the nanotube surfaces. The mixed nanotubes discussed above display uniform fluorescence along their length demonstrating that a small fraction of added Rh17-22 peptide can serve as an effective non-perturbing probe of Aβ(16-22) nanotube assembly. However, as a pure peptide Rh17-22 does not form nanotubes but rather assembles as a fiber, suggesting that the charged rhodamine can impact assembly. Such structural polymorphism in mixed peptide assemblies has not been extensively explored, but given the complexity of the cellular environment where

disease develops [29, 61, 62], mixed assemblies may well control critical etiologically significant pathways. Maybe more significantly given the location of the fluorophore, the Rh17-22 peptide allows the surface of the nanotubes to be probed optically with respect to rhodamine packing density, organization, and molecular dynamics.

When the Aβ(16-22) peptides are assembled with <1% Rh17-22 peptide, the nanotubes are homogeneously fluorescent (Figure 3–8a) and FLIM analyses yield homogeneous lifetime values of 3.1 ns (Figure 3–8c, red line). However, in assemblies prepared with slightly higher Rh17-22 percentages, even as little as 1-2%, the nanotubes [63] fluorescence lifetime values are both shorter and display far greater diversity (Figure 3–8c, blue line). Most remarkable, FLIM analysis discerns heterogeneous lifetime distributions that exhibit distinct transition points along individual tubes (Figure 3–8b, d). These abrupt transitions at higher Rh17-22 ratios suggest that the rhodamine chromophore influences peptide aggregation in a cooperative manner, creating structurally distinct arrays that propagate along the tube surface. The exact structure of these domains and the mechanism for their propagation can now be explored in detail.

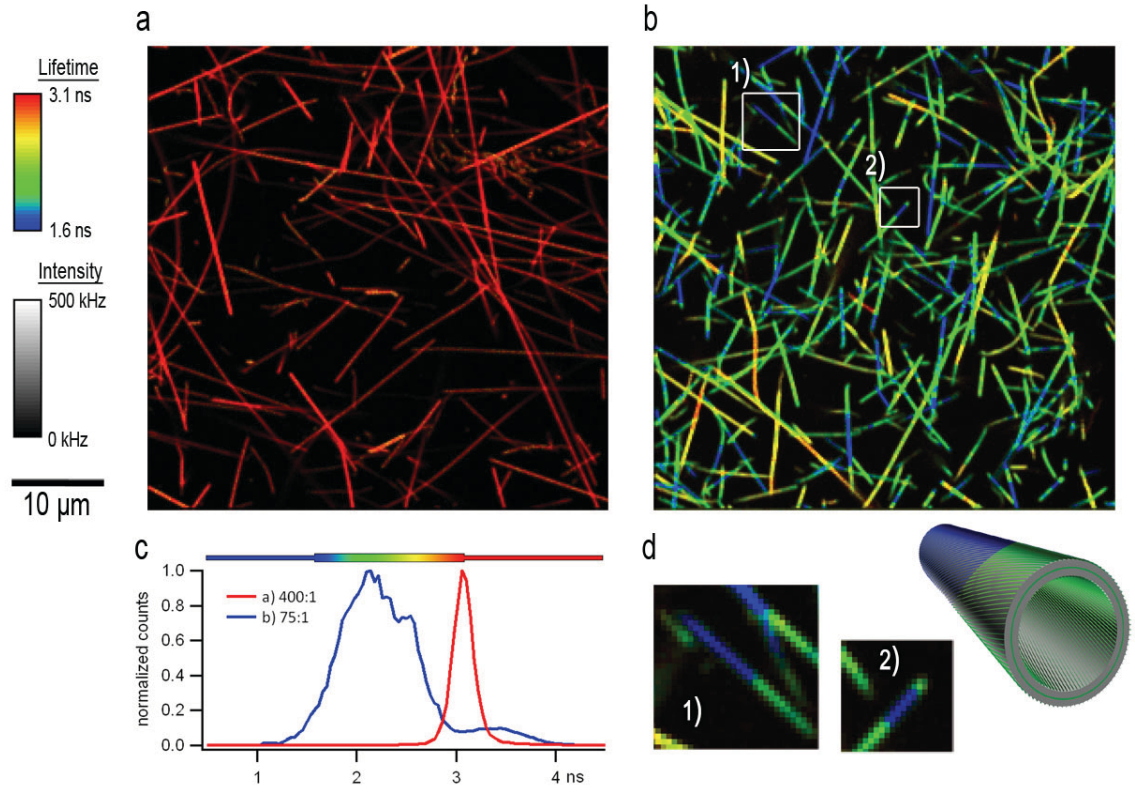

Figure 3–8 – Mature Aß(16-22): Rh17-22 nanotube assemblies observed using FLIM. (a) Nanotubes assembled with a 400:1 Aß(16-22):Rh17-22 ratio with homogeneous lifetime values. (b) Higher incorporation ratios, 75:1, lead to distinct heterogeneities of the fluorescence lifetimes. (c) FLIM image average lifetime histograms of 400:1 (red line) and 75:1 (blue line) Aß(16-22):Rh17-22 ratios. (d) Expansions (3X) and nanotube model of the regions indicated in (b) highlighting the distinct transitions along individual tubes.

The ability of FLIM to spatially resolve these heterogeneities should prove invaluable for imaging and defining elements critical for heterogeneity and dynamics on the surface of amyloidogenic structures [29, 61, 62, 64]. Such heterogeneous populations and diverse assembly environments that appear to underlie the phenotypic dementia and toxicity in

Alzheimer's and other amyloid diseases [10, 29, 61, 62] can now be correlated with subtle structural changes in the assembled phases.

3.7 Functional Energy Transfer

In addition to understanding disease, these materials now provide scaffolds for designing multifunctional bionanostructures with chemical potential gradients. The high water mark in such systems are found in the ordered long-range pigment assemblies of reaction centers in the light-harvesting complexes of photosynthesis [65]. These ordered pigment arrays have provided inspiration for synthetic physical/chemical energy inter-conversions, and the paracrystalline structure of the cross-β nanotubes now provide a new and exploitable scaffold.

Energy transfer along the tube surface was first investigated *via* Förster energy resonance transfer (FRET) [46] on Rh16-22:Aβ(16-22) mixed nanotube scaffolds. The detailed atomic-level structure of peptide nanotubes defined structural models for the binding sites of the negatively charged histochemical dye Congo red (CR) [44]. CR binds with its long axis parallel to the β-sheet H-bonds and within the grooves on the tube surface formed by the lamination of adjacent β-sheets. The negatively charged florescent Alexa 555 dye, a planar aromatic molecule with a similar sulfate substitution to Congo red, forms an efficient FRET pair with rhodamine-110. At a Rh16-22:A555 ratio of 4:1, the average dye separation was estimated to be ~10 nm. Indeed, a peak fluorescence lifetime shift from 3.7 ns with only Rh16-22 labeled tubes to 3.3 ns is observed in the presence of A555, corresponding to a FRET efficiency of 11%. We rule out the possibility that this reduction in lifetime arises from A555 stimulation as calculated data models suggest this only results in a peak lifetime shift to 3.6 ns [46]. This ability to generate

long-range ordered arrays of pigments on self-assembled peptide nanotubes provides a critical first step for functionalized bio-inspired nanomaterials with light-harvesting capability.

3.8 Closing Perspective

While the root cause of protein misfolding diseases has been doggedly investigated for over 100 years, and the ubiquitous cross-β architecture of amyloid has been known for well over 50 years [4, 24-26], the subtleties of cross-β assembly pathway, the polymorphic nature of its phases, and the functional diversity of its architecture are only now being revealed. From a field that began with image analysis of tissue samples, electron and fluorescence microscopy are now revealing the nanoscale images necessary to build atomic resolution models, exploring the energetic landscapes for its assembly, and uncovering the subtle changes in environment that dictate its morphological and structural forms. In Richard Feynman's famous 1959 talk "There's plenty of room at the bottom" where he describes the control of individual atoms for the creation of designer nanomaterials, amyloid assemblies could not be more apt. As we enter an era in which our understanding of Nature's materials is grounded at the atomic level, we can rightly hope that this level of understanding will not only help prevent the deleterious health side of amyloid's structure, but will lead to the construction and exploitation of unique functional materials that have yet to emerge through chemical evolution.

3.9 Acknowledgements

The authors' work that was mentioned in this chapter was supported in part by U.S. DOE (ER15377), NASA Astrobiology Program, under the NSF Center for Chemical Evolution CHE-1004570, and NSF CBC-0739189 and DMR-0907435.

3.10 Literature Cited

1. Virchow, R., *Zur Cellulose-Fruge*. Virchows Arch., 1855. **8**: p. 140-144.
2. Sipe, J.D. and A.S. Cohen, *Review: History of the Amyloid Fibril*. J. Struct. Biol., 2000. **130**(2-3): p. 88-98.
3. Cohen, A.S. and E. Calkins, *Electron Microscopic Observations on a Fibrous Component in Amyloid of Diverse Origins*. Nature, 1959. **183**(4669): p. 1202-3.
4. Eanes, E.D. and G.G. Glenner, *X-Ray Diffraction Studies on Amyloid Filaments*. J. Histochem. Cytochem., 1968. **16**(11): p. 673-7.
5. Doyle, L., *Lardaceous Disease: Some Early Reports by British Authors (1722-1879)*. J. R. Soc. Med., 1988. **81**(12): p. 729-31.
6. Divry, P. and M. Florkin, *The Optic Properties of Amyloid*. C. R. Seances Soc. Biol. Ses Fil., 1927. **97**: p. 1808-1810.
7. Jin, L.-W., et al., *Imaging Linear Birefringence and Dichroism in Cerebral Amyloid Pathologies*. Proc. Natl. Acad. Sci. U. S. A., 2003. **100**(26): p. 15294-15298.
8. LeVine, H., 3rd, *Thioflavine T Interaction with Synthetic Alzheimer's Disease Beta-Amyloid Peptides: Detection of Amyloid Aggregation in Solution*. Protein Sci., 1993. **2**(3): p. 404-10.
9. Nilsson, M., *Techniques to Study Amyloid Fibril Formation in Vitro*. Methods, 2004. **34**(1): p. 151-160.
10. Walker, L.C., et al., *Inducible Proteopathies*. Trends Neurosci., 2006. **29**(8): p. 438-43.

11. Inge-Vechtomov, S.G., G.A. Zhouravleva, and Y.O. Chernoff, *Biological Roles of Prion Domains*. Prion, 2007. **1**(4): p. 228-35.

12. Fowler, D.M., et al., *Functional Amyloid - from Bacteria to Humans*. Trends Biochem. Sci., 2007. **32**(5): p. 217-24.

13. Hammer, N.D., J.C. Schmidt, and M.R. Chapman, *The Curli Nucleator Protein, Csgb, Contains an Amyloidogenic Domain That Directs Csga Polymerization*. Proc. Natl. Acad. Sci. U. S. A., 2007. **104**(30): p. 12494-9.

14. Iconomidou, V.A. and S.J. Hamodrakas, *Natural Protective Amyloids*. Curr. Protein Pept. Sci., 2008. **9**(3): p. 291-309.

15. Romero, D., et al., *Amyloid Fibers Provide Structural Integrity to Bacillus Subtilis Biofilms*. Proc. Natl. Acad. Sci. U. S. A., 2010. **107**(5): p. 2230-4.

16. Barlow, D.E., et al., *Characterization of the Adhesive Plaque of the Barnacle Balanus Amphitrite: Amyloid-Like Nanofibrils Are a Major Component*. Langmuir, 2010. **26**(9): p. 6549-56.

17. Halfmann, R., et al., *Prions Are a Common Mechanism for Phenotypic Inheritance in Wild Yeasts*. Nature, 2012. **482**(7385): p. 363-U1507.

18. Geddes, A.J., et al., *"Cross-Beta" Conformation in Proteins*. J. Mol. Biol., 1968. **32**(2): p. 343-58.

19. Parker, K.D. and K.M. Rudall, *Structure of the Silk of Chrysopa Egg-Stalks*. Nature, 1957. **179**(4566): p. 905-906.

20. Gregory, D.M., et al., *Dipolar Recoupling Nmr of Biomolecular Self-Assemblies: Determining Inter- and Intrastrand Distances in Fibrilized Alzheimer's Beta-Amyloid Peptide*. Solid State Nucl. Magn. Reson., 1998. **13**(3): p. 149-66.

21. Benzinger, T.L., et al., *Propagating Structure of Alzheimer's Beta-Amyloid(10-35) Is Parallel Beta-Sheet with Residues in Exact Register*. Proc. Natl. Acad. Sci. U. S. A., 1998. **95**(23): p. 13407-12.

22. Spencer, R.G., et al., *An Unusual Peptide Conformation May Precipitate Amyloid Formation in Alzheimer's Disease: Application of Solid-State Nmr to the Determination of Protein Secondary Structure*. Biochemistry, 1991. **30**(43): p. 10382-7.

23. Benzinger, T.L., et al., *Two-Dimensional Structure of Beta-Amyloid(10-35) Fibrils*. Biochemistry, 2000. **39**(12): p. 3491-9.

24. Makin, S., et al., *Molecular Basis for Amyloid Fibril Formation and Stability*. Proc. Natl. Acad. Sci. U. S. A., 2005. **102**(2): p. 315-320.

25. Sawaya, M.R., et al., *Atomic Structures of Amyloid Cross-Beta Spines Reveal Varied Steric Zippers*. Nature, 2007. **447**(7143): p. 453-7.

26. Kirschner, D.A., et al., *Synthetic Peptide Homologous to Beta Protein from Alzheimer Disease Forms Amyloid-Like Fibrils in Vitro*. Proc. Natl. Acad. Sci. U. S. A., 1987. **84**(19): p. 6953-7.

27. Petkova, A.T., et al., *Self-Propagating, Molecular-Level Polymorphism in Alzheimer's ß-Amyloid Fibrils*. Science, 2005. **307**(5707): p. 262-5.

28. Nelson, R. and D. Eisenberg, *Recent Atomic Models of Amyloid Fibril Structure*. Curr. Opin. Struct. Biol., 2006. **16**(2): p. 260-265.

29. Eisenberg, D. and M. Jucker, *The Amyloid State of Proteins in Human Diseases*. Cell, 2012. **148**(6): p. 1188-203.

30. Jucker, M. and L.C. Walker, *Pathogenic Protein Seeding in Alzheimer Disease and Other Neurodegenerative Disorders*. Ann. Neurol., 2011. **70**(4): p. 532-40.

31. Aguzzi, A., M. Heikenwalder, and M. Polymenidou, *Mechanisms of Disease - Insights into Prion Strains and Neurotoxicity*. Nat. Rev. Mol. Cell Biol., 2007. **8**(7): p. 552-561.

32. Collinge, J. and A.R. Clarke, *A General Model of Prion Strains and Their Pathogenicity*. Science, 2007. **318**(5852): p. 930-936.

33. Chen, B., G.P. Newnam, and Y.O. Chernoff, *Prion Species Barrier between the Closely Related Yeast Proteins Is Detected Despite Coaggregation*. Proc. Natl. Acad. Sci. U. S. A., 2007. **104**(8): p. 2791-6.

34. Tjernberg, L.O., et al., *Arrest of ß-Amyloid Fibril Formation by a Pentapeptide Ligand*. J. Biol. Chem., 1996. **271**(15): p. 8545-8548.

35. Hilbich, C., et al., *Substitutions of Hydrophobic Amino Acids Reduce the Amyloidogenicity of Alzheimer's Disease Beta A4 Peptides*. J. Mol. Biol., 1992. **228**(2): p. 460-73.

36. Wood, S.J., et al., *Prolines and Amyloidogenicity in Fragments of the Alzheimer's Peptide Beta/A4*. Biochemistry, 1995. **34**(3): p. 724-30.

37. Williams, A.D., et al., *Mapping a Beta Amyloid Fibril Secondary Structure Using Scanning Proline Mutagenesis*. J. Mol. Biol., 2004. **335**(3): p. 833-842.

38. Williams, A.D., S. Shivaprasad, and R. Wetzel, *Alanine Scanning Mutagenesis of Abeta(1-40) Amyloid Fibril Stability*. J. Mol. Biol., 2006. **357**(4): p. 1283-94.

39. Childers, W.S., et al., *Phase Networks of Cross-Beta Peptide Assemblies*. Langmuir, 2012. **28**(15): p. 6386-6395.

40. Mehta, A.K., et al., *Facial Symmetry in Protein Self-Assembly*. J. Am. Chem. Soc., 2008. **130**(30): p. 9829-9835.

41. Balbach, J.J., et al., *Amyloid Fibril Formation by Aβ16-22, a Seven-Residue Fragment of the Alzheimer's B-Amyloid Peptide, and Structural Characterization by Solid State Nmr*. Biochemistry, 2000. **39**(45): p. 13748-13759.

42. Childers, W.S., et al., *Peptides Organized as Bilayer Membranes*. Angew. Chem., Int. Ed., 2010. **49**(24): p. 4104-4107.

43. Lu, K., et al., *Exploiting Amyloid Fibril Lamination for Nanotube Self-Assembly*. J. Am. Chem. Soc., 2003. **125**(21): p. 6391-6393.

44. Childers, W.S., et al., *Templating Molecular Arrays in Amyloid's Cross-ß Grooves*. J. Am. Chem. Soc., 2009. **131**(29): p. 10165-10172.

45. Dong, J., et al., *Controlling Amyloid Growth in Multiple Dimensions*. Amyloid, 2006. **13**(4): p. 206-215.

46. Liang, Y., et al., *Light Harvesting Antenna on an Amyloid Scaffold*. Chem. Commun., 2008(48): p. 6522-6524.

47. Liang, Y., D.G. Lynn, and K.M. Berland, *Direct Observation of Nucleation and Growth in Amyloid Self-Assembly*. J. Am. Chem. Soc., 2010. **132**(18): p. 6306-6308.

48. Childers, W.S., et al., *Peptide Membranes in Chemical Evolution*. Curr. Opin. Chem. Biol., 2009. **13**(5-6): p. 652-9.

49. Morris, A.M., M.A. Watzky, and R.G. Finke, *Protein Aggregation Kinetics, Mechanism, and Curve-Fitting: A Review of the Literature*. Biochim. Biophys. Acta, 2009. **1794**(3): p. 375-97.

50. Cohen, S.I., et al., *From Macroscopic Measurements to Microscopic Mechanisms of Protein Aggregation*. J. Mol. Biol., 2012. **421**(2-3): p. 160-71.

51. Woody, R.W., *Optical Properties of Polypeptides in Beta-Conformation*. Biopolymers, 1969. **8**(5): p. 669-683.

52. Chen, Y.H., J.T. Yang, and K.H. Chau, *Determination of Helix and Beta-Form of Proteins in Aqueous-Solution by Circular-Dichroism*. Biochemistry, 1974. **13**(16): p. 3350-3359.

53. ten Wolde, P.R. and D. Frenkel, *Enhancement of Protein Crystal Nucleation by Critical Density Fluctuations*. Science, 1997. **277**(5334): p. 1975-8.

54. Lomakin, A., N. Asherie, and G.B. Benedek, *Liquid-Solid Transition in Nuclei of Protein Crystals*. Proc. Natl. Acad. Sci. U. S. A., 2003. **100**(18): p. 10254-7.

55. Muschol, M. and F. Rosenberger, *Liquid-Liquid Phase Separation in Supersaturated Lysozyme Solutions and Associated Precipitate Formation/Crystallization*. J. Chem. Phys., 1997. **107**(6): p. 1953-1962.

56. Vekilov, P.G., *Phase Transitions of Folded Proteins*. Soft Matter, 2010. **6**(21): p. 5254-5272.

57. Elliot L, E., *Fluorescence Correlation Spectroscopy: Past, Present, Future*. Biophys. J., 2011. **101**(12): p. 2855-2870.

58. Thompson, N.L., *Fluorescence Correlation Spectroscopy*, in *Topics in Fluorescence Spectroscopy*, J.R. Lakowicz, Editor. 1991, Plenum: New York. p. 337-378.

59. Chen, Y., et al., *Fluorescence Fluctuation Spectroscopy*. Methods, 1999. **19**(2): p. 234-252.

60. Chen, Y., et al., *Molecular Brightness Characterization of Egfp in Vivo by Fluorescence Fluctuation Spectroscopy*. Biophys. J., 2002. **82**(1): p. 133-144.

61. Rosen, R.F., L.C. Walker, and H. Levine, 3rd, *Pib Binding in Aged Primate Brain: Enrichment of High-Affinity Sites in Humans with Alzheimer's Disease*. Neurobiol. Aging, 2011. **32**(2): p. 223-34.

62. Miller, Y., B. Ma, and R. Nussinov, *Polymorphism in Alzheimer Aβ Amyloid Organization Reflects Conformational Selection in a Rugged Energy Landscape*. Chem. Rev., 2010. **110**(8): p. 4820-38.

63. Anthony, N.R., et al. *Structural Heterogeneities of Self-Assembled Peptide Nanomaterials*. in *SPIE Photonics West*. 2012. San Francisco, CA: SPIE.

64. Nilsson, K.P.R., et al., *Imaging Distinct Conformational States of Amyloid-Beta Fibrils in Alzheimer's Disease Using Novel Luminescent Probes*. ACS Chem. Biol., 2007. **2**(8): p. 553-560.

65. Berg, J.M., J.L. Tymoczko, and L. Stryer, *Biochemistry*. 5th ed. 2002: W H Freeman.

Chapter 4

Phase Networks of Cross-β Peptide Assemblies

W. Seth Childers†, Neil R. Anthony‡, Anil K. Mehta†, Keith M. Berland‡*, and David G. Lynn†*

†Center for Fundamental and Applied Molecular Evolution, NSF/NASA Center for Chemical Evolution, Departments of Chemistry and Biology, and ‡Department of Physics, Emory University, Atlanta, GA

This chapter was published in:

W. Seth Childers, Neil R. Anthony, Anil K. Mehta, Keith M. Berland, David G. Lynn, Phase Networks of Cross-β Peptide Assemblies.

 28(15): p. 6386-6395.

4.1 Abstract

Recent evidence suggests that simple peptides can access diverse amphiphilic phases and that these structures underlie the robust and widely distributed assemblies implicated in nearly 40 protein mis-folding diseases. Here we exploit a minimal nucleating core of the Aβ peptide of Alzheimer's disease to map its morphologically accessible phases that include stable intermolecular molten particles, fibers, twisted and helical ribbons, and nanotubes. Analyses with both fluorescence lifetime imaging microscopy (FLIM) and transmission electron microscopy provide evidence for liquid-liquid phase separations, similar to the co-existing dilute and dense protein-rich liquid phases so critical for the liquid-solid transition in protein crystallization. We show that the observed particles are critical for transitions to the more ordered cross-β peptide phases – that are prevalent in all amyloid assemblies – and identify specific conditions that arrest assembly at the phase boundaries. We have identified a size dependence of the particles in order to transition to the para-crystalline phase and a width of the cross-β assemblies that defines the transition between twisted fibers and helically coiled ribbons. These experimental results reveal an interconnected network of increasing molecularly ordered cross-β transitions, greatly extending the initial computational models for cross-β assemblies.

Keywords:

amyloid, molten particles, molecular self-assembly, phase networks, Aβ(16-22) peptide, nanostructures, aggregation, oligomers, circular-dichroism, helical ribbons, nanotubes, morphological plasticity, and Alzheimer's disease

4.2 Introduction

Amphiphilic molecules can display complex phase behaviors when dispersed as aqueous liquids above a critical micelle concentration (CMC). These assemblies appear as beautifully ordered structures that grow into ellipsoids, cylinders, bilayer colloids and various cubic phases [1]. Amphiphile structure, concentration, temperature, media dielectric, pH and environmental sheer forces all impact their accessible phase transitions and morphology. A remarkably functional example is found in the lipid bilayers of biological membranes which can access diverse crystalline microphases critical for processes that range from cell signaling and transport to cell division and adhesion [2, 3].

Simple polypeptides can also self-assemble into related ordered phases [4-6], and in this case the morphological diversity of the cross-β assemblies appears to be etiologically relevant to several protein mis-folding diseases [7-11]. As a result, significant effort has focused on the initial events directing simple peptide fragments to assemble into such ordered phases [8, 12-14]. While the structural diversity of the assemblies remains under intense investigation [15-25], the nucleating core of the Aβ peptide of Alzheimer's disease, Aβ(16-22) / Ac-KLVFFAE-NH_2, has served as the principle model for many of these studies [15, 17-19, 22, 25-78]. Several computational approaches [28, 30, 32, 34, 35, 37-39, 43, 44, 47, 55, 61, 72], have all built on initially identified low-energy folded monomer conformations with exposed hydrophobic surfaces to probe the early assembly nucleation events. Monte Carlo analyses with 20 and 30 Aβ(16-22) peptides [15, 46] suggest intermolecular hydrophobic collapse to disordered fluid aggregates, predisposing the peptides for inter-chain hydrogen bonding and transitions to ordered

crystalline phases. Coarse-grained models [16, 54, 79-82] with up to 200 peptides [16] also indicate systems which initially collapse into disordered dynamic particles.

Increasingly, the developments in imaging methods are making it possible to validate these computational models experimentally. Using the Aβ(16-22) peptide, we have transcribed the emerging structural insights into an initial morphological network map of peptide assembly. Previously using fluorescence recovery after photobleaching (FRAP), we observed that Aβ(16-22) peptides form micron-sized particles composed of highly concentrated peptides in a liquid-like state that exchange quickly with dilute peptide monomers in solution [19]. At room temperature these fluid intermolecular molten particles are metastable, and transition into crystalline nanotubes [19] through a "sea-urchin-like" assembly characteristic of protein crystal growth processes [83]. Here we present experimental results that provide evidence for the assembly of dynamic yet structurally diverse particles with distinct crystalline cross-β phases. From these particles emerge a network of crystalline phases, arranged in a hierarchical tree defined by their increasing structural order, with specific context-dependent controls for many of the phase transitions. This emerging understanding of the rich phase behavior of peptide assemblies not only extends the computational predictions of this model peptide, but also provides insight into protein folding/misfolding pathways and reveals new design strategies essential for mesoscale peptide materials construction.

4.3 Results and Discussion

4.3.1 Accessible Cross-β Phases.

To explore the cross-β phases [84-87] accessible to the Aβ(16-22) peptide, we scored the impact that both temperature and solvent had on morphology with transmission electron microscopy (TEM). Aqueous mixtures with the H-bond accepting acetonitrile and H-bond accepting/donating methanol gave the widest range of homogeneous assemblies. At temperatures between 4° and 30°C in acidic 40% aqueous acetonitrile, Aβ(16-22) peptides assemble into homogeneous diameter nanotubes [29, 52, 77]. A diagnostic feature of the hollow nanotube is the distinct white edge lines that result from exclusion of uranyl acetate from the ordered tube walls and accumulation of uranyl acetate both inside and outside the hollow cavity (Figure 4–1a). This signature of peptide nanotubes has now been repeatedly confirmed with small angle X-ray and neutron scattering, atomic force and electron microscopy, cryo-etch SEM, and electron diffraction analyses [29, 64]. At elevated assembly conditions, between 30°C and 40°C, spherical particles dominate the TEM grids (Figure 4–1b), and are the only species observed at 37°C. The presence of particles on the EM grids was concentration dependent, and identical negatively-stained morphologies were observed with phosphotungestic acid, Nano-W and Nano-Van (data not shown). Two particle populations exist, with diameters of 88 ± 65 and 197 ± 63 nm (n=267) (Figure 4–1c), which are approximately 10× smaller than the intermediate molten particle assemblies characterized previously at room temperature (1-6 μm) [19]. Unlike the room temperature assemblies, the 37°C particles do not transition into fiber or nanotube phases. Above about 40°C, no assembled structures were identified by TEM.

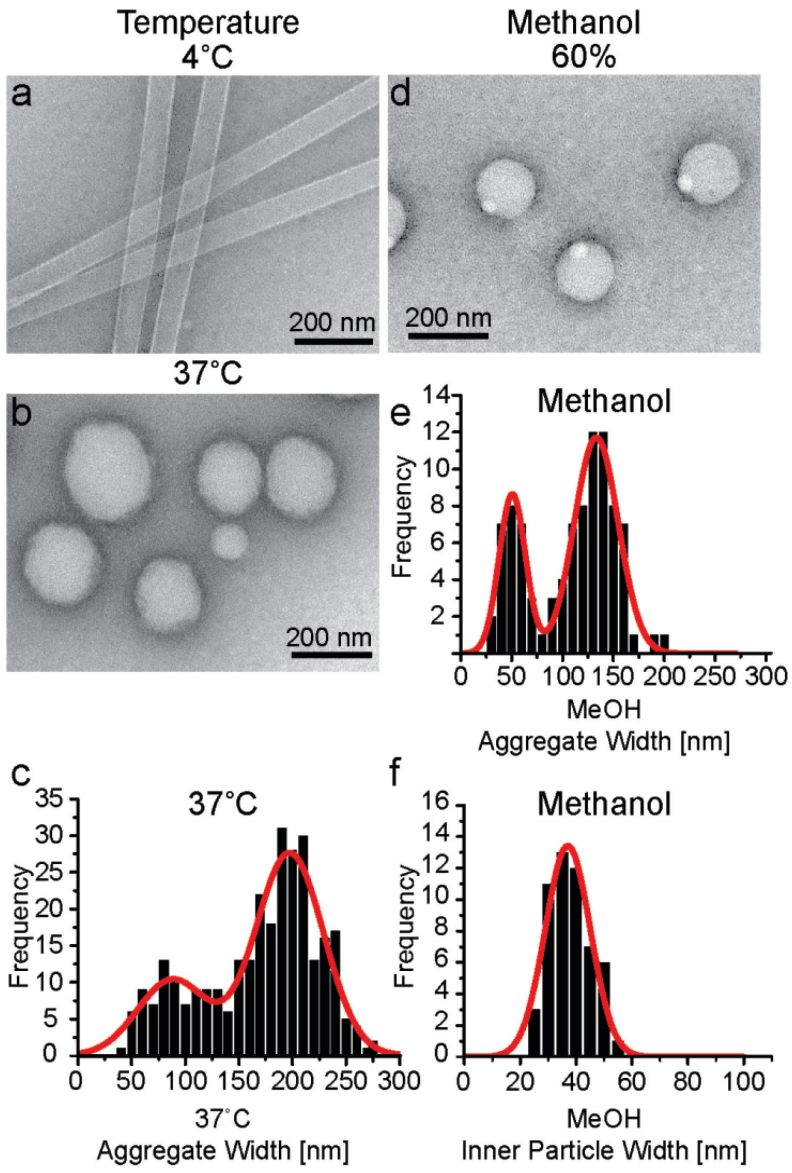

Figure 4–1 – TEM image analyses. Aβ(16-22) (1.3 mM) was allowed to assemble in the presence of 0.1% trifluoroacetic acid (TFA) at (a) 4°C and (b) 37°C in 40% acetonitrile and (d) at 4˚C in 60% methanol. Size distribution of the Aβ(16-22) particle assemblies (c) at 37°C in 40% acetonitrile, (e) at 4°C in 60% methanol, and (f) the internal spot within the spherical assembly formed in 60% methanol as shown in panel (d).

The transition temperature variance for these phases can be as high as ±10°C as the phase boundary is expected to depend strongly on differences in environmental conditions including peptide purity, salts, pH [52], and solvent [17, 25, 41, 68, 76, 88]. While systematic variation of acetonitrile percentages from 40-80% showed little impact on Aβ(16-22) nanotube assembly at room temperature, small heterogeneous populations of spherical structures co-existed with the nanotubes in 80% acetonitrile. In contrast, aggregation in H2O occurs very fast and the resulting assemblies transition rapidly into more heterogeneous mixtures of tubes and sheets. Methanol is a stronger H-bond acceptor/donor than acetonitrile, but the two have similar dielectric constants [89]. Previous investigations have demonstrated that the self-assembled morphology of various peptide assemblies can be modulated by the methanol/water ratio [17, 68] and this effect has been assigned to the competition in H-bonding between water and methanol [17]. Indeed, in the presence of either 20% or 40% methanol, the Aβ(16-22) peptides assemble into homogeneous nanotubes, but above 40% and up to 60% methanol, the spherical particles dominated the assembly and in 60% methanol only spherical particles were detected (Figure 4–1d). Quantitative measurements of the diameters again found two particle populations, 51 ± 25 nm and 133 ± 43 nm (n=91, Figure 4–1e), which are somewhat smaller than those formed in aqueous acetonitrile. Most strikingly however, all the larger particles contained a single spot, giving them an eyeball-like appearance (Figure 4–1d), with a diameter of 25 to 55 nm (n=51, Figure 4–1f). The reduced ability of this spot to accumulate stain gave it the appearance of the more ordered walls of the nanotubes (Figure 4–1a), suggesting that the spot contained greater crystalline order than the aggregate.

4.3.2Evaluating Internal Structure of the Particles.

Each of the mature 4°C, 28°C, and 37°C assemblies give significant circular dichroism (CD) spectra with ellipticity minima at 215 nm (Figure 4–2a), a signature diagnostic of β-strands. The intensity at 215 nm in the CD spectra for the 37°C and 28°C assemblies are only 20% and 33% of the 4°C nanotubes, respectively. These differences could reflect either varying degrees of assembly or different assembled structures, and indeed when the CD thermal melting profiles were fit to the sigmoidal form of the Boltzmann equation (Eq. (4.1)), a melting temperature, Tm, and a measure of melting cooperativity reflected in the slope k, helped resolve this difference (Figure 4–2b). The normalized CD melting curves for the nanotubes formed at 4°C and 28°C were identical, consistent with the lower intensity at 28°C being a similar structure with a reduced degree of assembly.

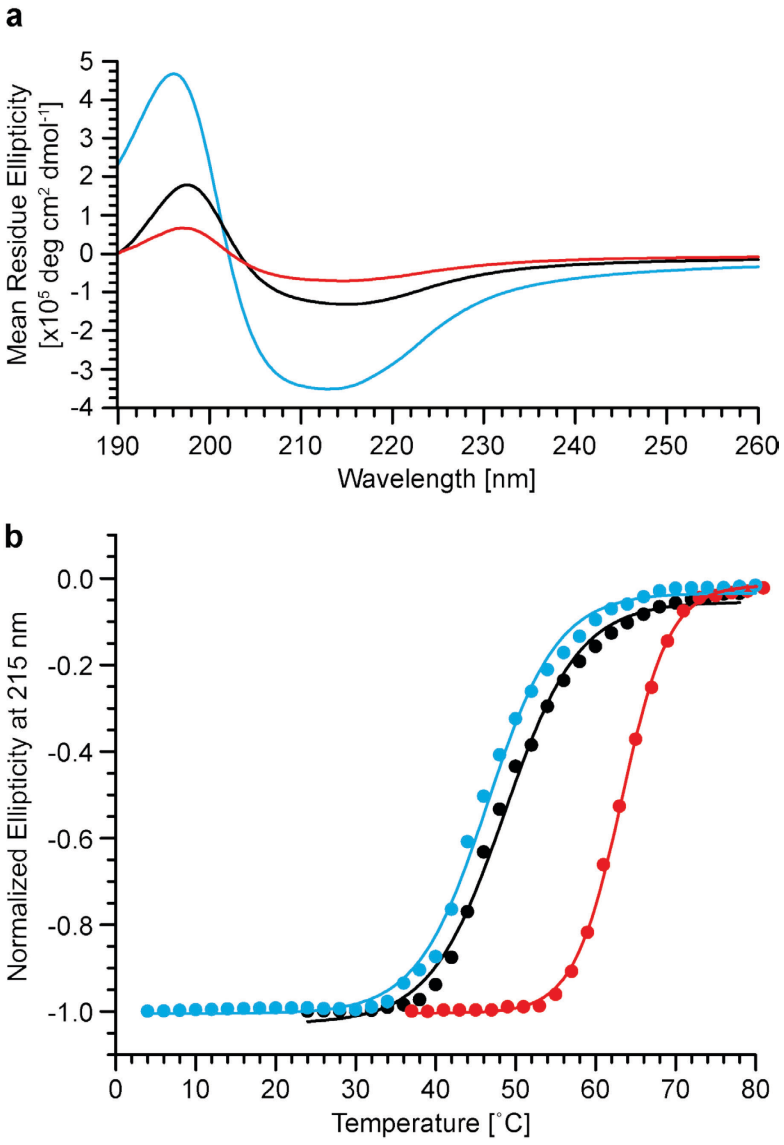

Figure 4–2 – Circular Dichroism (CD) of (a) Aβ(16-22) nanotubes assembled at 4°C (blue line), nanotubes assembles at 28°C (black line), and spherical particles assembled 37°C (red line), and (b) melting profiles normalized and fit to the sigmoidal form of the Boltzmann equation (Eq. (4.1)). The melting temperature Tm and the cooperativity value k are calculated for the 4°C nanotubes (T_m = 46.1°C; k = 4.9), the 28°C nanotubes (T_m = 48.6°C; k = 4.6), and for the 37°C spherical particles (T_m = 63.2°C; k = 2.9).

$$\theta \propto \left(1+\exp\left\{\frac{T_m - T}{k}\right\}\right)^{-1} \tag{4.1}$$

However, the particles displayed both a significantly higher Tm of 63.2 ± 2.9°C and greater cooperativity (Figure 4–2b). These observations motivated our efforts to enhance the contrast within the particles to distinguish between solid spheres, hollow vesicles or other possible structures forming within the particle that could exclude TEM stain. When Aβ(16-22) peptides were allowed assemble at 37°C in the presence of 1 wt% uranyl acetate, conditions which did not significantly alter assembly kinetics or morphology (Figure 4–3a), the stain was distributed within the particles and short rod-like architectures were readily resolved (Figure 4–3b). Similarly, warming the mature 4°C Aβ(16-22) nanotubes to 37°C in the presence of 2-wt% uranyl acetate (Figure 4–3c) gave an even more complex arrangement of assembled structures within the particles (Figure 4–3d). Qualitative assessment of these microphases suggested that as little as 20% to as much as 75% of the particle could be made up of these stain-excluding regions.

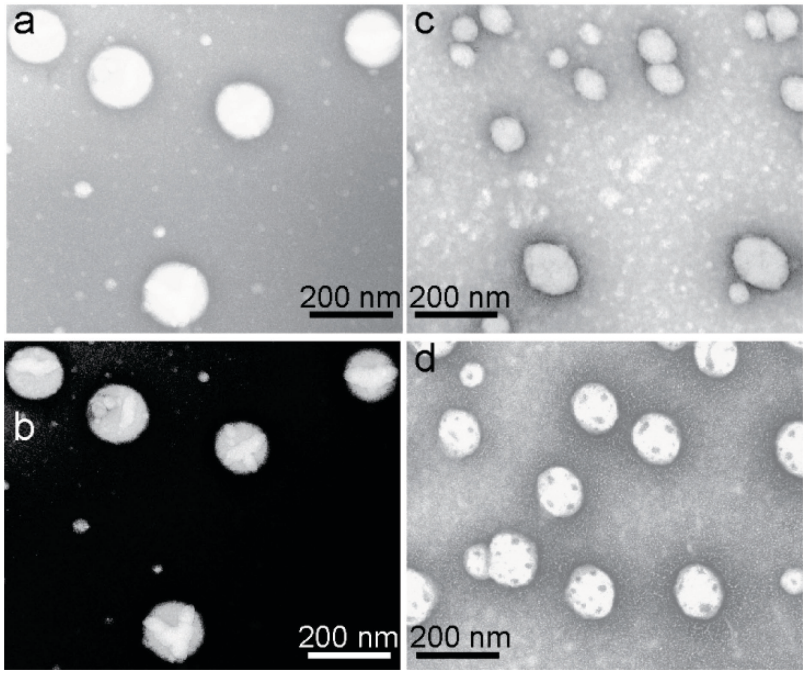

Figure 4–3 – Uranyl acetate contrast enhanced TEMs of particles. Aβ(16-22) solutions were adjusted to 1.3 mM in 40% acetonitrile and incubated at 37°C for 2 weeks with 1 wt% uranyl acetate. The TEM micrographs were processed to enhance contrast (a) between the spherical assemblies and the carbon film and (b) structures within individual particle assemblies. Mature nanotubes prepared with 1.3 mM Aβ(16-22) peptide incubated at 4°C were melted at 37°C for 2 weeks without (c) and with (d) 2 wt% uranyl acetate.

Analysis of the assemblies in solution has been developed with replacement of the N-terminal lysine residue of Aβ(16-22) with rhodamine 110 (R110) to give the fluorescent probe R110-LVFFAE-NH_2 (Rh17-22) [19]. The sub-diffraction limit particle assemblies described above (Figure 4–1b, d) could not be resolved, but at room temperature and at a Rh17-22:Aβ(16-22) ratio of 1:150 with 0.3 mM total peptide, micron-size fluorescent particles formed when suspended in 40% acetonitrile containing 0.1% TFA [19]. Figure 4–4 shows the data from Fluorescence Lifetime Imaging Microscopy (FLIM) [90] analysis of the assemblies adhered to the glass slide with growth extending in all directions below the slide surface (into the page). The majority of these growing assemblies exhibit a fluorescence lifetime of 3.2 ± 0.1 ns (yellow), relative to Rh17-22 in solution at 3.4 ± 0.1 ns. The significantly shorter lifetimes, as low as 2.5 ± 0.1 ns (blue), provide strong evidence for a different phase within the particles as a possible nucleation sites for the nanotube growth. These low lifetime regions within the more concentrated liquid particles are perhaps related to phases proposed for protein folding in which dehydration promotes crystallization [91] and the shorter lifetimes may well arise from fluorophore quenching within these molten particles.

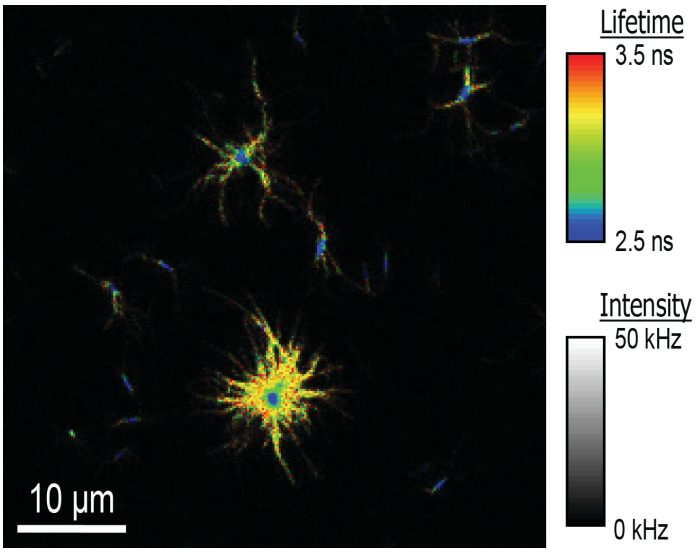

Figure 4–4 – Fluorescence lifetime image of micron sized particles. Rh17-22:Aβ(16-22) ratio of 1:150 was dissolved in an aqueous solution containing 40% acetonitrile and 0.1% TFA to a minimal assembly concentration of 0.3 mM. The colour scale represents the fluorescence lifetime at a given pixel and the brightness reflects the count rate. Different phases, including assembled nanotubes (3.2 ± 0.1 ns), particles, and particle center (2.5 ± 0.1 ns) of the Aβ(16-22):Rh17-22 co-assembly are resolved by their distinct lifetimes.

4.3.3The Paracrystalline Phases.

The cross-β nanotubes and fibers that emerge from the molten particles are paracrystalline. This phase exhibits a high-degree of order with stacked H-bonded β-sheets [12], but do not form the 3D long-range order of crystals. The formation of paracrystalline phases of the Aβ(16-22) peptide can be context-dependent, certainly as reflected in the pH-dependent β-sheet registry organization within fiber and nanotube morphologies [26, 51, 52]. Figure 4–5 contains images of the temperature and pH-driven transition into distinct phases from the molten particles formed at 37°C and low

pH (Figure 4–5a). When the incubation temperature was reduced to 4°C, the CD ellipticity at 215 nm slowly decreased from -64 to -271, consistent with more of the peptides adopting a β-sheet conformation and early sampling by TEM revealed thin assemblies emerging from and connecting to the particles (Figure 4–5b). Unlike the large assemblies that occur at room temperature with many structures emerging simultaneously [19], the particle size formed at elevated temperatures remains small (Figure 4–1c), and upon changing assembly temperature or pH, both nucleating and non-nucleating particles are observed. The nucleating particles can appear as monopolar or bipolar, with the structures emerging at opposite poles of the particle (Figure 4–5b, e). TEM analyses does make it difficult to differentiate the assemblies emerging from those particles and assemblies that are merely co-deposited on the EM grids, but we have been able to find no definitive evidence for assemblies forming independent of the particles.

The initial 37°C particle distribution (Fig 5a, 6a) has the size distribution previously shown in Figure 4–1c and that distribution is reproduced with the dashed-red lines in Fig 6c & e. During incubation at 4°C, the non-nucleating particle size distribution decreases dramatically (solid-red line Fig 6c) to an average width of 53±3 nm, such that after 1 week 23% of the particle population contains filaments (Figure 4–6a, b). This growth pattern suggests that not only do the filamentous assemblies originate within the spherical particle [19], but also that the emergence may be a function of particle size. Indeed, analysis of fluorescence images in Figure 4–4 indicate that some of the room temperature particles with widths greater than 1000 ± 500 nm nucleated more than 30 filaments, while particles less than 1000 ± 500 nm typically nucleated only 2 filaments and those below 100 nm were non-nucleating (Figure 4–6c, e). The significance of these

size limits are not yet clear, however the size of the particle clearly appears to influence filament nucleation frequency.

Likewise when the media pH is increased [26, 52], fibers emerge with growth occurring at opposite poles of the particle (Figure 4–5e). Some ribbons also appear with widths >100 nm (Figure 4–5f), but these do not persist. The non-nucleating particle diameter decreased dramatically to 51±3 nm (Figure 4–6e) and 28% of the particles nucleated filaments with widths that fit into two apparent populations: 27 ± 21 nm and 93 ± 117 nm (Figure 4–6d). This distribution between thin and thick filament assemblies emerging from the particles could represent distinct cross-β structures and imply that the free energy differences for nucleation of different polymorphic cross-β phases are significantly lower within the particle environment than in solution. Indeed, isotope-edited IR analyses suggest that early stages of Aβ(16-22) assembly sample a greater diversity of β-strand arrangements relative to the equilibrium fibril structures [36]. As the assemblies mature, fibers with homogenous widths of 10-30 nm (Figure 4–5g) dominate the images. These larger assemblies show characteristic striations along their surfaces, most consistent with fiber bundles, whereas fibers formed at lower temperatures appear as 5 nm filaments twisted together as dimers [52]. This difference in fiber bundling may be the result of the molten particles creating an environment where the fibers can grow side-by-side, increasing the probability of forming bundled fibers, or may simply imply that fibril bundling is temperature dependent.

Further, the reduced particle dimensions observed upon changing both pH and temperature is consistent with the larger particles having a higher propensity to nucleate and disappear, resulting in the observed relative increase in the number of smaller particles. These small particles could be off-pathway structures and/or once a nucleation

event occurs the particles could fuse to create the sizes necessary for propagation. Thus far, such fusion events have not been observed. Alternatively, the junction between small particles and filaments could be too weak to hold up to the dehydration events that occur during TEM sample preparation, also preventing them from being observed. And at even higher orders of assembly, the filaments that emerge and remain connected to the molten particles have average widths of 64 ± 24 nm and range from 10 to 100 nm (Figure 4–6b). Some intermediate assemblies display this "beads on a string" morphology that further transform into ribbons (Figure 4–5c) and nanotubes (Figure 4–5d), following the smooth progression of the change in molar elipticity [92].

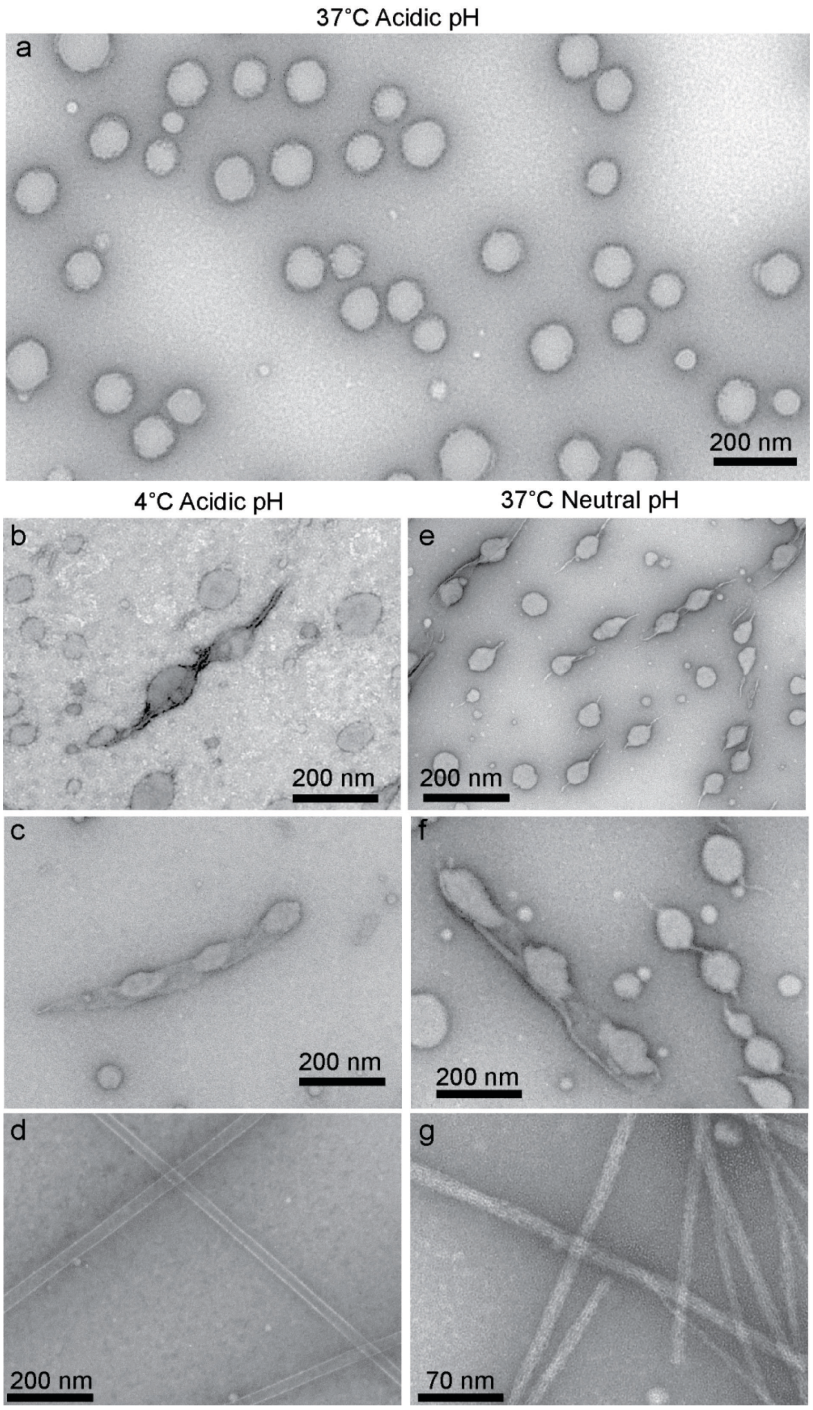

Figure 4–5 – TEM images of (a) mature Aβ(16-22) assemblies formed at 37°C in acidic media and adjusted either (b, c) to 4°C for 2 weeks, or (e, f) to neutral pH and analyzed after 1 week or (d, g) after 2 weeks where the major component are tubes or bundled filaments respectively.

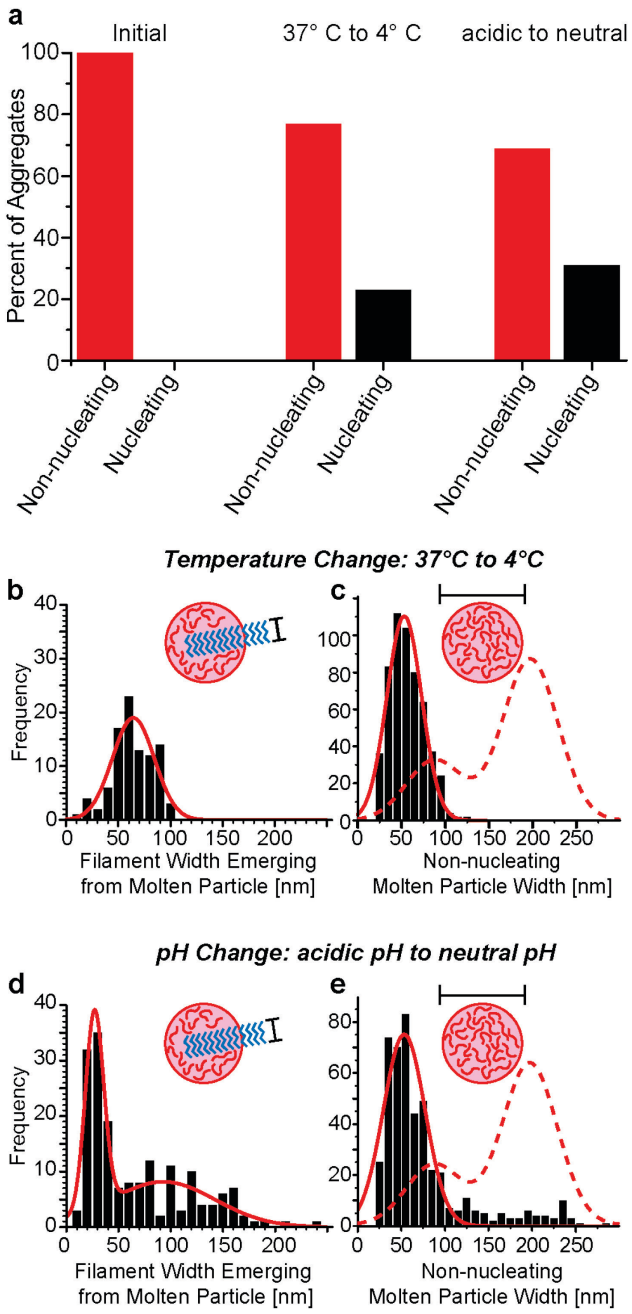

Figure 4–6 – Quantitative assessment of temperature- and pH-induced changes in particle populations. Panel a shows the percentage of the initial populations, as in Figure 1b, c. After 1 week under the indicated altered conditions, the particles have either exposed (nucleating) or non-exposed (non-nucleating) paracrystalline filaments. The filament widths emerging from the 37°C to 4°C temperature change (b) were fit to a

single population with a center of 64 ± 2nm and full-width half-max (FWHM) of 47 ± 4 nm. In contrast, the acidic to neutral pH change filaments (d) fit to two Gaussians with centres at 27 ± 1 nm (FWHM = 21 ± 3 nm) and 93 ± 13 nm (FWHM = 117 ± 30 nm). Analysis of non-nucleating molten particle fit a single population, temperature (c) of 53 ± 1nm (FWHM of 47 ± 3 nm) and pH (e) to 51 ± 2 nm (FWHM = 54 ± 5 nm). For comparison, the initial particle distribution at 37°C and acidic pH, from Figure 1e, are shown as dashed red lines.

We were concerned about the impact that drying the samples for TEM could have on ribbon morphology, and it appears to predominately impact the ribbon pitch length, as lengths were highly variable for thin ribbons and most ribbons had a pitch length more than 2× the pitch observed in mature nanotubes. In contrast, the material properties that govern tilt angle appeared to be less impacted by drying (Figure 4–7). As the filaments grow and become independent of the particles, the thinner filaments display a twisted architecture (Figure 4–7a) while the wider ribbons access a helical topology with a constant tilt angle of 25 ± 5° (Figure 4–7b), the same tilt angle as the mature nanotubes [52, 57]. As is shown in Figure 4–7c, there is a clear width-dependent transition from twisted to helical ribbons at a width of 35-45 nm (or 35-45 laminates, Figure 4–7d). This sharp width-dependent transition of ribbons with twisted curvature to helical cylindrical curvature has been proposed [93-96] and experimentally observed in amphiphile assemblies [23, 97-99], twist-nematic-elastomer films [96] and seed pod tissue [95]. In this case, the phase transition [96] between twisted and helically coiled ribbons may be due to energetic differences of twisting a ribbon at the center versus the edges of the Gaussian curved ribbon, and when ribbons reach the width threshold of 40 laminates, they transition to helical architecture with a defined tilt angle [98]. The molecular level

structural changes that drive this topological transition may well reflect the tension created by the hydrogen-bonding between β-strands that promotes the inherent twisting of β-sheets [100] (<40 laminates), and the complementary packing of the side chains in the laminate [12, 24, 52] that define the ribbon helical pitch (>40 laminates).

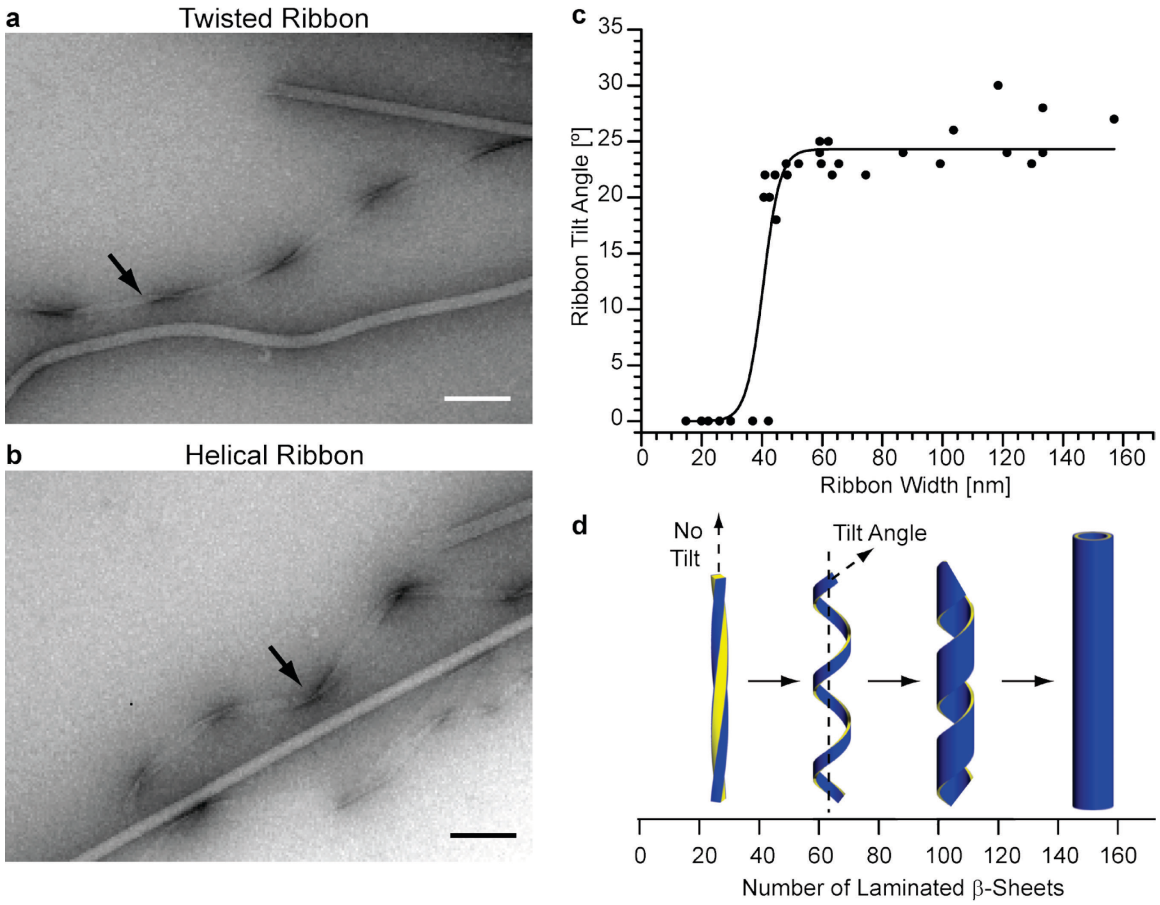

Figure 4–7 – Analysis of Aβ(16-22) ribbon tilt and ribbon width. Electron micrographs of (a) twisted ribbons and (b) helical ribbons. (c) Plot of measured tilt angle vs. ribbon width. (d) Diagram displaying a progression from twisted fibers to helical ribbons to hollow nanotubes.

4.4 Conclusion

Almost 100 years ago, James William McBain postulated the existence of "colloidal ion" assemblies that are now known as the dynamic and entropically ordered micelle [101]. Our growing understanding of the cross-β fold suggests that the more functionalized polyamide backbone and sidechain distributions of the natural polypeptides can sample both the vast conformational richness of folded proteins [29, 52] as well as the mesoscale paracrystalline order of surfactant assemblies [57]. Recent computation [16, 46, 54, 81, 82] investigations have argued for the existence of context-dependent microphases, and certainly the fluid intermolecular molten particles [19] observed with the simple heptapeptide Ac-KLVFFAE-NH_2 provides experimental support for these proposals. However, our results reveal a far richer array of structures, where much as in protein folding, environment dramatically impacts transitions to the different crystalline phases (Figure 4–8). The FLIM analyses further support the previously observed liquid-like initial phases [19], similar to the co-existing dilute and dense protein-rich liquid phases that appear to be so critical for the crystallization of many proteins [91]. The uranyl actetate negative stain of the thermally arrested particles (Fig 3b) confirms the presence of filament-like structures forming in these particles, further supporting the existence of metastable liquid-liquid phase separation (LLPS) characteristics proposed for the dense protein-rich liquid phases necessary in protein crystallization [83, 91, 102, 103]. The apparently desolvated phases, possibly analogous to the molten globules of protein folding, could well set the stage for secondary structure formation and ordered assembly. Indeed, the more thermostable molten particle β-sheet secondary structure (Figure 4–2) suggests the surface free energy at the interface between small cross-β crystallites and the dense peptide-rich liquid clusters within the molten particles may be significantly less than between crystallites in solution [102, 103].

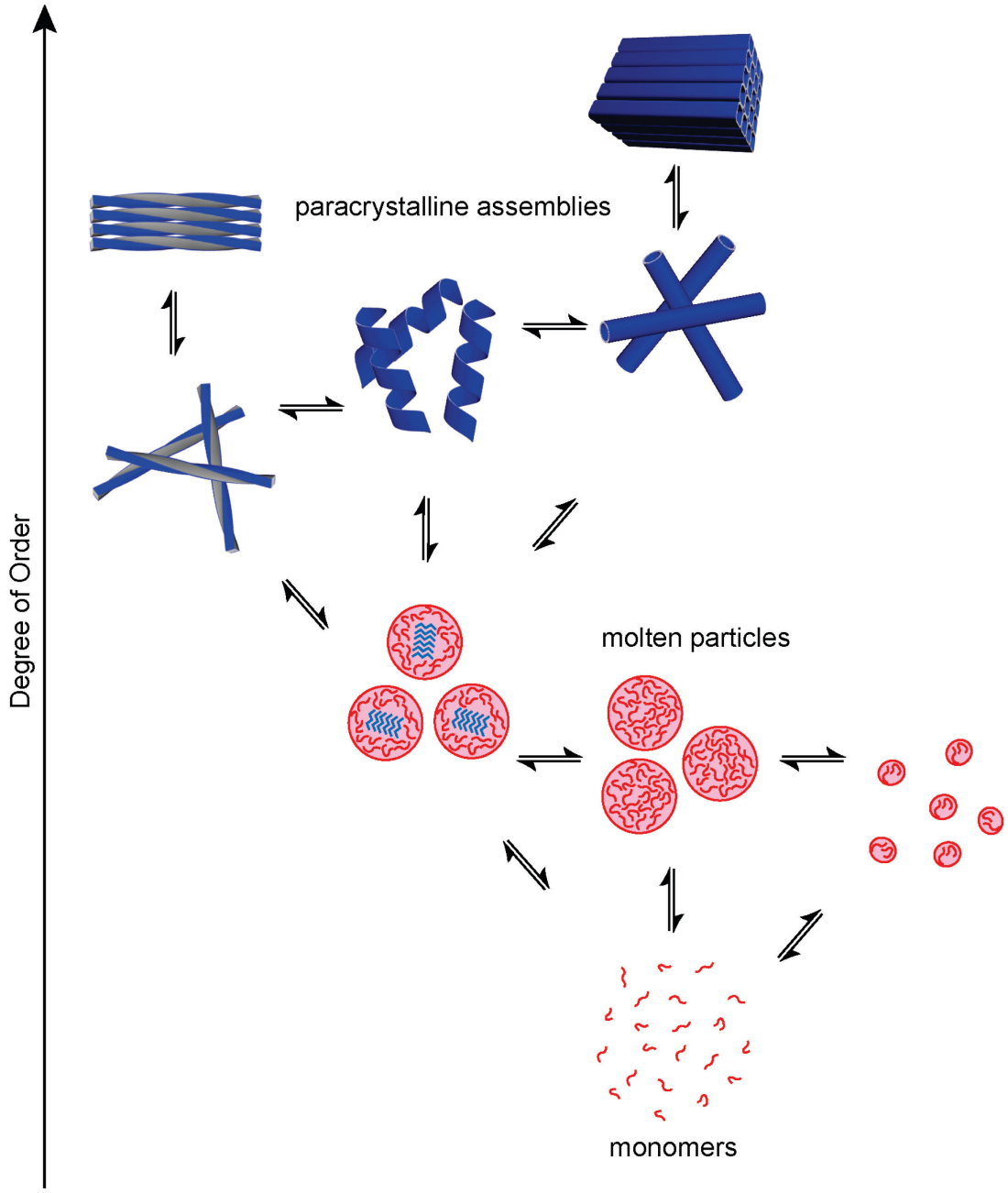

Figure 4–8 – Network diagram indicating observed phase transitions. Each phase exhibits thermodynamic barriers that can be ordered as a network.

The experimental results also suggest that the particles can have diameters of 10-6000 nm, and there is a particle size-dependence to seeding the transition to crystalline phases. The emerging structures compete for monomers both within the particle and

after they emerge in solution, and it is the conditional differentiation of these different propagation events that allows the growth of the ordered phases to be arrested at the particle surface by elevated temperature or organic solvents. Further, once the ribbon/fiber phases emerge from the particle and begin growing in the aqueous environment, they display a distinct and dynamic width-dependent transition from thin twisted fibers to wide helical ribbons, ones that can ultimately fuse to form hollow monodisperse diameter nanotubes [29]. This ribbon plasticity, in contrast to the more rigid lanreotide nanotubes that fix their helical pitch at very early stages of assembly through a hairpin like β-sheet held together by cysteine disulfides [104], adds an important design criteria for materials engineering.

Paracrystalline filaments with widths from 5 nm to 250 nm can emerge from the molten particles and a width dependent morphology is observed with filaments < 40 nm forming twisted fibers and > 40 nm forming helical ribbons. These molten particles therefore appear at a branch points (Fig 8) that can lead directly to twisted fibers, helical ribbons, and hollow nanotubes [19]. Branch points identify the self-assembly pathway as a phase network (Figure 4–8) rather than the simpler linear self-assembly pathway. This approach has allowed us to map the phase networks for this cross-β assembly (Figure 4–8). The ability to dissect the relationship between peptide conformation, aggregation configuration, and morphological flexibility opens the possibility of controlling the phase boundary transitions in the misfolding in amyloid diseases and to better understand their use in the design of peptide materials.

Taken together, the ability of these simple oligopeptide assemblies to hybridize the physical elements of surfactant phase behavior with the conformational richness of folded proteins suggests that we may have only scratched the morphological surface of

the accessible phase space [12]. Indeed, the tubes and fibers themselves can serve as building blocks for even higher order mesoscopic materials [42] (Figure 4–8), as addition of divalent ions allow tubes and fibers to bundle. As the polypeptides themselves get longer, the array of structural forms should expand in complexity and functional diversity much as already seen in the proteins associated with amyloid disease states [105]. This mapping of the rich context-dependent phase behavior of simple peptides should establish constraints for more extensive computational modeling and set the stage for creating atomic scale models and engineering new functional materials [106, 107, 108].

4.5 Methods

4.5.1 Peptide Synthesis, Purification and Assembly

Peptides were synthesized using a Liberty CEM Microwave Automated Peptide Synthesizer (NC, USA) and a FMOC-Rink Amide MBHA Resin (AnaSpec, CA, USA). FMOC-Rink Amide MBHA Resin was swollen using dimethylformamide for 15 minutes. Microwave assisted FMOC deprotection was completed using 20% piperdine and 0.1M N-Hydroxybenzotriazole (HOBt) in dimethylformamide at 45-55°C for 180 sec, followed by 3X dimethylformamide flushes. Each FMOC-amino acid coupling step was performed using 0.1M FMOC protected amino acid, and activated with 0.1 M 2-(1H-Benzotriazole-1-yl)-1,1,3,3-tetramethyluronium hexafluorophosphate (HBTU), and 0.2M N,N–Diisopropylethylamine (DIEA) in DMF. Coupling temperatures using microwave activation were maintained between 75 and 82°C for 300 sec. Each coupling step was rinsed with three aliquots of dimethylformamide. Final acetylation of the N-terminus was achieved by addition 20% acetic anhydride in dimethylformamide.

Resin was filtered and washed with dichloromethane and allowed to air dry. Peptides were cleaved from the resin using trifluoroacetic acid/thioanisole/1,2-ethanedithiol/anisole (90:5:3 2, v/v/v/v) at room temperature for 3 hrs. The cleaved peptide-TFA solution was filtered, and precipitated by drop-wise addition to cold (-20°C) diethyl ether. Precipitated product was centrifuged at 3000 rpm for 3 min, and the pellet was further washed 3 times with cold diethyl ether. Dried peptides were dissolved in minimal volume of 40% acetonitrile + 0.1% trifluoroacetic acid and purified by RP-HPLC using a C18-reverse phase column with an acetonitrile-water gradient. In each

case, the peptide purity was evaluated by HPLC. Molecular weight was confirmed by MALDI-TOF using a 2,5-dihydroxybenzoic acid matrix.

Aβ(16-22), Ac-KLVFFAE-NH2, (1.3 mM) was dissolved in 40% CH3CN/H2O with 0.1% TFA using vortexing and sonication at room temperature. Solutions were then split and stored under quiescent conditions and temperature was controlled at 4°C, 28°C, and 37°C for 1 month. Concentrated Aβ(16-22) assemblies in methanol/water mixtures were initially dissolved in 20% methanol with 0.1% TFA using vortexing and sonication. Once dissolved, methanol or water was added to the peptide solutions to adjust the aliquot methanol concentration from 20-70% methanol. Each aliquot was then stored at 4°C for 1-month incubation period. To study the internal structure of the observed assemblies, 1.3 mM Ac-KLVFFAE-NH2 peptides were assembled by adding 1 to 2 wt% uranyl acetate as a contrast agent.

4.5.2Transmission Electron Microscopy Imaging

After addition to TEM grids, the amyloid peptide assemblies were allowed to adsorb for 1 min before excess peptide solution was wicked away with filter paper. Freshly prepared 2-wt % uranyl acetate solutions (pre incubated at 4°C, 28°C, and 37°C) were added to TEM grids and incubated for 3-5 minutes before wicking and then placed in a vacuum dessicator overnight. TEM micrographs were recorded with a Philips 410 TEM at magnifications ranging from 7100x to 69 000x with a Tungsten filament at an accelerating voltage of 80 kV. Negatives were scanned at 2000 dpi resolution on an Agfa DuoScan flatbed scanner (Agfa Corp., Ridgefield Park, NJ). All staining solutions were prepared fresh and filtered prior to staining to minimize distinguishable artifacts.

Our standard TEM protocols control for three main issues: (a) buffer-induced artifacts, (b) inherent sample reproducibility, and (c) statistical averaging of the assemblies. These criteria have provided high confidence in the assignment of protein assemblies, specifically the molten particles. Although phosphotungestic acid, Nano-W (nanoprobes), and Nano-Van (nanoprobes) all revealed particles, these negative stains were limited to neutral conditions. In contrast, uranyl acetate stain could also be used under acidic conditions and provided the cleanest background. Altered staining temperature (4°C, 37°C) did not create staining artifacts in the solvent controls. Diluting the peptide solution prior to addition to EM grid was important in optimizing the imaging. Sparse cubic dark crystals artifacts from uranyl acetate stain was observed in peptide-free solutions of buffer and aqueous acetonitrile/methanol control, which were easily distinguishable from the particles. Up to four independently synthesized peptide batches were prepared, while some batch-to-batch variability in the phase temperatures was noted, only reproducible assemblies were used for TEM comparisons. Sample size distribution and counts are reported for all samples and any structures that could not be counted across multiple grids were not included in these analyzes.

4.5.3Circular Dichroism and Melting Temperatures

An aliquot (15-70 μL) of amyloid nanotube and spherical particles were placed in 0.1 mm path length demountable window cell with Teflon tape wrapped around the window edges to minimize evaporation. Initially, CD at 215 nm was recorded over a 15 minute period at controlled temperature (4°C, 28°C, or 37°C) until CD of solution stabilized. After temperature incubation, wavelength scans over 185-300 nm were recorded at a scanning rate of 100 nm/min with a resolution of 0.2 nm and bandwidth of 4nm using a Jasco J-810 spectropolarimeter. Three successive wavelength scans were averaged for

each sample. Buffer control spectra were averaged and subtracted from the sample spectra. The ellipticity ($[\theta]_{obs}$, mdeg) was converted to mean residue ellipticity ($[\theta]$, $deg \cdot cm^2 \cdot dmol^{-1}$) with the equation $[\theta]=[\theta]_{obs}/(10 \times n \times C \times l)$, in which, n is the number of peptide bonds, C is the concentration (mol/L) and l is the path length of the cell (cm). For melting temperature profiles, the ellipticity at 215 nm was recorded as a function of temperature in increments of 2°C and fit to the sigmoidal form of the Boltzmann equation.

4.5.4Fluorescence Lifetime Sample Preparation

Small amounts of dry peptide (1-2 mg), weighed in the microfuge tube to an accuracy of ~50 μg, were disaggregated in hexafluoroisopropanol (HFIP). This solution was aliquoted into ~10 new microfuge tubes, and allowed to evaporate in a fume hood before re-entering storage at 4°C. On use, each aliquot was dissolved in 2 μM Rh17-22 in 40% acetonitrile (AcCN) 0.1% TFA solution to give a total peptide concentration of 0.3 mM, at the critical concentration for assembly, followed by alternating sonication and vortexing to ensure complete dissolution. A small amount of the resulting solution, ~15 μL, was loaded onto a microscope slide, and enclosed with a coverslip sealed around the edges with nail polish.

4.5.5Fluorescence Lifetime Imaging Microscopy

Two-photon excitation was provided by an ultrafast (~100 fs pulses at 80 MHz) Ti:Sa laser (Spectra Physics, Santa Clara, CA) tuned to 780 nm, from which the intensity was attenuated using a λ/2 plate and polarizing cube. The laser beam was scanned using an x-y pair of galvanometer mirrors (6215H, Cambridge Technology, Lexington, MA) before

entering a 5× beam expanding telescopic optical setup that terminates on the rear aperture of an Olympus 60× water immersion objective lens (UPLSAPO60XW, Olympus, Melville, NY; NA = 1.2) mounted in an inverted microscope (IX71, Olympus, Melville, NY). Introduction into the optical path of the objective was achieved via reflection from a dichroic mirror (675 DCSX, Chroma Technology, Brattleboro, VT). The epifluorescent collected light passes the dichroic mirror and a low pass filter before impinging on a PMT detector (H7422P-40, Hamamatsu Corporation, Bridgewater, NJ). Detector signals are sent to a TCSPC module (PicoHarp300, PicoQuant GmbH, Germany) and analyzed using SymPhoTime software.

Each image acquisition consisted of 10 frames at 256×256 pixels with dimensions 50×50 μm and a pixel dwell time of 0.5 ms. The excitation power at the sample was 2 mW, and the images were acquired approximately 2 μm below the glass surface to avoid scattering. Reported fluorescence lifetime values were achieved using PicoQuant's 'fastFLIM', which measures the barycenter of the exponential decay, and as such is a reliable measure of the average lifetime fluorescence decay value. Non-linear least-squares data fits using a maximum likelihood estimator (MLE) (data not shown) indicate an identical trend albeit with an increased amount of noise.

4.6 Acknowledgments

We are grateful to Jeannette Taylor and Hong Yi in the Emory Robert P. Apkarian Microscopy Core for TEM advice and training, to NSF (CHE-0131013) for CD instrumentation, and to the U.S. DOE (ER15377), NASA Astrobiology Program, under the NSF Center for Chemical Evolution, CHE-1004570 and NSF-CBC-0739189 for support.

4.7 References

1. Seddon, J.M., Templer, R. H. , *Polymorphism of Lipid-Water Systems* in *Handbook of Biological Physics*, R. Lipowsky, Sackmann E. , Editor. 1995, Elsevier Science.
2. Lingwood, D. and K. Simons, *Lipid Rafts as a Membrane Organizing Principle*. Science, 2010. **327**: p. 46-50.
3. Singer, S.J. and G.L. Nicolson, *Fluid Mosaic Model of the Structures of the Cell-Membranes* Science, 1972. **175**(4023): p. 720.
4. Zhang, S.G., et al., *Spontaneous Assembly of a Self-Complementary Oligopeptide to Form a Stable Macroscopic Membrane*. Proceedings of the National Academy of Sciences of the United States of America, 1993. **90**(8): p. 3334-3338.
5. Vauthey, S., et al., *Molecular Self-Assembly of Surfactant-Like Peptides to Form Nanotubes and Nanovesicles*. Proceedings of the National Academy of Sciences of the United States of America, 2002. **99**(8): p. 5355-5360.
6. Hamley, I.W., *Self-Assembly of Amphiphilic Peptides*. Soft Matter, 2011. **7**(9): p. 4122-4138.
7. Walker, L.C., et al., *Inducible Proteopathies*. Trends in Neurosciences, 2006. **29**(8): p. 438-443.
8. Chiti, F. and C.M. Dobson, *Protein Misfolding, Functional Amyloid, and Human Disease*. Annual review of biochemistry, 2006. **75**: p. 333-66.
9. Pedersen, J.S. and D.E. Otzen, *Amyloid-a State in Many Guises: Survival of the Fittest Fibril Fold*. Protein science : a publication of the Protein Society, 2008. **17**(1): p. 2-10.
10. Kodali, R. and R. Wetzel, *Polymorphism in the Intermediates and Products of Amyloid Assembly*. Current opinion in structural biology, 2007. **17**(1): p. 48-57.
11. Wiltzius, J.J., et al., *Molecular Mechanisms for Protein-Encoded Inheritance*. Nature structural & molecular biology, 2009. **16**(9): p. 973-8.
12. Dong, J., et al., *Controlling Amyloid Growth in Multiple Dimensions*. Amyloid, 2006. **13**(4): p. 206-15.

13. Naito, A. and I. Kawamura, *Solid-State Nmr as a Method to Reveal Structure and Membrane-Interaction of Amyloidogenic Proteins and Peptides*. Biochimica et biophysica acta, 2007. **1768**(8): p. 1900-12.

14. Knowles, T.P. and M.J. Buehler, *Nanomechanics of Functional and Pathological Amyloid Materials*. Nature nanotechnology, 2011. **6**(8): p. 469-79.

15. Cheon, M., et al., *Structural Reorganisation and Potential Toxicity of Oligomeric Species Formed During the Assembly of Amyloid Fibrils*. Plos Computational Biology, 2007. **3**(9): p. e173.

16. Auer, S., et al., *A Generic Mechanism of Emergence of Amyloid Protofilaments from Disordered Oligomeric Aggregates*. Plos Computational Biology, 2008. **4**(11): p. e1000222.

17. Castelletto, V., et al., *Influence of the Solvent on the Self-Assembly of a Modified Amyloid B Peptide Fragment. I. Morphological Investigation*. Journal of Physical Chemistry B, 2009. **113**(29): p. 9978-9987.

18. Castelletto, V., et al., *Helical-Ribbon Formation by a B-Amino Acid Modified Amyloid B-Peptide Fragment*. Angewandte Chemie-International Edition, 2009. **48**(13): p. 2317-2320.

19. Liang, Y., D.G. Lynn, and K.M. Berland, *Direct Observation of Nucleation and Growth in Amyloid Self-Assembly*. Journal of the American Chemical Society, 2010. **132**(18): p. 6306-6308.

20. Ahmed, M., et al., *Structural Conversion of Neurotoxic Amyloid-B(1-42) Oligomers to Fibrils*. Nature Structural & Molecular Biology, 2010. **17**(5): p. 561-569.

21. Jehle, S., et al., *Solid-State Nmr and Saxs Studies Provide a Structural Basis for the Activation of Ab-Crystallin Oligomers*. Nat Struct Mol Biol, 2010. **17**(99): p. 1037-1042.

22. Hamley, I.W., et al., *Influence of the Solvent on the Self-Assembly of a Modified Amyloid Beta Peptide Fragment. Ii. Nmr and Computer Simulation Investigation*. Journal of Physical Chemistry B, 2010. **114**(2): p. 940-951.

23. Adamcik, J., et al., *Direct Observation of Time-Resolved Polymorphic States in the Self-Assembly of End-Capped Heptapeptides*. Angewandte Chemie International Edition, 2011. **50**: p. 5495 –5498.

24. Sawaya, M.R., et al., *Atomic Structures of Amyloid Cross-B Spines Reveal Varied Steric Zippers*. Nature, 2007. **447**(7143): p. 453-457.

25. Madine, J., et al., *Fibrils and Nanotubes Assembled from a Modified Amyloid-B Peptide Fragment Differ in the Packing of the Same B-Sheet Building Blocks*. Chem Commun (Camb), 2012. **48**(24): p. 2976-8.

26. Balbach, J.J., et al., *Amyloid Fibril Formation by Aβ16-22, a Seven-Residue Fragment of the Alzheimer's B-Amyloid Peptide, and Structural Characterization by Solid State Nmr*. Biochemistry, 2000. **39**(45): p. 13748-59.

27. Ma, B. and R. Nussinov, *Stabilities and Conformations of Alzheimer's Beta -Amyloid Peptide Oligomers (Aβ16-22, Aβ16-35, and Aβ10-35): Sequence Effects*. Proc Natl Acad Sci, 2002. **99**(22): p. 14126-31.

28. Klimov, D.K. and D. Thirumalai, *Dissecting the Assembly of Aβ(16-22) Amyloid Peptides into Antiparallel B Sheets*. Structure, 2003. **11**(3): p. 295-307.

29. Lu, K., et al., *Exploiting Amyloid Fibril Lamination for Nanotube Self-Assembly*. Journal of the American Chemical Society, 2003. **125**(21): p. 6391-3.

30. Favrin, G., A. Irback, and S. Mohanty, *Oligomerization of Amyloid Aβ16-22 Peptides Using Hydrogen Bonds and Hydrophobicity Forces*. Biophysical Journal, 2004. **87**(6): p. 3657-64.

31. Gordon, D.J., et al., *Increasing the Amphiphilicity of an Amyloidogenic Peptide Changes the B-Sheet Structure in the Fibrils from Antiparallel to Parallel.* Biophysical Journal, 2004. **86**(1 Pt 1): p. 428-34.

32. Hwang, W., et al., *Kinetic Control of Dimer Structure Formation in Amyloid Fibrillogenesis*. Proceedings of the National Academy of Sciences of the United States of America, 2004. **101**(35): p. 12916-12921.

33. Klimov, D.K., J.E. Straub, and D. Thirumalai, *Aqueous Urea Solution Destabilizes Aβ(16-22) Oligomers*. Proceedings of the National Academy of Sciences of the United States of America, 2004. **101**(41): p. 14760-5.

34. Santini, S., N. Mousseau, and P. Derreumaux, *In Silico Assembly of Alzheimer's Aβ(16-22) Peptide into B-Sheets*. Journal of the American Chemical Society, 2004. **126**(37): p. 11509-11516.

35. Santini, S., et al., *Pathway Complexity of Alzheimer's B-Amyloid Aβ16-22 Peptide Assembly*. Structure, 2004. **12**(7): p. 1245-55.

36. Petty, S.A. and S.M. Decatur, *Experimental Evidence for the Reorganization of B-Strands within Aggregates of the Aβ(16-22) Peptide*. Journal of the American Chemical Society, 2005. **127**(39): p. 13488-9.

37. Gnanakaran, S., R. Nussinov, and A.E. Garcia, *Atomic-Level Description of Amyloid B-Dimer Formation*. Journal of the American Chemical Society, 2006. **128**(7): p. 2158-2159.

38. Rohrig, U.F., et al., *Stability and Structure of Oligomers of the Alzheimer Peptide Aβ16-22: From the Dimer to the 32-Mer*. Biophysical Journal, 2006. **91**(9): p. 3217-29.

39. Derreumaux, P. and N. Mousseau, *Coarse-Grained Protein Molecular Dynamics Simulations*. The Journal of Chemical Physics, 2007. **126**(2): p. 025101.

40. Gehman, J.D., et al., *Boltzmann Statistics Rotational-Echo Double-Resonance Analysis*. J Phys Chem B, 2007. **111**(27): p. 7802-11.

41. Krysmann, M.J., V. Castelletto, and I.W. Hamley, *Fibrillisation of Hydrophobically Modified Amyloid Peptide Fragments in an Organic Solvent*. Soft Matter, 2007. **3**(11): p. 1401-1406.

42. Lu, K., et al., *Macroscale Assembly of Peptide Nanotubes*. Chem. Commun (Camb), 2007(26): p. 2729-31.

43. Meinke, J.H. and U.H.E. Hansmann, *Aggregation of B-Amyloid Fragments*. The Journal of Chemical Physics, 2007. **126**(1): p. 014706-5.

44. Nguyen, P.H., et al., *Monomer Adds to Preformed Structured Oligomers of Aβ-Peptides by a Two-Stage Dock-Lock Mechanism*. Proceedings of the National Academy of Sciences of the United States of America, 2007. **104**(1): p. 111-116.

45. Soto, P., M.A. Griffin, and J.E. Shea, *New Insights into the Mechanism of Alzheimer Amyloid-B Fibrillogenesis Inhibition by N-Methylated Peptides*. Biophysical Journal, 2007. **93**(9): p. 3015-25.

46. Cheon, M., et al., *Calculation of the Free Energy Barriers in the Oligomerisation of Aβ Peptide Fragments*. Frontiers in Bioscience, 2008. **13**: p. 5614-5622.

47. Irback, A. and S. Mitternacht, *Spontaneous B-Barrel Formation: An All-Atom Monte Carlo Study of Aβ(16-22) Oligomerization*. Proteins-Structure Function and Bioinformatics, 2008. **71**(1): p. 207-214.

48. Krone, M.G., et al., *Role of Water in Mediating the Assembly of Alzheimer Amyloid-B Aβ16-22 Protofilaments*. Journal of the American Chemical Society, 2008. **130**(33): p. 11066-72.

49. Krysmann, M.J., et al., *Self-Assembly and Hydrogelation of an Amyloid Peptide Fragment*. Biochemistry, 2008. **47**(16): p. 4597-4605.

50. Liang, Y., et al., *Light Harvesting Antenna on an Amyloid Scaffold*. Chemical Communications, 2008(48): p. 6522-6524.

51. Liang, Y., et al., *Cross-Strand Pairing and Amyloid Assembly*. Biochemistry, 2008. **47**(38): p. 10018-10026.

52. Mehta, A.K., et al., *Facial Symmetry in Protein Self-Assembly*. Journal of the American Chemical Society, 2008. **130**(30): p. 9829-9835.

53. Oh, K.I., et al., *B-Azidoalanine as an Ir Probe: Application to Amyloid Aβ(16-22) Aggregation*. The journal of physical chemistry. B, 2008. **112**(33): p. 10352-7.

54. Bellesia, G. and J.E. Shea, *Effect of B-Sheet Propensity on Peptide Aggregation*. Journal of Chemical Physics, 2009. **130**(14): p. 145103-10.

55. Brovchenko, I., et al., *Thermal Expansivity of Amyloid Β(16-22) Peptides and Their Aggregates in Water*. Physical chemistry chemical physics : PCCP, 2009. **11**(25): p. 5035-40.

56. Childers, W.S., et al., *Templating Molecular Arrays in Amyloid's Cross-Β Grooves*. Journal of the American Chemical Society, 2009. **131**(29): p. 10165-72.

57. Childers, W.S., et al., *Peptide Membranes in Chemical Evolution*. Curr Opin Chem Biol, 2009. **13**(5-6): p. 652-9.

58. Elgersma, R.C., D.T. Rijkers, and R.M. Liskamp, *Ph Controlled Aggregation Morphology of Aβ(16-22): Formation of Peptide Nanotubes, Helical Tapes and Amyloid Fibrils*. Advances in experimental medicine and biology, 2009. **611**: p. 239-40.

59. Elgersma, R.C., et al., *Microwave-Assisted Click Polymerization for the Synthesis of Aβ(16-22) Cyclic Oligomers and Their Self-Assembly into Polymorphous Aggregates*. Org Biomol Chem, 2009. **7**(21): p. 4517-25.

60. Liu, F.F., et al., *Molecular Insight into the Inhibition Effect of Trehalose on the Nucleation and Elongation of Amyloid Β-Peptide Oligomers*. The journal of physical chemistry. B, 2009. **113**(32): p. 11320-9.

61. Lu, Y., et al., *Thermodynamics and Dynamics of Amyloid Peptide Oligomerization Are Sequence Dependent*. Proteins-Structure Function and Bioinformatics, 2009. **75**(4): p. 954-63.

62. Park, J., B. Kahng, and W. Hwang, *Thermodynamic Selection of Steric Zipper Patterns in the Amyloid Cross-Β Spine*. PLoS Comput Biol, 2009. **5**(9): p. e1000492.

63. Xiu, P., et al., *Manipulating Biomolecules with Aqueous Liquids Confined within Single-Walled Nanotubes*. Journal of the American Chemical Society, 2009. **131**(8): p. 2840-5.

64. Childers, W.S., et al., *Peptides Organized as Bilayer Membranes*. Angewandte Chemie International Edition, 2010. **49**(24): p. 4104-7.

65. Inouye, H., et al., *Differential Effects of Phe19 and Phe20 on Fibril Formation by Amyloidogenic Peptide Aβ16–22 (Ac-Klvffae-Nh2)*. Proteins: Structure, Function, and Bioinformatics, 2010. **78**(10): p. 2306-2321.

66. Straub, J.E. and D. Thirumalai, *Principles Governing Oligomer Formation in Amyloidogenic Peptides*. Current Opinion in Structural Biology, 2010. **20**(2): p. 187-95.

67. Wallace, J.A. and J.K. Shen, *Probing the Strand Orientation and Registry Alignment in the Propagation of Amyloid Fibrils*. Biochemistry, 2010. **49**(25): p. 5290-5298.

68. Chaudhary, N. and R. Nagaraj, *Impact on the Replacement of Phe by Trp in a Short Fragment of Aβ Amyloid Peptide on the Formation of Fibrils*. Journal of peptide science, 2011. **17**(2): p. 115-23.

69. Cheon, M., I. Chang, and C.K. Hall, *Spontaneous Formation of Twisted Aβ(16-22) Fibrils in Large-Scale Molecular-Dynamics Simulations*. Biophysical Journal, 2011. **101**(10): p. 2493-501.

70. Debeljuh, N., C.J. Barrow, and N. Byrne, *The Impact of Ionic Liquids on Amyloid Fibrilization of Aβ16-22: Tuning the Rate of Fibrilization Using a Reverse Hofmeister Strategy*. Physical Chemistry Chemical Physics, 2011. **13**(37): p. 16534-16536.

71. Li, H., et al., *Carbon Nanotube Inhibits the Formation of B-Sheet-Rich Oligomers of the Alzheimer's Amyloid-B(16-22) Peptide*. Biophysical journal, 2011. **101**(9): p. 2267-76.

72. Nguyen, P.H., M.S. Li, and P. Derreumaux, *Effects of All-Atom Force Fields on Amyloid Oligomerization: Replica Exchange Molecular Dynamics Simulations of the Aβ(16-22) Dimer and Trimer*. Physical chemistry chemical physics : PCCP, 2011. **13**(20): p. 9778-88.

73. Senguen, F.T., et al., *Clarifying the Influence of Core Amino Acid Hydrophobicity, Secondary Structure Propensity, and Molecular Volume on Amyloid-B 16-22 Self-Assembly*. Mol Biosyst, 2011. **7**(2): p. 497-510.

74. Senguen, F.T., et al., *Probing Aromatic, Hydrophobic, and Steric Effects on the Self-Assembly of an Amyloid-B Fragment Peptide*. Mol Biosyst, 2011. **7**(2): p. 486-96.

75. Shanmugam, G. and P.L. Polavarapu, *Isotope-Assisted Vibrational Circular Dichroism Investigations of Amyloid B Peptide Fragment, Aβ(16-22)*. Journal of structural biology, 2011. **176**(2): p. 212-9.

76. Sivakamasundari, C., S. Nandakumar, and R. Nagaraj, *Effect of Replacing Phenylalanine Residues by Para-Substituted Phenylalanines on the Aggregation Behavior of Aβ16-22*. Protein and peptide letters, 2011.

77. Tao, K., et al., *Self-Assembly of Short Aβ(16-22) Peptides: Effect of Terminal Capping and the Role of Electrostatic Interaction*. Langmuir, 2011. **27**(6): p. 2723-2730.

78. Viet, M.H., et al., *Inhibition of Aggregation of Amyloid Peptides by B-Sheet Breaker Peptides and Their Binding Affinity*. The journal of physical chemistry. B, 2011. **115**(22): p. 7433-46.

79. Nguyen, H.D. and C.K. Hall, *Molecular Dynamics Simulations of Spontaneous Fibril Formation by Random-Coil Peptides*. Proceedings of the National Academy of Sciences of the United States of America, 2004. **101**(46): p. 16180-16185.

80. Pellarin, R. and A. Caflisch, *Interpreting the Aggregation Kinetics of Amyloid Peptides*. Journal of Molecular Biology, 2006. **360**(4): p. 882-92.

81. Auer, S., C.M. Dobson, and M. Vendruscolo, *Characterization of the Nucleation Barriers for Protein Aggregation and Amyloid Formation*. Hfsp Journal, 2007. **1**(2): p. 137-146.

82. Pellarin, R., E. Guarnera, and A. Caflisch, *Pathways and Intermediates of Amyloid Fibril Formation*. Journal of Molecular Biology, 2007. **374**(4): p. 917-24.

83. Muschol, M. and F. Rosenberger, *Liquid-Liquid Phase Separation in Supersaturated Lysozyme Solutions and Associated Precipitate Formation/Crystallization*. Journal of Chemical Physics, 1997. **107**(6): p. 1953-1962.

84. Astbury, W.T., S. Dickinson, and K. Bailey, *The X-Ray Interpretation of Denaturation and the Structure of the Seed Globulins*. Biochemical Journal, 1935. **29**(10): p. 2351-2360 1.

85. Parker, K.D. and K.M. Rudall, *Structure of the Silk of Chrysopa Egg-Stalks*. Nature, 1957. **179**(4566): p. 905-906.

86. Geddes, A.J.P., K. D.; Atkinds, E. D. T.; Beighton, E., *"Cross-B" Conformation in Proteins*. J. Mol. Biol., 1968. **32**: p. 343.

87. Sunde, M. and C.C. Blake, *From the Globular to the Fibrous State: Protein Structure and Structural Conversion in Amyloid Formation*. Quarterly Reviews of Biophysics, 1998. **31**(1): p. 1-39.

88. Krysmann, M.J., et al., *Self-Assembly of Peptide Nanotubes in an Organic Solvent*. Langmuir, 2008. **24**(15): p. 8158-8162.

89. Marcus, Y., *Properties of Solvents*. Wiley Series in Solution Chemistry ; V. 4. 1998: Wiley. 254p.

90. Borst, J.W. and A.J.W.G. Visser, *Fluorescence Lifetime Imaging Microscopy in Life Sciences*. Measurement Science & Technology, 2010. **21**(10).

91. Lomakin, A., N. Asherie, and G.B. Benedek, *Liquid-Solid Transition in Nuclei of Protein Crystals*. Proceedings of the National Academy of Sciences of the United States of America, 2003. **100**(18): p. 10254-7.

92. Dong, J.J., R.P. Apkarian, and D.G. Lynn, *Imaging Amyloid Beta Peptide Oligomeric Particles in Solution*. Bioorganic & Medicinal Chemistry, 2005. **13**(17): p. 5213-5217.

93. Selinger, J.V., F.C. MacKintosh, and J.M. Schnur, *Theory of Cylindrical Tubules and Helical Ribbons of Chiral Lipid Membranes*. Physical review E, 1996. **53**(4): p. 3804-3818.

94. Ghafouri, R. and R. Bruinsma, *Helicoid to Spiral Ribbon Transition*. Physical review letters, 2005. **94**(13): p. 138101.

95. Armon, S., et al., *Geometry and Mechanics in the Opening of Chiral Seed Pods*. Science, 2011. **333**(6050): p. 1726-30.

96. Sawa, Y., et al., *Shape Selection of Twist-Nematic-Elastomer Ribbons*. Proceedings of the National Academy of Sciences of the United States of America, 2011. **108**(16): p. 6364-8.

97. Ziserman, L., et al., *Unraveling the Mechanism of Nanotube Formation by Chiral Self-Assembly of Amphiphiles*. Journal of the American Chemical Society, 2011. **133**(8): p. 2511-7.

98. Pashuck, E.T. and S.I. Stupp, *Direct Observation of Morphological Transformation from Twisted Ribbons into Helical Ribbons*. Journal of the American Chemical Society, 2010. **132**(26): p. 8819-21.

99. Ziserman, L., et al., *Curvature Instability in a Chiral Amphiphile Self-Assembly*. Physical review letters, 2011. **106**(23): p. 238105.

100. Lakdawala, A.S., et al., *Dynamics and Fluidity of Amyloid Fibrils: A Model of Fibrous Protein Aggregates*. Journal of the American Chemical Society, 2002. **124**(51): p. 15150-15151.

101. McBain, J.W., *Mobility of Highly Charged Micelles*. Transactions of the Faraday Society, 1913. **9**: p. 99-102.

102. Vekilov, P.G., *Phase Transitions of Folded Proteins*. Soft Matter, 2010. **6**(21): p. 5254-5272.

103. ten Wolde, P.R. and D. Frenkel, *Enhancement of Protein Crystal Nucleation by Critical Density Fluctuations*. Science, 1997. **277**(5334): p. 1975-8.

104. Pouget, E., et al., *Elucidation of the Self-Assembly Pathway of Lanreotide Octapeptide into B-Sheet Nanotubes: Role of Two Stable Intermediates*. Journal of the American Chemical Society, 2010. **132**(12): p. 4230-41.

105. Spitzer, J. and B. Poolman, *The Role of Biomacromolecular Crowding, Ionic Strength, and Physicochemical Gradients in the Complexities of Life's Emergence*. Microbiology and Molecular Biology Reviews, 2009. **73**(2): p. 371-388.

106. Fowler, D.M., et al., *Functional Amyloid - from Bacteria to Humans*. Trends Biochem Sci, 2007. **32**(5): p. 217-224.

107. Giraldo, R., *Amyloid Assemblies: Protein Legos at a Crossroads in Bottom-up Synthetic Biology*. Chembiochem, 2010. **11**(17): p. 2347-57.

108. Childers, W.S., et al., *Toward Intelligent Material*, in *Molecular Self-Assembly: Advances and Applications*, A. Li, Editor. 2012, Pan Stanford Publishing Singapore.

Chapter 5

Mapping Amyloid-β(16-22) Nucleation Pathways using Fluorescence Lifetime Imaging Microscopy

Neil R. Anthony*, Anil K. Mehta†, Yan Liang†, David G. Lynn†, and Keith M. Berland*

*Department of Physics, Emory University, Atlanta, GA

†Center for Fundamental and Applied Molecular Evolution, NSF/NASA Center for Chemical Evolution, Departments of Chemistry and Biology, Emory University, Atlanta, GA

5.1 Introduction

Investigations of the protein aggregates associated with neurodegenerative diseases have continued to highlight the increasingly urgent need for better treatments [1]. Given the pathology of the disease, such treatments are tied to a better understanding of the complex landscape of biopolymer folding, specifically protein misfolding events [2-5]. Transient soluble molten globule monomers and dynamic oligomers are central to both folding and misfolding, and these intermolecular phases may provide critical on- and off-pathway intermediates in the formation of the β-sheet rich peptide phases that appear to be central to the etiology of dementia and cellular toxicity [4, 6-14]. Understanding the subtleties of the inter- and intra-molecular peptide interactions that determine protein aggregation is thus vital for a pathogenic understanding leading to the development of therapeutic strategies.

Hydrophobically-driven peptide collapse creates a reduced dielectric environment critical for intra-molecular peptide assembly [15-19]. These dynamic intermolecular aggregates have been predicted in numerous protein aggregation simulations [20-23] and observed experimentally [24-27]. Nucleating seeds capable of templating elongation and growth have also been observed once a critical concentration (CC) of peptide has been achieved [28], together with a lag-phase that typically precedes amyloid growth [29, 30]. In addition, air-water-interfaces (AWIs) have been shown to accelerate the nucleation process; both in deleterious protein aggregation [31-33] and functional bio-aggregates [34-36], the presence of interfaces can lead to differing aggregate morphology, nucleation pathways, altered membrane interactions, and possibly different roles in toxicity [37-41].

Surfaces such as AWIs, hydrophobic-hydrophilic interfaces (HHIs), and lipid bilayers and micelles continue to be identified as local environments critical for phase transitions [31, 33, 42-46]. Nevertheless, capturing nucleation events and nascent growth at these soluble pre-fibrillar intermediate stages has proven to be inherently difficult due to their transient nature. Numerous experiments have employed the sensitivity and specificity of fluorescence measurements to assist in identifying transient species [41, 47]. The amyloid specific dye thioflavin-T (ThT) [48] has been used to quantify amyloid formation at AWIs in bulk solution [49], and spatially resolved fiber growth on glass surfaces using total internal reflection microscopy (TIRFM) [39, 50-52]. In addition, TIRFM has been employed to observe 2D diffusion of weakly adsorbed amyloid-β (Aß) peptides, where nucleation is limited to surface adhered peptides [53].

Here we investigate mechanisms to control the initial phase transition into aggregates and the subsequent nucleation events within the molten globules. Using one of the most investigated model amyloid systems, Aß(16-22) (see [28] and references therein; Chapter 4), we have previously followed the initial nucleation stages of cross-β peptide nanotubes utilizing a small fraction (~1%) of rhodamine-labeled peptides [24]. Lys16 of Aß(16-22) was replaced with rhodamine-110 (R110) to produce a positively charged label, denoted Rh17-22, that co-assembled with Aß(16-22) and became incorporated into the final cross-β phase [24]. Aß(16-22) co-assembled with Rh17-22 allowed the dynamic phases present during nucleation to be captured, whereby 'molten globule' aggregates adhered to glass surfaces were directly observed as centers of nucleation and growth of cross-β nanotube structures [24].

We investigate the effects of AWIs and HHIs on solutions of Aβ(16-22) above and below the peptides critical assembly concentration. The combination of concentrations and

interfaces allow us to probe the different stages of the nucleation pathways. Using aeration and vortexing to introduce AWIs and hydrophobic plastic to represent HHIs, we determine that introduced interfaces lead to varying amounts of nucleation, and allow access to previously uncharacterized intermediate morphologies suspected to be on-pathway seeds to nanotube growth. We also demonstrate that solvent evaporation leading to changes in solubility can be used to control nucleation. Fluorescence lifetime imaging microscopy (FLIM) of the morphologies, accessed utilizing these different interfaces, allows the nucleation process to be mapped out in terms of known and inferred structures. Further, we expand on previous work by recreating the growing molten globules, and follow the evolution of these aggregates using FLIM to further resolve the fluorescence lifetime of the nucleation events. We have thus followed the morphology and fluorescence lifetime of Aβ(16-22) peptide as it aggregates and forms into paracrystalline cross-β nanotubes. Using numerous interfaces allows for the morphology, environment, and to some degree, structure of Aβ(16-22) to be mapped from monomer to paracrystalline nanotube.

5.2 Results

Although our earlier investigations did not define a role for air-water-interfaces (AWIs) in the nucleation of Aß(16-22):Rh17-22 nanotubes [24], due to the increase in reports of sensitivity to interfaces [31, 33, 42-46] we revisit the previous study. 0.5 mM Aβ(16-22)/Rh17-22 (250:1) dissolved in 40% aqueous MeCN pH 2 was loaded twice onto a microscope slide and sealed with coverslip glass ([24]; Figure 5–1a). During loading, the solvent spreads out across the glass (Figure 5–1a; frame 1-3), dramatically increasing the air and glass surface interactions available to the peptide solution, while the evaporation of solvents increases concentration and decreases the solubility. As seen previously [24], growth originates from numerous molten globules on the glass surface after ~24 hrs (Figure 5–1b). Nascent growth from molten globules exhibits a shorter persistence length than fully mature nanotubes, and forms a somewhat meshed network between growing centers. Alternatively, the same sample was also loaded into the thin gap of a pre-set slide /coverslip vessel using capillary action. Capillary action into the cavity formed by the slide / coverslip eliminates both evaporation and the air-solution interface. In contrast to the air-loaded solutions, after 24 hrs no significant nucleation could be detected (Figure 5–1c) with only small aggregate spots detected on the glass surfaces, appearing to form at local impurities.

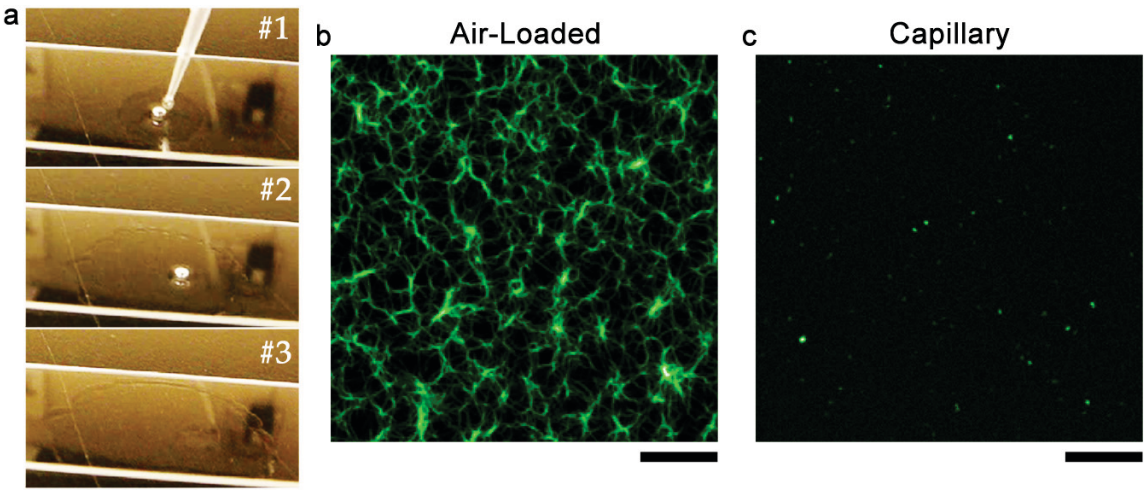

Figure 5–1 – Role of air-water-interface (AWI) in sample loading. The air-loaded protocol (a) of adding a drop of 0.5 mM Aß(16-22)/Rh17-22 (250:1) is repeated twice before covering with a cover slip. After ~24 hrs, the air-loaded mixtures produce nucleating aggregates at the glass surface (b). Loading by capillary action on a preset slide/coverslip vessel only small aggregates are seen on the glass (c). Scale bar 10 μm.

As evaporation and AWIs appear to be the two key differences between the loading protocols, we further investigated these factors by aerating or evaporating aliquots of 0.04 mM Aß(16-22)/Rh17-22 (200:1) in 40% MeCN pH 2 aqueous solution over a period of 2 weeks, followed by inspection in a chamber box well to remove loading effects. The critical concentration (CC) for this Aß(16-22) peptide was ~0.5 mM, although this concentration varies depending on the synthetic batch. Here, aeration refers to air being repeatedly pushed into solution using a pipette tip and pipettor, while evaporation occurs by leaving the sample under the fume hood, providing a constant flow of air over the open container. The weight of evaporated solution was monitored to match the weight loss of aerated solution for comparison. Figure 5–2 shows fluorescence images of both aerated (left) and evaporated (right) samples. Aeration leads to fewer, but more elongated nanotubes, while evaporation leads to shorter nanotubes and numerous

smaller morphologies. It becomes difficult to distinguish between aggregate seeds and small nanotube sections below a length of 2-3 μm. Also, the evaporated sample shows an increase in the amount of surface-adhered Rh17-22 peptide. As to be expected, when starting with peptide concentrations below the critical assembly concentration, it is clear that the increased peptide concentration and decreased solubility due to the relative evaporation of H_2O and MeCN allows for increased nucleation.

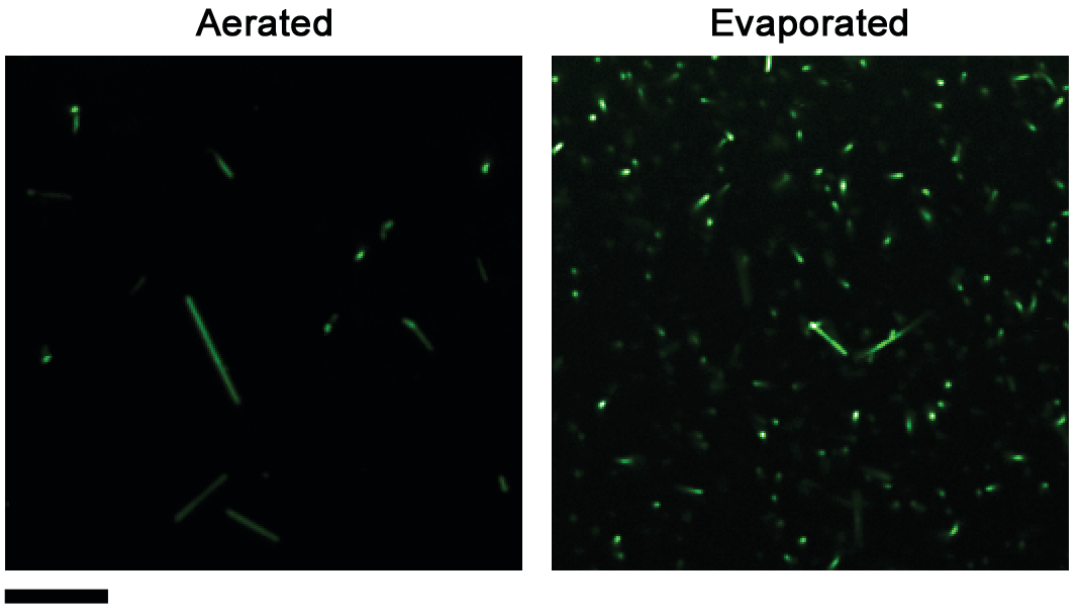

Figure 5–2 – Comparison of evaporation and reduced solubility in accessing nucleation events. Aeration (left) produces longer more uniform nanotube growth, whereas evaporation (right) has considerable more small fragments and a greater surface coating. Scale bar 10 μm.

Utilizing the role of interfaces and solubility to control access to nucleation pathways, we assembled peptide mixtures above and below the critical assembly concentration (CC). The CC for this Aß(16-22) peptide batch was independently confirmed to be ~0.35 mM. Aliquots of 0.3 mM and 0.4 mM Aß(16-22)/Rh17-22 mixtures (200:1) were separated

and (i) aerated, (ii) vortexed, or (iii) not agitated (quiescent conditions) during the initial assembly stages. To attenuate the potential for disrupting the assemblies over time, both aeration and vortexing were performed periodically and with reduced frequency at later stages. Also, to reduce the affects of evaporation shown above, aeration was introduced 10 times less frequently. To provide an additional hydrophobic interface, previously shown to accelerate nucleation [49], we also prepared (iv) a quiescent sample containing a piece of pipette tip. The micro-centrifuge tubes used for assembly were polypropylene and the Eppendorf pipette tips contain anti-static additives to increase their hydrophobicity. Under these conditions, the first nanotube morphologies were detected within approximately one week, although the samples were incubated for approximately 1 month before imaging (Figure 5–3).

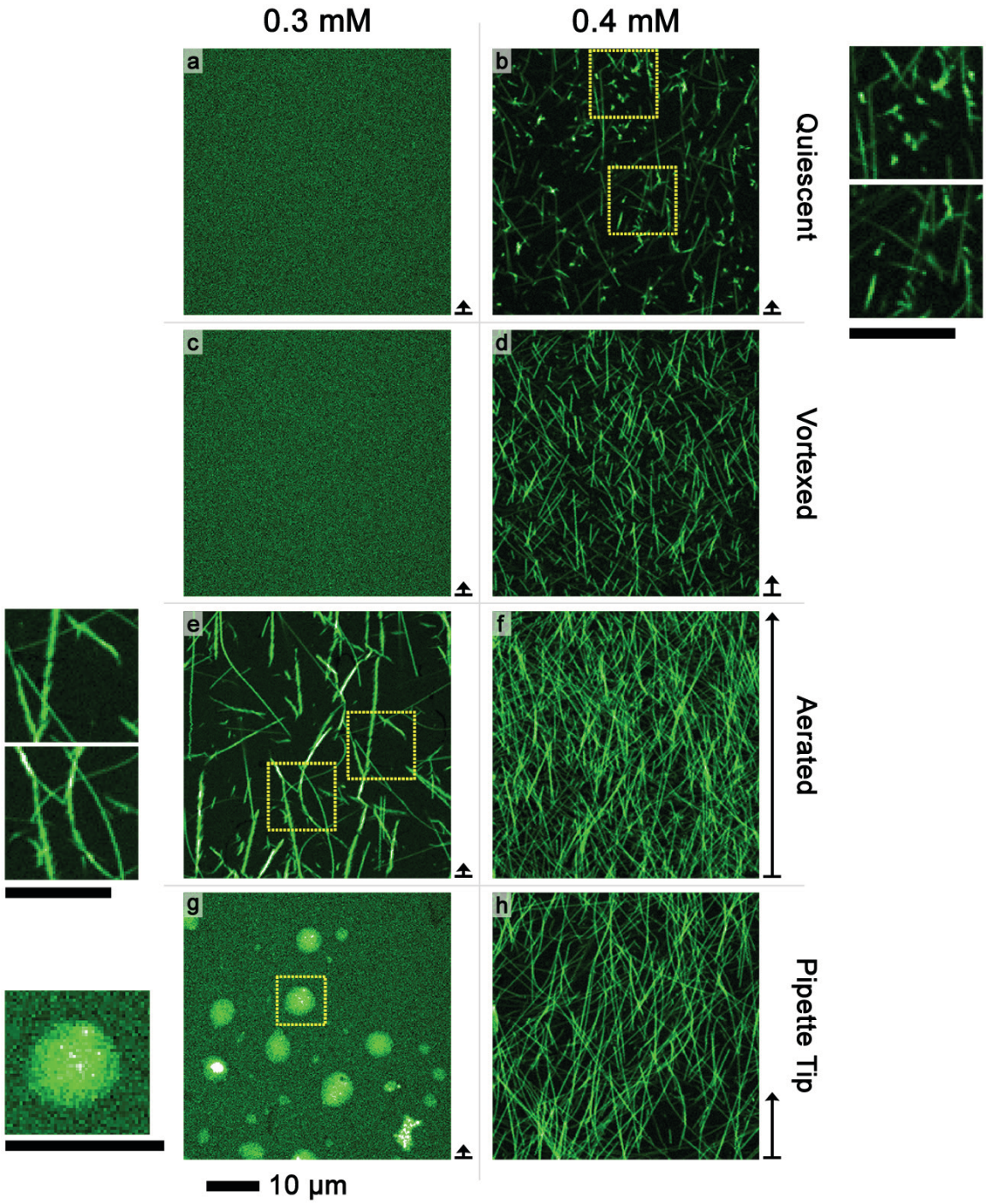

Figure 5–3 – The effect of interfaces in nucleating assembles. Aß(16-22) solutions below (0.3 mM; left column) and above (0.4 mM; right column) the critical assembly concentration (CC) were allowed to assemble under quiescent conditions, quiescent conditions with permanent hydrophobic-hydrophilic-interface (HHI; pipette tip),

periodic vortexing or aeration during the initial assemble period. Each image is a single ~1 μm thick z-section acquired near the bottom of a chamber box well. Depth indicators at the right hand side of each image denote the height of the nanotube meshed network filling the chamber well normalized to the 0.4 mM aerated conditions sample, with approximately 20 μm. Quiescent (a) and vortexed (c) conditions appeared as homogeneous solutions below the CC (0.3 mM; left column), while aeration (e) induces tube growth together with a large amount of small aggregates that appear to be mostly bundled around the nanotube morphology (see ×2 zoom inserts to left of panel). The 0.3 mM solution with permanent HHI (g) produced heterogeneous aggregates that are mostly diffuse containing varying degrees of denser sections (see ×3 zoom inserts to left of panel). All solutions above the CC (0.4 mM; right column) assemble into nanotube morphologies. Quiescent conditions above the CC (b) produce only a small amount to tube growth together with a similar aggregate morphology to that seen in (e) (see ×2 zoom inserts to right of panel). Vortexing (d), aeration (f), and permanent HHI (h) samples contain nanotubes morphologies only of differing depths.

As shown in Figure 5–3a, the 0.3 mM quiescent Aβ(16-22):Rh17-22 mixture did not assemble below the CC as determined by the homogeneous fluorescence across the entire sample volume. The same homogeneous fluorescence was evident for the below CC vortexed conditions (Figure 5–3c). In contrast, aeration below the CC (Figure 5–3e) showed considerable nanotube growth in addition to morphology resembling bundles of aggregated assemblies. Nanotubes are readily identified as long persistence length fluorescent rods with uniform diameter and fluorescence (Figure 3–3). The bundled assemblies appear jagged with irregular morphologies (Figure 5–3e; ×2 zoom inserts to left of panel). We estimate that the solution lost by aeration is approximately 10-15% by weight, increasing the 0.3 mM aerated sample to an effective concentration similar to

that of the 0.4 mM quiescent conditions (Figure 5–3b), together with a small reduction in solubility due to the relative vapor pressures of the solvent mixture. The below CC solution containing a permanent HHI produced numerous small diffuse aggregates of varying density, with an additional morphology manifesting as spots and clusters of spots (Figure 5–3g).

Above the CC, all 0.4 mM samples display nanotube morphologies. In addition to the clearly distinguishable homogeneously fluorescent nanotubes, the 0.4 mM sample under quiescent conditions contained a small amount of the bundled aggregate morphologies (Figure 5–3b; ×2 zoom inserts to right of panel) as seen in the 0.3 mM aerated sample, which are not seen in the remaining 0.4 mM samples. The vortexed and aerated samples (Figure 5–3d & f respectively) display increasing amounts of nanotube growth. Each image shown is a z-section of the sample approximately 1 μm thick, and thus does not reveal how much of the chamber box well was filled with nanotubes. The depth indicators on each image convey the amount of nanotube mesh network filling the bottom of the chamber box, shown as a relative fraction of the 0.4 mM aerated sample (Figure 5–3f). The 0.3 mM aerated and 0.4 mM quiescent samples contain a single z-section, while the mesh network of the 0.4 mM aerated sample extends approximately 20 μm above the surface. The pipette tip also significantly increased the amount of nanotube growth at concentration of 0.4 mM, where the measured mesh of nanotubes extended ~5 μm from the chamber surface (Figure 5–3h). Taken together, the introduction of interfaces correlates with an increase in nanotube assembly, allowing for subsequent analyses.

Fluorescence lifetime imaging microscopy (FLIM) probes the environment of the Rh17-22 label at different stages of nucleation across the sample. The average

fluorescence lifetime of Rh17-22 in solution is 3.45 ns, identical to the homogeneous fluorescence lifetime of both 0.3 mM quiescent and vortexed samples, suggesting that these solutions are predominantly non-interacting monomers (Figure 5–4a&b). In comparison, the average fluorescence lifetime of Rh17-22 incorporated into nanotube morphologies is approximately 3 ns, presented as yellow in FLIM images (Figure 5–4c & e-h), and the peak at 3 ns in FLIM image histograms (Figure 5–4i). In addition, the fluorescence lifetime of the bundled aggregates is also reduced (Figure 5–4c). The reduction in fluorescence lifetime along these jagged elongated assemblies appears heterogeneous, giving an average lifetime ranging from 2.4 to 2.8 ns. The same bundled aggregates can be seen in the 0.4 mM quiescent sample, yet with smaller domain size and a longer average lifetime. FLIM data of diffuse aggregates nucleated using HHIs revealed a fluorescence lifetime of approximately 2.8 ns (Figure 5–4 d), and dense spots with lifetimes as low as 2.5 ns.

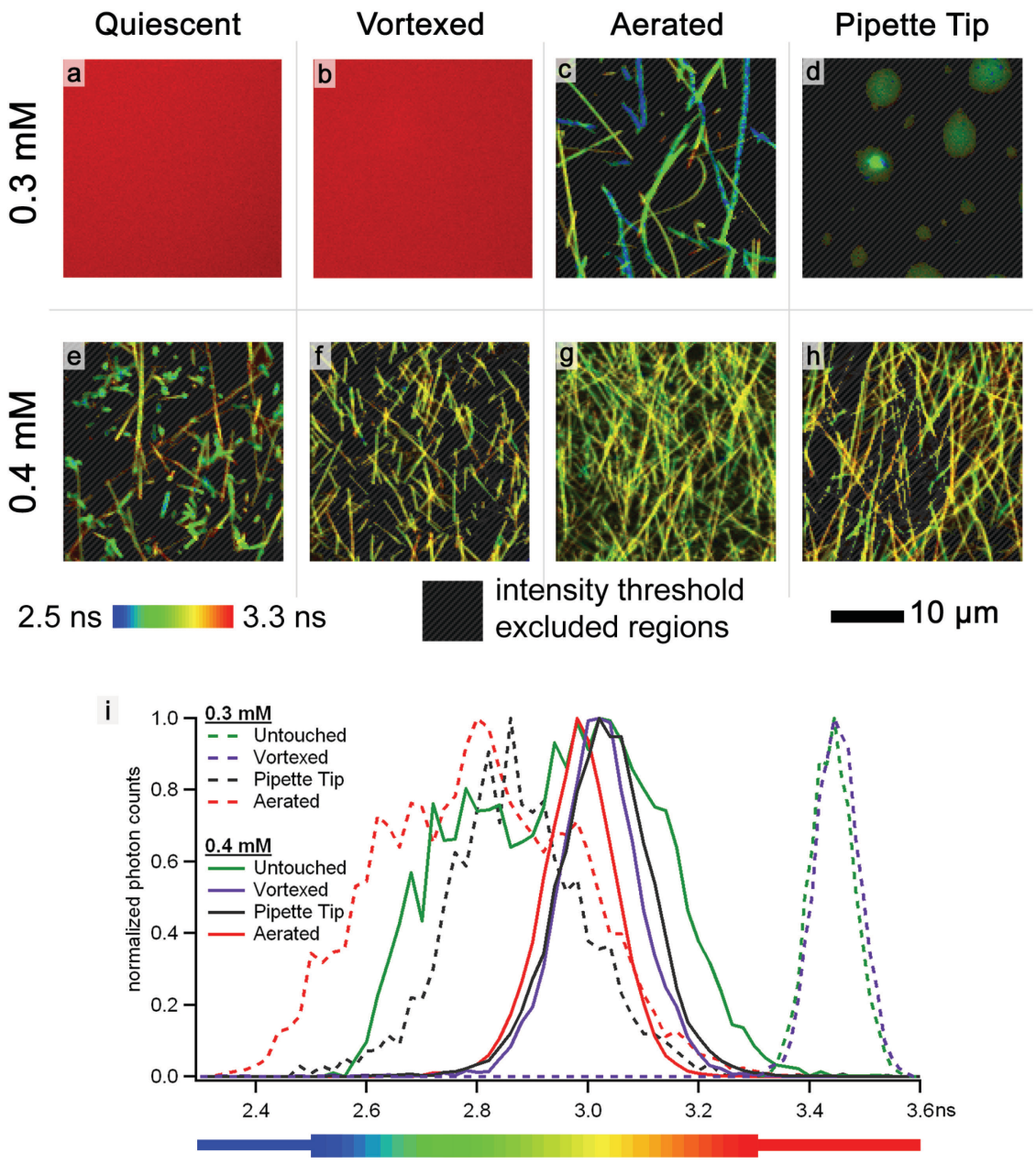

Figure 5–4 – Fluorescence lifetime imaging microscopy (FLIM) analyses of 0.3 and 0.4 mM aliquots of Aβ(16-22):Rh17-22 assemblies (a-h). Distributions of average fluorescence lifetimes for each image are shown in the histogram (i). Intensity threshold regions (grey striped areas) in images c-h are omitted from corresponding histogram distribution to reduce contribution of background signal from monomer and surface

bound peptides. 0.3 mM quiescent (a) and vortexed (b) solutions exhibit average fluorescence lifetimes of 3.45 ns consistent with monomer solutions. 0.3 mM aerated solution (c) contains both 3 ns lifetime nanotubes and bundled aggregate assemblies exhibiting heterogeneous lifetimes ranging from 2.4 to 2.8 ns. Diffuse green aggregates with lifetimes of ~2.8 ns seen in the 0.3 mM pipette tip sample (d) contain small intense spots of shorter lifetime, ~2.6 ns. The above CC 0.4 mM sample in quiescent conditions (e) contains a small amount of nanotubes and bundled aggregates with lifetimes of approximately 2.8 ns. Nanotubes in (e) show regions of longer lifetime, assumed to be a larger contribution from background monomer, either due to being out of focus or incorporation of less Rh17-22 label. 0.4 mM aerated, vortexed and pipette tip containing samples exhibit differing amounts of nanotube growth that have a fluorescence lifetime of approximately 3 ns.

Given that nucleation can be accelerated by the AWI and evaporation, and that the growing molten globule aggregates can be followed once adhered to the coverslip glass surface, we were able to track the initial stages of nucleated growth using FLIM analysis. Time-lapse FLIM acquisitions reveal an initial fluorescence lifetime for the small aggregates of approximately 2.5 ns (Figure 5–5a; 0 to 5 hrs). As these aggregates grow in size, short nanotubes appear at the periphery of the aggregate, where the number of growing tubes appears correlated with aggregate size [28]. Concurrent with tube growth, the aggregates experience a reduction in average lifetime from 2.5 to 2.1 ns (Figure 5–5b), consistent with fluorescence quenching due to a local increase in peptide concentration, corroborating peptide packing and solvent exclusion within the aggregate. Highlighting a ROI containing just nascent tube growth reveals an average fluorescence lifetime with a peak of 2.7 ns (Figure 5–5c), a fraction lower than mature nanotubes.

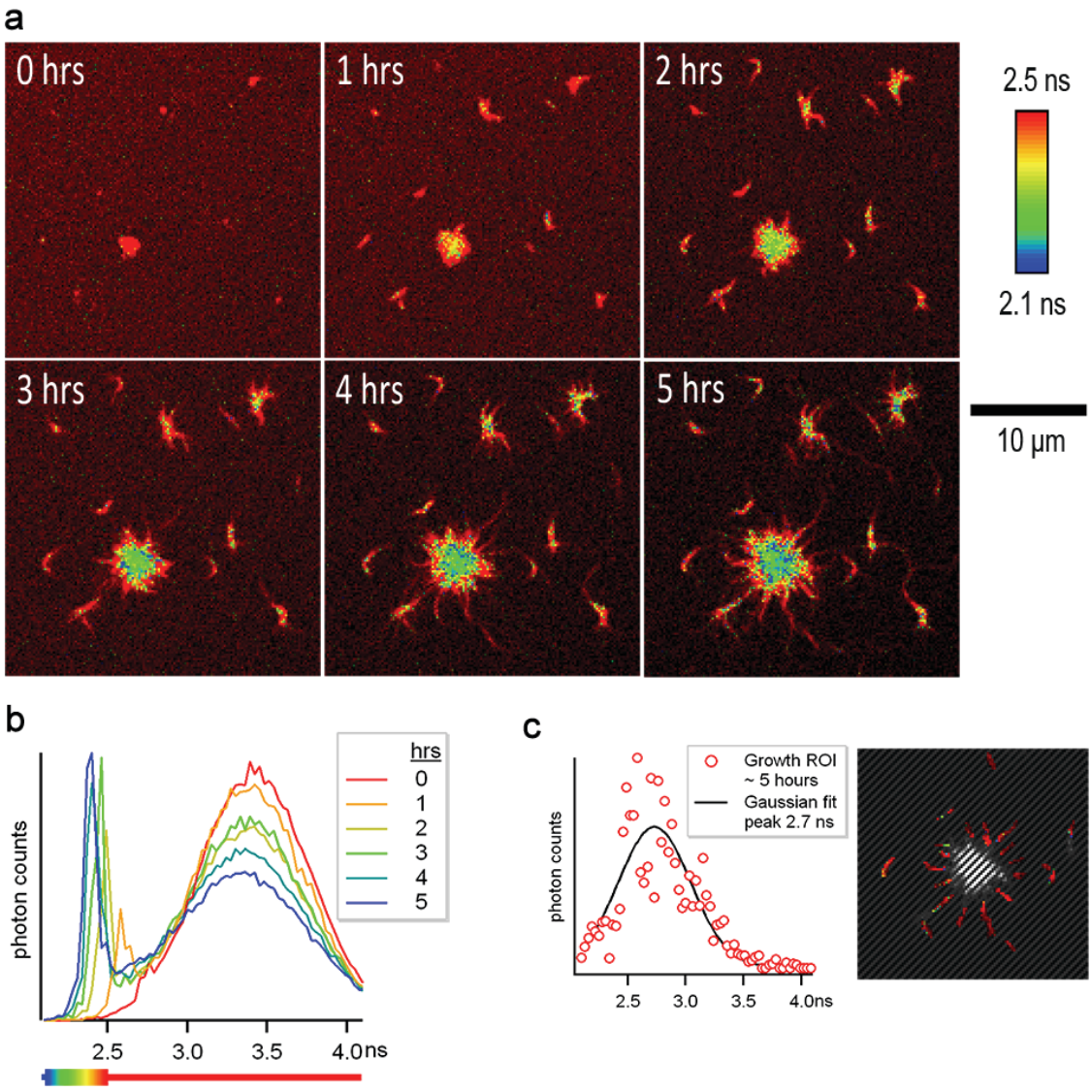

Figure 5–5 – FLIM analysis of assembly and propagation of aggregate phases at the glass surface. Small aggregates adhered to the surface of the glass observed over time (a) are seen to increase in size and serve as the epicenter of growing tubes. The increase in size is correlated with the amount of growth and a decrease in fluorescence lifetime. FLIM histograms of each time step (b) show a rise in the peak ~ 2 ns, and a decrease in the broad peak ~ 3.5 ns which originates from solution and randomly adhered monomers. Highlighted new tube growth ROI at 5 hours shows nascent growth lifetime of approximately 2.7 ns (c).

On surveying the full area of air-loaded samples, Rh17-22 deposits suspected to be evidence of previous AWIs have been observed in the locality of growing aggregates (Figure 5–6a). To gain additional perspective on these aggregate nuclei, slides were prepared using the air-loading process and AWIs were followed with an EMCCD camera. After applying solution to the slide, the fluorescence was uniform across the sample (Figure 5–6b, panel 1). After addition of the coverslip, AWIs formed at bubbles and deposits were most obvious along the air escape pathways which appear as streaks of fluorescence (Figure 5–6b, red arrow). During the AWI collapse, small aggregates are consistently observed in flowing solution (Figure 5–6b, yellow arrows).

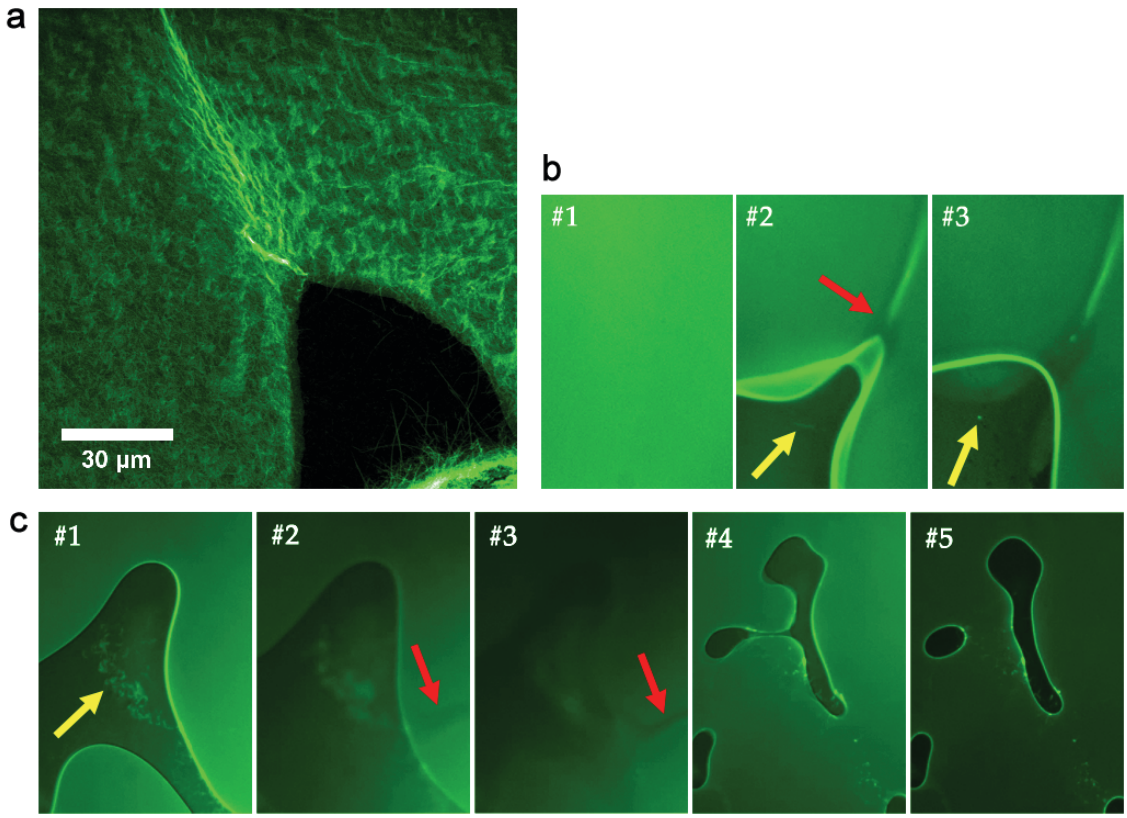

Figure 5–6 – Capturing the possible origins of nucleating phases. The localities of molten globule aggregates are repeatedly found near remnants of previous AWIs (a). Capturing the behavior of these compressed bubbles as they form (b) and change (c) reveals aggregates both at AWIs and on the glass surface. The initial air-loading (b, panel 1) and subsequent coverslip addition (b, panels 2 & 3) show the formation of tracks where escaping air movement deposits peptide on the glass surfaces (b, red arrow). Initial bubble collapses are frequently accompanied by aggregates flowing in solution (b, yellow arrows). Thin-film aggregates captured at glass interfaces in air regions appear mobile (c, yellow arrow; see supplemental video). Compression, post loading, forces air to escape (c, red arrows) displacing thin-film aggregates to newly formed AWIs and glass interfaces (c, panels 4 & 5).

In addition to AWIs, the glass surfaces are further locations of peptide interactions. Thin film interactions between the glass surface and the trapped air regions appear dynamic (see supplementary video). A slowly moving collection of fluorescent aggregates can be seen in the trapped air-region in Figure 5–6c, yellow arrow, that become attached at the periphery of trapped air-region seen in panels 4 & 5. Applying pressure to the upper coverslip, during Figure 5–6c panels 2 & 3, forces air to exit to the right hand side of the frame (Figure 5–6c, red arrows). The remaining air-region then settles (Figure 5–6c, panels 4 & 5), separating into multiple regions. During this process the thin-film region of aggregates has been displaced, sequestered by the AWIs, and deposited on the glass surface in solution. Taken together, these data suggest that nucleating phases originate from a combination of numerous interface interactions and changes in solubility.

5.3 Discussion

Numerous studies have implicated interfaces in amyloid nucleation [44-46, 49, 53-55]. These earliest phase transitions in amyloid assembly have been correlated with cellular toxicity [11, 56, 57], as on and off the nucleation pathway [4, 6-14], and certainly as short lived and hard to detect intermediates. Accordingly, we sought a simplified system to recreate, image, and characterize the nucleation of cross-β assemblies using interfaces. The nucleating core of the Aβ peptide of Alzheimer's disease, Aβ(16-22), provides a simple model peptide where the thermodynamic assemblies are structurally well defined [58]. Rhodamine-containing probes have also been developed as robust fluorescence reporters of assembly [24]. Here, using numerous interfaces, we have mapped the environmental responsiveness of Aβ(16-22) assembly, from monomer to paracrystalline nanotube.

Using peptide solutions below and above the CC we have utilized the role of interfaces to access multiple stages of nanotube growth, including suspected transient intermediate structures (Figure 5–3b,e&g; Figure 5–4c,d&e). The combination of aeration, together with the small reduction in solubility clearly leads to a large amount of nucleation above the CC, and many aggregates seen adhered to nanotube structures below the CC (Figure 5–4c). These aggregates are thought to be on-pathway, corroborated by the thick mesh of tube growth, and the absence of aggregates, seen in the 0.4 mM Aerated sample (Figure 5–4g). The constantly present HHI provides a small perturbation from the below CC monomer solution, seen as diffuse aggregates (Figure 5–4d), not seen in either the quiescent or vortexed conditions. Vortexing did appear to assist nucleation enough to transition the smaller aggregates of the quiescence sample into tube growth, another reason to suspect these aggregates are on-pathway. Taken together, we assign the order

of nucleation propensity for the protocol used, from low to high, as: Quiescent, Vortexed, HHI, and Aerated.

The accelerated growth shown in Figure 5–1 may be in part due to the large amounts of AWI present during the loading protocol. An additional factor that may play a significant role in directing the nucleation pathway is seen in the remnants of compression and exit tracks of trapped bubbles during loading. Real time capture of these AWIs forming during slide loading corroborates the association of the AWI with nucleation (Figure 5–6). Inspection of the numerous trapped air-regions during the air-loading protocol revealed that, in addition to peptide interactions at the AWI, mobile thin film aggregates are also present (see supplemental videos). These 'rafts' of peptide aggregates are analogous to the 2D diffusion characterized by Shen *et al.* [53], where weakly adhered peptide surface diffusion was seen as a critical precursor for nucleation, and are observed to transition from thin-film to AWIs during air-region displacement. We conjecture that thin-film and AWI aggregates contain the same nucleating phases observed within growing molten globules.

Dramatic changes in the AWI topology during rapid bubble collapse and escape trajectories seen during the sample loading protocol are likely occurring during solution aeration as bubbles form at the pipette tip and collapse at the surface. During formation, bubble 'pinch-off' at the pipette tip end can lead to dramatic topological fluctuations [59], micron-sized satellite bubbles [59], and rupturing of the trailing bubble edge as it leaves the pipette tip [60]. Conversely, at the end of the bubbles' lifespan, the small scale violent nature of bubble collapse at the bulk AWI surface can lead to sharp increases in local pressure and interface concentrations. In addition to the possible transfer to the bulk solution AWI *via* bubble flow, peptide-peptide interactions may be occurring at the

dynamic bubble AWI during bubble formation and collapse. These results are pertinent to almost all experimentalists that encounter AWIs when investigating hydrophobic, hydrophilic, amphiphilic or polar molecules. The further understanding of interfaces present during sample preparation and loading may provide insight into the broad range of subtlety differing results seen in amyloid research.

We begin to characterize the effects of the different introduced interfaces *via* comparison of fluorescence lifetimes with identifiable morphologies that are previously determined structures: nanotubes [58], and molten globules [24]. Assessing FLIM data throughout the different stages of the nucleation pathway, and inferring the mechanism of fluorescence quenching, we map out pathway stages in terms of fluorescence lifetime values. Figure 5–7 summarizes the above FLIM data with a proposed mapping between inferred structures and measured fluorescence lifetimes. Monomer solutions consistently exhibit a lifetime of 3.45 ns (Figure 5–7a), and as the peptide density increases with hydrophobic collapse (driven by any combination of concentration, time, interfaces, or solubility) we observe a decrease in the fluorescence lifetime value (Figure 5–7a-d). The reduced lifetime of observed diffuse aggregates containing punctate regions of higher density with shorter lifetime corroborate this collapse into nuclei (Figure 5–7c). This density-increase lifetime-decrease continues until a high-density, low-lifetime nucleating phase is formed (<2 ns; Figure 5–7d), which appears to be similar to the liquid-liquid phases reported previously [28]. The reduction in fluorescence lifetime during these initial hydrophobic collapse stages is presumed to result from de-solvation leading to increased random inter-molecule quenching. Recapturing nucleating aggregates at glass interfaces, we observe a concurrent decrease in fluorescence lifetime on the increase in aggregate size and eventual emergence of nascent nanotube growth (Figure 5–5). From this minima in lifetime value, the

formation of ordered cross-β structure marks the return to longer lifetime values (Figure 5–7d-f). Bundled aggregate morphologies (Figure 5–7e) are presumed to contain the nuclei required for tube growth. The increase in fluorescence lifetime is due to an increase in ordered peptide that returns the rhodamine reporter to a more solvated environment. The greatest amount of peptide order and rhodamine solvation terminates with nanotube structures having a lifetime of 3 ns (Figure 5–7f).

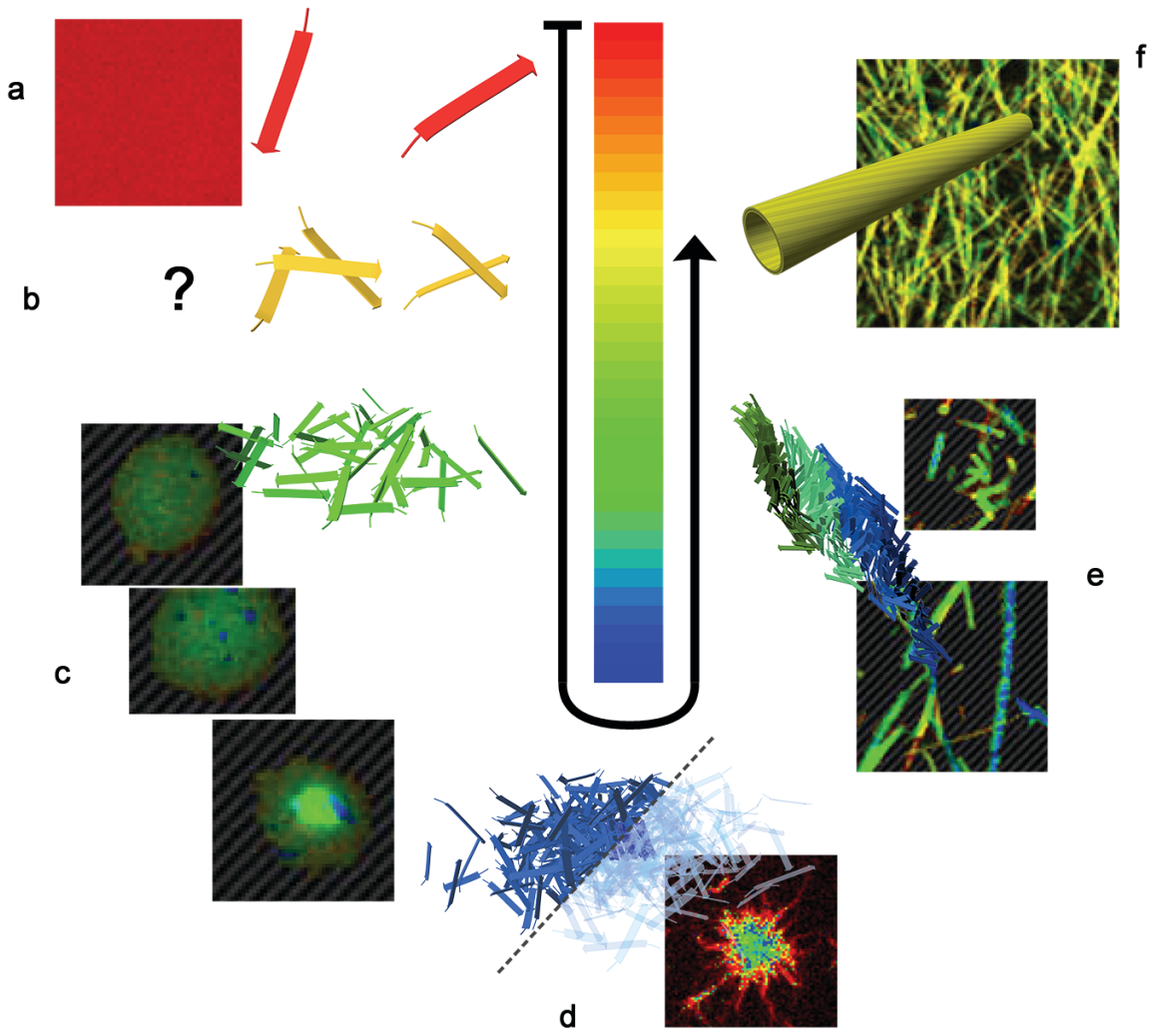

Figure 5–7 – Proposed mapping of nucleation pathway using fluorescence lifetime and morphology. Monomer solutions (a; red) hydrophobically collapse into dense solvent excluding aggregates that harbor conditions for nucleation (a-d). The initial

dimerization is not observable, but inferred (b; orange [down]). Diffuse aggregates begin to exclude solvent (c; green [down]) and show punctate blue regions. High density collapsed molten globules exhibit nucleation (d; blue [minima]). Right-hand side of dashed line shows transparent peptide to highlight nuclei formation within dense aggregate. Bundled nuclei (e; blue/green [up]) increase in order, slowly exposing Rh17-22 to the solvent. Nanotube thermodynamic minima (f; yellow [up]) marks the end point of peptide order and Rh17-22 solvation.

5.4 Conclusions

The data presented here verifiy the importance of interfaces in the nucleation of Aß(16-22) nanotubes. Using aeration, vortexing and hydrophobic plastic surfaces we have provided a snapshot of the Aß(16-22) nucleation pathway. Using FLIM analysis, we have begun the mapping of this pathway in terms of fluorescence lifetimes and peptide morphologies. The corresponding nucleation-lifetime-morphology mapping has been verified using time lapse FLIM data of nucleating aggregates. In addition, we have investigated some subtleties of sample loading protocols that lead to considerably accelerated nucleation. Taken together, these data highlight the importance of interfaces in nucleation, and the potential benefits of FLIM analysis for investigations of the dynamics of peptide aggregation.

5.5 Methods

5.5.1 Peptide Synthesis

Peptides were synthesized using an Applied Biosystems ABI431 FMOC solid phase synthesizer following standard protocols as outlined in the manuscript. Peptides were cleaved from the resin using trifluoroacetic acid/thioanisole/1,2-ethanedithiol/anisole (90:5:3 2, v/v/v/v), precipitated from the cleavage solution and washed repeatedly using excess cold (-20°C) diethyl ether. Purification was performed using reverse phase HPLC with acetonitrile/water gradients containing 0.1% TFA, and the collected samples were lyophilized to white powder and stored at 4°C. Molecular weights of all peptides were verified by MALDI-TOF mass spectrometry using a 2,5-dihydroxybenzoic acid matrix. Aß(17-22) N-terminal acylated with rhodamine 110 (Rh17-22) were synthesized using the same FMOC and coupling protocols.

5.5.2 Fluorescence Lifetime Sample Preparation

Small amounts of dry peptide (1-2 mg), weighed in the microfuge tube to an accuracy of ~50 μg, were disaggregated in hexafluoroisopropanol (HFIP). This solution was aliquoted into ~10 new microfuge tubes, and allowed to evaporate in a fume hood before re-entering storage at 4°C. On use, each aliquot was dissolved in Rh1722 in 40% acetonitrile (MeCN) 0.1% TFA solution to give the required total peptide concentration, followed by alternating sonication and vortexing to ensure complete dissolution. Concentrations of Rh17-22 solutions were verified by absorption using a molar extinction coefficient of 81000 $cm^{-1}M^{-1}$ at 498 nm.

5.5.3 Fluorescence Lifetime Imaging Microscopy

Two-photon excitation was provided by an ultrafast (~100 fs pulses at 80 MHz) Ti:Sa laser (Spectra Physics, Santa Clara, CA) tuned to 780 nm, from which the intensity was attenuated using a λ/2 plate and polarizing cube. The laser beam was scanned using an x-y pair of galvanometer mirrors (6215H, Cambridge Technology, Lexington, MA) before entering a 5× beam expanding telescopic optical setup that terminates on the rear aperture of an Olympus 60× water immersion objective lens (UPLSAPO60XW, Olympus, Melville, NY; NA = 1.2) mounted in an inverted microscope (IX71, Olympus, Melville, NY). Introduction into the optical path of the objective was achieved via reflection from a dichroic mirror (675 DCSX, Chroma Technology, Brattleboro, VT). The epifluorescent collected light passes the dichroic mirror and a low pass filter before impinging on a PMT detector (H7422P-40, Hamamatsu Corporation, Bridgewater, NJ). Detector signals are sent to a TCSPC module (PicoHarp300, PicoQuant GmbH, Germany) and analyzed using SymPhoTime software.

Each image acquisition consisted of 10 frames at 256×256 pixels with dimensions 50×50 μm and a pixel dwell time of 0.5 ms. The excitation power at the sample was 2 mW, and the images were acquired approximately 2 μm below the glass surface. Reported fluorescence lifetime values were achieved using PicoQuant's 'fastFLIM', which measures the barycenter of the exponential decay, and as such are approximate values with a variance ~0.1 ns. Gray 45° striped areas in FLIM images (Figure 5–4) indicate regions not included in FLIM histograms to emphasize morphologies over background solution.

5.5.4In Situ Sample Loading Video

Samples were loaded onto a 22 × 50 mm #1.5 coverslip in custom holder and enclosed with a 22 × 30 mm coverslip. Excitation was provided using an X-Cite 120 (Lumen Dynamics, Canada), using a standard eGFP filter set. Collected movie frames were recorded using an iXon EMCCD camera (Andor, CT) at 30 frames per second.

5.6 References

1. Selkoe, D.J., *Preventing Alzheimer's Disease*. Science, 2012. **337**(6101): p. 1488-92.
2. Eisenberg, D. and M. Jucker, *The Amyloid State of Proteins in Human Diseases*. Cell, 2012. **148**(6): p. 1188-203.
3. Benilova, I., E. Karran, and B. De Strooper, *The Toxic Aß Oligomer and Alzheimer's Disease: An Emperor in Need of Clothes*. Nature Neuroscience, 2012. **15**(3): p. 349-357.
4. Walsh, D.M. and D.J. Selkoe, *A Beta Oligomers - a Decade of Discovery*. Journal of Neurochemistry, 2007. **101**(5): p. 1172-1184.
5. Chiti, F. and C.M. Dobson, *Protein Misfolding, Functional Amyloid, and Human Disease*, in *Annual Review of Biochemistry*. 2006. p. 333-366.
6. Stefani, M., *Structural Features and Cytotoxicity of Amyloid Oligomers: Implications in Alzheimer's Disease and Other Diseases with Amyloid Deposits*. Progress in Neurobiology, 2012. **99**(3): p. 226-245.
7. Gosal, W.S., et al., *Competing Pathways Determine Fibril Morphology in the Self-Assembly of Beta2-Microglobulin into Amyloid*. J Mol Biol, 2005. **351**(4): p. 850-64.
8. Smith, A.M., et al., *Direct Observation of Oligomeric Species Formed in the Early Stages of Amyloid Fibril Formation Using Electrospray Ionisation Mass Spectrometry*. Journal of Molecular Biology, 2006. **364**(1): p. 9-19.
9. Kodali, R. and R. Wetzel, *Polymorphism in the Intermediates and Products of Amyloid Assembly*. Current Opinion in Structural Biology, 2007. **17**(1): p. 48-57.
10. Necula, M., et al., *Small Molecule Inhibitors of Aggregation Indicate That Amyloid Beta Oligomerization and Fibrillization Pathways Are Independent and Distinct*. Journal of Biological Chemistry, 2007. **282**(14): p. 10311-10324.
11. Larson, M.E. and S.E. Lesne, *Soluble Aß Oligomer Production and Toxicity*. Journal of Neurochemistry, 2012. **120**: p. 125-139.

12. Caughey, B. and P.T. Lansbury, *Protofibrils, Pores, Fibrils, and Neurodegeneration: Separating the Responsible Protein Aggregates from the Innocent Bystanders*. Annual Review of Neuroscience, 2003. **26**: p. 267-298.

13. Laganowsky, A., et al., *Atomic View of a Toxic Amyloid Small Oligomer*. Science, 2012. **335**(6073): p. 1228-1231.

14. Kirkitadze, M.D., G. Bitan, and D.B. Teplow, *Paradigm Shifts in Alzheimer's Disease and Other Neurodegenerative Disorders: The Emerging Role of Oligomeric Assemblies*. Journal of Neuroscience Research, 2002. **69**(5): p. 567-577.

15. Li, I.T.S. and G.C. Walker, *Signature of Hydrophobic Hydration in a Single Polymer*. Proceedings of the National Academy of Sciences, 2011. **108**(40): p. 16527-16532.

16. Tanizaki, S., et al., *Conformational Sampling of Peptides in Cellular Environments*. Biophysical Journal, 2008. **94**(3): p. 747-759.

17. Fernández, A., *Intramolecular Modulation of Electric Fields in Folding Proteins*. Physics Letters A, 2002. **299**(2–3): p. 217-220.

18. Daidone, I., et al., *Dehydration-Driven Solvent Exposure of Hydrophobic Surfaces as a Driving Force in Peptide Folding*. Proc Natl Acad Sci U S A, 2007. **104**(39): p. 15230-5.

19. Berne, B.J., J.D. Weeks, and R. Zhou, *Dewetting and Hydrophobic Interaction in Physical and Biological Systems*. Annu Rev Phys Chem, 2009. **60**: p. 85-103.

20. Krone, M.G., et al., *Role of Water in Mediating the Assembly of Alzheimer Amyloid-β Aβ16-22 Protofilaments*. Journal of the American Chemical Society, 2008. **130**(33): p. 11066-72.

21. Cheon, M., et al., *Structural Reorganisation and Potential Toxicity of Oligomeric Species Formed During the Assembly of Amyloid Fibrils*. Plos Computational Biology, 2007. **3**(9): p. e173.

22. Hwang, W., et al., *Kinetic Control of Dimer Structure Formation in Amyloid Fibrillogenesis*. Proceedings of the National Academy of Sciences of the United States of America, 2004. **101**(35): p. 12916-12921.

23. Brovchenko, I., et al., *Thermal Expansivity of Amyloid ß(16-22) Peptides and Their Aggregates in Water*. Physical chemistry chemical physics : PCCP, 2009. **11**(25): p. 5035-40.

24. Liang, Y., D.G. Lynn, and K.M. Berland, *Direct Observation of Nucleation and Growth in Amyloid Self-Assembly*. J. Am. Chem. Soc., 2010. **132**(18): p. 6306-6308.

25. Plakoutsi, G., et al., *Evidence for a Mechanism of Amyloid Formation Involving Molecular Reorganisation within Native-Like Precursor Aggregates*. Journal of Molecular Biology, 2005. **351**(4): p. 910-922.

26. Carulla, N., et al., *Experimental Characterization of Disordered and Ordered Aggregates Populated During the Process of Amyloid Fibril Formation*. Proceedings of the National Academy of Sciences, 2009. **106**(19): p. 7828-7833.

27. Bader, R., et al., *Probing the Mechanism of Amyloidogenesis through a Tandem Repeat of the Pi3-Sh3 Domain Suggests a Generic Model for Protein Aggregation and Fibril Formation*. Journal of Molecular Biology, 2006. **356**(1): p. 189-208.

28. Childers, W.S., et al., *Phase Networks of Cross-Beta Peptide Assemblies*. Langmuir, 2012. **28**(15): p. 6386-6395.

29. Morris, A.M., M.A. Watzky, and R.G. Finke, *Protein Aggregation Kinetics, Mechanism, and Curve-Fitting: A Review of the Literature*. Biochim. Biophys. Acta, 2009. **1794**(3): p. 375-97.

30. Cohen, S.I.A., et al., *From Macroscopic Measurements to Microscopic Mechanisms of Protein Aggregation*. Journal of Molecular Biology, 2012. **421**(2-3): p. 160-171.

31. Jiang, D., et al., *A Kinetic Model for Beta-Amyloid Adsorption at the Air/Solution Interface and Its Implication to the Beta-Amyloid Aggregation Process*. Journal of Physical Chemistry B, 2009. **113**(10): p. 3160-3168.

32. Jean, L., Chiu F. Lee, and David J. Vaux, *Enrichment of Amyloidogenesis at an Air-Water Interface*. Biophysical Journal, 2012. **102**(5): p. 1154-1162.

33. Chi, E.Y., et al., *Amyloid-ß Fibrillogenesis Seeded by Interface-Induced Peptide Misfolding and Self-Assembly*. Biophysical Journal, 2010. **98**(10): p. 2299-2308.

34. Szilvay, G.R., et al., *Self-Assembled Hydrophobin Protein Films at the Air−Water Interface: Structural Analysis and Molecular Engineering†*. Biochemistry, 2007. **46**(9): p. 2345-2354.

35. Fowler, D.M., et al., *Functional Amyloid - from Bacteria to Humans*. Trends Biochem. Sci., 2007. **32**(5): p. 217-24.

36. Macindoe, I., et al., *Self-Assembly of Functional, Amphipathic Amyloid Monolayers by the Fungal Hydrophobin Eas*. Proceedings of the National Academy of Sciences, 2012. **109**(14): p. E804-E811.

37. Sani, M.A., J.D. Gehman, and F. Separovic, *Lipid Matrix Plays a Role in Abeta Fibril Kinetics and Morphology*. Febs Letters, 2011. **585**(5): p. 749-754.

38. Qiang, W., W.-M. Yau, and R. Tycko, *Structural Evolution of Iowa Mutant B-Amyloid Fibrils from Polymorphic to Homogeneous States under Repeated Seeded Growth*. Journal of the American Chemical Society, 2011. **133**(11): p. 4018-4029.

39. Alexandrescu, A.T., et al., *Heterogeneous Amylin Fibril Growth Mechanisms Imaged by Total Internal Reflection Fluorescence Microscopy*. Biochemistry, 2011. **50**(14): p. 2808-2819.

40. Bokvist, M. and G. Grobner, *Misfolding of Amyloidogenic Proteins at Membrane Surfaces: The Impact of Macromolecular Crowding*. Journal of the American Chemical Society, 2007. **129**(48): p. 14848-+.

41. Gorbenko, G.P., *Fluorescence Spectroscopy of Protein Oligomerization in Membranes*. Journal of Fluorescence, 2011. **21**(3): p. 945-951.

42. Schladitz, C., et al., *Amyloid-Beta-Sheet Formation at the Air-Water Interface*. Biophysical Journal, 1999. **77**(6): p. 3305-3310.

43. Hoernke, M., et al., *Triggers for Beta-Sheet Formation at the Hydrophobic-Hydrophilic Interface: High Concentration, in-Plane Orientational Order, and Metal Ion Complexation*. Langmuir, 2011. **27**(23): p. 14218-14231.

44. Sharp, J.S., J.A. Forrest, and R.A.L. Jones, *Surface Denaturation and Amyloid Fibril Formation of Insulin at Model Lipid–Water Interfaces*. Biochemistry, 2002. **41**(52): p. 15810-15819.

45. Lopes, D.H.J., et al., *Mechanism of Islet Amyloid Polypeptide Fibrillation at Lipid Interfaces Studied by Infrared Reflection Absorption Spectroscopy*. Biophysical Journal, 2007. **93**(9): p. 3132-3141.

46. Lee, C.F., et al., *Combined Effects of Agitation, Macromolecular Crowding, and Interfaces on Amyloidogenesis*. Journal of Biological Chemistry, 2012. **287**(45).

47. Munishkina, L. and A. Fink, *Fluorescence as a Method to Reveal Structures and Membrane-Interactions of Amyloidogenic Proteins*. Biochimica et Biophysica Acta (BBA) - Biomembranes, 2007. **1768**(8): p. 1862-1885.

48. LeVine, H., 3rd, *Thioflavine T Interaction with Synthetic Alzheimer's Disease Beta-Amyloid Peptides: Detection of Amyloid Aggregation in Solution*. Protein Sci., 1993. **2**(3): p. 404-10.

49. Morinaga, A., et al., *Critical Role of Interfaces and Agitation on the Nucleation of Aβ Amyloid Fibrils at Low Concentrations of Aβ Monomers*. Biochimica et Biophysica Acta (BBA) - Proteins & Proteomics, 2010. **1804**(4): p. 986-995.

50. Ban, T., et al., *Real-Time and Single Fibril Observation of the Formation of Amyloid Beta Spherulitic Structures*. Journal of Biological Chemistry, 2006. **281**(44): p. 33677-33683.

51. Yagi, H., et al., *Visualization and Classification of Amyloid β Supramolecular Assemblies*. Biochemistry, 2007. **46**(51): p. 15009-15017.

52. Ramachandran, G. and J.B. Udgaonkar, *Evidence for the Existence of a Secondary Pathway for Fibril Growth During the Aggregation of Tau*. Journal of Molecular Biology, 2012. **421**(2-3): p. 296-314.

53. Shen, L., et al., *A Mobile Precursor Determines Amyloid-B Peptide Fibril Formation at Interfaces*. Journal of the American Chemical Society, 2012. **134**(34): p. 14172-14178.

54. Nichols, M.R., et al., *Amyloid-B Aggregates Formed at Polar-Nonpolar Interfaces Differ from Amyloid-B Protofibrils Produced in Aqueous Buffers*. Microscopy Research and Technique, 2005. **67**(3-4): p. 164-174.

55. Brezesinski, G., E. Maltseva, and H. Möhwald, *Adsorption of Amyloid B (1-40) Peptide at Liquid Interfaces*. Zeitschrift für Physikalische Chemie, 2007. **221**(1): p. 95-111.

56. Ferreira, S.T., M.N.N. Vieira, and F.G. De Felice, *Soluble Protein Oligomers as Emerging Toxins in Alzheimer's and Other Amyloid Diseases*. Iubmb Life, 2007. **59**(4-5): p. 332-345.

57. Sahoo, B., et al., *On the Stability of the Soluble Amyloid Aggregates*. Biophysical Journal, 2009. **97**(5): p. 1454-1460.

58. Mehta, A.K., et al., *Facial Symmetry in Protein Self-Assembly*. J. Am. Chem. Soc., 2008. **130**(30): p. 9829-9835.

59. Thoroddsen, S.T., T.G. Etoh, and K. Takehara, *Experiments on Bubble Pinch-Off*. Physics of Fluids, 2007. **19**(4).

60. Burton, J.C., R. Waldrep, and P. Taborek, *Scaling and Instabilities in Bubble Pinch-Off*. Physical Review Letters, 2005. **94**(18).

Chapter 6

Possible Pathways to the Molten Globule

Neil R. Anthony*, Anil K. Mehta†, David G. Lynn†, and Keith M. Berland*

*Department of Physics, Emory University, Atlanta, GA

†Center for Fundamental and Applied Molecular Evolution, NSF/NASA Center for Chemical Evolution, Departments of Chemistry and Biology, Emory University, Atlanta, GA

6.1 Introduction

The ubiquitous cross-β structure associated with protein misfolding diseases is thought to be independent of amino acid sequence [1-4], even hypothesized to evolutionarily precede functional single amino acid sequence proteins [5, 6]. The crucial stages of cross-β formation occur within hydrophobically collapsed molten globules [2, 7-10] that harbor desolvated environments allowing increased inter- and/or intra-molecular interactions required for structural formation. The initially explored conformations within dense peptide phases are suspected to determine subsequent assembly pathways and morphology [11-16], and as such are of vital interest for understanding and controlling the subtleties of peptide folding and aggregation.

The exact pathways that lead to nucleation within these unordered phases, and the resulting morphologies and structures determined by these pathways are of keen interest in both amyloidogenic pathology and biomaterials engineering. In disease etiology, understanding the turning points accessible during the nucleation pathway, and the diversity of available pathways, are under investigation with the aim of delineating cellular toxicity from bio-functional amyloid structures [17-20]. Currently, soluble oligomers are suspected as key factors in toxicity, yet their origin and downstream affects are topics of intense research [21-27]. In biomaterials engineering, the final structural and morphological product is paramount, and as such, the control and understanding of key stages are important for nanomaterials development [28-31].

Interfaces such as air-water-interfaces (AWIs), hydrophobic-hydrophilic interfaces (HHIs), and lipid bilayers, exhibit local heterogeneous environments important for nucleation [32-39] (Chapter 5). The amphiphilic nature common to amyloidogenic

peptides leads to a propensity for alignment at interfaces [34, 40, 41]. In addition to amyloid's affinity for heterogeneous interfaces, providing increased local concentrations and stabilization, the addition of exogenous factors such as nucleobases and metal ions have also been identified as factors in nucleating polymorphic and toxic species [34, 42-45]. Conversely, these factors have also been shown to inhibit amyloid formation, highlighting the subtleties of their role in amyloid nucleation [44].

Using the nucleating core of amyloid-β, Aß(16-22), as a model system (see [10] and references therein), we have previously observed nucleation and growth from within dense, unstructured, molten globules [9]; an observation made possible by co-assembling with rhodamine labeled monomer, Rh17-22. Rh17-22 is created by replacing Lys-16 of Aß(16-22) with a similarly charged R110 dye molecule, and can be successfully incorporated (<1%) without significantly affecting the final morphology and cross-β structure [9]. The covalently attached R110 used as a fluorescence reporter can also be considered an exogenous factor that potentially affects nucleation pathways, in addition to affecting the surface physiochemical nature of the final nanotube structure. Previous work demonstrating energy transfer between a similarly incorporated Rh16-22 label and non-specifically bound Alexa molecules along the surfaces of cross-β nanotubes serves as a prime example of a functionalized bionanomaterial [46]. The Aß(16-22):Rh17-22 cross-β structures provides a convenient overlapping model system between co-factors in cross-β nucleation and functionalized bionanomaterials. In certain cases, in which the Rh17-22 label incorporation is increased (>1%), heterogeneities can be seen along individual structures [47] (Chapter 7), highlighting the importance of this exogenous factor.

Previous observations of molten globules, both adhered to glass surfaces and in solution, have been reported to produce dramatic nanotube growth [9], although the exact origin of the nucleus is still under investigation. Repetitions of this experiment reveal that nucleation from molten aggregates is not ubiquitous across that sample; i.e. only a certain number of aggregates observed at the glass surfaces were seen to nucleate nanotube structures. We hypothesize that a combination of surface impurities and the increased hydrophobicity of Rh17-22 play a role in the accelerated nucleation seen in molten globules. The work presented in the previous chapter (Chapter 5) demonstrates a correlation between interfaces and the proliferation from molten aggregates, and as such, we extend our studies to include investigation of the glass interfaces present. In addition to glass surfaces, the interactions of the planar R110 molecule in Rh17-22 have not been thoroughly investigated, and their perturbation to the system during the crucial nucleation stages is unknown.

Here we investigate the interactions of low concentration R110 and Rh17-22 solutions with glass surfaces over time to understand the role of Rh17-22 in formation of molten globule aggregates and subsequent nucleation of cross-β structure. We show that both the R110 and Rh17-22 initially collapse into small aggregates at impurities on the glass surface. Rh17-22 aggregates however, develop heterogeneous morphologies and increasing amounts of ordered structures determined by second harmonic generation (SHG). Fluorescence lifetime phasor analysis indicates a two-phase peptide system analogous to liquid-liquid-phase-separations, previously shown to be critical for transitions to the more ordered cross-β peptide phases [10] (Chapter 4). We also highlight the propensity for Aß(16-22):Rh17-22 nucleation at the surface of unstructured R110 aggregates compared to structured Rh17-22 aggregates.

6.2 Results

To investigate the role Rh17-22 in the formation of dense peptide aggregates observed at glass surfaces we follow low concentration (~2μm) Rh17-22 40% MeCN pH 2 solutions over time. During the first 8 hours after loading a mostly homogeneous fluorescence is observed at the glass surface (Figure 6–1; 0-8 hrs). Between 8 and 19 hours dense aggregates are seen on the surface of the coverslip and the microscope slide. In addition, observed solution Rh17-22 signal decreases as surface aggregate signals increase. Aggregates are observed on both surfaces, but from here onwards we focus on the coverslip glass due to a lesser background of nonspecifically bound molecules compared to the microscope slide glass. The glass surfaces are used 'as is', with only the superficial cleaning from the suppliers, and as such, we assume that small imperfections/impurities on the glass surfaces serve as nucleation points for the hydrophobic peptide collapse. We observe the same aggregate formation using solutions of R110 (Figure 6–2b), suggesting that the hydrophobic xanthene ring structure of the R110 molecule plays a role in the Rh17-22 collapse.

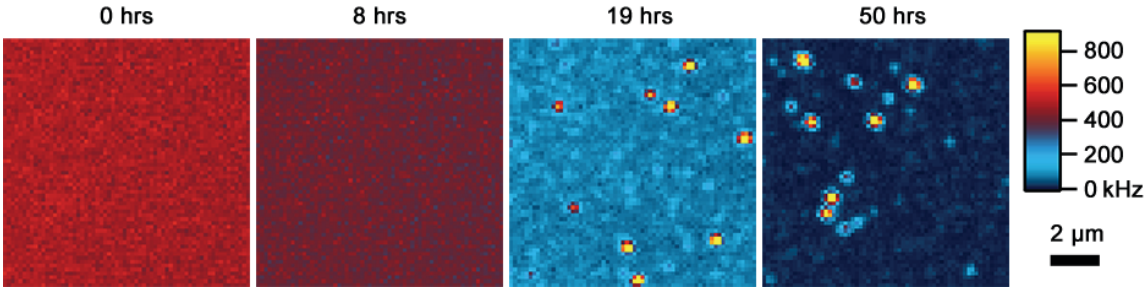

Figure 6–1 – Fluorescence intensity time lapse of 2μM Rh17-22 at the surface of a microscope coverslip. All time points are scaled to the same intensity threshold as indicated by the intensity scale.

Analyzing these aggregates using fluorescence lifetime imaging (FLIM) allows for comparison of the local environment of the rhodamine dyes within these hydrophobically collapsed molten globules. Rh17-22 and R110 molecules in solution exhibit average fluorescence lifetimes of approximately 3.5 and 3.3 ns respectively (Figure 6–2c; dashed lines). The increase in fluorescence lifetime on covalently attaching R110 to Aß(17-22) is likely a result of the stabilization and restrained motion of the xanthene and phenyl ring structures relative to each other [48]. Both R110 and Rh17-22 form dense aggregates at the glass surface when imaged after approximately 48 hours (Figure 6–2a&b). The fluorescent lifetime of R110 within the dense aggregates is quenched to approximately 2.8 ns (Figure 6–2d & e, red line). R110 randomly adhered to the glass surface is quenched from the 3.3 ns monomer lifetime down to 3.2 ns. The reduction in fluorescence lifetime for aggregate and adhered R110 are as expected, whereby aggregates are more quenched than surface adhered molecules. In stark contrast, Rh17-22 aggregates are dramatically quenched to average fluorescence lifetimes as short as 0.4 ns (Figure 6–2c & e, blue line). In addition to short lifetime aggregates, Rh17-22 within smaller aggregates seen as red spots in the FLIM analysis (Figure 6–2c), and Rh17-22 adhered to the glass surface, comprise the broad FLIM histogram peak at approximately 3.1 ns (Figure 6–2e). Aggregates of intermediate size are also present, exhibiting an average lifetime reduced to approximately 1.3 ns, seen as green spots. Time lapse (data not shown) of surface aggregates reveals static structures over time periods up to ~hrs, and we assume that 2D surface diffusion does not play a major role [49].

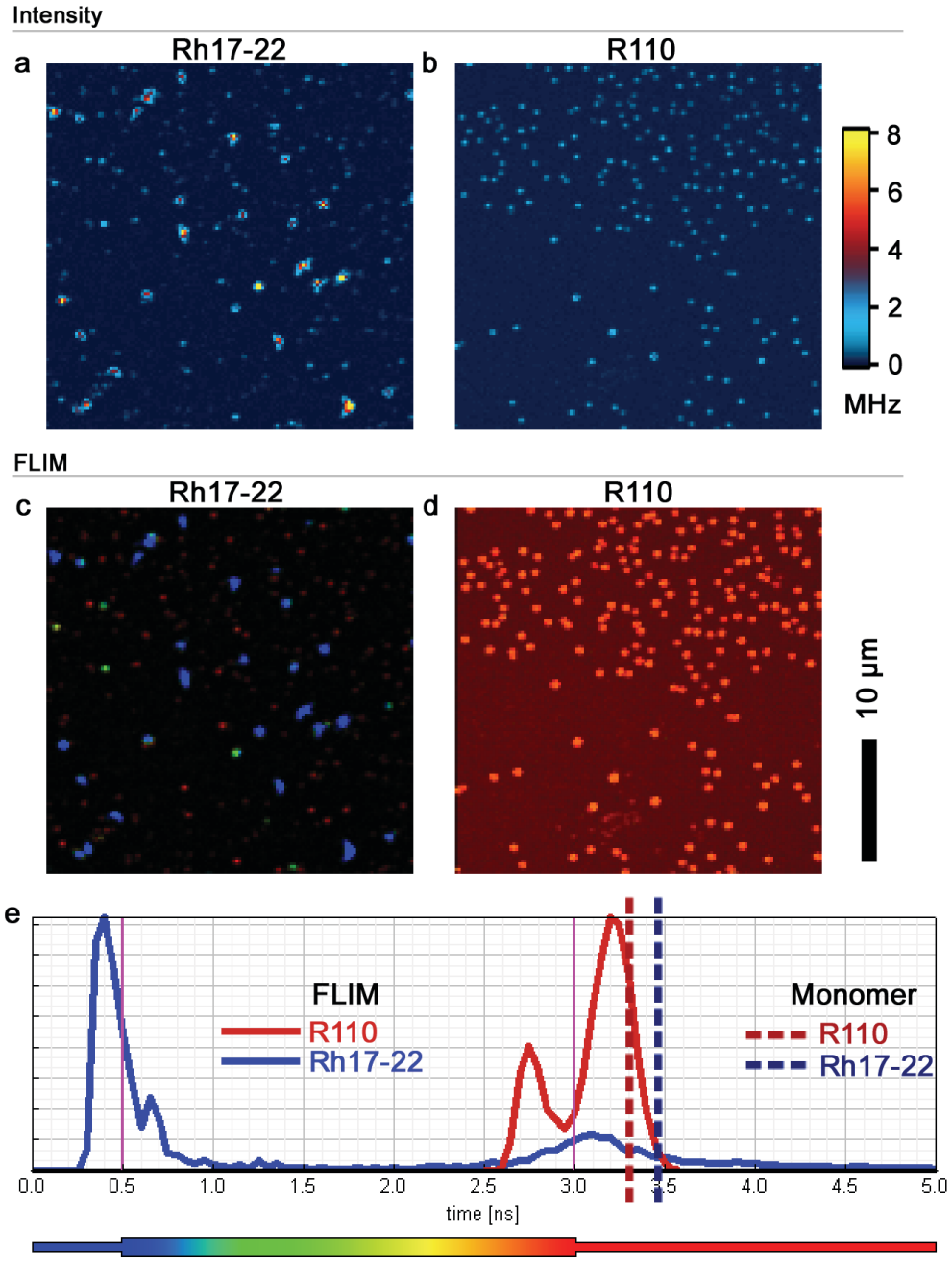

Figure 6–2 – Fluorescence intensity and average fluorescence lifetime images of hydrophobically collapsed rhodamine dye formed at glass surfaces. 2µM Rh17-22 (a & c) and R110 (b & d) form similar sized aggregate surface aggregates during ~ 24hrs. Average fluorescence lifetime color scale indicated horizontally below the corresponding FLIM histograms (c). Monomer solution fluorescence lifetime indicated by dashed lines.

The short fluorescence lifetimes indicate for Rh17-22 aggregates are less than the width of the instrument response function (IRF) of the detector, and as such, it is difficult to distinguish between very short lifetimes and instantaneous non-linear processes such as second harmonic generation (SHG) signals. Generating a second harmonic signal requires a noncentrosymmetric molecular packing, leading to an asymmetric electronic response when excited by the intense electric field produced at the focus of a high NA objective lens using two-photon excitation [50, 51]. The chiral nature of peptide backbones produces a small but finite amount of second harmonic signal, although far too weak to be distinguished from background noise. If sufficient quantities of chiral molecules are arranged such that the relative phase of the second harmonic signal is constructive (phase matched) then the SHG signal is discernable.

We find that a fraction of the signal observed in Figure 6–2 is due to SHG. Using an excitation wavelength of 890 nm provided an optimal SHG signal, identifiable as a peak at $\lambda_{ex}/2 = 445$ nm. Figure 6–3e shows an example spectrum that includes both the SHG second harmonic and Rh17-22 fluorescence emission. Using a band pass filter (represented by two blue lines) to collect only the SHG signal we are able to compare fluorescence + SHG images (Figure 6–3a&b) with SHG only images (Figure 6–3c&d). It is instantly apparent that Rh17-22 surface aggregates contain significant amounts of SHG compared to R110 aggregates. A very small amount of signal is present in the band pass filtered R110 image, consistent with the very small amounts of filter bleed through; SHG at 445 nm was not seen in emission spectra from R110 aggregates (data not shown). The shape and size of Rh17-22 aggregates present in both rows is consistent between images, with SHG originating more so from the larger aggregates. Given the almost

symmetric nature of R110's structure, SHG signals must originate from inter-molecular Rh17-22 packing.

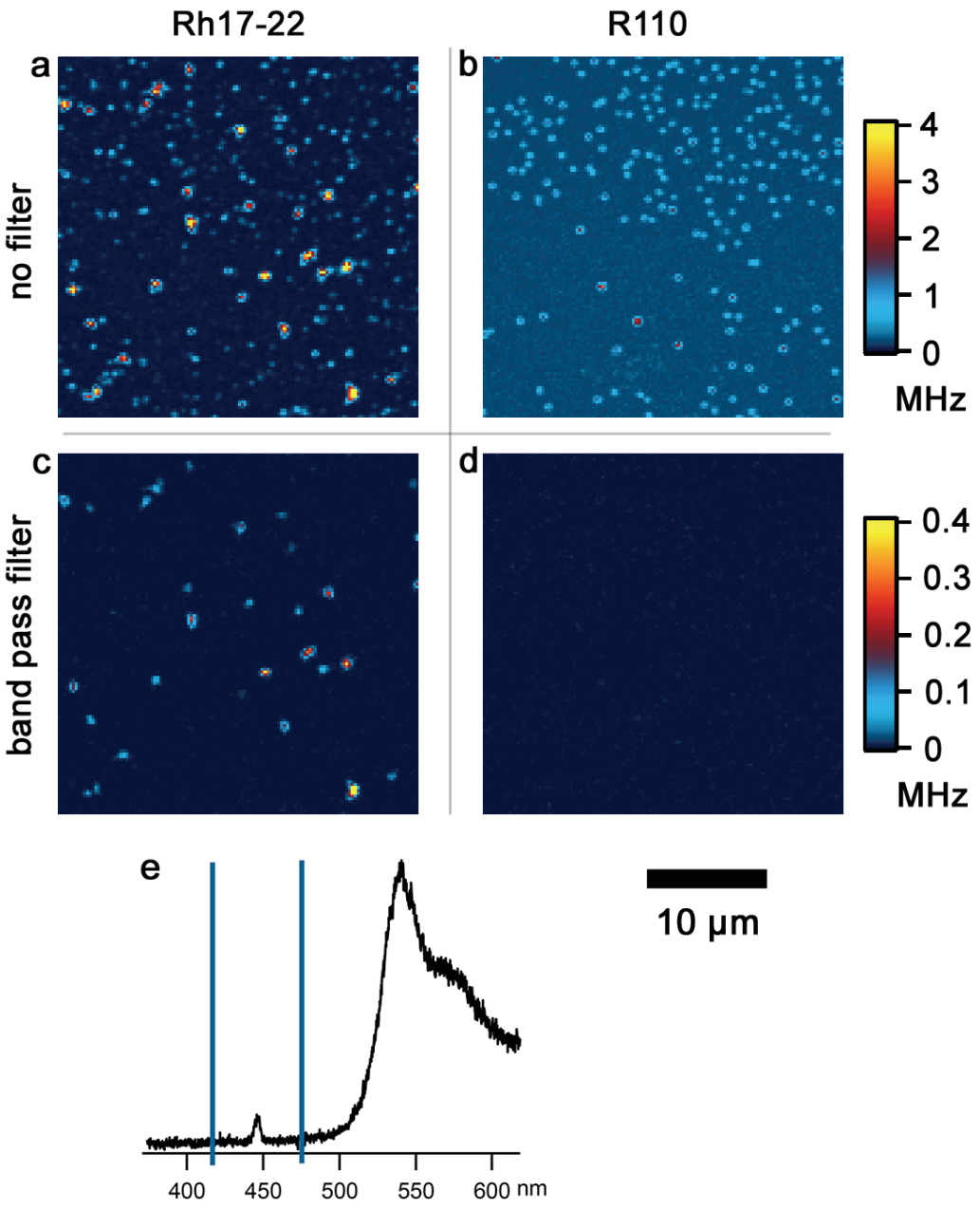

Figure 6–3 – Second harmonic generation (SHG) signals observed from within rhodamine aggregates. Comparison of the combined fluorescence + SHG signal (a & b), and the SHG signal only (c & d). SHG signals are isolated using a band pass filter (e;

blue lines) to collect only the second harmonic peak at 445 nm corresponding to half the 890 nm excitation wavelength. Spectra beyond ~500 nm emitted from R110 of Rh17-22.

The quenched fluorescence lifetime and SHG signal of the Rh17-22 surface aggregates was interpreted using phasor analysis (Figure 6–4), which can quickly identify fluorescence lifetime components and quenching processes without fitting decay data [52, 53]. Moreover, phasor analysis can be performed without *a priori* knowledge of the number of decay components in each FLIM image pixel. In a phasor plot representation of FLIM data, a single exponential species would correspond to a single point on the "universal circle" (the additional semi-circle traced across the 2D-histogram; Figure 6–4b) [52, 53]. FLIM pixels containing multiple exponential decay values lead to phasor plot points that are vector sums of the single exponential phasors [52, 53]. For example, a FLIM pixel containing two single exponential species corresponds to a phasor point on the chord connecting two points of the universal circle, at a distance between the two points that represents the relative amount of each species.

We performed phasor analysis on a denser region of surface aggregates, providing an increased signal from aggregates in the analysis. The average fluorescence lifetimes of these more densely packed aggregates exhibit the same distribution as shown in Figure 6–2c, although the larger aggregates appear to exhibit a change in lifetime at their periphery, seen as a green edge on the blue aggregates (Figure 6–4a). Some aggregates appear 'two-tone', comprised of different lifetime sections (bottom right and bottom left), corroborating the heterogeneous nature of the aggregation processes. Phasor analysis (Figure 6–4b) indicates that the majority of the FLIM image signal is from a single exponential (on the semi-circle) equivalent to a fluorescence lifetime of approximately 3.1 ns (seen in the small aggregates and surface background of Figure 6–

2c). In addition, the phasor plot contains a 'tail' along a chord that connects the 3.1 ns single lifetime signal to another point on the semi-circle close to a value of zero. The finite width of the detector instrument response function (IRF) used in these FLIM measurements results in a zero lifetime intensity signal appearing as a single exponential with a short but finite value on the phasor plot universal circle. Given the ~1 ns wide IRF used, it is difficult to discern the origin of the very short fluorescent lifetimes in the FLIM image. When taken together with the phasor plot it strongly suggests that these short lifetime signals originate from the non-linear SHG process attainable with two-photon excitation. Highlighting which regions of the phasor plot correspond which locations in the FLIM image reveals that the single exponential 3.1 ns signal is indeed located at the small aggregates and the weakly adhered surface peptide (Figure 6–2b&c; red ROI/overlay). Highlighting the locations of the 'tail' seen in the phasor plot (Figure 6–2b&c; Green ROI/overlay), comprised of linear mixtures of 3.1 ns and ~0 ns components, verifies that reduced lifetimes stem from dense surface aggregates.

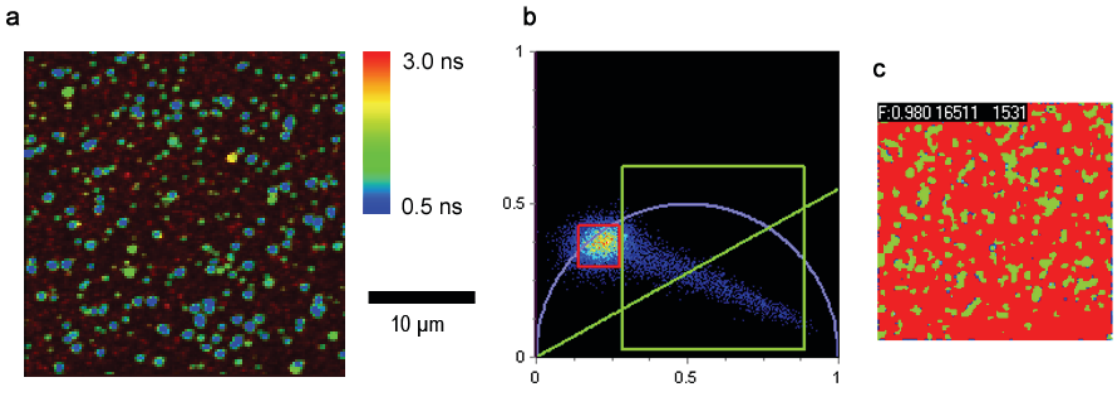

Figure 6–4 – Phasor analysis of fluorescence and SHG signal originating from Rh17-22 aggregates. Decay data from a FLIM image showing a dense region of highly quenched Rh17-22 aggregates (a) is used to produce the phasor plot (b). A large fraction of the signal originates from a single exponential species located approximately 3.1 ns (red ROI

and highlight (c)). A 'tail' of signal is seen connecting the chord between 3.1 ns and ~0 ns (green ROI and highlight (c)).

In addition to aggregate spot morphologies, a small number of random elongated fluorescent structures were observed at times starting between 48 and 72 hours. These particular elongated morphologies have not been seen previously, across a wide range of R110, Rh17-22 , and Aß(16-22):Rh17-22 samples, and are not thought to be sample impurities. We assume that ordered Rh17-22 molecules within certain molten globule aggregates have nucleated a conformation that allows propagation along the glass surface. We see in Figure 6–5c that a linear chain of surface aggregates appears to be connected, reminiscent of the transitioning stages of nucleating phases observed previously [10] (Figure 4–5). Elongated morphologies were not found to exhibit SHG signals.

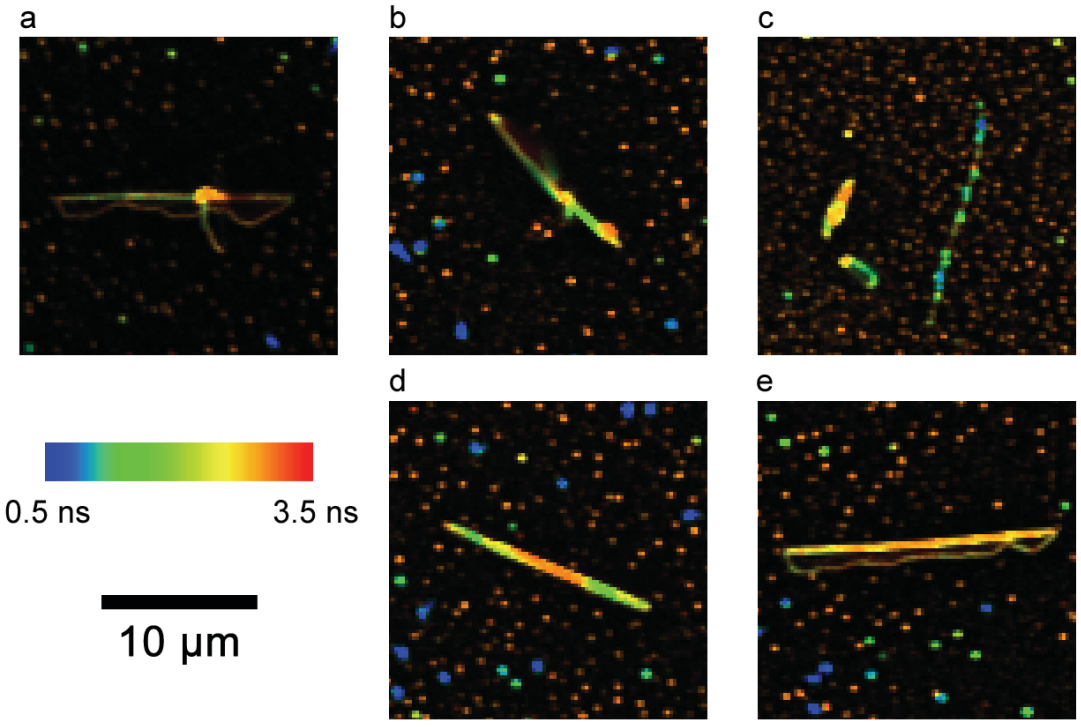

Figure 6–5 – Varied elongated structural morphologies also present at glass surfaces at times > 2 days. A remarkable combination of rigid and meandering structures are present (a & e). Some cases show what may be the initial steps of a coalescing of smaller aggregates (c; RHS vertical chain).

As a preliminary test to ascertain the nucleating propensity of rhodamine induced surface spots, we replaced the solution surrounding the surface aggregates with a 0.5 mM Aß(16-22), 1 µM Rh17-22 mixture; concentrations sufficiently high concentration to nucleate growth in solution after approximately 1 week. Opening the edges of sealed samples allowed the new solution to be introduced *via* capillary action and subsequently resealed. Revisiting the sample after ~20 hrs allows us to compare the ability of rhodamine and Rh1722 aggregate spots to seed new nanotube/fiber growth. Somewhat unintuitively, R110 spots appear nucleate nanotube growth across the majority of the

sample. Given the increased amounts of order within the Rh17-22 aggregate spots, one would assume a higher propensity to nucleate new growth. After approximately 3 days, both R110 and Rh17-22 nucleate a large amount of growth (data not shown) suggesting that the Rh17-22 spots initially hinder the growth, which eventually rearranges to allow for nucleation. The average fluorescence lifetime of both aggregate types after loading additional peptide are seen to be ~2 ns, while the elongated growth from R110 aggregates exhibits an average lifetime of ~3 ns.

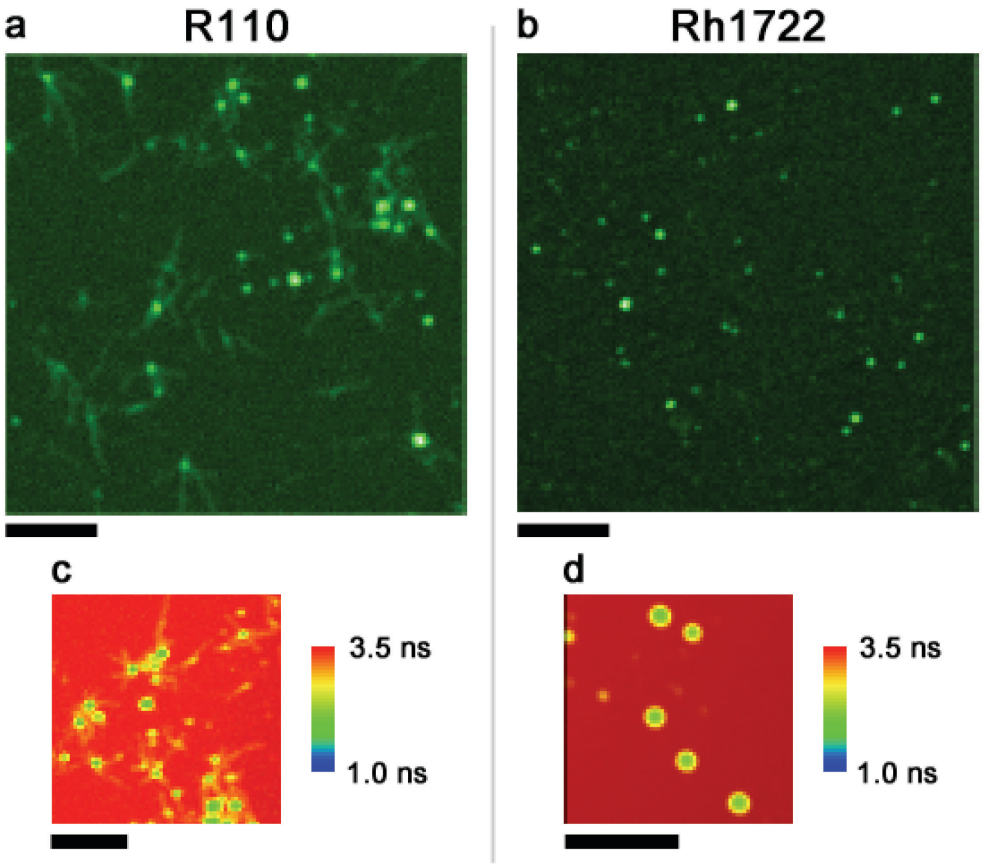

Figure 6–6 –Surface spots as a nucleation seeds for 0.5 mM Aß(16-22): 1 µM Rh17-22 mixtures. R110 spots (left) and Rh17-22 spots (right) after exposure to Aß(16-22):Rh17-22 solution for approximately 1 day. Fluorescence intensity (a & b)

reveals that R110 spots harbor conditions for more accelerated growth. FLIM analysis (c & d) shows of growth from R110 spots with an average lifetime of approximately 2.9 ns, with both R110 and Rh17-22 aggregate spots displaying a lifetime of around 2.2 ns. All scale bars 5 μm.

6.3 Discussion

The hypothesis that hydrophobically collapsed molten globule aggregates lead to phase transitions from disordered to ordered β-sheet structures has been previously investigated *via* simulations [2, 7, 8]. Experimental observations and analyses, however, are just beginning to be elucidated [9, 10]. Current experimental techniques do not have the capability to dynamically resolve the molecular interactions present during the critical phase transitions of cross-β formation. Here we have combined fluorescence and non-linear optical techniques to bolster the resolvable information available from hydrophobically collapsed Rh17-22 and R110 molecules. FLIM data report on the local environment (~nm) of the rhodamine dye, and SHG signals indicate numerous repetitions of nm scale molecular packing.

The much reduced lifetime seen in Rh17-22 aggregates is comprised of two distinct species. Phasor analysis indicates that one species within the aggregates is a quenched fluorescence, reduced from 3.4 ns to 3.1 ns, the same as that seen in smaller aggregates and surface adhered molecules. The second species is a very short lifetime that hard to separate from an instantaneous 'lifetime' originating from SHG. As the detector IRF is ~1 ns, it becomes very hard to distinguish fluorescence lifetimes <1 ns when convoluted with the IRF. Emission spectra of aggregates confirms the presence of SHG, indicated by the peak at $\lambda_{ex}/2$, and spectrally filtered image acquisition corroborate that the majority of larger aggregates produce SHG. Phasor plot analysis shows a distribution of points lying on the chord between 3.1 ns and ~0 ns. The location of each point on the connecting chord represents the ratio of signal originating from each species. These data indicate that each FLIM pixel within the dense aggregates contains a varying amount of

the two distinct peptide phases, analogous to liquid-liquid phase separation reported previously (Chapter 4) [10].

At sufficiently high concentration (~ mM) Rh17-22 solutions have been previous seen to form fiber morphologies viewed using electron microscopy. As we are considering bulk solution concentration three orders of magnitude lower we might not expect to see fiber formation, yet with the dramatic increase in concentration achieved transitioning from 3D to 2D and the large amounts of locally condensed peptide within these partially structured molten globules, it is likely that concentrations are high enough to nucleate β-sheet structures. While the underlying structure of the somewhat bizarre elongated morphologies shown in Figure 6–5 remains to be determined, we suspect that ordered phases observed within Rh17-22 aggregates may nucleate the correct seeds required for elongation and growth.

When Aß(16-22) co-assembles with ~1% Rh17-22 it forms out-of-register anti-parallel nanotubes at pH2 with a symmetric β-sheet lamination [54]. Given that Aß(16-22) fibers adopt in-register antiparallel β-sheet structure as at pH7 with asymmetric lamination [54], we conjecture that ordered phases within Rh17-22 aggregates have also adopted the in-register asymmetric configuration, incongruous to seeding nanotube growth. Conversely, the disordered R110 aggregates provide a heterogeneous and hydrophobic interface congruous for nucleating anti-parallel symmetric nanotube growth.

6.4 Conclusions

Here we have demonstrated the ability to capture molten globules displaying varying stages of aggregation at glass surfaces for subsequent analysis. We show that over time

Rh17-22 forms a two-phase peptide system within dense hydrophobically collapsed molten globule aggregates. The propensity for nucleation within these phases is corroborated by numerous cases of elongated growth. Conversely, the propensity for nanotube nucleation at the periphery of Rh17-22 aggregates is hindered compared to the unstructured R110 aggregates. We have shown that FLIM and phasor analyses together with non-linear SHG microscopy provide unique insights into this model amyloidogenic system. The combined control and analyses shown has potential as a test bed for nucleation seed experiments.

6.5 Methods

6.5.1 Peptide Synthesis and Sample Preparation

Rh17-22 were synthesized as outlined by Applied Biosystems using a FMOC solid phase ABI431 synthesizer. Completed peptides were cleaved from the resin using TFA/thioanisole/ethanedithiol/anisole (90/5/3/2), and precipitated from cleavage solution, and washed repeatedly with ice-cold diethyl ether. Purification was performed using reverse phase HPLC with acetonitrile/water gradients containing 0.1% TFA, and the collected samples were lyophilized for storage. Peptide molecular weights were verified using MALDI mass spectrometry.

Dry Rh17-22 peptide (1-2 mg) were disaggregated using hexafluoroisopropanol (HFIP) and allowed to evaporate in a fume hood before re-entering storage at 4°C. On use, each aliquot was dissolved in 40% acetonitrile (MeCN) 0.1% TFA solution to give a total peptide concentration of 2 μM, Concentrations of both rhodamine solutions were verified by absorption using a molar extinction coefficient of 81000 $cm^{-1}M^{-1}$ at 498 nm. Approximately 15 μL was loaded between a microscope slide and coverslip, and sealed with clear nail polish.

6.5.2 Laser Scanning Microscopy

The home built laser scanning microscope setup is described in detail elsewhere [chapter ref][ref]. Briefly, 780 nm 80 MHz excitation was provided by a Ti:Sa laser (Spectra Physics, Santa Clara, CA). An Olympus 60× water immersion objective lens (UPLSAPO60XW, Olympus, Melville, NY; NA = 1.2) was mounted in an inverted

microscope (IX71, Olympus, Melville, NY), a dichroic mirror (675 DCSX, Chroma Technology, Brattleboro, VT), and collection using a PMT detector (H7421-40, Hamamatsu Corporation, Bridgewater, NJ). Power for LSM images was set to 2 mW at the objective focus. LSM control and image formation was performed using in-house Visμm software.

6.5.3Fluorescence Lifetime Imaging Microscopy

Re-directed photon collection at a current output PMT detector (H7421-40, Hamamatsu Corporation, Bridgewater, NJ) signals were sent to a TCSPC module (PicoHarp300, PicoQuant GmbH, Germany) and analyzed using SymPhoTime software. Image acquisition was continuously acquired until sufficient photon statistics were available (>1000 photons per pixel) for the regions of interest. Average fluorescence lifetime values were reported by PicoQuant's 'fastFLIM'.

6.5.4Phasor Analysis

Pre-histogrammed images exported from SymPhoTime were imported into SimFCS2.0 (LFD, Enrico Gratton) for analysis. The phasor absolute was calibrated using exports from images of rhodamine 6G and a fluorescence lifetime of 4.1 ns. Phasor plots were not smoothed using the Enrico- (E-) button before selecting ROIs.

6.5.5Emission Spectra

Image points were selected using on axis points using Visμm. Light was re-directed to a spectrometer (SpectraPro-150, Acton Research) connected to a CCD camera (Roper Scientific, NTE/CCD-1340/400-EMB) using a multi-mode fiber optic cable.

6.5.6SHG Measurements

Laser excitation of 890 nm produced the intense electric fields required for SHG, collected as above using LSM with the inclusion of a band pass filter (D455/60, Chroma), with power at the sample set to 6 mW.

6.6 References

1. Wetzel, R., S. Shivaprasad, and A.D. Williams, *Plasticity of Amyloid Fibrils*. Biochemistry, 2007. **46**(1): p. 1-10.
2. Auer, S., et al., *A Generic Mechanism of Emergence of Amyloid Protofilaments from Disordered Oligomeric Aggregates*. Plos Computational Biology, 2008. **4**(11): p. e1000222.
3. Dobson, C.M., *Protein Misfolding, Evolution and Disease*. Trends in Biochemical Sciences, 1999. **24**(9): p. 329-332.
4. Pedersen, J.S. and D.E. Otzen, *Amyloid—a State in Many Guises: Survival of the Fittest Fibril Fold*. Protein Science, 2008. **17**(1): p. 2-10.
5. Greenwald, J. and R. Riek, *On the Possible Amyloid Origin of Protein Folds*. Journal of Molecular Biology, 2012. **421**(4-5): p. 417-426.
6. Childers, W.S., et al., *Peptide Membranes in Chemical Evolution*. Curr. Opin. Chem. Biol., 2009. **13**(5-6): p. 652-9.
7. Krone, M.G., et al., *Role of Water in Mediating the Assembly of Alzheimer Amyloid-β Aβ16-22 Protofilaments*. Journal of the American Chemical Society, 2008. **130**(33): p. 11066-72.
8. Klimov, D.K. and D. Thirumalai, *Dissecting the Assembly of Aβ(16-22) Amyloid Peptides into Antiparallel β Sheets*. Structure, 2003. **11**(3): p. 295-307.
9. Liang, Y., D.G. Lynn, and K.M. Berland, *Direct Observation of Nucleation and Growth in Amyloid Self-Assembly*. J. Am. Chem. Soc., 2010. **132**(18): p. 6306-6308.
10. Childers, W.S., et al., *Phase Networks of Cross-Beta Peptide Assemblies*. Langmuir, 2012. **28**(15): p. 6386-6395.
11. Nichols, M., et al., *Rapid Assembly of Amyloid-B Peptide at a Liquid/Liquid Interface Produces Unstable B-Sheet Fibers†*. Biochemistry, 2005. **44**(1): p. 165-173.

12. Kodali, R. and R. Wetzel, *Polymorphism in the Intermediates and Products of Amyloid Assembly*. Current Opinion in Structural Biology, 2007. **17**(1): p. 48-57.

13. Pryor, N.E., M.A. Moss, and C.N. Hestekin, *Unraveling the Early Events of Amyloid-ß Protein (Aß) Aggregation: Techniques for the Determination of Aß Aggregate Size*. International Journal of Molecular Sciences, 2012. **13**(3): p. 3038-3072.

14. Goldsbury, C., et al., *Multiple Assembly Pathways Underlie Amyloid-ß Fibril Polymorphisms*. Journal of Molecular Biology, 2005. **352**(2): p. 282-298.

15. Petkova, A.T., et al., *Self-Propagating, Molecular-Level Polymorphism in Alzheimer's ß-Amyloid Fibrils*. Science, 2005. **307**(5707): p. 262-5.

16. Miller, Y., B. Ma, and R. Nussinov, *Polymorphism in Alzheimer Aß Amyloid Organization Reflects Conformational Selection in a Rugged Energy Landscape*. Chem. Rev., 2010. **110**(8): p. 4820-38.

17. Ramachandran, G. and J.B. Udgaonkar, *Evidence for the Existence of a Secondary Pathway for Fibril Growth During the Aggregation of Tau*. Journal of Molecular Biology, 2012. **421**(2-3): p. 296-314.

18. Ma, B. and R. Nussinov, *Selective Molecular Recognition in Amyloid Growth and Transmission and Cross-Species Barriers*. Journal of Molecular Biology, 2012. **421**(2-3): p. 172-184.

19. van Grondelle, W., et al., *Spontaneous Fibrillation of the Native Neuropeptide Hormone Somatostatin-14*. J Struct Biol, 2007. **160**(2): p. 211-23.

20. Fowler, D.M., et al., *Functional Amyloid - from Bacteria to Humans*. Trends Biochem. Sci., 2007. **32**(5): p. 217-24.

21. Colletier, J.-P., et al., *Molecular Basis for Amyloid-B Polymorphism*. Proceedings of the National Academy of Sciences, 2011. **108**(41): p. 16938-16943.

22. Lambert, M.P., et al., *Diffusible, Nonfibrillar Ligands Derived from a Beta(1-42) Are Potent Central Nervous System Neurotoxins*. Proceedings of the National Academy of Sciences of the United States of America, 1998. **95**(11): p. 6448-6453.

23. Benilova, I., E. Karran, and B. De Strooper, *The Toxic Aß Oligomer and Alzheimer's Disease: An Emperor in Need of Clothes*. Nature Neuroscience, 2012. **15**(3): p. 349-357.

24. Larson, M.E. and S.E. Lesne, *Soluble Aβ Oligomer Production and Toxicity*. Journal of Neurochemistry, 2012. **120**: p. 125-139.

25. Pimplikar, S.W., *Reassessing the Amyloid Cascade Hypothesis of Alzheimer's Disease*. International Journal of Biochemistry & Cell Biology, 2009. **41**(6): p. 1261-1268.

26. Kirkitadze, M.D., G. Bitan, and D.B. Teplow, *Paradigm Shifts in Alzheimer's Disease and Other Neurodegenerative Disorders: The Emerging Role of Oligomeric Assemblies*. Journal of Neuroscience Research, 2002. **69**(5): p. 567-577.

27. Caughey, B. and P.T. Lansbury, *Protofibrils, Pores, Fibrils, and Neurodegeneration: Separating the Responsible Protein Aggregates from the Innocent Bystanders*. Annual Review of Neuroscience, 2003. **26**: p. 267-298.

28. Huang, R., et al., *Solvent and Surface Controlled Self-Assembly of Diphenylalanine Peptide: From Microtubes to Nanofibers*. Soft Matter, 2011. **7**(14): p. 6418-6421.

29. Gao, X.Y. and H. Matsui, *Peptide-Based Nanotubes and Their Applications in Bionanotechnology*. Advanced Materials, 2005. **17**(17): p. 2037-2050.

30. Cui, H.G., M.J. Webber, and S.I. Stupp, *Self-Assembly of Peptide Amphiphiles: From Molecules to Nanostructures to Biomaterials*. Biopolymers, 2010. **94**(1): p. 1-18.

31. He, L., A.F. Dexter, and A.P.J. Middelberg, *Biomolecular Engineering at Interfaces*. Chemical Engineering Science, 2006. **61**(3): p. 989-1003.

32. Chi, E.Y., et al., *Amyloid-β Fibrillogenesis Seeded by Interface-Induced Peptide Misfolding and Self-Assembly*. Biophysical Journal, 2010. **98**(10): p. 2299-2308.

33. Schladitz, C., et al., *Amyloid-Beta-Sheet Formation at the Air-Water Interface*. Biophysical Journal, 1999. **77**(6): p. 3305-3310.

34. Hoernke, M., et al., *Triggers for Beta-Sheet Formation at the Hydrophobic-Hydrophilic Interface: High Concentration, in-Plane Orientational Order, and Metal Ion Complexation*. Langmuir, 2011. **27**(23): p. 14218-14231.

35. Sharp, J.S., J.A. Forrest, and R.A.L. Jones, *Surface Denaturation and Amyloid Fibril Formation of Insulin at Model Lipid–Water Interfaces*. Biochemistry, 2002. **41**(52): p. 15810-15819.

36. Lopes, D.H.J., et al., *Mechanism of Islet Amyloid Polypeptide Fibrillation at Lipid Interfaces Studied by Infrared Reflection Absorption Spectroscopy*. Biophysical Journal, 2007. **93**(9): p. 3132-3141.

37. Jiang, D., et al., *A Kinetic Model for Beta-Amyloid Adsorption at the Air/Solution Interface and Its Implication to the Beta-Amyloid Aggregation Process*. Journal of Physical Chemistry B, 2009. **113**(10): p. 3160-3168.

38. Lee, C.F., et al., *Combined Effects of Agitation, Macromolecular Crowding, and Interfaces on Amyloidogenesis*. Journal of Biological Chemistry, 2012. **287**(45).

39. Jean, L., et al., *Competing Discrete Interfacial Effects Are Critical for Amyloidogenesis*. Faseb Journal, 2010. **24**(1): p. 309-317.

40. Engin, O. and M. Sayar, *Adsorption, Folding, and Packing of an Amphiphilic Peptide at the Air/Water Interface*. The Journal of Physical Chemistry B, 2012. **116**(7): p. 2198-2207.

41. Jean, L., Chiu F. Lee, and David J. Vaux, *Enrichment of Amyloidogenesis at an Air-Water Interface*. Biophysical Journal, 2012. **102**(5): p. 1154-1162.

42. Liu, P., et al., *Nucleobase-Directed Amyloid Nanotube Assembly*. Journal of the American Chemical Society, 2008. **130**(50): p. 16867-16869.

43. Dong, J., et al., *Modulating Amyloid Self-Assembly and Fibril Morphology with Zn(Ii)*. Journal of the American Chemical Society, 2006. **128**(11): p. 3540-3542.

44. Faller, P., *Copper and Zinc Binding to Amyloid-Beta: Coordination, Dynamics, Aggregation, Reactivity and Metal-Ion Transfer*. Chembiochem, 2009. **10**(18): p. 2837-2845.

45. Adlard, P.A. and A.I. Bush, *Metals and Alzheimer's Disease*. Journal of Alzheimers Disease, 2006. **10**(2-3): p. 145-163.

46. Liang, Y., et al., *Light Harvesting Antenna on an Amyloid Scaffold*. Chem. Commun., 2008(48): p. 6522-6524.

47. Anthony, N.R., et al. *Structural Heterogeneities of Self-Assembled Peptide Nanomaterials*. in *SPIE Photonics West*. 2012. San Francisco, CA: SPIE.

48. Vogel, M., et al., *Structural Relaxation of Rhodamine Dyes with Different N-Substitution Patterns - a Study of Fluorescence Decay Times and Quantum Yields*. Chemical Physics Letters, 1988. **147**(5): p. 452-460.

49. Shen, L., et al., *A Mobile Precursor Determines Amyloid-B Peptide Fibril Formation at Interfaces*. Journal of the American Chemical Society, 2012. **134**(34): p. 14172-14178.

50. Corn, R. and D. Higgins, *Optical Second Harmonic Generation as a Probe of Surface Chemistry*. Chemical Reviews, 1994. **94**(1): p. 107-125.

51. Campagnola, P.J., et al., *High-Resolution Nonlinear Optical Imaging of Live Cells by Second Harmonic Generation*. Biophysical Journal, 1999. **77**(6): p. 3341-3349.

52. Colyer, R.A., C. Lee, and E. Gratton, *A Novel Fluorescence Lifetime Imaging System That Optimizes Photon Efficiency*. Microscopy Research and Technique, 2008. **71**(3): p. 201-213.

53. Redford, G.I. and R.M. Clegg, *Polar Plot Representation for Frequency-Domain Analysis of Fluorescence Lifetimes*. Journal of Fluorescence, 2005. **15**(5): p. 805-815.

54. Mehta, A.K., et al., *Facial Symmetry in Protein Self-Assembly*. J. Am. Chem. Soc., 2008. **130**(30): p. 9829-9835.

Chapter 7

Structural Heterogeneities of Self-Assembled Peptide Nanomaterials

Neil R. Anthony*, Anthony J. Bisignano†, Anil K. Mehta†, David G. Lynn†, and Keith M. Berland*

* Department of Physics, Emory University, Atlanta, GA 30322

† Departments of Chemistry and Biology and the Center for Chemical Evolution, Emory University, Atlanta, GA 30322

This chapter was published in:

Anthony NR, Bisignano AJ, Mehta AK, Lynn DG, Berland KM. Structural heterogeneities of self-assembled peptide nanomaterials. SPIE Proceedings Vol. 8226, Multiphoton Microscopy in the Biomedical Sciences XII.

7.1 Abstract

We use Fluorescence Lifetime Imaging Microscopy (FLIM) and Second Harmonic Imaging Microscopy (SHIM) to investigate the fundamental molecular mechanisms responsible for nucleation and growth of amyloidogenic-derived nanomaterials. The nanomaterials are assembled from of Amyloid-ß(16-22), specifically Ac-KLVFFAE-NH2, the nucleating core of the Alzheimer's Amyloid-ß protein. We describe how FLIM and SHIM can be used to follow different nucleation pathways and to quantify structural heterogeneities within these complex nanomaterials. New evidence suggests that different structures emerge from distinct nucleation pathways and these insights inform our understanding of the peptide self-assembly mechanisms. We discuss these insights in the context of a top down understanding of amyloidogenic diseases, the bottom up control of functional nanomaterials and the discovery of real-time structural indicators for nanofabrication strategies.

Keywords

Nanomaterials, Self-Assembly, Amyloid-ß, Diphenylalanine, TCPSC, FLIM, SHIM.

7.2 Introduction

The cross-ß protein structure associated with neurodegenerative diseases is thought to nucleate within oligomers formed during intermolecular association [1-3], yet the exact mechanisms that determine the self-assembly pathways remain elusive. The specific interactions involved in nucleating and propagating cross-ß structures are important for the understanding the progression, and designing possible therapies, for amyloidogenic diseases. Moreover, understanding these molecular processes will also allow for further rational design of self-assembling amyloid-inspired peptides that have been used to create unique organic nanomaterials [4-6].

The central hydrophobic core of Amyloid-ß, Aß(16-22) (KLVFFAE), is one of the shortest cross ß-sheet forming sequences and serves as an excellent model system for investigating self-assembly, including numerous stages of peptide interactions and functionality, both experimentally [7-15] and *in silico* [16-21]. Simple peptide sequences of this kind, which self-assemble into complex supramolecular structures, play functional roles ranging from chemical evolution [22, 23] to functionalized nanomaterials that act as light harvesting antenna [6].

Aß(16-22) assembles into several known distinct morphologies, the most notable being fibers and nanotubes. At neutral pH, Aß(16-22) forms twisted 5 nm wide fibers [9, 11, 24] comprised of antiparallel in-register ß-sheets and appear morphologically indistinguishable from those seen in studies of the full Aß(1-40) peptide [25-27]. Conversely, acidic conditions lead to a shift in registry such that the structure is dominated by the interactions of the Phe dyad (F19F20) [11], and subsequently assembles into nanotubes approximately 50 nm in diameter [7, 12]. As a continuation to

simpler peptide interactions, this Phe dyad, when studied independently, forms crystalline supramolecular structures that have been studied extensively by Gazit *et al.* [28-32]. The resulting structures and morphologies formed by these simple motifs are reasonably well established, yet the assembly dynamics and pathway to these structures are only beginning to be elucidated.

Increasingly, the final assembled amyloidogenic structures have been found to be dependent on the assembly solution and available interfaces. For example, different protic ionic liquids (pILs) can control the rate of fibrillization of Aß(16-22), ranging from dramatically accelerating to completely arresting growth [33]. In addition, Aß(16-22) nanotubes disassemble and reassemble into fibers upon changing solution pH [7, 11], and Phe-Phe crystalline nanotubes form into peptide quantum dots upon changing solution from H2O to MeOH [34]. Furthermore, the degree of solvation can also affect morphology. Krysmann et al. show a distinct difference between cyro-TEM and TEM data sets due to conformational changes during drying [35]. Surfaces and interfaces also play a key role in both the initial nucleation events and final assembled structures. For example, solution interfaces such as with air or mica, have been shown to decrease pre-nucleation lag time [36-38], and introduce distinct populations with distinct properties [38, 39]. Polymorphisms have been observed in multiple studies [40-44] and predicted in simulation [45-47]. Pathways associated with differing morphologies have been suggested as better suited as therapeutic targets for amyloidogenic disease [48].

The dynamics of fibril growth have been visualized utilizing non-specifically bound thioflavin-t (ThT) fluorescence [49, 50] and atomic force microscopy (AFM) [37, 51-53]. In addition, atomic level structure has been monitored with nuclear magnetic resonance (NMR) [27, 54, 55] and infrared spectroscopy [15, 56, 57]. All these approaches use

different preparations that involve a variety of surfaces during assembly. Thus, given the effects of interfaces on nucleation, which can lead to changes in structure and morphology, it is very possible that independent dynamic and structural measurements are investigating subtly different peptide assemblies. Bulk spectroscopic measurements such as NMR and FTIR record the dominant, or average, structure in a given sample, and spatially resolved measurements such as ThT fluorescence and AFM report only on morphology. Previously, rhodamine-110 labeled Aß(17-22) (Rh17-22) has been mixed with Aß(16 22) to provide fluorescence contrast for real time visualization of nucleation and growth processes [58]. Here, we employ fluorescence lifetime imaging microscopy (FLIM) to simultaneously investigate spatially resolved dynamics, and structural information inferred from the fluorescence properties of the incorporated rhodamine reporter. Consequently, this labeled system provides a stage for us to test the effects of incorporating exogenous factors within nanotube structures for functionalization purposes. In this article we report on heterogeneities observed along individual labeled nanotubes, as well as our initial investigation into the structural causes of these differences.

Observed heterogeneities in our FLIM data suggest that long-range order can be propagated by local changes that 'nucleate' different stable structures. To further illustrate the effects of local structural changes on long-range order, we demonstrate that extremely small admixtures of Aß(16-22) can dramatically alter the resulting morphology of crystalline Phe-Phe structures. A working knowledge of local structural changes and potential long-range order nucleation points in para-crystalline peptide materials may play a role in understanding the complicated pathways available to toxic amyloidogenic aggregates. In addition, our observations suggest that controlling

incorporation rates and distributions of exogenous species for label incorporation and/or functionalization will be essential for further peptide nanostructure designs.

7.3 Results and Discussion

7.3.1 Aß(16-22) Polymorphism

Above a critical nucleation concentration (CNC), mixtures of Aß(16-22):Rh17-22 in low pH 40% AcCN solutions readily self-assemble into homogeneously fluorescent nanotubes (Figure 7–1a) [58]. We have empirically determined the CNC for this system to be approximately 0.35 μM. Over a wide range of Aß(16-22):Rh17-22 ratios and maturation times, nanotubes quiescently self-assembled above the CNC (supra-CNC) display a homogeneous fluorescent lifetime of approximately 3.1 ns (Figure 7–1b; 1e, blue line), and we refer to them as standard nanotubes. It has been discovered that a subset of aged nanotubes possess heterogeneities in their fluorescent lifetime along individual tubes, generally seen as having considerably shorter fluorescence lifetimes (Figure 7–1c; 1e, red line). These heterogeneities appear in a curious stepwise fashion, abruptly transitioning from one lifetime value to another. The background solution displays the same fluorescence lifetime and diffusion coefficient as Rh17-22 monomers, suggesting that the environment of the monomer 'pool' has not changed significantly. However, it is not known if the unlabeled Aß(16-22) solution population has oligomerized, nor if the abrupt changes in lifetime region formed during growth, or are something that slowly developed during maturation of the structures.

These structures are also dynamic, as the ends display dynamic regrowth over a period of at least 10 hours. This regrowth is presumably due to addition of the available peptide in solution following agitation during sample loading (data not shown), and occurs at a rate

that slows as the solution monomer concentration decreases. This data suggests that the rate of regrowth is proportional to the monomer concentration. Interestingly, this new growth has a fluorescent lifetime that is independent of the tube on which it is templated. We observe a constant fluorescence intensity and lifetime throughout the new growth even though the solution concentration is decreasing, which further suggests that there is no difference in the percentage of incorporated Rh17-22. The combination of heterogeneous fluorescent lifetimes and templated growth suggest that the Rh17-22 within this subset of aged tubes has accessed a kinetically trapped conformation that does not propagate during regrowth.

TEM images revealed that these solutions contained populations of both ribbons and tubes (Figure 7–1d). These populations appeared mostly distinct, inasmuch as transitions from a ribbon to a tube, and vice versa, were uncommon. Given that the persistence length is likely a function of the structure [59], the rigid structures observed using fluorescence are inconsistent with ribbon structures, and it may be that these aged tubes are more susceptible to deterioration upon staining and dehydration [35].

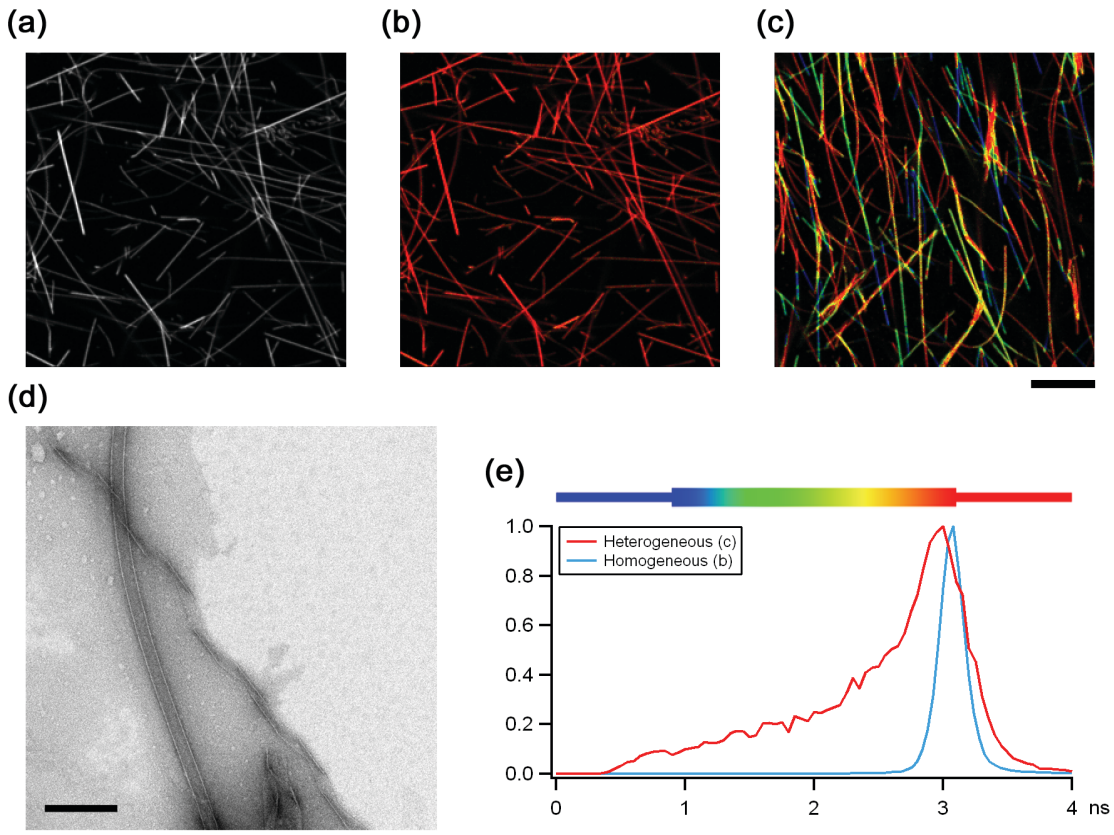

Figure 7–1 – Standard Aß(16-22):Rh17-22 fluorescent nanotubes display a homogeneous fluorescence intensity along individual tubes (a), and exhibit a homogeneous fluorescence lifetime value (b). Previously assembled tubes display heterogeneities in fluorescence lifetime along the lengths of individual tubes in the form of distinct steps to shorter fluorescence lifetime values (c). Standard fluorescent nanotubes have homogeneous fluorescent lifetimes of approximately 3.1 ns (e; blue line), compared to the wider lifetime distribution of heterogeneous tubes (e; red line). TEM images reveal a population of ribbons and nanotubes (d). The normalized histogram of lifetime values for these heterogeneous structures (e; red line) shows a broad distribution, stretched towards lower values when compared to standard tubes (e; blue line). Fluorescent images scale bar, 10 μm, and TEM, 300 nm.

Solutions prepared below the CNC (infra-CNC) remain as monomer (Figure 7–2b,d; black line) for extended periods, while solutions above the CNC (supra-CNC) form nanotubes at a rate that increases with concentration (Figure 7–2c,d;blue line). In contrast, when infra-CNC solutions were aerated, introducing many air-water-interfaces (AWI)s, nucleation was induced leading to the subsequent growth of nanotubes (Figure 7–2a,d;red line), demonstrating the importance of interfaces in the nucleation process. Furthermore, these infra-CNC AWI-induced nanotubes exhibit a significantly shorter average fluorescent lifetime than tubes quiescently assembled supra-CNC (Figure 7–2d), suggesting that in addition to inducing nucleation, interfaces can lead to structural polymorphisms. Moreover, these infra-CNC AWI-induced tubes have distinct regions of differing fluorescent lifetime values, which bear a similarity to the heterogeneities of the aged tube above (Figure 7–1c). In contrast to the heterogeneous structures shown in Figure 7–1c, TEM images (Figure 7–2e) reveal a morphology that is identical to standard Aß(16-22) nanotubes, with [6, 58] and without fluorescent labeling [10, 11].

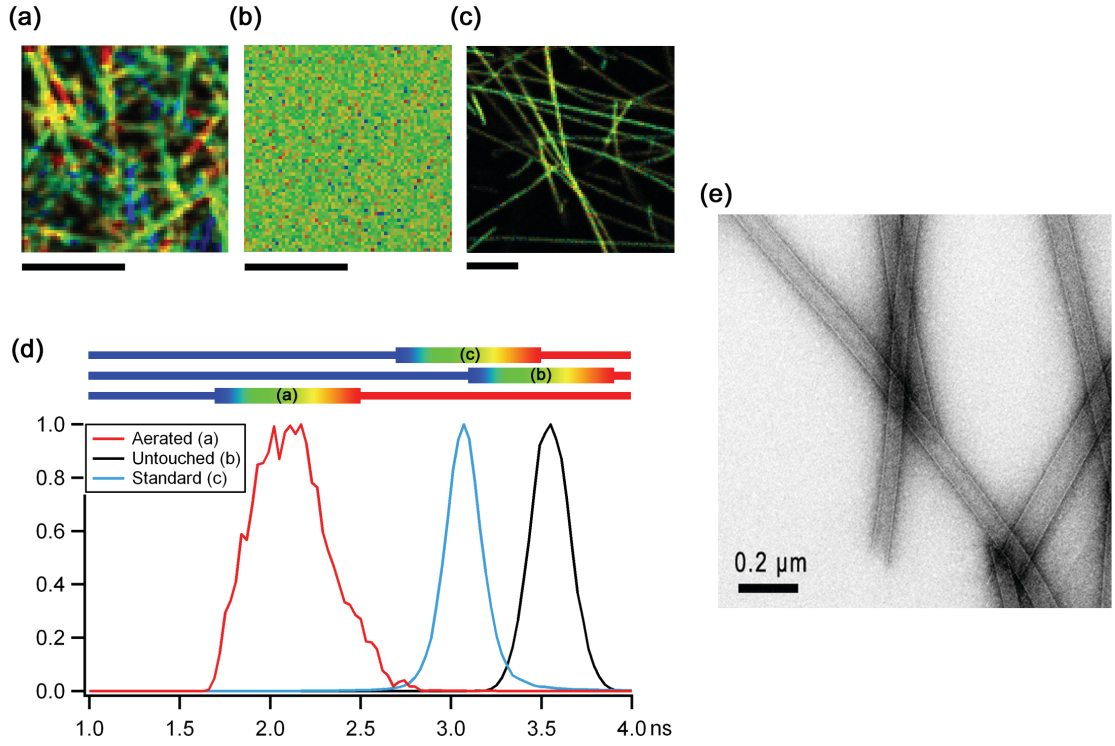

Figure 7–2 – The dense mesh of nanotubes nucleated by aeration (a, d; red line) exhibit a shorter, more heterogeneous fluorescence lifetime compared to supra-CNC standard tubes (c, d; blue line). Untouched infra-CNC solutions do not nucleate nanotubes over long time periods (~ months) and remain in monomer form (b, d; black line). The three color scales shown in (d) all have the same width to allow for comparison of heterogeneity in each image. TEM shows that infra-CNC AWI-induced nanotubes exhibit morphology identical to standard supra-CNC nanotubes.

Nanotubes also nucleate from within amorphous aggregates [58], and are seen to preferentially adhere to the microscope slide surfaces during sample loading (Figure 7–3a). We observe heterogeneities in lifetime values for nanotubes growing from amorphous aggregates when the Aß(16-22):Rh17-22 ratio is as low as 50:1. While some rhodamine dye interaction and corresponding lifetime shift is expected as the labeled

peptide concentration is increased relative to the unlabeled concentration, we would expect Rh17-22 incorporation and quenching to also be uniform throughout the assembled nanotubes. However, this is not the case. We observe distinct transitions to different fluorescence lifetimes that propagate over relatively long length scales, which is strong evidence for locally distinct structures. These heterogeneities are similar to those observed in the subset of aged (Figure 7–1c) and sub-CNC AWI-induced nanotubes (Fig 2a) suggesting that subtlety different nucleation and aging processes can access similar structures. In addition to heterogeneities, these lower ratio nascent tubes exhibit a fluorescence lifetime distribution that is shifted to lower lifetimes (Figure 7–3c), comparable to the infra-CNC AWI-induced nanotubes (Figure 7–2a; d, red line). While it is not possible to prepare TEM grids from these samples, the shorter persistence length suggests that these structures may in fact be ribbons. These data support the concept that different structural regions appear to be stable over finite length scales, leaving the intriguing question of the mechanisms of this phenomenon to further investigations.

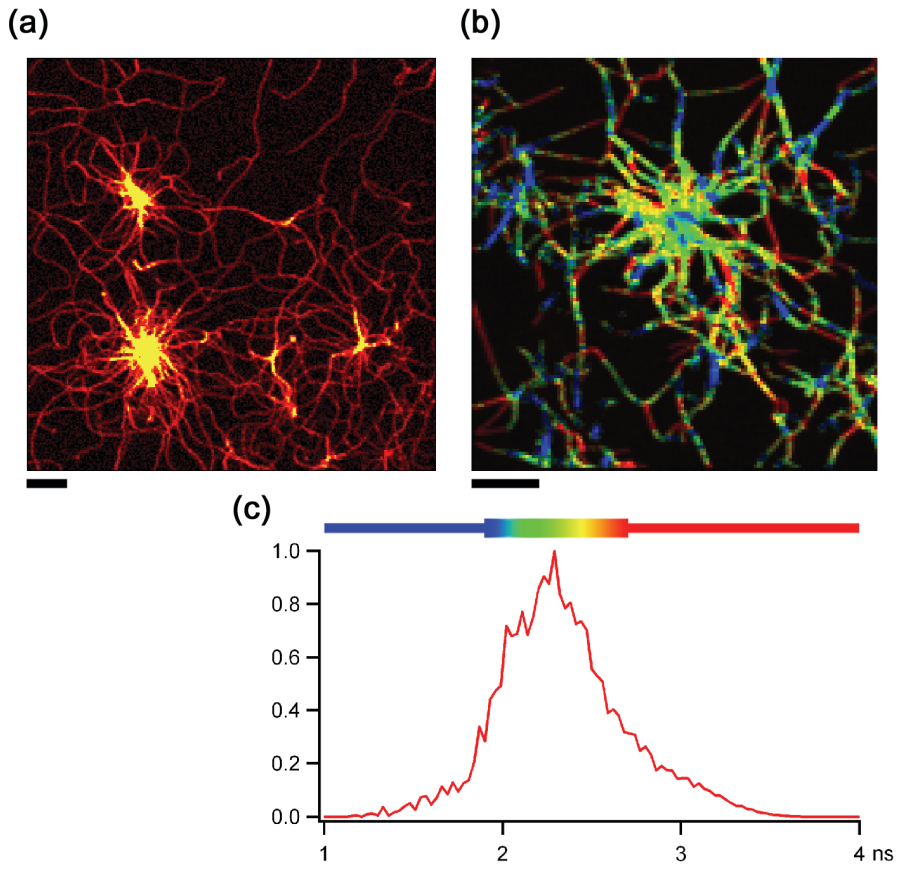

Figure 7–3 – Nascent fluorescent nanotubes formed within amorphous aggregates phases adhere to glass surfaces (a; fluorescence intensity image). FLIM data of these recently formed tubes (b; 50:1 Aß(16-22):Rh17-22) show abrupt changes in fluorescence lifetime along individual tube sections. The FLIM histogram (c) reveals a lifetime distribution shifted to lower values, comparable to the infra-CNC AWI-induced nanotubes shown in Figure 7–2a; d, red line. Scale bars 5 µm.

Taken together, the heterogeneities observed in the subset of aged tubes (Figure 7–1c), sub-CNC AWI-induced tubes (Figure 7–2a), and nascent low ratio tubes (Figure 7–3a), show that different nucleation pathways can access these observed structural heterogeneities. What is not yet understood is the reason for the abrupt transitions between regions of different lifetime along individual tubes. Preliminary molecular

mechanics simulations suggest that Rh17-22 can access multiple energetically allowed conformations (Figure 7–4), which leads us to question the possible conformations of Rh17-22 peptides within the packing structure. It may be possible that the transitions in lifetime correspond to trapped conformations or structures such as rhodamine orientations or registry shifts [15]. Of the numerous available conformations of rhodamine in the Rh17-22 incorporated label, two shown in Figure 7–4 (purple and cyan) suggest than the xanthene ring system could interact with the neighbouring ß-sheet laminates. Other possible thermodynamically unfavorable conformations, such as a peptide backbone cis-trans isomerization [60, 61], may also be the cause of these locally propagating structures. Moreover, these data suggest that a kinetic trap accessed during peptide addition can propagate to subsequent peptide additions, creating a local nucleation point for an alternative long-range packing order.

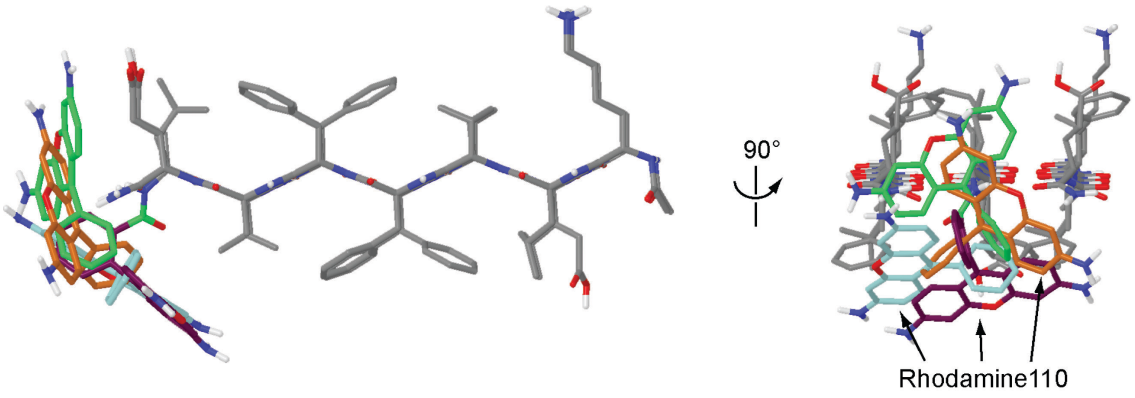

Figure 7–4 – Possible conformations of rhodamine110 when covalently attached to residues 17-22. Three peptides in in an anti-parallel out-of-register ß-sheet configuration are shown. The peptide carbon atoms are colored grey. Four rhodamine110 conformations are shown with the carbon atoms colored orange, green, cyan and purple. The rhoadmine110 colored purple will interact with the peptide side chains from the adjacent sheet.

While it is not known at which stage in the nucleation and growth process that these observed polymorphisms may occur, we hypothesis that the morphology may be determined by local structure at the growing ends of these predominantly linear structures, and thus propagate as they elongate. We have previously shown that nanotube tip growth occurs in a monomer solution [58], but the exact interactions occurring at the growing nanotube tips have not been resolved. These interactions may include frustrated hydrophobic interactions, misaligned peptide registry, and multiple monomer competition [62]. While simulations of ß-sheet formation predict kinetically trapped peptides with misaligned registry [17], and the possibility of α-helix intermediates [18, 19], it has not been possible to experimentally measure these small transient morphologies. The data above of distinct rhodamine110 fluorescence lifetimes is consistent with distinct rhodamine110 environments and further experiments are in progress to correlate atomic-level environment to fluorescence lifetime.

7.3.2 Polymorphism of Phe-Phe Assemblies Directed by Aß(16-22)

The data above indicate that assembly environment influences the long-range order of the 7-residue peptide Aß(16-22). We hypothesized that if π-π interactions of NH2-Phe-Phe-OH can direct Aß(16-22) assembly, then structural heterogeneity should be propagated from small changes in local structure of crystalline diphenylalanine structures. During evaporation from methanol solution, ~50 mM diphenylalanine alone assembles into extended crystalline structures (Figure 7–5a & b), and this structure, determined by X-ray powder diffraction (data not shown), is consistent with previously reported diphenylalanine crystal structures [34, 63, 64]. The inclusion of ~50 nM Aß(16-

22), resulting in a 1:106 ratio of Aß(16-22):Phe-Phe, leads to nucleation of a completely new morphology. These 'fern-like' morphologies propagates over length scales many orders of magnitude larger than the included Aß(16-22), and exhibit a handed, somewhat fractal, growth pattern (Figure 7–5c & d). This nucleating peptide is at a concentration significantly below the CNC, hence cannot produce these vast additional structures. Therefore, we conclude that the interaction of Aß(16-22) with Phe-Phe crystals produces templates for new long-range ordered Phe-Phe growth.

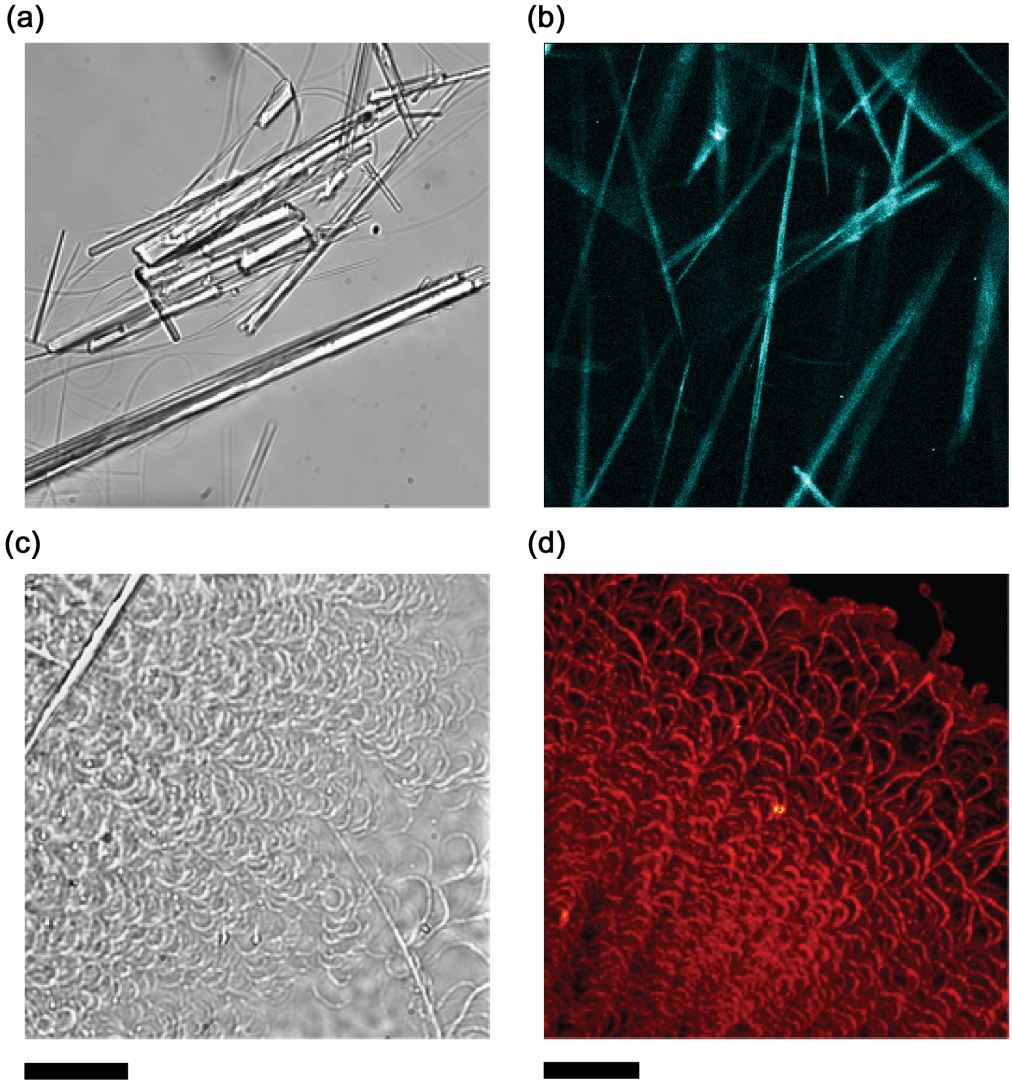

Figure 7–5 – Self-assembled diphenylalanine nanostructures form elongated crystal structures (a) that exhibit strong second harmonic generation signals (b). The addition of 1 to 106 Aß(16-22) produces additional long-range chiral structures that growth from the elongated crystals in waves (c), which instead exhibit mostly autofluorescence (d). Scale bars are 30 μm.

These elongated Phe-Phe crystalline phases exhibit a strong second harmonic generation (SHG) signal [63, 65], and provides the contrast seen in Figure 7–5b. Conversely, the fern structures that propagate in waves from the surface of the crystals possess a broad autofluorescence, which makes up the majority of the signal shown in Figure 7–5d, and suggests an amorphous array of conjugate π-π interactions. SHG signals have been previously observed in di-peptide nanotubes, and are believed to arise from the noncentrosymmetric molecular packing within the crystal structure [63].

In the above structures, the Phe dyad (F19F20) of the Aß(16-22) nanotubes are thought to dominate the packing structure via aryl stacking interactions between ß-sheet strands [12, 28]. While the specificity of Phe-Phe interactions are debated [66-69], it is clear that they play a strong role in final morphology, whereby nanotubes [68] and tapes [69] can be formed at neutral pH by substitution for residues that have increased hydrophobicity, molecular volume and ß-sheet propensity. Although thermodynamically unstable, it may be possible that a rotation about the Cß- CϒH bond of either Phe residue leads to an altered aryl stacking which propagates to neighboring ß-strands. These aryl interactions are the intrinsic component of the crystalline structure in Phe-Phe nanomaterials [31]. Furthermore, the Phe dyad of Aß(16-22) presumably provides a nucleus for an additional packing structure seen in the chiral fern-like growths (Figure 7–5c & d).

7.4 Conclusions

During transversal of the assumed rough energy docking landscape at the growing edge of the tube or other structure, it is quite possible that registry errors may occur, or external impurities may bind, that affect the local structure of the lamination, ß-sheet, or aryl interactions. While it is conceivable that a quasi-crystalline structure could withstand multiple defects without deleterious effects to the bulk structure, our data suggest these defects might propagate to form structural motifs that are not observed via other methods. Given that we see heterogeneities in nascent tubes, we propose that these long-range order nucleation sites are initiated during peptide addition, as part of a hydrophobic collapse around the tube end, akin to the original hydrophobic collapse that forms the cross-ß structures. Also, it is possible that ionic impurities could act to help salt-out the monomers (cf. Debeljuh et al.), stabilizing its linear structure and accelerating fibrillization. This kind of ionically ordered water interaction, possibly liquid crystal interaction [70], could further align the monomers that are being sequestered in the dynamic hydrophobic templating interaction.

Understanding the nucleus of self-assembly is important to targeting disease and rational design of novel peptide nanomaterials. We have presented data that suggests that we should think more in terms of understanding the multiple nuclei of self-assembly, as there may be secondary nucleation events [71] that are prerequisites for certain polymorphisms. It is commonly thought that the final supramolecular structure is determined during nucleation, and that different nucleation environments can produce the different observed polymorphisms. We have described an abrupt transition in nanotube fluorescence lifetime, believed to be representative of structure, which show

long-range order can nucleate and propagate from very small local changes. The spatially transient nature of these propagating, locally homogeneous regions suggests that these structures are kinetically trapped as opposed to thermodynamically stable. This compelling data leads us to think of nucleation processes as dynamic and possibly iterative in nature.

7.5 Materials and Methods

7.5.1 Peptide Synthesis

Aß(16-22) peptide was synthesized using standard FMOC solid phase protocols outlined in the manuscript on an Applied Biosystems ABI431 synthesizer. Peptides were then cleaved from the resin using trifluoroacetic acid/thioanisole/1,2-ethanedithiol/anisole (90:5:3 2, v/v/v/v), precipitated from the cleavage solution and washed repeatedly using excess cold (-20°C) diethyl ether. Purification was performed using reverse phase HPLC with acetonitrile/water gradients containing 0.1% TFA, and the collected samples were lyophilized to white powder and stored at 4°C. Molecular weights of all peptides were verified by MALDI-TOF mass spectrometry using a 2,5-dihydroxybenzoic acid matrix. Aß(17-22) N-terminal acylated with rhodamine 110 (Rh17-22) were synthesized using the same FMOC and coupling protocols.

7.5.2 Amyloid Assembly

Small amounts of dry Aß(16-22) peptide (1-2 mg) were disaggregated in hexafluoroisopropanol (HFIP), aliquoted into ~10 microfuge tubes, and allowed to evaporate in a fume hood before re-entering storage at 4°C. On use, each aliquot was dissolved in a Rh17-22 in 40% acetonitrile (AcCN) 0.1% TFA solution to give the desired

total peptide concentration and unlabeled to labeled ratio, followed by alternating sonication and vortexing to ensure complete dissolution. A small amount of the resulting solution, ~15 µl, was loaded onto a microscope slide, and enclosed with a coverslip sealed around the edges with nail polish.

7.5.3 Diphenylalanine Assembly

Microscope slides were sonicated in soap solution, isopropanol, acetone, and hydrogen peroxide, and sonicated in ultrapure H2O (18.2 MΩ) between each step, to prepare ultraclean glass surfaces. Di-L-phenylalanine peptide, purchased from Sigma-Aldrich (cat. P4126), were disaggregated using HFIP, and allowed to evaporate in a fume hood before use. A 50 mM methanol solution of Phe-Phe, and a 50 nM Aß(16-22) 40% acetonitrile (AcCN) 0.1% TFA solution were prepared separately, followed by alternating sonication and vortexing to ensure complete dissolution. A small amount, ~15 µl, of just Phe-Phe, and separately, a mixture of Phe-Phe and Aß(16-22), were loaded onto clean microscope slides and allowed to evaporate. A subsequent aliquot of each solution was re-added and enclosed with a coverslip sealed around the edges with nail polish. Due to the porous nature of nail polish, these samples eventually evaporate, after which the samples are imaged.

7.5.4 Optical Microscopy

Two-photon excitation was provided by an ultrafast (~100 fs pulses at 80 MHz) Ti:Sa laser (Spectra Physics) tuned to 780 nm for FLIM and 890 nm for SHIM. Intensity was attenuated using a λ/2 plate and polarizing cube. The laser beam was scanned using an x-y pair of galvanometer mirrors (6215H, Cambridge Technology) before entering a 5× beam expanding telescopic optical setup that terminates on the rear aperture of an Olympus 60× water immersion objective lens (UPLSAPO60XW, Olympus; NA = 1.2)

mounted in an inverted microscope (IX71, Olympus). Introduction into the optical path of the objective was achieved via reflection from a dichroic mirror (675 DCSX, Chroma Technology). Collected light passes the dichroic mirror and a low pass filter before being directed to the detector set up.

For FLIM data sets, the collected light was directed to a current output PMT detector (H7422P-40, Hamamatsu Corporation). Detector signals are sent to a TCSPC module (PicoHarp300, PicoQuant GmbH) and analyzed using SymPhoTime software. The excitation power at the sample was varied between 0.5 and 2 mW depending on the collected count rate. The images are acquired near to glass surfaces, ~1-2 μm, as these structures remain stationary long enough for FLIM data to be acquired, ~2-5 mins. Reported fluorescence lifetime values were achieved using PicoQuant's 'fastFLIM', which measures the barycenter of the exponential decay, and as such is a reliable measure of the average lifetime fluorescence decay value. SHIM data sets were acquired by directing the collected light to a photon counting PMT detector (H7421-40, Hamamatsu Corporation), after reflection from a 505DCXR dichroic mirror and transmission through a bandpass filter D455/60M (Chroma Technology). Autofluorescence data sets were acquired by directing the light unimpeded onto the photon counting PMT. The degree of SHG and autofluorescence was assessed using a spectrometer, coupled via a multimode fiber optic. Brightfield microscope images were collected using an iXon EMCCD camera (Andor).

7.5.5 Electron Microscopy

Aliquots (20 μl) of peptide solutions were applied to TEM grids (Carbon film coated 200 mesh, Electron Microscopy Sciences) and allowed to adsorb for 1 min before excess solution was wicked away with filter paper. Uranyl acetate (10 μl of 5% solution, Sigma-Aldrich) was added for 2 mins to negatively stain the sample. Excess fluid was wicked

away with filter paper and the grids were dried under house vacuum overnight prior to analysis. TEM micrographs were recorded with a Philips 410 TEM with a Tungsten filament at an accelerating voltage of 75 kV. Images were acquired using the incorporated CCD camera (Gatan).

7.6 Acknowledgments

We are grateful to Jeannette Taylor and Hong Yi in the Emory Robert P. Apkarian Microscopy Core for TEM advice and training, and to grants NSF MCB0817966, NSF DMR0907435, U.S. DOE (ER15377), NASA Astrobiology Program, under the NSF Center for Chemical Evolution, CHE-1004570, and NSF-CBC-0739189 for support for funding.

7.7 References

1. Lambert, M.P., et al., *Diffusible, Nonfibrillar Ligands Derived from a Beta(1-42) Are Potent Central Nervous System Neurotoxins*. Proceedings of the National Academy of Sciences of the United States of America, 1998. **95**(11): p. 6448-6453.
2. Haass, C. and D.J. Selkoe, *Soluble Protein Oligomers in Neurodegeneration: Lessons from the Alzheimer's Amyloid Beta-Peptide*. Nature Reviews Molecular Cell Biology, 2007. **8**(2): p. 101-112.
3. Kayed, R., et al., *Common Structure of Soluble Amyloid Oligomers Implies Common Mechanism of Pathogenesis*. Science, 2003. **300**(5618): p. 486-489.
4. Zhang, S., *Fabrication of Novel Biomaterials through Molecular Self-Assembly*. Nature Biotechnology, 2003. **21**(10): p. 1171-1178.

5. Rosenman, G., et al., *Bioinspired Peptide Nanotubes: Deposition Technology, Basic Physics and Nanotechnology Applications*. Journal of Peptide Science, 2011. **17**(2): p. 75-87.

6. Liang, Y., et al., *Light Harvesting Antenna on an Amyloid Scaffold*. Chem. Commun., 2008(48): p. 6522-6524.

7. Lu, K., et al., *Exploiting Amyloid Fibril Lamination for Nanotube Self-Assembly*. J. Am. Chem. Soc., 2003. **125**(21): p. 6391-6393.

8. Lu, K., et al., *Macroscale Assembly of Peptide Nanotubes*. Chemical Communications, 2007(26): p. 2729.

9. Balbach, J.J., et al., *Amyloid Fibril Formation by Aβ16-22, a Seven-Residue Fragment of the Alzheimer's B-Amyloid Peptide, and Structural Characterization by Solid State Nmr*. Biochemistry, 2000. **39**(45): p. 13748-13759.

10. Dong, J., et al., *Controlling Amyloid Growth in Multiple Dimensions*. Amyloid, 2006. **13**(4): p. 206-215.

11. Mehta, A.K., et al., *Facial Symmetry in Protein Self-Assembly*. J. Am. Chem. Soc., 2008. **130**(30): p. 9829-9835.

12. Childers, W.S., et al., *Peptides Organized as Bilayer Membranes*. Angewandte Chemie International Edition, 2010. **49**(24): p. 4104-7.

13. Childers, W.S., et al., *Templating Molecular Arrays in Amyloid's Cross-β Grooves*. J. Am. Chem. Soc., 2009. **131**(29): p. 10165-10172.

14. Chaudhary, N. and R. Nagaraj, *Impact on the Replacement of Phe by Trp in a Short Fragment of Abeta Amyloid Peptide on the Formation of Fibrils*. Journal of Peptide Science, 2011. **17**(2): p. 115-23.

15. Petty, S.A. and S.M. Decatur, *Experimental Evidence for the Reorganization of Beta-Strands within Aggregates of the Aβ(16-22) Peptide*. Journal of the American Chemical Society, 2005. **127**(39): p. 13488-9.

16. Chebaro, Y. and P. Derreumaux, *Targeting the Early Steps of Aβ16-22 Protofibril Disassembly by N-Methylated Inhibitors: A Numerical Study*. Proteins, 2009. **75**(2): p. 442-52.

17. Santini, S., N. Mousseau, and P. Derreumaux, *In Silico Assembly of Alzheimer's Aβ(16-22) Peptide into β-Sheets*. Journal of the American Chemical Society, 2004. **126**(37): p. 11509-11516.

18. Santini, S., et al., *Pathway Complexity of Alzheimer's β-Amyloid Aβ16-22 Peptide Assembly*. Structure, 2004. **12**(7): p. 1245-1255.

19. Klimov, D.K. and D. Thirumalai, *Dissecting the Assembly of Aβ(16-22) Amyloid Peptides into Antiparallel β Sheets*. Structure, 2003. **11**(3): p. 295-307.

20. Brovchenko, I., et al., *Thermal Expansivity of Amyloid β(16-22) Peptides and Their Aggregates in Water*. Physical chemistry chemical physics : PCCP, 2009. **11**(25): p. 5035-40.

21. Bellesia, G. and J.E. Shea, *Effect of β-Sheet Propensity on Peptide Aggregation*. Journal of Chemical Physics, 2009. **130**(14).

22. Childers, W.S., et al., *Peptide Membranes in Chemical Evolution*. Curr. Opin. Chem. Biol., 2009. **13**(5-6): p. 652-9.

23. Carny, O. and E. Gazit, *A Model for the Role of Short Self-Assembled Peptides in the Very Early Stages of the Origin of Life*. The FASEB Journal, 2005. **19**(9): p. 1051-1055.

24. Liang, Y., et al., *Cross-Strand Pairing and Amyloid Assembly*. Biochemistry, 2008. **47**(38): p. 10018-10026.

25. Malinchik, S.B., et al., *Structural Analysis of Alzheimer's Beta(1-40) Amyloid: Protofilament Assembly of Tubular Fibrils*. Biophysical Journal, 1998. **74**(1): p. 537-545.

26. Walsh, D.M., et al., *Amyloid β-Protein Fibrillogenesis - Detection of a Protofibrillar Intermediate*. Journal of Biological Chemistry, 1997. **272**(35): p. 22364-22372.

27. Petkova, A.T., et al., *A Structural Model for Alzheimer's Beta-Amyloid Fibrils Based on Experimental Constraints from Solid State Nmr*. Proceedings of the National Academy of Sciences of the United States of America, 2002. **99**(26): p. 16742-16747.

28. Gazit, E., *A Possible Role for Π-Stacking in the Self-Assembly of Amyloid Fibrils*. The FASEB Journal, 2002. **16**(1): p. 77-83.

29. Kol, N., et al., *Self-Assembled Peptide Nanotubes Are Uniquely Rigid Bioinspired Supramolecular Structures*. Nano Letters, 2005. **5**(7): p. 1343-1346.

30. Adler-Abramovich, L., et al., *Thermal and Chemical Stability of Diphenylalanine Peptide Nanotubes: Implications for Nanotechnological Applications*. Langmuir, 2006. **22**(3): p. 1313-1320.

31. Reches, M. and E. Gazit, *Designed Aromatic Homo-Dipeptides: Formation of Ordered Nanostructures and Potential Nanotechnological Applications*. Physical Biology, 2006. **3**(1): p. S10-S19.

32. Reches, M. and E. Gazit, *Controlled Patterning of Aligned Self-Assembled Peptide Nanotubes*. Nature Nanotechnology, 2006. **1**(3): p. 195-200.

33. Debeljuh, N., C.J. Barrow, and N. Byrne, *The Impact of Ionic Liquids on Amyloid Fibrilization of Aβ16-22: Tuning the Rate of Fibrilization Using a Reverse Hofmeister Strategy*. Physical Chemistry Chemical Physics, 2011. **13**(37): p. 16534-16536.

34. Amdursky, N., et al., *Elementary Building Blocks of Self-Assembled Peptide Nanotubes*. Journal of the American Chemical Society, 2010. **132**(44): p. 15632-15636.

35. Krysmann, M.J., et al., *Self-Assembly and Hydrogelation of an Amyloid Peptide Fragment*. Biochemistry, 2008. **47**(16): p. 4597-4605.

36. Morinaga, A., et al., *Critical Role of Interfaces and Agitation on the Nucleation of Aβ Amyloid Fibrils at Low Concentrations of Aβ Monomers*. Biochimica et Biophysica Acta (BBA) - Proteins & Proteomics, 2010. **1804**(4): p. 986-995.

37. Zhu, M., et al., *Surface-Catalyzed Amyloid Fibril Formation*. Journal of Biological Chemistry, 2002. **277**(52): p. 50914-50922.

38. Nichols, M.R., et al., *Amyloid-B Aggregates Formed at Polar-Nonpolar Interfaces Differ from Amyloid-B Protofibrils Produced in Aqueous Buffers*. Microscopy Research and Technique, 2005. **67**(3-4): p. 164-174.

39. Chi, E.Y., et al., *Amyloid-Beta Fibrillogenesis Seeded by Interface-Induced Peptide Misfolding and Self-Assembly*. Biophysical Journal, 2010. **98**(10): p. 2299-308.

40. Petkova, A.T., et al., *Self-Propagating, Molecular-Level Polymorphism in Alzheimer's β-Amyloid Fibrils*. Science, 2005. **307**(5707): p. 262-5.

41. Goldsbury, C., et al., *Multiple Assembly Pathways Underlie Amyloid-β Fibril Polymorphisms*. Journal of Molecular Biology, 2005. **352**(2): p. 282-298.

42. Colletier, J.-P., et al., *Molecular Basis for Amyloid-B Polymorphism*. Proceedings of the National Academy of Sciences, 2011. **108**(41): p. 16938-16943.

43. Kodali, R., et al., *Aβ(1–40) Forms Five Distinct Amyloid Structures Whose B-Sheet Contents and Fibril Stabilities Are Correlated*. Journal of Molecular Biology, 2010. **401**(3): p. 503-517.

44. Kodali, R. and R. Wetzel, *Polymorphism in the Intermediates and Products of Amyloid Assembly*. Current Opinion in Structural Biology, 2007. **17**(1): p. 48-57.

45. Zheng, J., H. Jang, and R. Nussinov, *β(2)-Microglobulin Amyloid Fragment Organization and Morphology and Its Comparison to Aβ Suggests That Amyloid Aggregation Pathways Are Sequence Specific*. Biochemistry, 2008. **47**(8): p. 2497-2509.

46. Rohrig, U.F., et al., *Stability and Structure of Oligomers of the Alzheimer Peptide Aβ16-22: From the Dimer to the 32-Mer*. Biophysical Journal, 2006. **91**(9): p. 3217-3229.

47. Han, W. and Y.D. Wu, *Molecular Dynamics Studies of Hexamers of Amyloid-Beta Peptide (16-35) and Its Mutants: Influence of Charge States on Amyloid Formation*. Proteins, 2007. **66**(3): p. 575-87.

48. Bitan, G., et al., *Amyloid β-Protein (Aβ) Assembly: Aβ 40 and Aβ 42 Oligomerize through Distinct Pathways*. Proceedings of the National Academy of Sciences of the United States of America, 2003. **100**(1): p. 330-335.

49. Alexandrescu, A.T., et al., *Heterogeneous Amylin Fibril Growth Mechanisms Imaged by Total Internal Reflection Fluorescence Microscopy*. Biochemistry, 2011. **50**(14): p. 2808-2819.

50. Ban, T., et al., *Direct Observation of Aβ Amyloid Fibril Growth and Inhibition*. Journal of Molecular Biology, 2004. **344**(3): p. 757-767.

51. Kowalewski, T. and D.M. Holtzman, *In Situ Atomic Force Microscopy Study of Alzheimer's Beta-Amyloid Peptide on Different Substrates: New Insights into Mechanism of Beta-Sheet Formation*. Proceedings of the National Academy of Sciences of the United States of America, 1999. **96**(7): p. 3688-3693.

52. Goldsbury, C., et al., *Watching Amyloid Fibrils Grow by Time-Lapse Atomic Force Microscopy*. Journal of Molecular Biology, 1999. **285**(1): p. 33-39.

53. Blackley, H.K.L., et al., *In-Situ Atomic Force Microscopy Study of B-Amyloid Fibrillization*. Journal of Molecular Biology, 2000. **298**(5): p. 833-840.

54. Gordon, D.J., R. Tappe, and S.C. Meredith, *Design and Characterization of a Membrane Permeable N-Methyl Amino Acid-Containing Peptide That Inhibits a Beta(1-40) Fibrillogenesis*. Journal of Peptide Research, 2002. **60**(1): p. 37-55.

55. Gordon, D.J., et al., *Increasing the Amphiphilicity of an Amyloidogenic Peptide Changes the ß-Sheet Structure in the Fibrils from Antiparallel to Parallel*. Biophysical Journal, 2004. **86**(1 Pt 1): p. 428-34.

56. Kim, Y.S., et al., *2d Ir Provides Evidence for Mobile Water Molecules in Beta-Amyloid Fibrils*. Proceedings of the National Academy of Sciences of the United States of America, 2009. **106**(42): p. 17751-17756.

57. Decatur, S.M., *Elucidation of Residue-Level Structure and Dynamics of Polypeptides Via Isotopp-Edited Infrared Spectroscopy*. Accounts of Chemical Research, 2006. **39**(3): p. 169-175.

58. Liang, Y., D.G. Lynn, and K.M. Berland, *Direct Observation of Nucleation and Growth in Amyloid Self-Assembly*. J. Am. Chem. Soc., 2010. **132**(18): p. 6306-6308.

59. Knowles, T.P., et al., *Role of Intermolecular Forces in Defining Material Properties of Protein Nanofibrils*. Science, 2007. **318**(5858): p. 1900-3.

60. Scherer, G., et al., *Barriers to Rotation of Secondary Amide Peptide Bonds*. Journal of the American Chemical Society, 1998. **120**(22): p. 5568-5574.

61. Nguyen, K., M. Iskandar, and D.L. Rabenstein, *Kinetics and Equilibria of Cis/Trans Isomerization of Secondary Amide Peptide Bonds in Linear and Cyclic Peptides*. The Journal of Physical Chemistry B, 2010. **114**(9): p. 3387-3392.

62. Lee, C.F., et al., *Elongation Dynamics of Amyloid Fibrils: A Rugged Energy Landscape Picture*. Physical Review E, 2009. **80**(4): p. 041906.

63. Amdursky, N., et al., *Structural Transition in Peptide Nanotubes*. Biomacromolecules, 2011. **12**(4): p. 1349-1354.

64. Gorbitz, C.H., *The Structure of Nanotubes Formed by Diphenylalanine, the Core Recognition Motif of Alzheimer's β-Amyloid Polypeptide*. Chemical Communications, 2006(22): p. 2332-2334.

65. Campagnola, P.J. and L.M. Loew, *Second-Harmonic Imaging Microscopy for Visualizing Biomolecular Arrays in Cells, Tissues and Organisms*. Nature Biotechnology, 2003. **21**(11): p. 1356-1360.

66. Tatko, C.D. and M.L. Waters, *Selective Aromatic Interactions in B-Hairpin Peptides*. Journal of the American Chemical Society, 2002. **124**(32): p. 9372-9373.

67. Chung, D.M., et al., *The Absence of Favorable Aromatic Interactions between B-Sheet Peptides*. Journal of the American Chemical Society, 2005. **127**(28): p. 9998-9999.

68. Senguen, F.T., et al., *Probing Aromatic, Hydrophobic, and Steric Effects on the Self-Assembly of an Amyloid-Beta Fragment Peptide*. Mol Biosyst, 2011. **7**(2): p. 486-96.

69. Senguen, F.T., et al., *Clarifying the Influence of Core Amino Acid Hydrophobicity, Secondary Structure Propensity, and Molecular Volume on Amyloid-β 16-22 Self-Assembly*. Mol Biosyst, 2011. **7**(2): p. 497-510.

70. Zheng, J.M., et al., *Surfaces and Interfacial Water: Evidence That Hydrophilic Surfaces Have Long-Range Impact*. Advances in Colloid and Interface Science, 2006. **127**(1): p. 19-27.

71. Knowles, T.P., et al., *An Analytical Solution to the Kinetics of Breakable Filament Assembly*. Science, 2009. **326**(5959): p. 1533-7.

Chapter 8

Global Analysis of Fluorescence Lifetime and Correlation Spectroscopy: τFCS

Neil R. Anthony, Peng Guo, and Keith M. Berland

Department of Physics, Emory University, Atlanta, GA 30322

The theory of this chapter, together with simulated data is currently in press:

Neil Anthony, Keith Berland, Global Analysis in Fluorescence Correlation Spectroscopy and Fluorescence Lifetime Microscopy. In: Methods in Enzymology, Chapter 7.

The chapter shown here demonstrating experimental data, together with a concise edit sans theory, are in preparation for Biomedical Optics and Nature Biophotonics respectively.

8.1 Abstract

Fluorescence correlation spectroscopy (FCS) and related fluorescence fluctuation methods have become important research tools for investigations of molecular systems in a variety of complex environments. Successful analysis of fluctuation measurements provides unique information that is otherwise difficult to measure, such as molecular concentrations and interaction stoichiometry. Information recovery *via* fluctuation data curve fitting can present complicating challenges, especially in cases with limited resolution and/or undetermined fitting models. Here, we discuss a new global analysis technique called τFCS that couples multiple modes of data acquisition, specifically FCS and fluorescence lifetime. We demonstrate a dramatically enhanced sensitivity and resolution in fluctuation measurements, including the capability to recover the concentrations from a two-component mixture even when the species have identical diffusion coefficients and molecular brightness values, provided their fluorescent lifetimes are distinct. We also demonstrate how τFCS provides useful tools for model discrimination in FCS curve fitting.

8.2 Introduction and Background

Modern scientific studies increasingly demand accurate characterization of spatial and temporal dynamics of specifically identifiable molecules, whilst measuring the molecular and chemical interactions that are integral to understanding molecular level functioning in biological, chemical, and materials science applications. Fluorescence microscopy has thus become an ever more popular research tool due to high spatial resolution [1-6], single molecule sensitivity [7-11], spectral selectivity, temporal resolution [10, 12], and generally low invasiveness [13, 14]. A variety of high powered microscopy based

fluorescence acquisition and data analysis techniques have emerged that have dramatically advanced the desired capability to accurately characterize the molecular level behavior of experimental systems. Examples include fluorescence lifetime imaging (FLIM) [15-17], Förster resonance energy transfer (FRET) microscopy [18-20], and a variety of fluorescence fluctuation spectroscopy (FFS) methods [21-26]. Each of these methods offers important capabilities and advantages for different experimental requirements. Here we focus on fluctuation methods, which offer unique capabilities to measure dynamics over a wide range of time-scales as well as to accurately measure molecular concentrations and directly read-out the stoichiometric composition of interacting molecular species due to the self-calibrating nature of fluctuation measurements. FFS techniques have proven to be remarkably useful for characterizing molecular dynamics and interactions within complex systems [27-31].

All FFS methods rely on statistical analysis of spontaneous spatial and/or temporal fluctuations in fluorescence intensity. Information recovery from measured fluorescence fluctuations requires accurate models for physical or chemical processes driving the fluctuations, in addition to information regarding the composition of the experimental system such as number of unique fluorescent species present. In complex systems, such information is often not available *a priori*. While there have been many examples demonstrating the capability to determine correct physical models and sample composition through curve fitting, FFS data analysis generally has limited capacity for model discrimination, and there are many experimental conditions for which distinguishing correct physical models through curve-fitting of FFS data alone may be impossible. Moreover, molecular dynamics and interactions that may be of critical importance are often beyond the fundamental resolution limits of FFS analysis.

A variety of innovations in FFS data acquisition and analysis methods have been developed to overcome some of these limitations. For example, the development of dual-color cross correlation spectroscopy and molecular brightness based assays such as PCH, FIDA and cumulants [10, 22, 23, 25, 30, 32-35] have leveraged analysis of amplitude fluctuations to quantify molecular interactions even for cases where temporal fluctuation analysis alone is insufficient to resolve the same interactions. These advances have proven highly effective for many experimental requirements, although limitations on resolution and model discrimination capabilities can still cause problems such that further improvements in FFS methods could provide significant benefits.

One important approach to enhance resolution in fluorescence measurements has been the use of multi-parameter fluorescence detection (MFD) to simultaneously acquire numerous spectroscopic signatures such as fluorescence lifetimes, excitation or emission spectra, or fluorescence anisotropy, each of which may offer unique information that can help resolve complex sample composition [36-40]. Simultaneous analysis of the multiple spectral signatures acquired using MFD can greatly reduce false assumptions that commonly occur at the resolution limits of the single techniques alone. However, MFD alone does not by itself increase the resolution available from any particular spectral analysis approach when each is employed sequentially, separate from the others.

One powerful method to improve experimental resolution when curve fitting multiple related data sets is to utilize global analysis [41-47]. Global analysis takes advantage of the fact that some of the fundamental or 'global' parameters characterizing an experimental system will remain constant across multiple experimental data sets [48] while other conditional or 'local' parameters can vary with each individual sample condition or experimental measurement details. For example, systematically varied

experimental conditions such as excitation wavelength [49], solution pH [50], or molecular concentration [51] can alter the local parameters unique to each individual measurement while leaving the global parameters common across all measurements unchanged. Curve fitting using common global parameters 'linked' across multiple data sets reduces the number of free parameters and effectively constrains the parameter space that can fit all experimental data simultaneously. Such constraints can greatly enhance model discrimination capabilities in curve fitting routines since it is less likely that an incorrect physical model can simultaneously fit multiple data sets with varied experimental conditions or varied sample conditions. The approach of linking global parameters across multiple data sets has only been implemented for experimental measurements using only a single data acquisition mode for each data set (e.g. lifetime, anisotropy, etc.), although in principle this need not be the case.

In this work, we introduce a new approach to FFS analysis which leverages both the enhanced information content and model discrimination capabilities of multi-parameter fluorescence measurements and the improved curve-fitting capabilities of global analysis, and we demonstrate that this approach leads to dramatic improvements in FFS measurement capabilities. The specific implementation introduced below combines fluorescence correlation spectroscopy (FCS) with fluorescence lifetime microscopy, referred to as τFCS. These two acquisition modes have previously been combined in an elegant software filter based analysis protocol, referred to as FLCS [52, 53]. The method introduced here is fundamentally different from that approach. The τFCS method instead introduces simultaneous global analysis of both fluorescence lifetime and FCS data, i.e. simultaneous curve fitting of two distinct experimental data types with globally linked fundamental system parameters. Both FLCS and τFCS fundamentally transform the resolution limits of FCS, allowing resolution of multiple species with identical

diffusion coefficients, provided their fluorescence lifetimes are different, something which is not possible without methods such as FLCS or τFCS [54]. We find that the τFCS approach offers significant practical advantages and has less demanding requirements on signal statistics than FLCS to recover accurate curve-fitting results. We demonstrate below the capability to accurately measure the concentrations of two-component mixtures even for the case where a second species has lower molecular brightness than the dominant molecular species and constitutes only a few percent of the molecules within the sample. Such enhanced resolution extends far beyond the resolution in typical FCS measurements. Moreover, the fundamental strategy of combining multi-parameter fluorescence acquisition with global analysis is easily extended to other fluorescence measurement modes (e.g. anisotropy, FRET) with minimal theoretical modifications, and should thus be widely applicable in most experimental systems where FFS measurements are used.

8.3 Theory

Simultaneous global fitting of both lifetime and FCS data requires that the theory for each be written in terms of common linkable parameters. Traditionally, lifetime theory is written in terms of the excited state lifetime values and fraction intensities of each molecular species, with no direct link to the concentration or molecular brightness values that are used in FFS theory. We thus introduce a complete theory describing fluorescence lifetime decay histograms in terms of the molecular concentrations and molecular brightness parameters used in FFS. Fluorescence lifetime measurements require pulsed laser excitation sources, and thus τFCS theory describes pulsed laser excitation, spans picosecond to second time scales, and incorporates effects due to saturation and finite fluorescence lifetimes [55-59]. To completely describe fluorescence

dynamics under pulsed excitation in terms of common fluorescence parameters we must consider both micro- and macro-time scales. Micro-time (ps to ns) is used to describe the excited state dynamics of fluorescent molecules following pulsed excitation, and resets to zero after each incident laser pulse. Macro-time (μs to s) describes longer time scale behavior, such as fluorescence fluctuations due to physical or chemical dynamics, and is continuous from the start of the experiment. Our lab works exclusively with two-photon microscopy [56, 57, 59, 60], so the theory presented below is for two-photon laser excitation, although the details could be easily applied for single photon excitation with only minor modifications. A detailed derivation of the following theory can be found in reference [61].

8.3.1 Two-photon fluorescence measurements

Considering the micro-time photodynamics of a single molecular species, treated as a simple two state model (N_0 : ground state; N_1: excited state), we previously derived an expression describing the steady state probability that a molecule will occupy the excited state immediately after a laser pulse passes through the sample [57, 60], with:

$$N_{1a}(\mathbf{r}) = \frac{\left(1 - e^{-2W(\mathbf{r})\alpha}\right)}{2\left(1 - e^{-2W(\mathbf{r})\alpha} e^{-\Gamma/f_p}\right)} \tag{8.1}$$

Here, $W(\mathbf{r})$ represents two-photon excitation rate [62] for pulsed laser excitation that includes saturation and finite lifetime effects, with a spatial dependence determined by the spatial profile of the focused laser excitation source. The laser pulse repetition rate is f_p, and for simplicity the temporal pulse profile is assumed to have constant amplitude with pulse width α, an assumption that has no important consequences for this work. The parameter Γ is the inverse of the fluorescence lifetime, and is the spontaneous

relaxation rate of excited state molecules. For a molecular concentration $C(\mathbf{r},t)$, we expect fluorescence emission of $\Gamma e^{-\Gamma t'} C(\mathbf{r},t) N_{1a}(\mathbf{r})$ photons per unit volume per unit time following each laser pulse. The measured instantaneous fluorescence signal, $F_{inst}(t',t)$, is the integrated signal from the full sample volume given by:

$$F_{inst}(t',t) = \kappa\Gamma e^{-\Gamma t'} \int C(\mathbf{r},t) N_{1a}(\mathbf{r}) d\mathbf{r} \tag{8.2}$$

where κ is a sample and equipment dependent constant that incorporates all parameters describing the excitation and optical collection efficiencies, such as absorption cross sections, quantum yields, detector efficiencies.

Equation (8.2) contains two distinct time variables that characterize the micro- (t') and macro-time (t) variations in the fluorescence signal. To measure fluorescence lifetimes, we are interested in the micro-time behavior, and in principle, Eq. (8.2) represents the fluorescence decay curve following each laser pulse. However, in practice, limited photon numbers require that fluorescence lifetime measurements are performed over millions of excitation pulses, with macro-time averaged histograms accumulated to give the micro-time resolved average fluorescence signal:

$$\left\langle F_{inst}(t') \right\rangle = \frac{1}{T}\int_0^T F_{inst}(t',t)\, dt = \kappa\Gamma \left\langle C \right\rangle e^{-\Gamma t'} \int N_{1a}(\mathbf{r})\, d\mathbf{r} \tag{8.3}$$

where the total acquisition time, *T*, is sufficiently long that the spatial and temporal concentration fluctuations are averaged out. Alternatively, for FFS measurements we are primarily interested in the macro-time variations in fluorescence and can instead average out the micro-time behavior. The macro-time averaged fluorescence signal thus depends explicitly on the time dependent concentration and can be written as:

$$F(t) = f_p \int_0^{1/f_p} F_{inst}(t',t)\, dt' = \kappa f_p \left(1 - e^{-\Gamma/f_p}\right) \int dr\ C(r,t) N_{1a}(r) \tag{8.4}$$

While $F(t)$ averages out the micro-time dynamics we omit the angular brackets indicating temporal averaging to avoid notational confusion when presenting FCS theory below. One can of course average over both micro- and macro-times to find the average fluorescence intensity:

$$\langle F \rangle = \kappa f_p \left(1 - e^{-\Gamma/f_p}\right) \langle C \rangle \int N_{1a}(\mathbf{r})\, d\mathbf{r} \tag{8.5}$$

For purposes of notation consistency with FCS measurements, it is convenient to rewrite the fluorescence signal in terms of an "effective" molecular excitation rate, $\langle W_{eff}(\mathbf{r}) \rangle$, that describes the time-average number of excitation events per second at position **r**. The effective excitation rate has a simple relationship with the average fluorescence intensity given by $\langle F \rangle = \kappa \langle C \rangle \int \langle W_{eff}(\mathbf{r}) \rangle d\mathbf{r}$ [59, 60]. Comparison with Eq. (8.5) indicates that $\langle W_{eff}(\mathbf{r}) \rangle = N_{1a}(\mathbf{r}) f_p \left(1 - e^{-\Gamma/f_p}\right)$. Using this notation, we can rewrite Eqs. (8.3) and (8.4) above as:

$$\langle F_{inst}(t') \rangle = \frac{\kappa \Gamma e^{-\Gamma t'}}{f_p \left(1 - e^{-\Gamma/f_p}\right)} \langle C \rangle \int \langle W_{eff}(\mathbf{r}) \rangle d\mathbf{r} \tag{8.6}$$

and

$$F(t) = \kappa \int dr\ C(r,t) \langle W_{eff}(r) \rangle \tag{8.7}$$

Writing the fluorescence signals in terms of $\langle W_{eff}(\mathbf{r}) \rangle$ allows for direct comparison with standard FFS theoretical considerations. In particular, FFS measurements often refer to an "observation volume" [59, 63] which is defined as:

$$V = \frac{1}{\langle W_{eff}(0) \rangle} \int \langle W_{eff}(r) \rangle dr \equiv \int \langle \hat{W}_{eff}(r) \rangle \tag{8.8}$$

where $\langle \hat{W}_{eff}(r) \rangle$ is the normalized fluorescence excitation probability that defines the profile of the observation volume, again including both saturation and finite lifetime

effects. Higher order moments of $\left\langle \hat{W}_{eff}(r) \right\rangle$ are generally also needed to fully describe FFS theory. For FCS the additional required parameter is called the gamma factor [21, 63, 64] given by:

$$\gamma = \frac{\int \left\langle \hat{W}(\mathbf{r}) \right\rangle^2 d\mathbf{r}}{\int \left\langle \hat{W}(\mathbf{r}) \right\rangle d\mathbf{r}} \tag{8.9}$$

This parameter characterizes the uniformity of the fluorescence signal from molecules located at various locations within the volume and the effective steepness of the boundary defining the volume. We note that some authors prefer to incorporate the gamma factor into their definition of the volume, defining an effective detection volume as $V_{eff} = V/\gamma$ [27, 64, 65].

Using this volume notation, we can write the average fluorescence signal as:

$$\left\langle F \right\rangle = \kappa \left\langle C \right\rangle \left\langle W_{eff}(0) \right\rangle V \equiv \psi \left\langle C \right\rangle V \tag{8.10}$$

where we have introduced the "molecular brightness" parameter $\psi = \kappa \left\langle W_{eff}(0) \right\rangle$, so named because it reports the average number of fluorescence photons measured per molecule per second [10, 22, 66]. We note that molecular brightness is not a fundamental quantity, but depends both molecular properties (cross section and quantum yield), excitation conditions (laser power, pulse width, and beam waist), and the measurement instrumentation (detector and collection optics efficiencies).

Returning to Eqs. (8.6) and (8.7) we can write the full time dependence of the fluorescence signals as:

$$\left\langle F_{inst}(t') \right\rangle = \frac{\psi \left\langle C \right\rangle V}{\left(1 - e^{-\Gamma/f_p}\right)} \frac{\Gamma}{f_p} e^{-\Gamma t'} \tag{8.11}$$

and

$$F(t) = \psi \int dr\ C(r,t) \left\langle \hat{W}_{eff}(r) \right\rangle \tag{8.12}$$

8.3.2 Fluorescence Lifetime and FCS Data

Using the above theory it is straight forward to express the data from both lifetime and FCS measurements in terms of common global parameters. For lifetime data, which is composed of histograms from a total of $f_p T$ laser pulse cycles, and binned into time channels of width $\Delta t'$, the recorded signal can be written as:

$$F_{hist}^{data}(t') = \sum_i \frac{T \Delta t' \psi_i \langle C_i \rangle V}{\tau_i \left(1 - e^{-1/\tau_i f_p}\right)} e^{-t'/\tau_i} \tag{8.13}$$

where the subscript i represents each independent fluorescence species within the sample, and emission rates are replaced by fluorescence lifetimes, $\tau_i = 1/\Gamma_i$. Similarly, using well developed FCS theory [21, 59, 63, 67, 68] the correlation function for a multi-component sample is described as:

$$G(\tau_{fcs}) = \frac{\left\langle \delta F(t) \delta F(t + \tau_{fcs}) \right\rangle}{\langle F \rangle^2} = \frac{\gamma}{V} \frac{\sum_i \psi_i^2 \langle C_i \rangle A_i(\tau_{fcs})}{\left(\sum_i \psi_i \langle C_i \rangle \right)^2} \tag{8.14}$$

where $A_i(\tau_{fcs})$ represents the temporal relaxation of the correlation function for species i. For example, for pure diffusion with diffusion coefficient D in a three dimensional Gaussian volume with radial beam waist w_0, and an axial beam waist $a w_0$:

$$A(\tau_{fcs}) = \left(1 - \frac{8D\tau_{fcs}}{w_0^2}\right)^{-1} \left(1 - \frac{8D\tau_{fcs}}{a^2 w_0^2}\right)^{-1/2} \tag{8.15}$$

Equations (8.13), (8.14) & (8.15) clearly show how simultaneously acquired lifetime and FCS data sets depend on common global parameters, here concentration and molecular brightness, in addition to unique measurement specific parameters such as their diffusion coefficient and fluorescence lifetime. Subsequent data analysis using these linked global parameters facilitates enhanced model discrimination and constrains fitting parameter space to greatly enhance overall experimental resolution, as demonstrated below. We also note the different functional dependencies on these global parameters, whereby the amplitude of the lifetime data scales with the $\langle C \rangle \psi$ while the amplitude of the FCS data scales with $\psi^2 \langle C \rangle$. These differences in parameter dependence provide significant constraints for model discrimination in fitting routines.

8.3.3 Possible Additional Constraints

Beyond global fitting of multiple data types there may be additional theoretical constraints that can further reduce the number of free parameters used in curve fitting, effectively increasing experimental resolution. For example, while molecular brightness and fluorescence lifetime are generally independent parameters for different fluorescent molecules, they are not independent for the same molecule measured in different environmental conditions. These constraints will be specific to a given experimental system, and as such, must be evaluated on a case by case basis. For example, in a binding experiment in which a single fluorophore has different fluorescence lifetimes when free or bound, we expect their lifetime-brightness ratios to be equal, $\frac{\tau_{free}}{\psi_{free}} = \frac{\tau_{bound}}{\psi_{bound}}$. This allows us to reduce the number fit parameters by describing one parameter in terms of the other three.

The theory introduced above accurately describes fluorescence signals originating entirely from the molecular species of interest. In many cases there may be an additional background signal arising from room light, scattered laser light, or background fluorescence from sample contaminants or autofluorescence. If the background signal is significant compared to the signal of interest, then the background must be corrected for to accurately apply τFCS theory. The correction depends on the nature of the background. For room light or other time-constant background signals the correction for lifetime data is performed simply by subtracting the background from the total signal, while the correction for FCS requires a corrected correlation function. For an independently measured background signal, $\langle B \rangle$, the corrected correlation function amplitude is given by [63, 69]:

$$G(\tau_{fcs})_{corrected} = G(\tau_{fcs})_{measured} \cdot \left(\frac{\langle F \rangle + \langle B \rangle}{\langle F \rangle} \right)^2 \tag{8.16}$$

Here $\langle F \rangle$ represents the fluorescence signal of interest described in Eq. (8.10) above, i.e. the measured background signal would need to be subtracted from the measured signal amplitude, $\langle F \rangle + \langle B \rangle$, to determine the value of the average fluorescence. If the background is not constant, with measurable lifetime or non-trivial fluctuation dynamics, then it must be treated as an additional molecular species according to the theory introduced above.

8.4 Methods

We demonstrate experimentally that τFCS can accurately recover molecular concentrations, diffusion coefficients, molecular brightnesses, and excited state lifetimes

from binary dye mixtures with very similar diffusion coefficients. In this case FCS measurements alone could not identify the presence of two distinct molecular species in the sample. We also use calculated data sets to demonstrate the capability to resolve these same sample properties even when the diffusion coefficients and molecular brightness values for each sample component are identical, illustrating the unique resolution enhancements introduced by using the multi-parameter fluorescence measurements with global fitting since no fluctuation methods alone could resolve such a sample.

8.4.1 Experimental

Measurements were performed using an updated version of a previously described home-built system [56, 70]. Briefly, two-photon excitation was provided by an ultrafast Titanium:Sapphire Tsunami laser (~100 fs pulses at 80 MHz ; Spectra Physics) tuned to 800 nm. Power was controlled using a λ/2 plate and polarizing cube, and was set to 5 mW at the sample. The beam was ported into an inverted microscope (IX71, Olympus) and expanded 4x before reflected by a dichroic mirror (675DCSX, Chroma Technology) into an Olympus 60× water immersion objective lens (UPLSAPO60XW, Olympus; NA = 1.2). Fluorescence signal collected by the objective passed through the dichroic mirror and a low pass filter (E700SP, Chroma Technology) before impinging on a hybrid photodetector (Becker and Hickl HPM 100-40; Boston Electronics). Data acquisitions of 200 s per titration point were collected using a time correlated single photon counting (TCSPC) module (PicoHarp300, PicoQuant GmbH). Laser pulse synchronization was provided by a battery powered fast photodiode (New Focus, Model 1621). The TCSPC histograms and autocorrelation curves were calculated using SymPhoTime software and exported for analysis in Igor Pro (Wavemetrics, Inc., OR). TCSPC histograms were

binned at 4 ps, and selected to contain approximately 5×10^7 counts. Autocorrelation curves were calculated from 0.0001 to 100 ms with 16 points per time coarsening (Nsub) using the entire 200 s data set.

Rhodamine 6G (R6G; Sigma Cat# 252433) and Rhodamine B (RhB; Sigma Cat# R6626) dye solutions were prepared in HBS-EP buffer (10 mM Hepes, 150 mM NaCl, 3 mM EDTA, 0.005% Polysorbate 20; TEKnova Cat# H8020). Concentration titrations were performed to obtain a calibrated series of dye mixtures, starting with an 800 µl mixture with R6G and RhB at 50 nM each, a 1:1 concentration ratio. Samples were loaded into an 8-well chamber boxes (Lab-Tek II; No. 1.5 coverglass, Nunc; Thermo Fisher). R6G/RhB concentrations ratios >1 were achieved by sequentially removing 400 µl of solution from the chamber and replacing it with 400 µl of 100 nM R6G. Concentration ratios <1 were similarly prepared by replacing the solution removed with 400 µl of 100 nM RhB. This method of preparing samples greatly reduces variation in sample concentrations due to surface absorption (see below) and is essential for preparing calibrated solution concentrations. This procedure provided sample mixtures with concentrations ranging from 4 to 97 nM for R6G and 4 to 89 nM for RhB, leading to a final R6G/RhB concentration ratio ranging from approximately 0.04 to 20.

FCS and Lifetime measurements were performed for each sample mixture in the complete titration range, with the full titration repeated three times. Data points and error bars reported reflect the average and standard deviation of these three repeated experiments. To ensure prepared samples concentrations matched their expected values, a series of control measurements were also performed in the same sample chamber with solutions of each dye solution independently (R6G or RhB alone), using FCS measurements to determine the actual sample concentration. The same procedure

described above was repeated, except that HBS-EP buffer without the second dye was used to dilute the concentration. In general, dye solutions in water were found to exhibit unstable fluorescence count rates due to interactions with surfaces and chamber coatings that are applied by the vendor. However, highly stable dye solutions were attained using HBS-EP buffer in combination with a repeated chamber box cleaning. To clean, a single chamber box well was washed with detergent, followed by repeated rinses with hot water, and finally scrubbed with a cotton swab using ultra-pure water. The cleaning procedure was repeated before each titration. Measurements of ultra-pure water in the cleaned chamber never showed signal above the background level of ~ 1 kHz, measured independently with the laser out of mode-lock.

8.4.2 Analysis

TCSPC histograms and FCS autocorrelation curves (ACFs) were analyzed using custom and native global analysis routines in Igor Pro. For τFCS analysis, a TCSPC histogram and the simultaneously acquired ACF are considered together as one independent τFCS data set (Figure 8–1A). All fits in Igor Pro were performed using a Levenberg-Marquardt non-linear least squares algorithm which minimizes the χ^2 value, for a τFCS data set defined as:

$$\chi^2 = \left(\sum_{i=0}^{k-1} \frac{\left(F_{hist}^{data}(x_i) - y_i \right)^2}{\sigma_{decay}(x_i)} + \sum_{i=k}^{k+l-1} \frac{\left(G(x_i) - y_i \right)^2}{\sigma_{fcs}(x_i)} \right) \tag{8.17}$$

where k and l are the number of data points in the lifetime histogram and the calculated autocorrelation function respectively. Observation volume parameters, w_0 and a, were calibrated using R6G in H_2O solution assuming a diffusion coefficient of 426 $\mu m^2 s^{-1}$ [71].

We present two different approaches for data analysis. The first is applicable when a τFCS data set is available for only a single sample condition, e.g. a single concentration ratio, which is a common experimental scenario. In this case, the analysis is 'global' in that the TCSPC and FCS data have common global fitting parameters (molecular concentration and molecular brightness) that are linked across the data types (each has a single value for both types of data), and other local parameters including the lifetimes and diffusion coefficients (Figure 8–1A). For this case, there is often insufficient resolution to obtain stable fitting results with no a priori knowledge, and independent measurement of a fluorescence lifetime, diffusion coefficient, or some other parameter(s) may be required for good curve fitting results. A second analysis approach is used when multiple τFCS data sets are available with one or more experimental variables, such as sample concentration, varied across the data sets (Figure 8–1B). For this case, the global fitting routine can be applied to all of the τFCS data sets simultaneously, with a single set of global parameters that are linked across all of the τFCS data sets and separate local parameter sets for each τFCS data set.

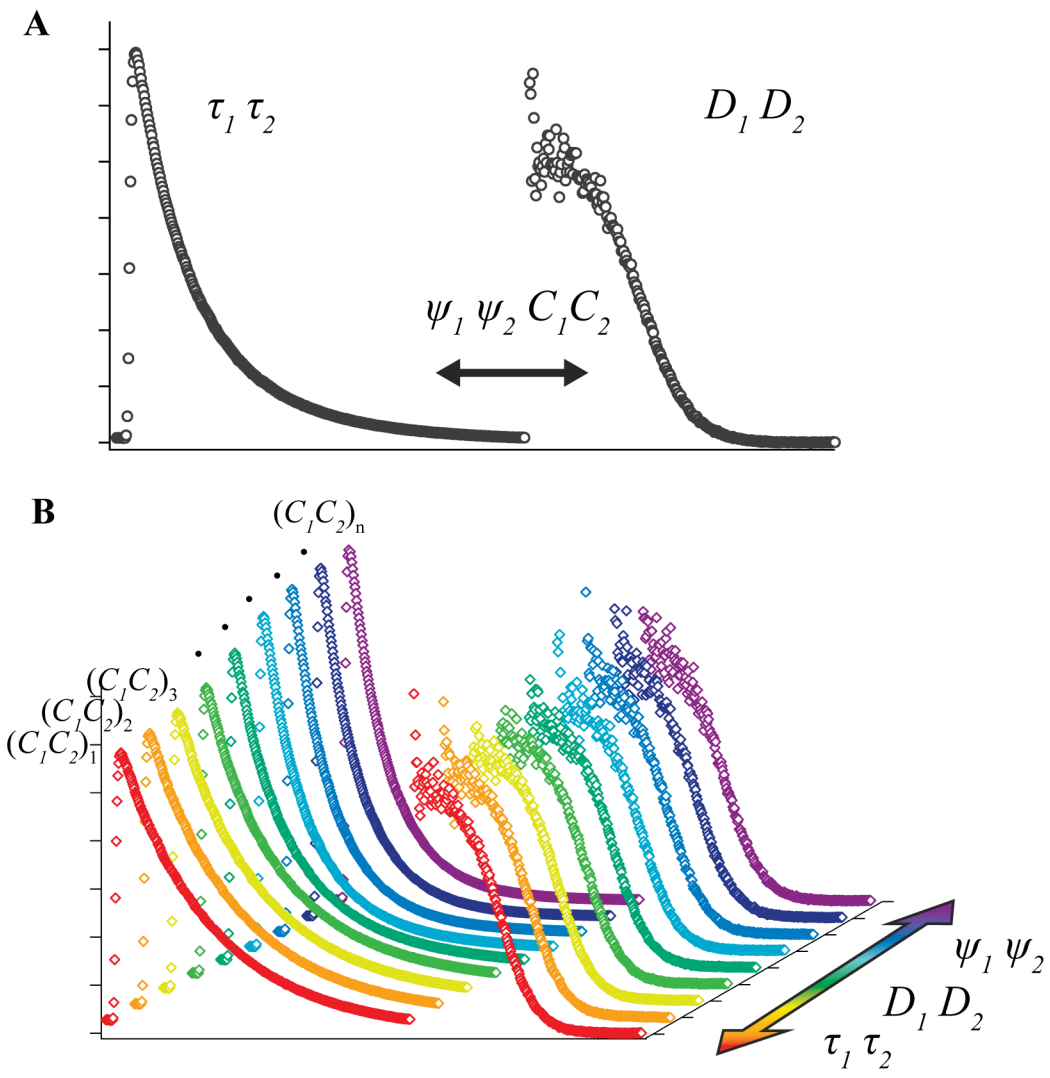

Figure 8–1 – Comparison of (A) τFCS and (B) global-τFCS analyses. τFCS analysis allows brightnesses and concentrations to be treated globally across the two data modalities due to common parameters now describing the amplitudes of both the lifetime decay and autocorrelation function. Global-τFCS intrinsically retains the pair-global relationship for each pair individually, in addition to treating the lifetimes, diffusion coefficients, and brightnesses as global parameters across all pairs of the titration. Data has been normalized for visual comparison.

8.4.3 Systematic Error

TCSPC histogram data sets were found to contain significant systematic non-Poissonian noise at GHz frequencies (Figure 8–2A; red line), believed to originate from differential non-linearities within the TCSPC module and other electronic noise. This systematic noise was found to vary linearly with total photon count per time bin in a highly reproducible manner such that this systematic noise could be easily subtracted from the signal. A data point of uncorrelated room light containing a comparable or greater number of photon counts as experimental acquisitions was recorded to determine the correction. A 100 point binomial smooth operation was performed to remove Poissonian noise while retaining the lower frequency systematic noise (Figure 8–2B; black line) [72]. The smoothed reference noise data set was then scaled by the photon counts and subtracted from the signal to remove the non-Poissonian systematic noise while retaining the inherent Poissonian noise [73]. This procedure was followed for all experimental TCSPC data sets.

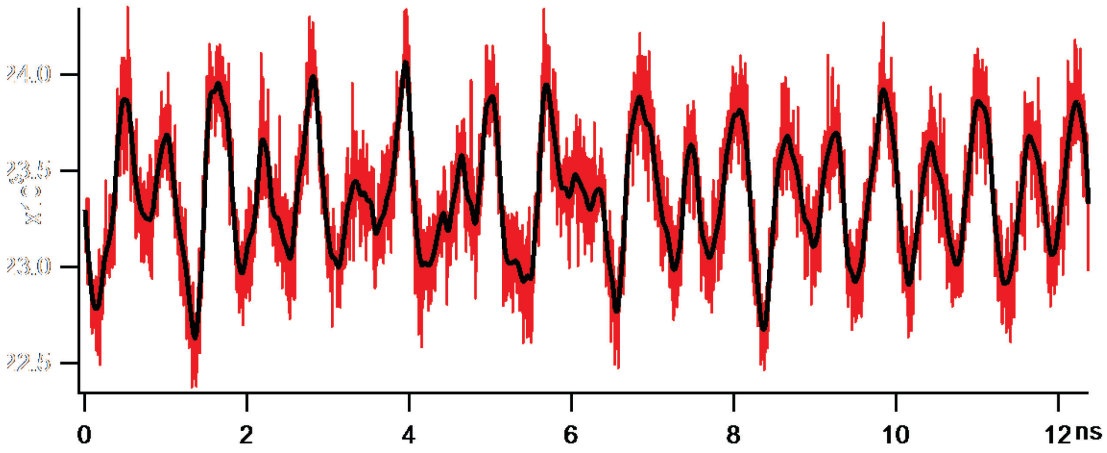

Figure 8–2 – Reference data set recorded using uncorrelated light to assess the systematic error in data acquisitions (red line). A 100 point binomial smoothed data set

(black line) removes Poissonian noise while retaining the lower frequencies used for data corrections.

Data fits to experimental decay curves included a temporal offset such that the peak of the instrument response function (IRF) corresponds to $t' = 0$, but were not reconvolved with the IRF during fitting. The IRF was recorded using hyper-Rayleigh scattering [74] from colloidal gold solutions (Sigma Cat# G1652) at low excitation powers.

8.4.4 Simulation

Simulated data sets were created using Eqs. (8.13) & (8.14) for a given parameter set followed by the addition of random noise. TCSPC histograms were created with a total of 5×10^5 counts followed by the addition of Poissonian noise for a given number of counts per bin. Noise added to ACFs was determined using noise levels from experimental ACFs acquired under comparable conditions [75]. The ACF acquisition time, *T*, for all calculated data sets was 30 seconds.

8.5 Results

The primary goal of this work is to demonstrate how experimental resolution and model discrimination capabilities in FFS can be dramatically enhanced by using MFD and global analysis, here shown through the implementation of τFCS. We thus use a mixture of Rhodamine 6G and Rhodamine B molecules, an experimental system for which a standard FCS experiment would not be capable of identifying the presence of two sample components nor accurately recovering their concentrations and other physical properties. This dye pair has a diffusion coefficient ratio of approximately 1.2 (D_{R6G} =

390 $\mu m^2 s^{-1}$; D_{RhB} = 465 $\mu m^2 s^{-1}$), considerably smaller than the minimum ratio of 1.6 previously reported as necessary to resolve multiple species by FCS [54]. This mixture would therefore appear as a single species using FCS analysis alone. The fluorescence lifetimes of these two dyes are sufficiently different (τ_{R6G} = 3.92 ns; τ_{RhB} = 1.63 ns), such that fluorescence lifetime measurements can easily resolve the two lifetime values, demonstrating the utility of MFD and the ability to detect the presence of multiple species. However, since lifetime fitting can only resolve lifetime values and fractional intensities, lifetime measurements alone cannot determine molecular concentrations, diffusion coefficients, or molecular brightnesses. Even after determining the presence of two species from the lifetime data, a traditional MFD approach fails to recover this information since the FCS analysis alone could still not achieve a stable fit for a two-component model. Conversely, τFCS analyses does produce a stable fit and accurate parameter recovery, thus providing a vastly improved functionality over FCS and/or TCSPC measurements alone.

To illustrate this method, we begin by analyzing individual τFCS data sets acquired from each of the prepared dye mixture ratios. As described above, the concentration of the two dyes ranges from approximately 4 to 97 nM, providing concentration ratios, reported as C_{R6G}/C_{RhB}, spanning across almost three orders of magnitude. The dye concentrations for each mixture are known from calibration measurements described in the methods, and comparing values recovered by τFCS to calibrated values of known dye concentrations allows us to assess the accuracy of this new analysis technique. We note that fitting of τFCS for a single sample condition (i.e. a single C_{R6G}/C_{RhB} concentration ratio) can work well, but resolution limits do require some a priori knowledge of the sample components to obtain stable data fits. Here we assume that the lifetime, molecular brightness, and diffusion coefficient of the R6G molecules (τ_{R6G}, ψ_{R6G} & D_{R6G})

can be measured independently, thus remaining as fixed fitting parameters during the τFCS analysis. Details of all parameter values are shown in Figure 8–3. τFCS fitting results (Figure 8–3; squares) can be compared to the known concentrations of dye molecules (Figure 8–3; solid lines), demonstrating accurate recovery of the molecular concentration, molecular brightness, and diffusion coefficient for each species in the rhodamine mixtures over a fairly wide range of concentration ratios. As noted above, FCS or lifetime measurements alone would not be capable of recovering these parameters. The R6G dye has a higher molecular brightness than the RhB, and together with being the calibrated and held dye during fitting its concentration (red squares) can be accurately measured across all points of the titration. The RhB concentrations (blue squares) are harder to measure due to the lower molecular brightness and free parameters of the RhB molecule, yet we still see accurate concentration measurements up to a concentration ratio of approximately 3. Above the concentration ratio of approximately 3 the recovered value of C_{RhB} becomes unstable in the curve fitting routines and is sensitive to initial parameter guesses due to the covariance of the molecular brightness and concentration parameters. These instabilities can also been seen in the recovery of the diffusion coefficient (Figure 8–3D) and brightness (Figure 8–3C) of RhB, which are otherwise quite accurate at lower concentration ratios. This observation is not unexpected since the molecular brightness of RhB is lower than the brightness of R6G, such that at higher concentration ratios the RhB signal becomes an increasingly small fraction of the total fluorescence signal. Also, since each molecular species' contribution to the measured correlation function amplitudes varies with the square of its molecular brightness, the molecule with lower brightness is harder to measure at lower concentrations than the brighter molecular species, in this case R6G. TCSPC measurements can accurately determine the fluorescence lifetimes of multiple

sample components independently of any FCS analysis, so the measured lifetime values do not exhibit similar instabilities even at high concentration ratios (Figure 8–3B).

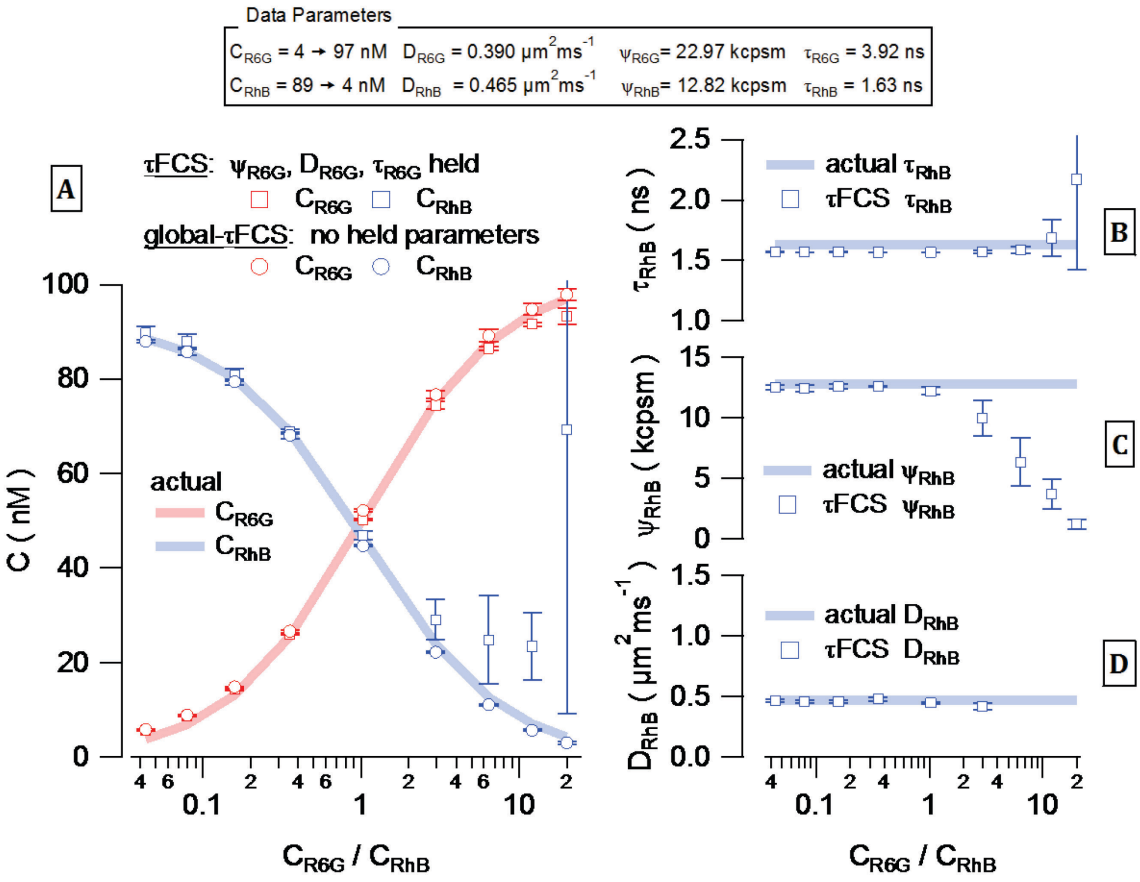

Figure 8–3 – τFCS analyses of combined FCS and lifetime data from mixtures of rhodamine 6G (R6G; red) and rhodamine B (RhB; blue). Absolute concentrations span approximately 3 to 97 nM, providing a calibrated concentration ratio, C_{R6G}/C_{RhB}, from 0.04 to 20. Recovered concentrations (A) using τFCS (squares) and global-τFCS (circles) in comparison to calibrated concentrations (solid lines). τFCS analysis is performed on each point in the titration and requires that D_{R6G}, ψ_{R6G}, and τ_{R6G} are known and held during fitting. Recovered C_{R6G} values are accurate across the entire titration, while C_{RhB} values become inaccurate above a ratio of approximately 3. The recovered D_{RhB} (D), ψ_{RhB} (C), and τ_{RhB} (B) values also become unstable and inaccurate above the same ratio. The

covariance relationship of the free parameters causes these instabilities when only a small fraction of RhB remains. Global-τFCS analysis recovers extremely accurate concentration values across the entire titration ratio range, and does not require any held parameters during fitting. These free parameters are consistent across all points of the titration; recovered single values are shown in Table 8–1A. Data points and error bars show the mean and standard deviation of 3 repeat titrations.

As shown above, combing TCSPC and FCS data for fitting as a single τFCS data set can result in greatly improved resolution of the molecular composition of a sample. The major limitations of the method, as introduced so far, are that some a priori knowledge of the sample was required for stable curve fitting and the full concentration range could not be accurately fit. Each of these limitations can be dramatically overcome if one leverages the full power of global analysis. Specifically, if an experimental parameter can be varied over a series of measurements then global analysis allows curve fitting of the entire measurement series with common experimental parameters across all of the data sets. Here we have systematically varied the rhodamine dye concentrations, acquiring τFCS data at each ratio, C_{R6G}/C_{RhB}. Full global analysis of the data involves simultaneously fitting all data sets with a single, globally linked parameter set for the lifetime, molecular brightness, and diffusion coefficient (τ, ψ & D) of each species in the sample. Two additional "local" fitting parameters, C_{R6G} and C_{RhB}, are associated with each individual data set to account for the different molecular concentrations of rhodamine dyes at each concentration ratio.

The results from the full global fit are shown as circles in Figure 8–3A, and the returned global parameters are shown in Table 8–1A. It is immediately apparent that the full global fits achieve remarkable accuracy across the entire measured concentration range.

This includes accurate recovery of the molecular concentration of RhB, the species with lower molecular brightness, even when it constitutes only a few percent of the molecules within the sample. This level of sensitivity for a minor species goes well beyond what is typically achievable in FCS measurements even for cases where the two species diffusion coefficients are sufficiently different to measure with FCS alone. Moreover, the τFCS approach to fluctuation measurements can greatly enhance sensitivity and resolution. We further note that these extraordinary results were obtained without any constraints on fitting parameters, and unlike the individually fit data sets the full global fits assume no prior knowledge of any molecular brightness, diffusion coefficient, or lifetime value. None-the-less, the fits returned stable fitting parameters with high accuracy across the entire data set. This offers a tremendous advantage for applications of this method. For complex experimental systems it may be impossible to isolate an individual molecular species for calibration purpose, or calibrations performed under one sample condition (e.g. diffusion coefficients for isolated molecules) may not accurately reflect actual values in a different sample condition (e.g. diffusion coefficients within a living cell). The full global analysis approach completely eliminates the need for any molecule specific calibration measurements, and still returns accurate results across a wide range of sample compositions.

A		*Full-Global*		*Cali.*
		Fit	Rel. Err	
R6G	***D***	0.387 ± 0.004	0.8%	**0.390 ± 0.008**
	τ	3.913 ± 0.004	0.2%	**3.921 ± 0.004**
	ψ	22.31 ± 0.18	2.9%	**22.97 ± 0.70**
RhB	***D***	0.463 ± 0.006	0.6%	**0.465 ± 0.014**
	τ	1.571 ± 0.002	3.7%	**1.632 ± 0.003**
	ψ	12.76 ± 0.08	0.5%	**12.82 ± 0.40**

B		*Full-Global*		*Calc.*
		Fit	Rel. Err	
Rh1	***D***	0.429 ± 0.002	0.2%	**0.430**
	τ	3.92 ± 0.04	0.0%	**3.92**
	ψ	14.98 ± 0.08	0.1%	**15.00**
Rh2	***D***	0.428 ± 0.001	0.5%	**0.430**
	τ	1.62 ± 0.01	0.6%	**1.63**
	ψ	14.99 ± 0.01	0.1%	**15.00**

Table 8–1 – Recovered fit parameters using full global analysis of rhodamine-6G and rhodamine-B experimental data (A), and idealized rhodamine species Rh1 and Rh2 calculated data sets to explore the possibility of identical diffusion coefficients and molecular brightness (B). No constraints were used and no parameters were held during the analysis. 'Fit' columns indicate average and standard deviation of three separated acquisitions/simulations. 'Rel. Err.' column provides the relative error between the returned fit values and the calibrated expected values, or the calculation values (blue columns).

There are two important principles underlying the success of the τFCS approach. First, by using MFD it is often possible to find a contrast parameter that can distinguish multiple sample components that may otherwise be disguised in a particular

measurement. In the case of τFCS, fluorescence lifetime serves as the contrast parameter, detecting the presence of two sample components where FCS alone would not be able resolve a second species. Second, and as equally important, global fitting of multiple measurement modes (e.g. FCS and TCSPC) simultaneously enhances the resolution of each individual method during curve fitting as different methods have unique functional dependencies on the global parameters. Here, for example, the amplitude of fluorescence lifetime data depends linearly on the molecular brightness while the FCS amplitude depends on a non-linear function the molecular brightness determined by the ratio of parameters given in Eq. (8.14). Thus, an analysis method that forces common global fitting parameters to account for total fluorescence signal across independent measurement modes has a greatly constrained fitting parameter space and produces much better curve fitting results. To further illustrate this principle, we show τFCS results for a computed model data sets in which two hypothetical dyes, Rhodamine-1 (Rh1) and Rhodamine-2 (Rh2), have identical molecular brightnesses and diffusion coefficients. Unlike the measurement shown above, where the molecular brightnesses were sufficiently different to be resolved by techniques such as PCH or Cumulant methods, fluctuation methods alone would not be able to resolve these hypothetical molecules.

Hypothetical Rh1 and Rh2 molecular mixtures have been modeled using calculated fluorescence lifetime decays and autocorrelation functions that mimic the parameters of the Rhodamine dye titrations shown in Figure 8–3. However, the molecular brightnesses are set equal at $\psi_{Rh1} = \psi_{Rh2} = 15$ kcpsm, and the diffusion coefficients equal at $D_{Rh1} = D_{Rh2} = 0.43\ \mu m^2 ms^{-1}$. The computed TCSPC histograms contain 5×10^6 photon counts and the FCS curve is created equivalent to a 30 s measurement. As before, each individual concentration can bit fit alone with good results, similar to those reported

above, but still requiring that the molecular brightness and diffusion coefficient for one of the two species is fixed. The recovered concentrations (Figure 8–4A; squares) for both Rh1 and Rh2 are extremely accurate across the entire concentration ratio range. In addition, the recovered lifetime (Figure 8–4B), brightness (Figure 8–42C) and diffusion coefficients (Figure 8–4D) of Rh2 are accurate within error across nearly all concentration ratios. More impressive again is the use of a full global analysis, simultaneously fitting all concentration ratios for this computed data set. The results of that analysis are shown in Figure 8–4A (circles), and Table 8–1B. We know of no analysis protocol that can produce comparable resolution of sample composition for mixtures such as these, especially given that this analysis can be completed with no *a priori* knowledge of the parameters for any of the sample components. We believe it greatly extends the general potential of fluctuation methods to resolve sample composition, stoichiometry, and molecular interactions, even for complex systems and mixtures for which no prior calibration is possible.

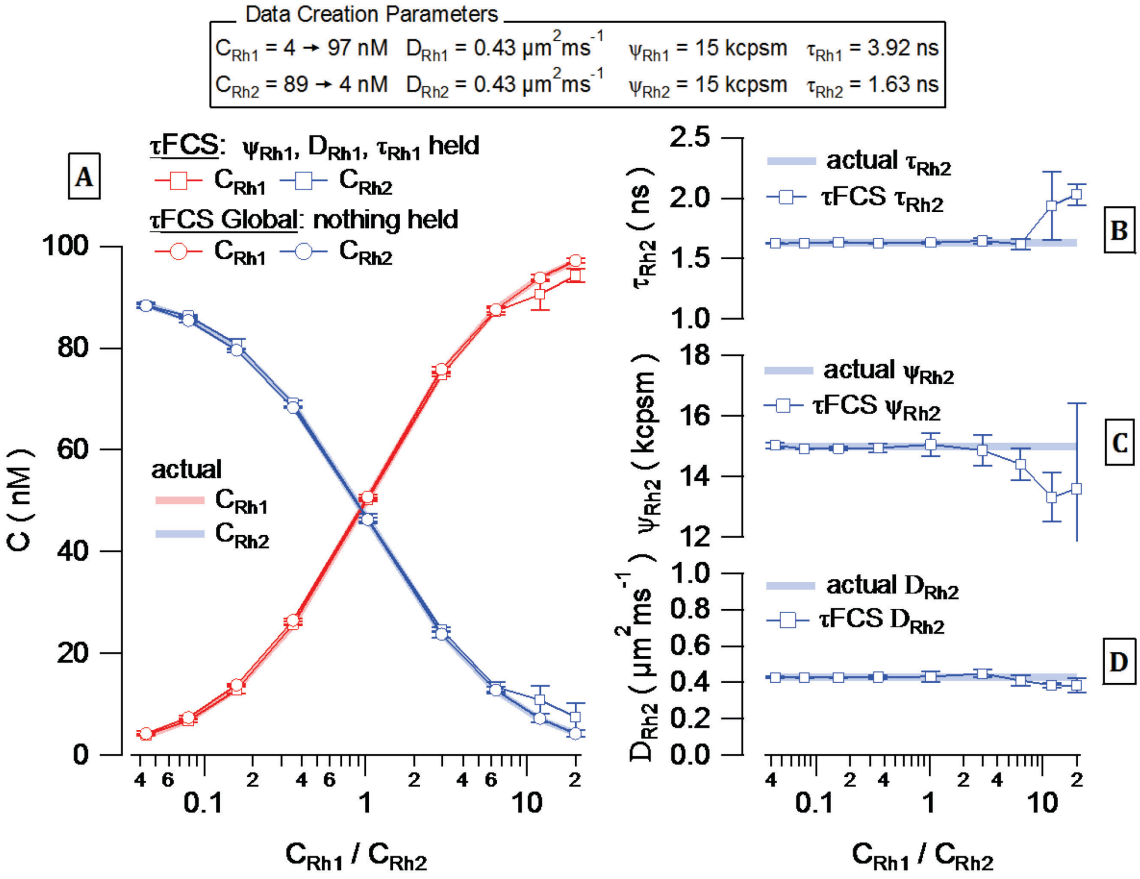

Figure 8–4 – τFCS analysis of calculated FCS and lifetime data simulating a two species titration mixture: species a (red) and species b (blue). Parameter values are chosen to mimic those of R6G (species a) and RhB (species b), except assigning an equal molecular brightnesses of $\psi_a = \psi_b = 15$kcpsm. Recovered concentrations (A) using τFCS (squares) in comparison to actual values used to create data sets (solid lines). τFCS analysis, performed on each point in the titration with D_a, ψ_a, and τ_a held fixed, recovers both concentrations accurately across the entire range of ratios. The amount of error increases for low concentrations of species b, the 'free' species in terms of parameters held. The increase in error is also reflected in τ_b (B), ψ_b (C), and D_b (D). Data points and error bars show the mean and standard deviation of 3 repeat calculated data sets.

To further illustrate how the τFCS approach reduces uncertainly in fluctuation analysis, we consider a simple ligand binding experiment in which a fluorescent ligand binds to a non-fluorescent receptor. When the receptor is larger than the ligand, the diffusion coefficient of the bound species will be smaller than for the free ligand. In many cases the difference in diffusion coefficient is sufficient for FCS to easily resolve the two components. Curve fitting for a variety of concentration conditions – bound and free – can then be used to determine dissociation constants and binding energetics [76, 77]. Easily overlooked in such an experiment is that the fluorescent ligand is often quenched or de-quenched upon binding, changing its molecular brightness value. A standard FCS measurement cannot independently resolve the change in brightness as the molecular brightness is covariant with the concentration during curve fitting. Standard FCS analysis in this situation thus requires one parameter, either brightness or concentration, to be held fixed during the curve fitting. If held fixed at an erroneous value, i.e. if one assumes molecular brightness does not change upon binding when it actually does, the concentration parameters recovered will also be incorrect. Moreover, there will be no indication that the analysis is wrong since the goodness of fit determined from the chi-squared parameter will be comparable for the correct and incorrect guesses. In principle one can fix this problem by calibrating the brightness values using independent measurements, provided each species (e.g. bound and free) can be isolated for measurement. However, in many experimental systems this may be difficult or impossible - especially experiments in living systems or complex materials applications - and at the very least introduces extra complications to the measurement. Conversely, τFCS can remove any source of error or confusion, as changes in molecular brightnesses are automatically measured *via* the combined MFD and global analyzes.

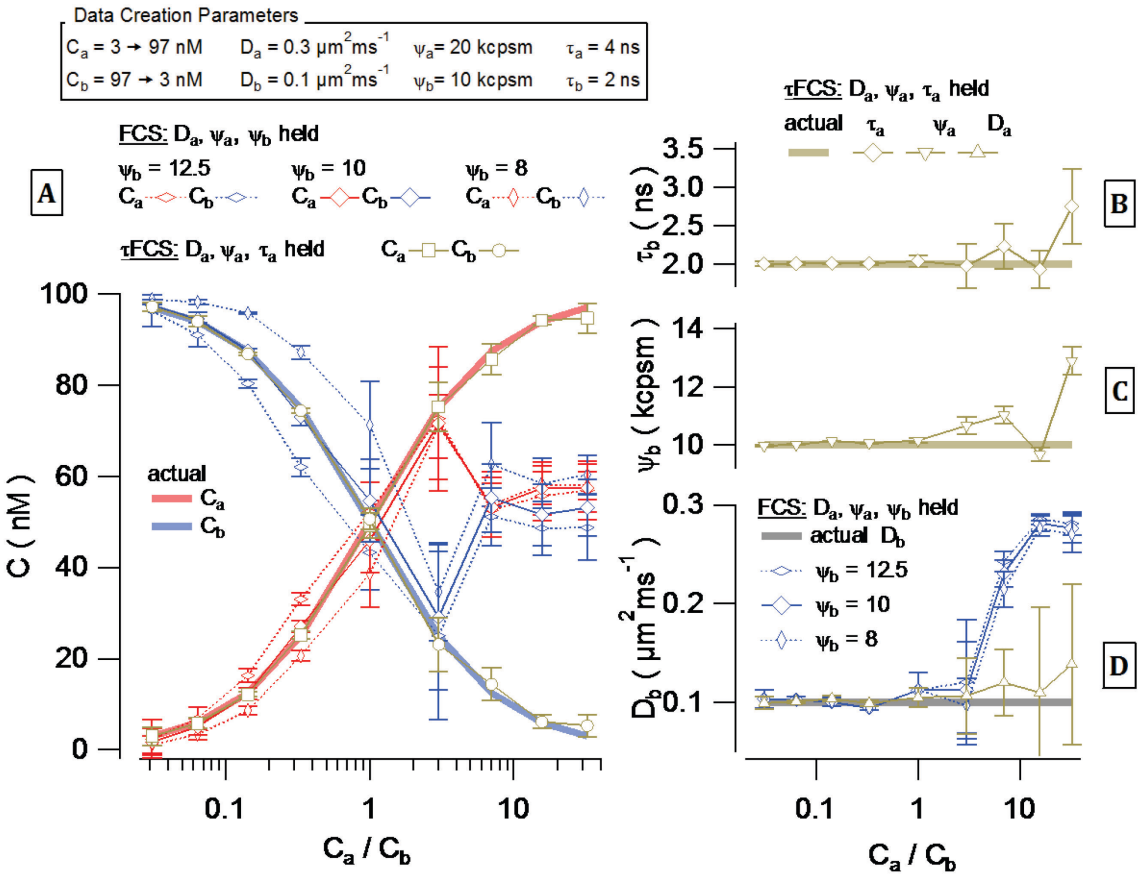

Figure 8–5 - Comparison of FCS and τFCS analyses showing the errors incurred from incorrect brightness values and the increased accuracy attained using τFCS. Two species data sets (a, red, and b, blue) calculated with D_a = 0.3 μm²ms⁻¹, D_b = 0.1 μm²ms⁻¹, ψ_a = 20 kcpsm, ψ_b = 10 kcpsm, τ_a = 4 ns, and τ_b = 2 ns. Using FCS only, the covariance of concentration and brightness requires that both brightnesses be known *a priori* to attain stable data fits. Concentrations recovered using FCS alone are accurate only when the correct brightness is used, ψ_b = 10 kcpsm (A; solid lines & diamonds), and only to a limited fraction of second species. Incorrect assumptions (dashed lines) of lower brightness, ψ_b = 6 (vertical diamonds), or a higher brightness, ψ_b = 14 (horizontal diamonds), return incorrect concentration values across the same range. The concentration ratio of approximately 3 corresponds to the point at which FCS analysis fails to distinguish the small fraction of the slower diffusing species (D). Beyond this

point, D_b transitions to D_a, and the recovered concentrations become unstable, centered around 50 nM. This indicates the amplitudes are shared between two species both with $D_a = D_b = 0.3\ \mu m^2 ms^{-1}$. D_a, ψ_a, and ψ_b are held parameters during FCS only analysis. Using τFCS, analysis is performed with ψ_b as a free parameter, and as such, no assumptions of the molecular brightness are required. τFCS recovers both concentrations successfully across the entire titration range, demonstrating the improved accuracy when using τFCS. In addition, τFCS correctly returns the ψ_b (C) and τ_b (B) parameters across the majority of the range. τ_a is an additional held parameter during τFCS analysis.

Figure 8–5 shows examples of how incorrect assumptions of molecular brightnesses can lead to significant errors in recovered concentrations. To illustrate this we calculated fluorescence lifetime decays and autocorrelation functions data sets for a new two species sample, a (Figure 8–5, red) and b (Figure 8–5, blue), using the molecular parameters $D_a = 0.3\ \mu m^2 ms^{-1}$, $D_b = 0.1\ \mu m^2 ms^{-1}$, $\psi_a = 20$ kcpsm, $\psi_b = 10$ kcpsm, $\tau_a = 4$ ns, and $\tau_b = 2$ ns. For illustration purposes we first analyze the calculated data using FCS at each point in the titration, where D_a, ψ_a, and ψ_b are fixed parameters as required for stable fitting. During the fitting process the brightness of species b was held fixed at three specific values, using either the correct molecular brightness ($\psi_b = 10$), a high ($\psi_b = 12.5$) or low ($\psi_b = 8$) assumed brightness value. As can been seen in Figure 8–5, incorrect assumptions (all dashed lines) of lower brightness, $\psi_b = 8$ (vertical diamonds), or a higher brightness, $\psi_b = 12.5$ (horizontal diamonds), return inaccurate concentration values. However, the difference in χ^2 values between fits using the correct and incorrect brightness values is not significant and as such inaccuracies can easily go unnoticed. Curve fitting using the correct brightness for ψ_b (A; solid lines/diamonds) shows more

accurate recovery of the concentrations as expected for FCS applications of this type. Noteworthy however is that even for this case, the fitting is accurate only up to a limited fraction of second species, becoming less precise towards the concentration ratio of 1, and begins to fail at concentration ratios greater than 3. Above this ratio the returned value for D_b transitions to the value of D_a, and the second species is no longer resolved.

In contrast, using τFCS recovers both concentrations successfully across the entire titration range (Figure 8–5A; gold squares and circles). This superior fitting result is achieved without any assumptions needed for the molecular brightness of species b since, unlike FCS, τFCS does not require using a fixed value of ψ_b for stable curve fitting. The τFCS fits also correctly return the values of lifetime, brightness, and diffusion coefficient for the second species, i.e. τ_b, ψ_b, and D_b, across the full concentration range (Figure 8–5 B, C, and D respectively). This is a highly demanding curve fitting situation for which FFS methods used alone – including molecular brightness based assays – would fail, which clearly demonstrates how τFCS dramatically advances FFS measurement capabilities. We also noted above how using MFD with global analysis enhances curve fitting accuracy for each measurement type over that measurement alone. This feature is clearly seen in this result, as the FCS alone measurement failed to recover accurate concentration values at higher concentration ratios even when the correct molecular brightness value was used for fitting. The τFCS results show no comparable difficulties.

8.5.1 Model Discrimination and resolution

We have demonstrated that τFCS can greatly advance FFS measurement capabilities. Two species samples that could not be resolved with FFS alone were easily and

accurately measured with τFCS and required no *a priori* knowledge of sample composition. Full global analysis also significantly extended the range of concentration ratios that can be measured, accurately recovering the concentration of both components of a sample, even in the case of a lower molecular brightness second species constituting only a few percent of the total molecules in the sample. These fits all assumed the presence of two sample components. For the data shown above, the lifetime measurements clearly indicated two molecular species were present such that the two species model used for curve fitting is easily justified. For many experiments, particularly within cells or other complex environments, the presence or absence of two sample components may not be known *a priori*. Thus, an important question to consider is how different the lifetime or diffusion coefficient values must be for curve fitting routines to reliably indicate the presence of two sample components. Selecting the correct model for data fitting is imperative for confident interpretation of results.

To investigate this question we use computationally generated data sets to determine the range of lifetime and diffusion coefficient ratios for which curve fitting to a single species indicated a sufficiently poor fit to reject the single component model. When single-species data fits appear correct, returning a χ_R^2 value close to 1, we concluded that the analysis could not reliably predict the presence of the second species. For the purposes of this example we arbitrarily define a χ_R^2 value of 1.3 as the threshold for model discrimination, where $\chi_R^2 < 1.3$ indicates a good fit (i.e. second-species not found). We note that for real experimental conditions the χ_R^2 threshold value could vary depending on the accuracy of estimates for random and systematic noise levels. Figure 8–6 shows the results from this analysis, plotted as cross sections of χ_R^2 surfaces. These χ_R^2 surfaces are compiled from analyses using four different single species models: FCS

alone (green lines), standard lifetime alone (yellow lines), lifetime using Eq. (8.13) with $\langle F \rangle$ constraint (blue lines), and τFCS, also with $\langle F \rangle$ constraint (red lines). Each surface point is the average χ_R^2 from three repetitions with unique simulated noise (see methods). All parameters were assumed to be unknown and none were fixed during the analyses. However, we did implement the average fluorescence constraint to remove fitting problems associated with the covariance of the concentration and molecular brightness. In practice, this is a readily available constraint as the average fluorescence intensity is always known from the experiment. Implementing this constraint would not be possible using lifetime alone, which simply has an amplitude parameter.

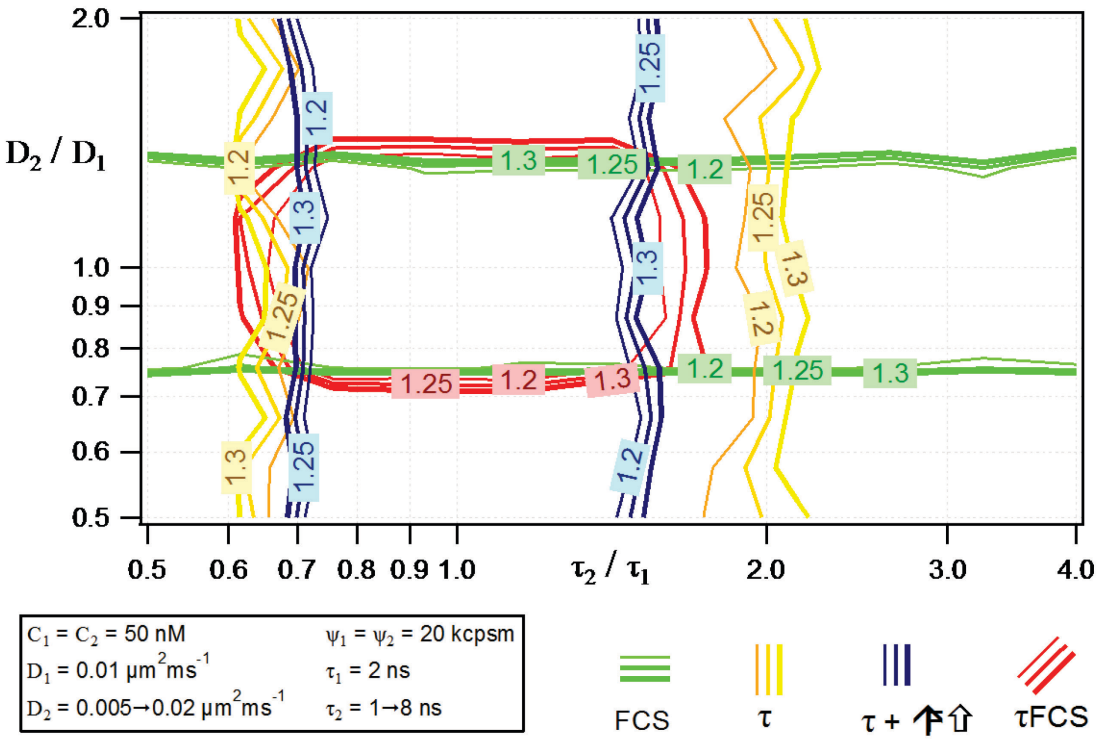

Figure 8–6 –Sections of χ_R^2 surfaces obtained from fitting single species models to calculated data of a binary mixture over a range of parameter values. Single species models used: FCS alone (green lines), lifetime alone (yellow lines), lifetime decay using

τFCS theory with $\langle F \rangle$ constraint (blue lines) and τFCS with $\langle F \rangle$ constraint (red lines). Line sections of full χ_R^2 surfaces indicate the boundaries at which a single species model sufficiently fits the two-species data. Using FCS alone, correct identifying a second species is attained using parameters outside of the horizontal area centered on $D_2/D_1 = 1$. Similarly, lifetime models discern a second species outside vertical areas around $\tau_1/\tau_2 = 1$. Comparison of lifetime alone (blue lines) and τFCS incorporated lifetime with $\langle F \rangle$ constraint (yellow lines) shows an improved model discrimination, in addition to greatly increasing the steepness of the χ_R^2 surface, leading to faster more accurate data fits. Pair-global analysis of τFCS combines the vertical and horizontal areas occupy a symmetric region centered on $\tau_1/\tau_2 = D_2/D_1 = 1$, allowing for concentration, diffusion and molecular brightness information to be identified over a much wider range of experimental parameters.

Model discrimination using FCS analysis alone yields a horizontal χ_R^2 valley centered at ratio of 1, as one would expect, with boundaries that are consistent with Meseth et al. [54]. Similarly, the two lifetime models yield vertical χ_R^2 valleys, with a slight asymmetry around the ratio of 1. This asymmetry is due to the finite pulse to pulse time window, in which the longer lifetimes of the second component do not fully decay at larger τ_2/τ_1 ratios. From these plots it is immediately clear that there are many experimental conditions for which either FCS or lifetime measurements alone cannot resolve two sample components. In contrast the τFCS approach greatly decreases the range of parameter space, centered at $\tau_1/\tau_2 = D_2/D_1 = 1$, for which two species cannot be clearly resolved. This clearly indicates that τFCS improves the confidence in model selection

over standard FFS methods, and also provides experimental guidelines for how different physical parameter values must be to be easily resolved experimentally using τFCS.

8.6 Discussion

τFCS offers unique advantages over other fluctuations techniques, made possible *via* theoretical considerations of fluorescence signals at both micro- and macro-time scales. The theory introduced here allows us to utilize the amplitudes of fluorescence lifetime decays histograms collected at micro-time scales, in connection with macro-time scale information of fluctuation techniques, such as molecular concentrations and brightnesses. Previously, fluorescence lifetime decay amplitudes of multi-component decays have been used to consider the relative fraction of each lifetime species present [78-80]. It has thus not been possible to determine more than the presence of multiple species and their relative fraction using fluorescence lifetime as a metric. The unique measurement capabilities of fluorescence fluctuation techniques, specifically the ability to accurately recover concentrations and dynamics, rely on either diffusion coefficients or molecular brightnesses to separate molecular species present in a given sample. Here we have extended the means to separate molecular species by including fluorescence lifetime as a distinguishing parameter, whilst retaining the unique measurement capabilities of fluctuation techniques.

The approach we have undertaken is quite general. Here we have combined fluorescence lifetime decays with fluorescence fluctuation ACFs, yet in principle the theoretical combination of different analytical techniques could be combined to extend upon τFCS. While a combination measurable molecular parameters can be simultaneously acquired [36-40], providing rigorous constraints on the interpretation of multiple data sets, MFD

approaches do not specifically enhance the resolution and resolvability of any given data type. Through our combined theory, which introduces common parameters across different data types, it is now possible to dramatically increase the sensitivity *via* global analyses. τFCS theory allows for global analysis across fluorescence lifetime and FCS data, calculated from a single TCSPC acquisition, and greatly enhances the resolution capabilities compared to each analysis when considered individually. It remains to be seen if other data modalities, calculated from information contained in TCSPC acquisitions such as time-resolved fluorescence anisotropy or FRET, can be incorporated to extend the full power of τFCS combined with global analysis.

We demonstrate experimentally that τFCS can successfully recover concentrations, molecular brightnesses, diffusion coefficients and fluorescence lifetimes from molecular species of similar molecular weight; a remarkable result considering it would not be possible using FCS alone. We also demonstrate using calculated data sets that the same accurate parameter recovery can be achieved from binary dye mixtures with identical molecular brightnesses and diffusion coefficients. These data highlight the power of the τFCS approach: the ability to recover information unique to fluctuation techniques, such as molecular concentrations, yet from within sample compositions for which all other fluctuation techniques would be ineffective.

The intrinsic global linkage of τFCS has been extended by acquiring multiple data points across a concentration titration, and subsequently analyzed as a complete full-global data set. Utilizing this kind of global analysis requires variations in experimental conditions, be it by design or happenstance, that do not alter the global parameters of inquiry. The early experiment of Knutson et al. [49] took advantage of the difference in emission spectra of two molecular species, resulting in independently varying decay

amplitudes of each species upon changing the collection wavelength. For each acquisition wavelength the fluorescence lifetimes remained unchanged, and as such, were treated globally across all data sets simultaneously. This variation in local parameters increases the constraints on the minimization resulting in faster and more accurate data fitting. Although each experimental system may have differing local and global parameters that will need individual assessment, the combined theory and analysis of τFCS allows more experimental options for attaining the varied data sets required for global analysis across τFCS acquisitions. The potential for greatly increased resolvability and accuracy during *in vivo* experiments, attained for example by varying excitation wavelengths, remains to be explored.

Using the full global analysis afforded by τFCS across the entire concentration titration dramatically increases the resolvability of molecular concentrations. The ability to accurately recover concentration values from <4% of a considerably less bright species is outstanding, especially considering that this corresponds to only 2 % of the acquired fluorescence signal. The enhanced sensitivity of these results is twofold: not only is it possible to accurately recover fit parameters from very small fractions of the entire signal, it is possible with no prior knowledge of the sample composition and no held molecular parameters during the fitting process. The freedom from parameter assumptions and calibrations, together with the marked improvement in accuracy highlight the benefits of using full global analyses with τFCS. As such this new approach will be beneficial in many biochemical and chemical assays, with an extremely appealing potential for *in vivo* experiments where unknown interactions are likely, signal to noise levels are low, and high sensitivity is required.

The improvement in resolvability and accuracy attained using τFCS analyses originate from a number of overlapping factors. In addition to the intrinsic global linkage provided *via* common amplitude parameters of both the lifetime decay and ACF, the functional form of each amplitude and their parameter dependencies further assist minimization routines during data fitting. For example, the molecular brightness is linear in τFCS decay amplitudes whilst being non-linear in the ACFs, which significantly constrains the models that can reasonably fit both data sets. In addition, the effects of saturation and finite pulse windows are also incorporated into τFCS theory, and while not explicitly investigated here, these factors will help retain resolution when higher powers or longer fluorescence lifetimes are present.

An equally important topic is that of determining the correct fit model using data alone, without prior assumptions of sample composition or the underlying physical process(es) driving the fluorescence fluctuations. τFCS's increased ability to resolve small fractions of different fluorescent species provides an inherent capacity in model discrimination, which we have demonstrated by distinguishing the presence of a second species across a wide range of parameter combinations. The array of χ_R^2 values demonstrates the increased parameter space for which τFCS can separate species and provides a metric for experimental design using the available custom Igor routines. Although we have not included fitting models that incorporate triplet state dynamics, we expect that τFCS will provide significantly more confidence in distinguishing photophysical effects from additional species, a commonly debated subject.

While τFCS will require additional TCSPC hardware if not available, it can be performed in any situation where standard FCS measurements are undertaken. Given the almost plug-and-play simplicity of recent TCSPC systems, together with our prediction that

desktop computers will soon be fast enough to perform the same task, we envision that the theoretically and globally combined τFCS method could entirely replace FCS alone.

8.7 Acknowledgments

We would like to thank NSF grants MCB-0817966 and DMR-0907435 for funding this project, and John Weeks of Wavemetrics for his help understanding the subtleties of Igor Pro's data fitting procedures.

8.8 References

1. Webb, R.H., *Confocal Optical Microscopy*. Reports on Progress in Physics, 1996. **59**(3): p. 427-471.
2. White, J.G., W.B. Amos, and M. Fordham, *An Evaluation of Confocal Versus Conventional Imaging of Biological Structures by Fluorescence Light-Microscopy*. Journal of Cell Biology, 1987. **105**(1): p. 41-48.
3. Hell, S.W. and J. Wichmann, *Breaking the Diffraction Resolution Limit by Stimulated-Emission - Stimulated-Emission-Depletion Fluorescence Microscopy*. Optics Letters, 1994. **19**(11): p. 780-782.
4. Hess, S.T., T.P.K. Girirajan, and M.D. Mason, *Ultra-High Resolution Imaging by Fluorescence Photoactivation Localization Microscopy*. Biophysical Journal, 2006. **91**(11): p. 4258-4272.
5. Huang, B., et al., *Three-Dimensional Super-Resolution Imaging by Stochastic Optical Reconstruction Microscopy*. Science, 2008. **319**(5864): p. 810-813.
6. Gustafsson, M.G.L., *Nonlinear Structured-Illumination Microscopy: Wide-Field Fluorescence Imaging with Theoretically Unlimited Resolution*. Proceedings of the National Academy of Sciences of the United States of America, 2005. **102**(37): p. 13081-13086.
7. Qian, H., M.P. Sheetz, and E.L. Elson, *Single-Particle Tracking - Analysis of Diffusion and Flow in 2-Dimensional Systems*. Biophysical Journal, 1991. **60**(4): p. 910-921.
8. Nie, S.M., D.T. Chiu, and R.N. Zare, *Real-Time Detection of Single-Molecules in Solution by Confocal Fluorescence Microscopy*. Analytical Chemistry, 1995. **67**(17): p. 2849-2857.
9. Weiss, S., *Fluorescence Spectroscopy of Single Biomolecules*. Science, 1999. **283**(5408): p. 1676-1683.
10. Chen, Y., et al., *Fluorescence Fluctuation Spectroscopy*. Methods, 1999. **19**(2): p. 234-252.

11. Haustein, E. and P. Schwille, *Single-Molecule Spectroscopic Methods*. Current Opinion in Structural Biology, 2004. **14**(5): p. 531-540.

12. Becker, W., et al., *Fluorescence Lifetime Imaging by Time-Correlated Single-Photon Counting*. Microscopy Research and Technique, 2004. **63**(1): p. 58-66.

13. Konig, K., *Multiphoton Microscopy in Life Sciences*. Journal of Microscopy-Oxford, 2000. **200**: p. 83-104.

14. Stephens, D.J. and V.J. Allan, *Light Microscopy Techniques for Live Cell Imaging*. Science, 2003. **300**(5616): p. 82-86.

15. Gadella Jr, T.W.J., T.M. Jovin, and R.M. Clegg, *Fluorescence Lifetime Imaging Microscopy (Flim): Spatial Resolution of Microstructures on the Nanosecond Time Scale*. Biophysical Chemistry, 1993. **48**(2): p. 221-239.

16. Bastiaens, P.I.H. and A. Squire, *Fluorescence Lifetime Imaging Microscopy: Spatial Resolution of Biochemical Processes in the Cell*. Trends in Cell Biology, 1999. **9**(2): p. 48-52.

17. Borst, J.W. and A. Visser, *Fluorescence Lifetime Imaging Microscopy in Life Sciences*. Measurement Science & Technology, 2010. **21**(10).

18. Selvin, P.R., *The Renaissance of Fluorescence Resonance Energy Transfer*. Nature Structural Biology, 2000. **7**(9): p. 730-734.

19. Sun, Y.S., et al., *Fret Microscopy in 2010: The Legacy of Theodor Forster on the 100th Anniversary of His Birth*. Chemphyschem, 2011. **12**(3): p. 462-474.

20. Förster, T., *Zwischenmolekulare Energiewanderung Und Fluoreszenz*. Annalen der Physik, 1948. **437**(1-2): p. 55-75.

21. Elson, E.L. and D. Magde, *Fluorescence Correlation Spectroscopy .1. Conceptual Basis and Theory*. Biopolymers, 1974. **13**(1): p. 1-27.

22. Chen, Y., et al., *The Photon Counting Histogram in Fluorescence Fluctuation Spectroscopy*. Biophysical Journal, 1999. **77**(1): p. 553-567.

23. Schwille, P., F.J. MeyerAlmes, and R. Rigler, *Dual-Color Fluorescence Cross-Correlation Spectroscopy for Multicomponent Diffusional Analysis in Solution*. Biophysical Journal, 1997. **72**(4): p. 1878-1886.

24. Kask, P., et al., *Fluorescence-Intensity Distribution Analysis and Its Application in Biomolecular Detection Technology*. Proceedings of the National Academy of Sciences of the United States of America, 1999. **96**(24): p. 13756-13761.

25. Wu, B. and J.D. Muller, *Time-Integrated Fluorescence Cumulant Analysis in Fluorescence Fluctuation Spectroscopy*. Biophysical Journal, 2005. **89**(4): p. 2721-2735.

26. Digman, M.A., et al., *Measuring Fast Dynamics in Solutions and Cells with a Laser Scanning Microscope*. Biophysical Journal, 2005. **89**(2): p. 1317-1327.

27. Schwille, P., et al., *Molecular Dynamics in Living Cells Observed by Fluorescence Correlation Spectroscopy with One- and Two-Photon Excitation*. Biophysical Journal, 1999. **77**(4): p. 2251-2265.

28. Digman, M.A. and E. Gratton, *Scanning Image Correlation Spectroscopy*. BioEssays, 2012. **34**(5): p. 377-385.

29. Elliot L, E., *Fluorescence Correlation Spectroscopy: Past, Present, Future*. Biophys. J., 2011. **101**(12): p. 2855-2870.

30. Kask, P., et al., *Two-Dimensional Fluorescence Intensity Distribution Analysis: Theory and Applications*. Biophysical Journal, 2000. **78**(4): p. 1703-1713.

31. Skinner, J.P., et al., *Determining Antibody Stoichiometry Using Time-Integrated Fluorescence Cumulant Analysis*. Journal of Physical Chemistry B, 2011. **115**(5): p. 1131-1138.

32. Berland, K.M., et al., *Scanning Two-Photon Fluctuation Correlation Spectroscopy: Particle Counting Measurements for Detection of Molecular Aggregation*. Biophysical Journal, 1996. **71**(1): p. 410-420.

33. Eigen, M. and R. Rigler, *Sorting Single Molecules - Application to Diagnostics and Evolutionary Biotechnology*. Proceedings of the National Academy of Sciences of the United States of America, 1994. **91**(13): p. 5740-5747.

34. Wu, B., Y. Chen, and J.D. Muller, *Dual-Color Time-Integrated Fluorescence Cumulant Analysis*. Biophysical Journal, 2006. **91**(7): p. 2687-2698.

35. Muller, J.D., *Cumulant Analysis in Fluorescence Fluctuation Spectroscopy*. Biophysical Journal, 2004. **86**(6): p. 3981-3992.

36. Widengren, J., et al., *Single-Molecule Detection and Identification of Multiple Species by Multiparameter Fluorescence Detection*. Analytical Chemistry, 2006. **78**(6): p. 2039-2050.

37. Brand, L., et al., *Single-Molecule Identification of Coumarin-120 by Time-Resolved Fluorescence Detection: Comparison of One- and Two-Photon Excitation in Solution*. Journal of Physical Chemistry A, 1997. **101**(24): p. 4313-4321.

38. Kühnemuth, R. and C.A.M. Seidel, *Principles of Single Molecule Multiparameter Fluorescence Spectroscopy*. Single Molecules, 2001. **2**(4): p. 251-254.

39. Weidtkamp-Peters, S., et al., *Multiparameter Fluorescence Image Spectroscopy to Study Molecular Interactions*. Photochemical & Photobiological Sciences, 2009. **8**(4): p. 470-480.

40. Nguyen, T.A., et al., *Fluorescence Polarization and Fluctuation Analysis Monitors Subunit Proximity, Stoichiometry, and Protein Complex Hydrodynamics*. PLoS ONE, 2012. **7**(5): p. e38209.

41. Vitali, M., et al., *Wide-Field Multi-Parameter Flim: Long-Term Minimal Invasive Observation of Proteins in Living Cells*. PLoS ONE, 2011. **6**(2): p. e15820.

42. Laptenok, S.P., et al., *Global Analysis of Forster Resonance Energy Transfer in Live Cells Measured by Fluorescence Lifetime Imaging Microscopy Exploiting the Rise Time of Acceptor Fluorescence*. Physical Chemistry Chemical Physics, 2010. **12**(27): p. 7593-7602.

43. Hoffmann, A., et al., *Mapping Protein Collapse with Single-Molecule Fluorescence and Kinetic Synchrotron Radiation Circular Dichroism Spectroscopy*. Proceedings of the National Academy of Sciences, 2007. **104**(1): p. 105-110.

44. Laurence, T.A., et al., *Probing Structural Heterogeneities and Fluctuations of Nucleic Acids and Denatured Proteins*. Proceedings of the National Academy of Sciences of the United States of America, 2005. **102**(48): p. 17348-17353.

45. Rahim, N.A.A., et al., *Methodological Considerations for Global Analysis of Cellular Flim/Fret Measurements*. Journal of biomedical optics, 2012. **17**(2): p. 026013-13.

46. Borst, J.W., et al., *Structural Changes of Yellow Cameleon Domains Observed by Quantitative Fret Analysis and Polarized Fluorescence Correlation Spectroscopy*. Biophys. J., 2008: p. biophysj.107.114587.

47. Previte, M.J.R., et al., *Spectrally Resolved Fluorescence Correlation Spectroscopy Based on Global Analysis*. Analytical Chemistry, 2008. **80**(9): p. 3277-3284.

48. Beechem, J.M., *Global Analysis of Biochemical and Biophysical Data*. Methods in Enzymology, 1992. **210**: p. 37-54.

49. Knutson, J.R., J.M. Beechem, and L. Brand, *Simultaneous Analysis of Multiple Fluorescence Decay Curves - a Global Approach*. Chemical Physics Letters, 1983. **102**(6): p. 501-507.

50. Skakun, V.V., et al., *Global Analysis of Fluorescence Fluctuation Data*. European Biophysics Journal, 2005. **34**(4): p. 323-334.

51. Chen, Y., et al., *Probing Ligand Protein Binding Equilibria with Fluorescence Fluctuation Spectroscopy*. Biophysical Journal, 2000. **79**(2): p. 1074-1084.

52. Kapusta, P., et al., *Fluorescence Lifetime Correlation Spectroscopy*. Journal of Fluorescence, 2007. **17**(1): p. 43-48.

53. Böhmer, M., et al., *Time-Resolved Fluorescence Correlation Spectroscopy*. Chemical Physics Letters, 2002. **353**(5-6): p. 439-445.

54. Meseth, U., et al., *Resolution of Fluorescence Correlation Measurements*. Biophysical Journal, 1999. **76**(3): p. 1619-1631.

55. Mertz, J., *Molecular Photodynamics Involved in Multi-Photon Excitation Fluorescence Microscopy*. The European Physical Journal D - Atomic, Molecular, Optical and Plasma Physics, 1998. **3**(1): p. 53-66.

56. Berland, K. and G.Q. Shen, *Excitation Saturation in Two-Photon Fluorescence Correlation Spectroscopy*. Applied Optics, 2003. **42**(27): p. 5566-5576.

57. Cianci, G.C., J. Wu, and K.M. Berland, *Saturation Modified Point Spread Functions in Two-Photon Microscopy*. Microscopy Research and Technique, 2004. **64**(2): p. 135-141.

58. Nagy, A., J.R. Wu, and K. Berland, *Photodynamics in Fluorescence Correlation Spectroscopy*. Biophysical Journal, 2004. **86**(1): p. 320A-320A.

59. Nagy, A., J. Wu, and K.M. Berland, *Observation Volumes and Gamma-Factors in Two-Photon Fluorescence Fluctuation Spectroscopy*. Biophys. J., 2005. **89**(3): p. 2077-2090.

60. Wu, J. and K. Berland, *Fluorescence Intensity Is a Poor Predictor of Saturation Effects in Two-Photon Microscopy: Artifacts in Fluorescence Correlation Spectroscopy*. Microscopy Research and Technique, 2007. **70**(8): p. 682-686.

61. Anthony, N.R. and K.M. Berland, *Global Analysis in Fluorescence Correlation Spectroscopy and Fluorescence Lifetime Microscopy*, in *Methods in Enzymology*. In Press, Elsevier B.V.

62. Xu, C. and W.W. Webb, *Multiphoton Excitation of Molecular Fluorophores and Nonlinear Laser Microscopy*, in *Topics in Fluorescence Spectroscopy*, J. Lakowicz, Editor. 1997, Plenum. p. 471-540.

63. Thompson, N.L., *Fluorescence Correlation Spectroscopy*, in *Topics in Fluorescence Spectroscopy*, J.R. Lakowicz, Editor. 1991, Plenum: New York. p. 337-378.

64. Mertz, J., C. Xu, and W.W. Webb, *Single-Molecule Detection by Two-Photon-Excited Fluorescence*. Optics Letters, 1995. **20**(24): p. 2532-2534.

65. Webb, W.W., *Fluorescence Correlation Spectroscopy: Inception, Biophysical Experimentations, and Prospectus*. Applied Optics, 2001. **40**(24): p. 3969-3983.

66. Chen, Y., et al., *Two-Photon Fluorescence Fluctuation Spectroscopy*, in *New Trends in Fluorescence Spectroscopy: Applications to Chemical and Life Sciences*, B. Valeur and J.C. Brochon, Editors. 2001, Springer-verlag: Berlin.

67. Krichevsky, O. and G. Bonnet, *Fluorescence Correlation Spectroscopy: The Technique and Its Applications*. Reports on Progress in Physics, 2002. **65**(2): p. 251-297.

68. Magde, D., W.W. Webb, and E. Elson, *Thermodynamic Fluctuations in a Reacting System - Measurement by Fluorescence Correlation Spectroscopy*. Physical Review Letters, 1972. **29**(11): p. 705-&.

69. Korlach, J., et al., *Characterization of Lipid Bilayer Phases by Confocal Microscopy and Fluorescence Correlation Spectroscopy*. Proceedings of the National Academy of Sciences of the United States of America, 1999. **96**(15): p. 8461-8466.

70. Berland, K.M., *Detection of Specific DNA Sequences Using Dual-Color Two-Photon Fluorescence Correlation Spectroscopy*. Journal of Biotechnology, 2004. **108**(2): p. 127-136.

71. Petrasek, Z. and P. Schwille, *Precise Measurement of Diffusion Coefficients Using Scanning Fluorescence Correlation Spectroscopy*. Biophysical Journal, 2008. **94**(4): p. 1437-1448.

72. Marchand, P. and L. Marmet, *Binomial Smoothing Filter - a Way to Avoid Some Pitfalls of Least-Squares Polynomial Smoothing*. Review of Scientific Instruments, 1983. **54**(8): p. 1034-1041.

73. Becker, W., *Advanced Time-Correlated Single Photon Counting Techniques*. 2005: Springer.

74. Mukhtar, E., F. Bergstrom, and L.B.A. Johansson, *Hyper Rayleigh Scattering Yields Improved Response Function in Analysing 2-Photon Excited Fluorescence*. Journal of Fluorescence, 2002. **12**(3-4): p. 481-484.

75. Starchev, K., J. Ricka, and J. Buffle, *Noise on Fluorescence Correlation Spectroscopy*. Journal of Colloid and Interface Science, 2001. **233**(1): p. 50-55.

76. Kelly, S.M., et al., *Recognition of Polyadenosine Rna by Zinc Finger Proteins*. Proceedings of the National Academy of Sciences of the United States of America, 2007. **104**(30): p. 12306-11.

77. Rigler, R., et al., *Specific Binding of Proinsulin C-Peptide to Human Cell Membranes*. Proceedings of the National Academy of Sciences of the United States of America, 1999. **96**(23): p. 13318-13323.

78. Beechem, J.M. and L. Brand, *Time-Resolved Fluorescence of Proteins*. Annual Review of Biochemistry, 1985. **54**: p. 43-71.

79. Evans, N.D., et al., *Glucose-Dependent Changes in Nad(P)H-Related Fluorescence Lifetime of Adipocytes and Fibroblasts in Vitro: Potential for Non-Invasive Glucose Sensing in Diabetes Mellitus*. Journal of Photochemistry and Photobiology B: Biology, 2005. **80**(2): p. 122-129.

80. Szmacinski, H. and J.R. Lakowicz, *Fluorescence Lifetime-Based Sensing and Imaging*. Sensors and Actuators B: Chemical, 1995. **29**(1–3): p. 16-24.

Chapter 9

Discussion

Throughout this dissertation I have demonstrated the application of microscopic techniques for the investigations of numerous stages of peptide aggregation and structure. While effective therapeutic strategies for peptide misfolding diseases such as Alzheimer's continue to be elusive [1], therapeutic strategies at the core of peptide misfolding diseases lays a ubiquitous cross-β tertiary peptide architecture [2]. As the cross-β motif may be the ancestor of protein tertiary structure in general [3, 4], it is likely entwined into many more biological pathways and systems than currently documented [4-9], further highlighting the root importance for a deeper understanding of the folding pathways of this motif. In this dissertation, I have discussed the role of pH, temperature, solvents, solubility, and interfaces for the control and capture of the earliest stages of the ubiquitous cross-β motif. In addition, I have characterized the nucleation pathway from monomer to paracrystalline nanotube in terms of morphology and fluorescence lifetime (Chapter 5), and identified single-structure heterogeneous domain nanotubes (Chapter 7).

Fully elucidating the pathways and networks of the cross-β motif will most likely be required before we can completely understand its role in both disease and as a functional biopolymer. More complete pathway information will allow precise delineation between the forces directing toxic, functional, non-toxic, and non-functional forms of amyloid. A common thread of the studies presented in chapters 2-6 is identification and characterization of the point of nucleation in the amyloid self-assembly pathway. This

phase transition is seen to occur within molten globules, whereby ordered peptide structures form within disordered hydrophobically collapsed aggregates. Identifying the presence and increase in peptide order, followed by the subsequent observations of elongating nanotube structures, identifies the location of this all-important transition. The initial stages of hydrophobic collapse have been interrogated in the form of pH, solvent, and temperature-arrested particle phases (Chapter 4), diffuse aggregates initiated by heterogeneous interfaces (Chapter 5), and the varying fractions of order seen within Rh17-22 molten globules (Chapter 6). Probing the local environment *via* Rh17-22 peptide fluorescence (Chapter 5) confirms the predicted stages of hydrophobic collapse [10-14], whereby solvent is expelled from peptide dense molten aggregates resulting in increased peptide-peptide interactions. Electron microscopy (EM) (Chapter 4) and second harmonic generation (SHG) imaging (Chapter 6) confirm the transition from the molten particle to a more ordered phase. However, the detection of small and transient oligomer species has remained elusive. Given the multitude of interfaces and differing local environments, both *in vitro* and *in vivo*, these initial oligomers are likely very different in their formation and structure, and require increased sensitivity to divulge their subtleties. Although the studies presented here are *in vitro*, the concepts and techniques used could be easily transferred and applied to studies of the full amyloid-β protein, or any other protein mis-folding investigations.

Our groups' previous study of Aß(16-22) nanotube nucleation and growth [14] suggested growth by monomer addition to the nanotube ends, as indicated by the diffusion coefficient measured using fluorescence correlation spectroscopy (FCS). The resolution of FCS requires a minimum of a five molecules (5-mer) to aggregate before they can be distinguished (assuming ideal conditions), and as such, we cannot rule out the possibility of dimer, trimers etc. Moreover, depending on the signal to noise attainable, a small

fraction of larger oligomers may not be readily resolvable using FCS analyses. Given the implicated toxicity and significance of transient oligomeric species in amyloidogenic disease, techniques sensitive enough to resolve these species would be extremely beneficial. In Chapter 8, I describe a newly developed combined analysis technique, τFCS, which is able to resolve species with identical diffusion coefficients, using their fluorescence lifetime as a distinguishing metric. The application of this technique has the potential to provide the much-needed resolvability of dynamic oligomeric species. The application τFCS can be extended to all situations that are currently investigated using FCS alone. Moreover, the concept of combined theoretical analyses coupled with globally linked data analysis has the potential to extend other quantitative fluorescence techniques. Time resolved anisotropy and fluorescence resonance energy transfer experiments would be the natural starting point for further extensions of this concept. Given the increases in data transfer rates of current computers, I envision that coming generations of computers will be able to directly collect the high time resolution data required for τFCS, without the need for expensive TCSPC hardware, and that τFCS will supersede FCS-only acquisitions.

The cross-β tertiary structure central to amyloidogenic diseases has isomorphic structural characteristics, suggested as a class of high-performance biomaterials [15]. These isomorphs have been characterized as distinct species, in which a single peptide conformation is propagated along the entire length of the assembly. Chapter 7 characterizes fluorescent nanotubes that exhibit domains with distinct fluorescence lifetimes along the length of individual peptide assembly. Analyses of these nanotubes have determined that structural differences exist in these discrete domains, occur during the self-assembly elongation phase, and propagates for many micrometers. In this study we have shown that FLIM analyses can distinguish variations in structure that are not

distinguishable with other techniques, such as EM and bulk measurements, highlighting the potential for fluorescence lifetime measurements in functionalized peptide engineering research. Uncovering the cause of the transitions and the factors responsible the long range propagation allows for the exciting potential of designer, modulated peptide nanomaterials. Richard Feynman's talk "There's plenty of room at the bottom," describing the control of individual atoms for the creation of designer nanomaterials, is becoming a closer and closer reality. The recent focus on of amyloid-inspired nanomaterials are utilizing the atomic interactions previously honed by nature, and their potential as functionalized, self-assembling, self-healing bionanomaterials are endless.

9.1 References

1. Selkoe, D.J., *Preventing Alzheimer's Disease*. Science, 2012. **337**(6101): p. 1488-92.
2. Nelson, R., et al., *Structure of the Cross-Beta Spine of Amyloid-Like Fibrils*. Nature, 2005. **435**(7043): p. 773-778.
3. Childers, W.S., et al., *Peptide Membranes in Chemical Evolution*. Curr. Opin. Chem. Biol., 2009. **13**(5-6): p. 652-9.
4. Greenwald, J. and R. Riek, *On the Possible Amyloid Origin of Protein Folds*. Journal of Molecular Biology, 2012. **421**(4-5): p. 417-426.
5. Knowles, T.P.J. and M.J. Buehler, *Nanomechanics of Functional and Pathological Amyloid Materials*. Nature Nanotechnology, 2011. **6**(8): p. 469-479.
6. Fowler, D.M., et al., *Functional Amyloid - from Bacteria to Humans*. Trends Biochem. Sci., 2007. **32**(5): p. 217-24.
7. Ma, B. and R. Nussinov, *Selective Molecular Recognition in Amyloid Growth and Transmission and Cross-Species Barriers*. Journal of Molecular Biology, 2012. **421**(2-3): p. 172-184.
8. Ramachandran, G. and J.B. Udgaonkar, *Evidence for the Existence of a Secondary Pathway for Fibril Growth During the Aggregation of Tau*. Journal of Molecular Biology, 2012. **421**(2-3): p. 296-314.
9. van Grondelle, W., et al., *Spontaneous Fibrillation of the Native Neuropeptide Hormone Somatostatin-14*. J Struct Biol, 2007. **160**(2): p. 211-23.
10. Auer, S., et al., *A Generic Mechanism of Emergence of Amyloid Protofilaments from Disordered Oligomeric Aggregates*. Plos Computational Biology, 2008. **4**(11): p. e1000222.
11. Childers, W.S., et al., *Phase Networks of Cross-Beta Peptide Assemblies*. Langmuir, 2012. **28**(15): p. 6386-6395.

12. Klimov, D.K. and D. Thirumalai, *Dissecting the Assembly of Aβ(16-22) Amyloid Peptides into Antiparallel β Sheets*. Structure, 2003. **11**(3): p. 295-307.

13. Krone, M.G., et al., *Role of Water in Mediating the Assembly of Alzheimer Amyloid-β Aβ16-22 Protofilaments*. Journal of the American Chemical Society, 2008. **130**(33): p. 11066-72.

14. Liang, Y., D.G. Lynn, and K.M. Berland, *Direct Observation of Nucleation and Growth in Amyloid Self-Assembly*. J. Am. Chem. Soc., 2010. **132**(18): p. 6306-6308.

15. Knowles, T.P., et al., *Role of Intermolecular Forces in Defining Material Properties of Protein Nanofibrils*. Science, 2007. **318**(5858): p. 1900-3.